# Tuscaloosa Marine Shale Laboratory

Final Report

## SUBMITTED BY

University of Louisiana at Lafayette
P.O. Box 44690
Lafayette, LA 70504-4690

## PRINCIPAL INVESTIGATOR

Dr. Ning Liu
Phone Number: 337-482-6544
Email: ning.liu@louisiana.edu

Signature:

## SUBMITTED TO

U.S. Department of Energy
National Energy Technology Laboratory
(Project Number: DE-FE0031575)

Report Date: March 30, 2022

## DISCLAIMER

# Acknowledgement

This research was sponsored by the U.S. Department of Energy through the National Energy Technology Laboratory (grant # DE-FE-0031575).

The contributions of the project team members and graduate students are greatly appreciated. They are Dr. Boyun Guo, Dr. Rui Zhang, Dr. Asadollah Hayatdavoudi, Dr. Raphael Hernandez, Dr. Mehdi Mokhtari, Dr. Prathmesh Naik Parrikar, Dr. David Borrok (Missouri University of Science and Technology), Dr. Saeed Saleh (University of Oklahoma), Dr. Chad R. Miller (University of Southern Mississippi), Dr. Gilles Bussod (Los Alamos National Laboratory), Mr. Philip Wortman, Mr. Maksym Chuprin, Miss. Sarah Traore, Miss. Cristina Mariana Ruse, Mr. Santosh Ghimire

## Abstract

The Tuscaloosa Marine Shale (TMS) in Louisiana and Mississippi is an Upper Cretaceous source rock formation sandwiched between the sands of the upper and lower Tuscaloosa sections. The TMS is believed to be the source rock for underlying prolific Tuscaloosa sand formation. The TMS has an unproven estimate of 7,000,000,000 bbls of recoverable oil while its current total average production is about 3,000 bbls of oil per day in 2017. In 2013 and 2014, more than 80 wells were drilled horizontally into the TMS that were fractured using multi-stage fracturing technology. The results from this have been mixed, but recent production for several wells show an appealing initial oil production rate of more than 1000 bbl/day. The preliminary core analysis by industry partners and a few literature studies shows that the TMS is one of the most clay-rich and sensitive shales to water. Due to these and other technical problems, there is high risk for the economic development of TMS compared to other shale plays. The experiences of major industrial players in the TMS show the necessity of open and collaborative efforts to better understand the critical gaps in the development of this challenging and potentially highly economic shale play to enable more cost-efficient and environmentally-sound recovery from this unconventional liquid-rich shale play.

The overall objective of this project is to form a consortium of science and industry partners to address the following six major objectives using scientific and technical approaches:

1. To improve wellbore integrity by better understanding the sources of the wellbore instability issues, proposing innovative mud and cement design for the TMS.

2. To improve formation evaluation using laboratory techniques for the evaluation of mineralogical composition, organic content, and produced-water chemistry as well as well log and geophysical analysis.

3. To determine the role of geologic discontinuities on fracture growth and shale creep behavior using digital image correlation technique.

4. To investigate the application of stable $CO_2$ foam and super-hydrophobic proppants for improved reservoir stimulation.

5. To better understand the nature of water/hydrocarbon/$CO_2$ flow in clay and organic-rich formation and the role of water/fluid interaction on recovery.

6. To prepare better socio-economic environment for TMS development by community engagement.

Subsequently, the TMS virtual laboratory conducted testing and analysis of various properties of rock and formation fluids from the TMS, including but not limited to the following:

Analyzing reports and logs to better understand the source of wellbore instability in TMS wells;

Experiments to design a customized cement based on TMS requirements;

Experiments to obtain the mineralogical and geochemical composition of TMS samples;

Seismic analysis of TMS geophysical data to better predict total organic carbon (TOC) content and brittleness in TMS;

Well log analysis to better estimate the TOC and geo-mechanical properties of TMS;

Experiments on formation water to understand the chemistry of produced water;

Experiments to determine the role of lamination and natural fractures on fracture propagation or rock deformation using digital image correlation technique in in-direct tensile tests, semi-circular bend test and creep tests;

Experiments to determine the stability and rheological properties of nanoparticle-stabilized $CO_2$ foam in TMS rock samples;

Experiments to determine fluid dynamics in un-propped TMS fractures and the role of nano-coating of proppants on fluid dynamics in fractures with proppants;

Micro-fluidics experiments to enhance the understanding of fluid dynamics in tight liquidrich pores with high clay content;

Socio-economic studies to better engage communities in TMS development.

# TABLE OF CONTENTS

# List of Figures

# List of Tables

## EXECUTIVE SUMMARY

This document is the Final Report for the U.S. Department of Energy under contract No. DEFE-0031575, a three-year contract with a no-cost extension entitled: "Tuscaloosa Marine Shale Laboratory (TMSL)." The research improved our knowledge and understanding some scientific and technical gap in Tuscaloosa Marine Shale (TMS) located in central Louisiana and Southern Mississippi. The University of Louisiana at Lafayette (the lead), the University of Oklahoma (OU), Missouri S&T, University of Southern Mississippi (USM) and Las Alamos National Laboratory (LANL) are academic members of this consortium working on various tasks of this project. TMSL consortium works closely with industry members and has received significant support in terms of whole cores, slabbed cores, cuttings, produced water samples, well logs, drilling and completion reports, mud logging reports, and other well data. This report covers the reporting period of May 1, 2018 through December 31, 2021.

This report summarizes the work completed under the above-mentioned contract. This document does not attempt to detail all the work that has been completed. Much of the work from this project has been reported in the previous quarterly reports and various publications, and thus will not be duplicated here, but generally only summarized for the previously published work.

Chapter 1 introduces the background of this project and a brief summary of the statement of work.

Chapter 2 discusses different approaches to improve the drilling practices in the TMS formation, which includes; i) investigation of rock-fluid interaction in term of compatibility; ii) development of more suitable drilling fluid systems for improving TMS drilling practices; and iii) investigation and development of lost circulation mud systems for mitigating fluid loss.

Chapter 3 summarizes different studies to improving TMS formation evaluation. TMS formation evaluation is performed as: (1) Characterization of brittleness and total organic carbon (TOC) of TMS with machine learning technique; (2) TMS properties from geophysical analysis; (3) Mineralogical composition, organic-richness and produced-water chemistry of TMS; (4) Ionic movement between TMS cores and water.

Chapter 4 presents the results of TMS rock properties with digital image correlation (DIC) system. TMS properties such as geomechanical properties, fracture toughness, fracture creep, and thermal conductivity are studied.

Chapter 5 evaluates $CO_2$ foam as a fracturing fluid and application super-hydrophobic proppant to improve fracturing performance in TMS. Nanoparticle-stabilized CO2 foam is proposed as the fracturing fluid and the foam rheology and leakoff are evaluated at different reservoir conditions. The application of super-hydrophobic proppants on fracture conductivity under different conditions is studied to understand the proppant surface property effect on fracture conductivity.

Chapter 6 evaluates the feasibility of enhancing hydrocarbon extraction in bituminous-rich shale lithologies at *in-situ*, downhole pressure and temperature conditions. Supercritical $CO_2$ with small amount of additives such as propanol and tetrahydrofuran displays more efficiency to extract hydrocarbon from shale.

Chapter 7 examines hydraulic fracturing from an economic development perspective by 1) the supply chain, 2) severance taxes, 3) workforce, and 4) business assistance programs for the industry in the TMS. The findings provide lessons and techniques for rural communities engaged with a shale economy to improve their socio-economic outcomes.

Chapter 8, "Technology Transfer," summarizes the numerous papers, reports, and presentations as a result of research performed under this contract.

# CHAPTER 1 Tuscaloosa Marine Shale

## 1.1 Introduction of Tuscaloosa Marine Shale

Tuscaloosa Marine Shale (TMS) is one of the three geologic units within the Upper Cretaceous Tuscaloosa Group. The group is located in the Gulf Coast region of the Central U.S. with producing zones in central Louisiana and southern Mississippi (Fig. 1.1). According to IHS Energy Group, as of 2016, 5.5 billion cubic feet of gas and 9.4 million barrels of low sulfur, 36-48 API gravity oil with GOR of 300-900 has been produced from around 80 horizontal wells in TMS. This productive area of the TMS encompasses around 1,800 square miles and varies in thickness between 400 ft in southern Mississippi to about 800 ft in Louisiana, with the depth of the base reaching over 14,000 ft in some sections. The mineralogy of the TMS is dominated by clay minerals, with values between 40 and 80 wt%, whereas the amount of quartz is 20 to 40 wt% and calcite is less than 40 wt%. The porosity of the TMS ranges from as low as 1% to around 10%. The amount of Total Organic Carbon in the basal TMS averages at 1.65 wt%, with Type II and Type III kerogen dominating, which suggests that the samples fall into the oil and wet gas window (Borrok et al., 2019).

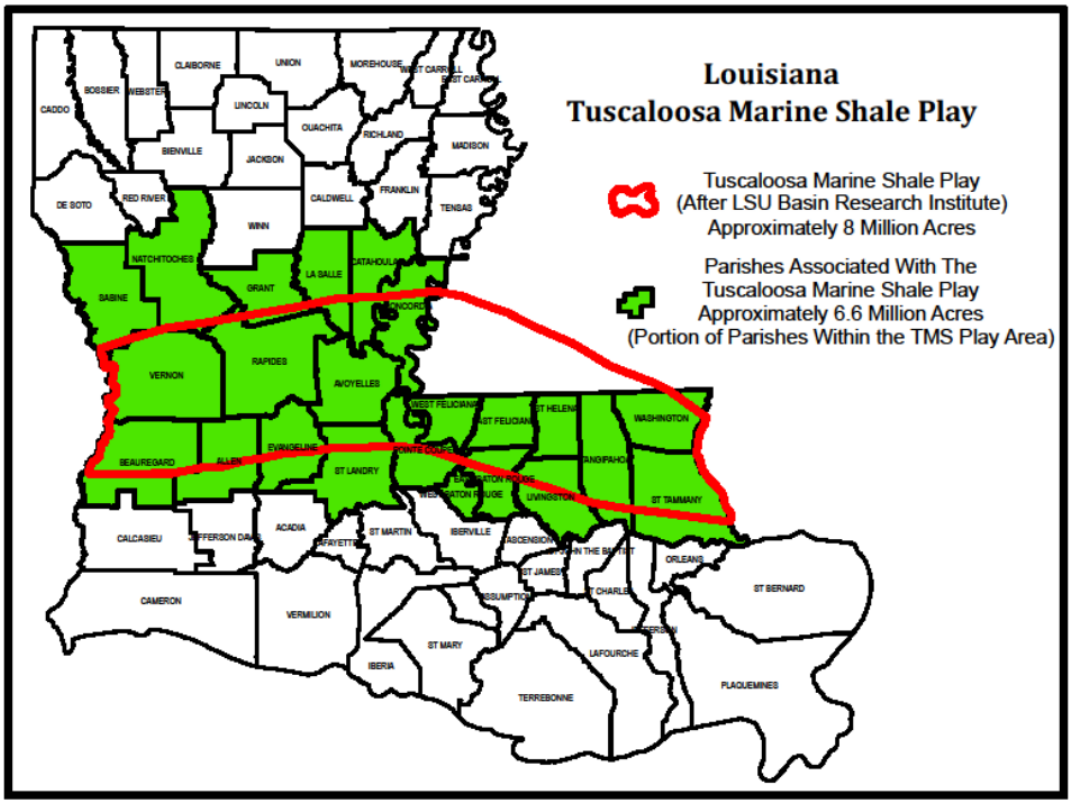


**Figure 1.1, Map showing outline of the TMS over Louisiana.**

The lower unit in the Tuscaloosa Group represents a transgressive phase; it was deposited onto mid-Cenomanian unconformity (Mancini et.al. 2008), and consists of arenaceous massive sand and argillaceous stringer sands, indicating high siliciclastic sediment supply. The middle unit (TMS) has been deposited conformably on the lower Tuscaloosa during a significant marine flooding event, represents the inundated depositional cycle, and is mostly grayish-black, fissile, and sandy in some regions (John et al., 1997). TMS is preserved in eastern Louisiana, southern Mississippi, and southwestern Alabama (Mancini et al., 2008). The upper unit represents the regressive depositional cycle (John et al., 1997), consists mostly of deltaic and fluvial sandstones and siltstones deposited conformably on top of TMS, indicating another increase in siliciclastic sediment supply.

### 1.2 Production Data in TMS

Although TMS is a relatively new development, production has been from the reservoirs of the Lower Tuscaloosa sands in Mississippi, Louisiana, and Alabama . The TMS was thought to be the source rock for most of the oil produced from the underlying lower Tuscaloosa massive sands (Echols, 1997). In the 1950s, oil and gas exploration was conducted from massive sandstones in the Lower Tuscaloosa in southern Alabama (Mancini et al., 2008). In September 1950, when operators targeting the Lower Tuscaloosa sands discovered that a large amount of oil and gas had flowed in from the TMS unit, the over-pressured zones were encountered for the first time.

In 1971, the Sun Oil Company drilled the well Sun #1 Spinks in Pike County, Mississippi (Lu et al., 2015). However, it was plugged and abandoned owing to none commercial production even though it was fractured with 30,000 lbs of sand (John et al., 1997). In 1974, another well Callon #1 Cutrer drilled in Tangipahoa Parish, Louisiana, was abandoned after running an uncemented liner through the TMS. The first successful exploration of TMS began in 1975 in Tangipahoa Parish, Louisiana (John et al., 2005). The Callon #2 Cutrer was fractured with about 80,000 pounds of sand and produced about 2,500 barrels of oil from the TMS over the interval from 11,073 to 11,644 ft before it was plugged in 1991 (John et al., 1997). In 1977, the Texas Pacific #1 Blades was drilled in Tangipahoa Parish, Louisiana. This well has produced more than 27,500 barrels of oil and is still producing a few barrels per day. Unfortunately, several vertical wells in TMS over the years failed to produce more than a few barrels of oil per day, which reduced the interest of TMS as a commercial oil resource.

Drilling activity to date was centered in Amite and Wilkinson Counties. The study area and locations of 89 TMS wells are presented in Figure 1.2. The production data of TMS wells as of April 2020 were gathered from the Mississippi Automated Resource Information System (MARIS) (www.maris.state.ms.us) and Strategic Online Natural Resources Information System (SONIS) (http://www.sonris.com). These two websites report well monthly production data of TMS wells. 79 TMS wells completed between 2011 and 2016 were considered in this investigation. Wells #1, #2, #4, #7, #9, #13, #17, #31, #32, and #58 in Figure 1.2 were not considered. As of April 2020, these 79 wells have cumulatively produced around 13.82 million barrels of oil and 9.04 billion cubic feet of gas.

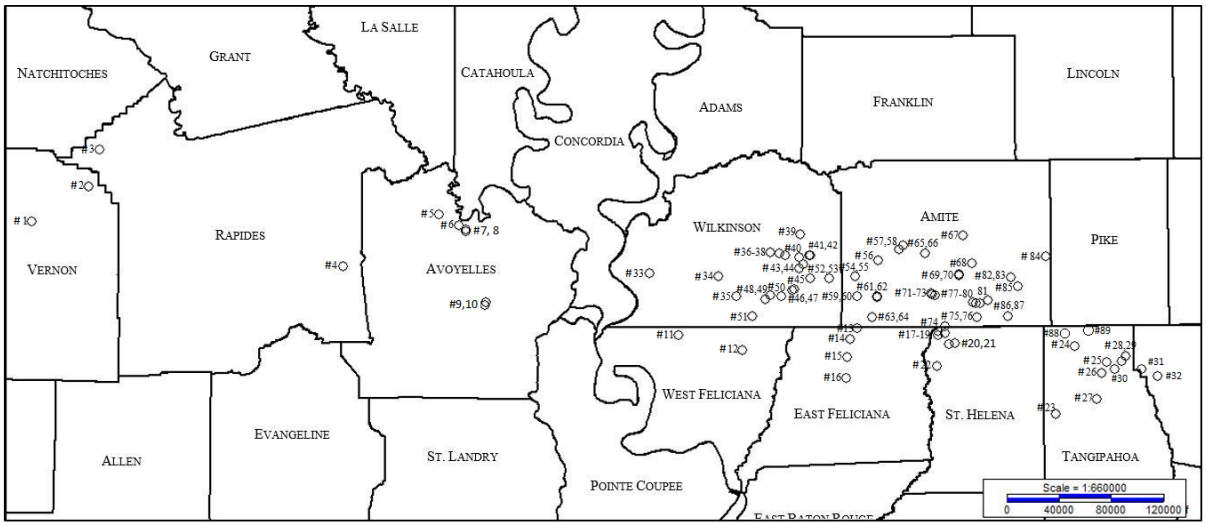


**Figure 1.2, Map showing the locations of TMS wells.**

***Initial Oil Production*** Figure 1.3 shows the initial oil production rate of 79 TMS wells completed between 2011 and 2016. The initial (peak) production is the average production of the month with the highest monthly production. A majority of TMS wells reached peak production within one or two months after the first production. Well #87 had the highest initial oil production rate than any other TMS wells. In 2015, well #87 was completed with a 9,754 effective lateral and fractured with 29 stages. It has the longest lateral in the TMS to date. The initial oil and gas production rates of well #87 were about 1,266 bbl/d and 38 Mcf/d (i.e., 1272 boe/d), respectively.

Well #70, a toe-down lateral, had the second-highest initial oil production rate among 79 TMS wells. In 2015, well #70 was completed with an effective lateral length of 7,138 ft and a 20 stage hydraulic fracturing operation. The total proppant and fluid pumped were 11,184,000 lbs and 126,279 barrels, respectively. It had a peak production rate of about 1,188 bbl/d of oil and 659 Mcf/d of gas (i.e., 1,298 boe/d), respectively. Therefore, well #70 had higher barrels of oil equivalent than well #87. Figure 1.3 also presents the statistical results of the initial oil production rate of 79 TMS wells. The peak oil production rate ranges from 68 to 1,266 bbl/d. The average initial oil production rate of 79 TMS wells was 586 bbl/d, six of which had an initial oil production rate of higher than 1,000 bbl/d.

Figure 1.4 shows the initial oil production bubble map of 79 TMS wells completed between 2011 and 2016. The green bubbles represent the locations of the top-six TMS wells with initial oil production of greater than 1,000 bbl/d. The numbers in the bubble map identify the corresponding order of the initial oil production rate of the top-six wells. Five of the top-six wells are in Amite County, and only one well is in Wilkinson County.

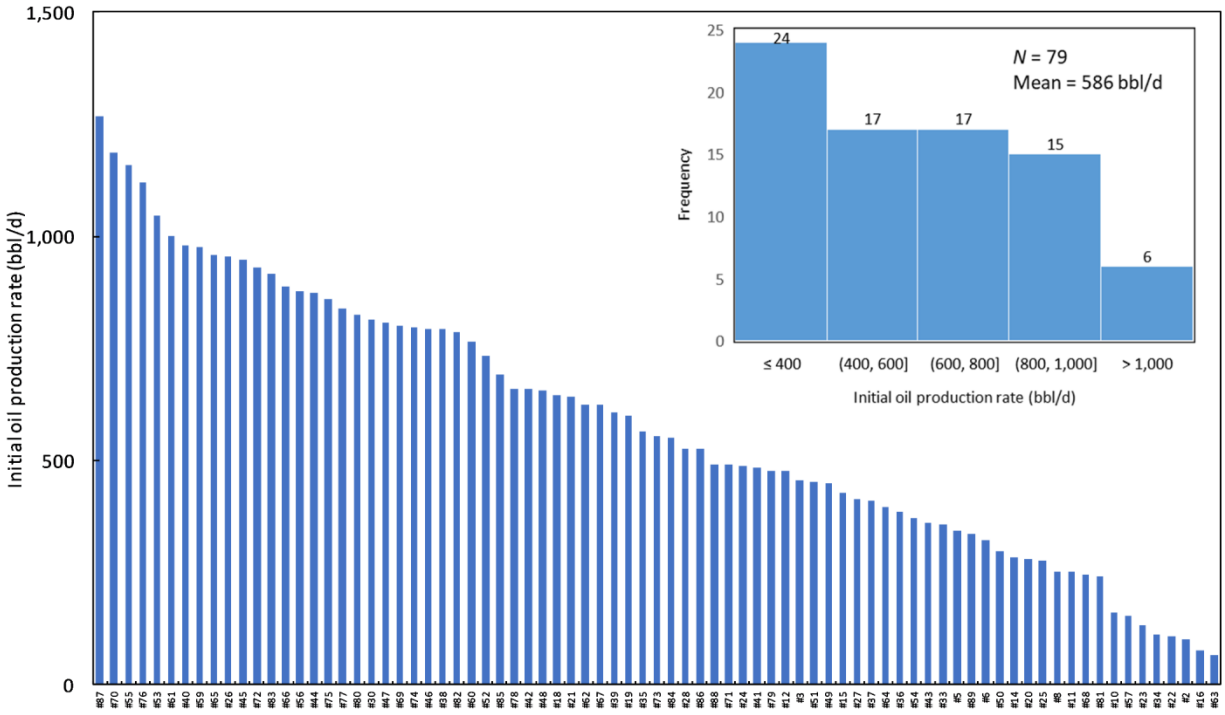


**Figure 1.3, Initial oil production rate of 79 TMS wells completed between 2011 and 2016.**

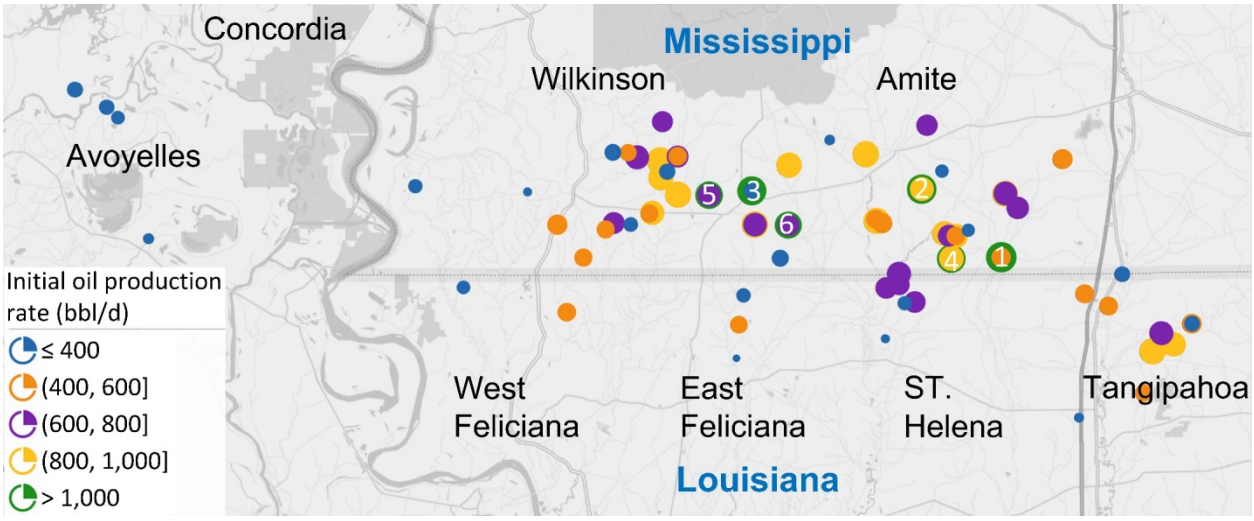


**Figure 1.4, Bubble map of the initial oil production rate of 79 TMS wells completed between 2011 and 2016. The green bubbles represent the locations of 6 TMS wells with initial oil production of greater than 1,000 bbl/d; and the numbers represent the corresponding descending order of initial oil production rate.**

***Initial Gas/Oil Ratio and Water Cut*** Figure 1.5 presents the statistical results of the initial gas/oil ratio (GOR) and water cut of TMS wells. It is worth mentioning that the two websites do not report oil, water, or gas production data for all the TMS wells. The initial GOR was in the range of 30 to 1,050 scf/bbl, with an average of 527 scf/bbl, meaning that TMS wells produced 85%–100% light crude oil (38°–45°API). The initial water cut of 53 TMS wells in Mississippi ranged from 0.01 to 0.66, with an average of 0.37. Figure1.6 shows the initial GOR bubble map of 78 TMS wells because one well did not report monthly gas production in the first two months. The green bubbles represent the locations of 12 TMS wells with initial GOR of higher than 800 scf/bbl. Well #51 has the highest initial GOR of 1,050 scf/bbl. This well was completed in 2014 with an effective lateral of 7,428 ft and fractured with 25 stages. The peak oil production rate was 453 bbl/d. For TMS wells with similar latitudes, the initial GOR in the western area is higher than that in the eastern area, which is consistent with the subsurface elevation and isopach changes within the study area. The structural dip of TMS is generally south-southwest; therefore, the initial GOR tends to decrease in the up-dip direction. Figure1.7 presents the initial water cut bubble map of 53 TMS wells in Mississippi that completed from 2011 to 2016. Most of the TMS wells in Mississippi produced a large amount of water. Hoffmann et al., (2020) indicated that the produced waters from the TMS are highly saline, and the chemistry comparison demonstrated a rapid shift from dilute fracturing fluid to the formation water. They also mentioned that 15%–110% of the water volume used for fracturing returned to the surface within 2–5 years. In addition, the produced water is probably derived from the Louann salt formation (Hoffmann et al., 2020). According to Figure 1.7, well #57 had the highest initial water cut of 0.66 among the 53 wells. The well was completed in 2012 with an effective lateral of 2,351 ft. The peak production was about 152 bbl/d of oil, 70 Mcf/d of gas (i.e., 164 boe/d), and 302 bbl/d of water.

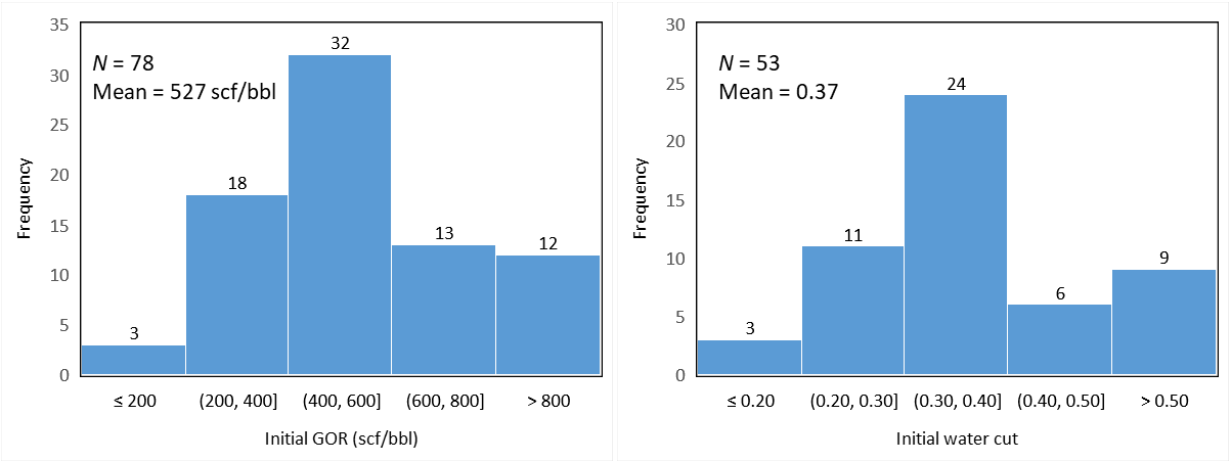


(a) Initial GOR (b) Initial water cut

**Figure 1.5 Statistical results of GOR and water cut for TMS wells completed between 2011 and 2016.**

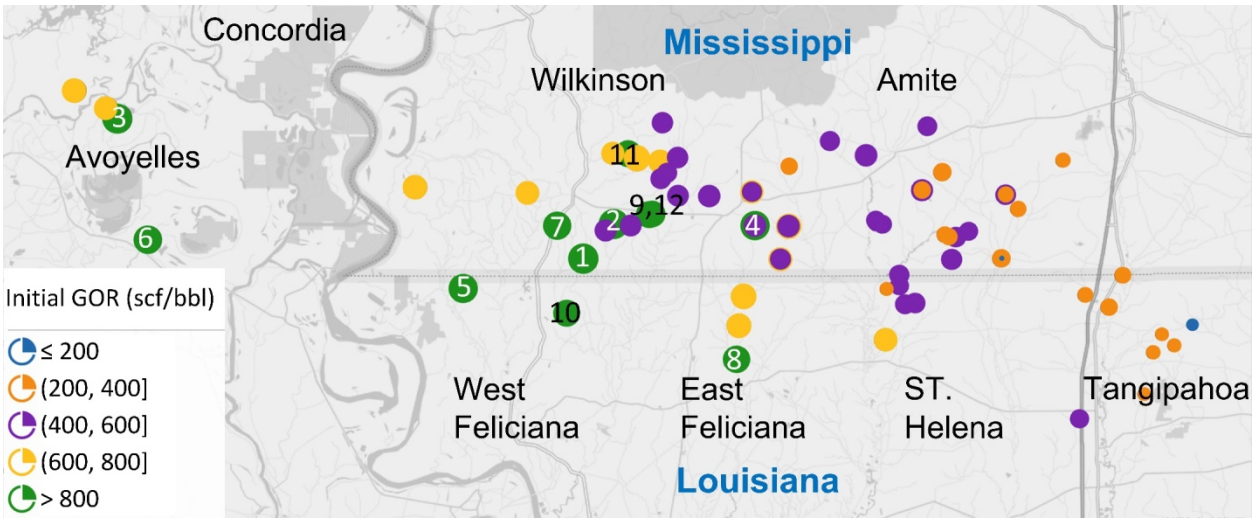


**Figure 1.6 Bubble map of initial GOR of 78 TMS wells completed between 2011 and 2016. The green bubbles represent the locations of 12 TMS wells with initial GOR of higher than 1,000 bbl/d; and the numbers represent the corresponding descending order of initial GOR.**

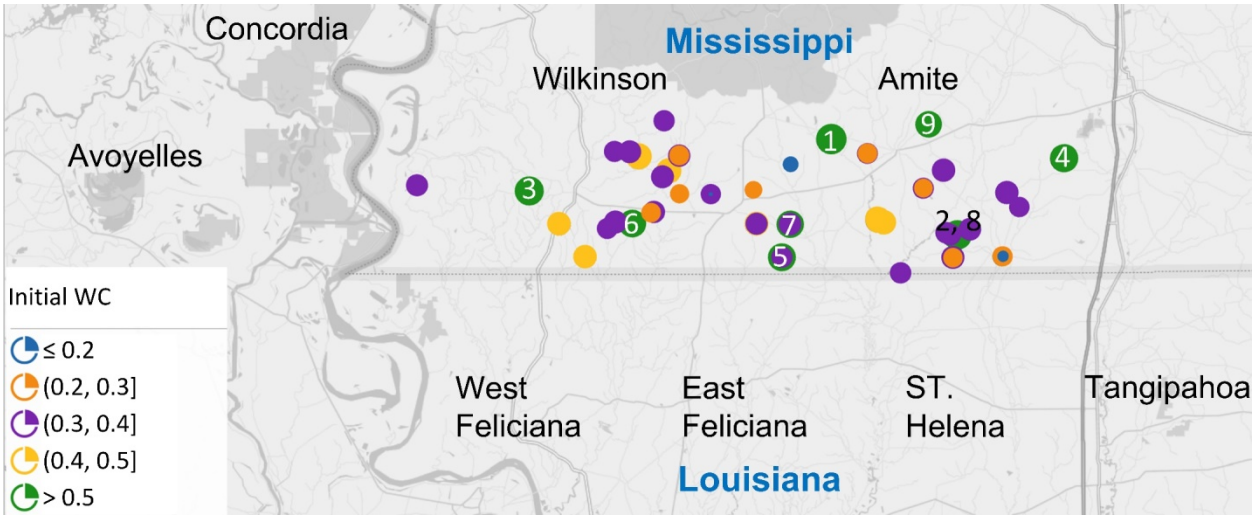


**Figure 1.7, Bubble map of initial water cut of 53 TMS wells completed between 2011 and 2016. The green bubbles represent the locations of the top 9 TMS wells with initial water cut of higher than 0.5, and the numbers represent their corresponding descending order of initial water cut.**

***Cumulative Oil Production*** As of April 2020, most of the TMS wells has produced for more than five years. However, the cumulative production time of two wells completed in 2016 was less than 44 months. Therefore, in this section, the 3-year (36 months) cumulative production was statistically analyzed. Figure 1.8 shows a histogram of the 3-year cumulative oil production of 79 TMS wells completed between 2011 and 2016. Well #70 had the highest 3-year cumulative oil

production of 421 Mbbl. As of April 2020, well #70 had produced 565,159 bbl of oil and 245,540 Mcf of gas in 62 months (i.e., 606,082 boe), and was still producing at the rate of approximately 171 bbl/d of oil and 144 Mcf/d of gas (i.e., 195 boe/d). Well #87, which had the highest initial oil production rate, fell to the second-highest well in 3-year cumulative oil production. It had produced 378,392 bbl of oil and 118,289 Mcf of gas (i.e., 398,107 boe) in 3 years. As of April 2020, well #87 has produced 476,754 bbl of oil and 156,165 Mcf of gas in 62 months (i.e., 502,782 boe) and is still producing at the rate of about 80 bbl/d of oil and 49 Mcf/d of gas (i.e., 88 boe/d).

At the 3-year producing anniversary, the cumulative oil production of the 79 TMS wells was between 12 and 421 Mbbl, averaged 142 Mbbl. Figure 1.9 presents the corresponding bubble map of the 79 TMS wells. 9 TMS wells, among which two are from Wilkinson County and seven from Amite County, had 3-year cumulative oil productions of higher than 250 Mbbl. Besides, the number of wells having cumulative oil production higher than 200 Mbbl in Wilkinson County is far less than that in Amite County.

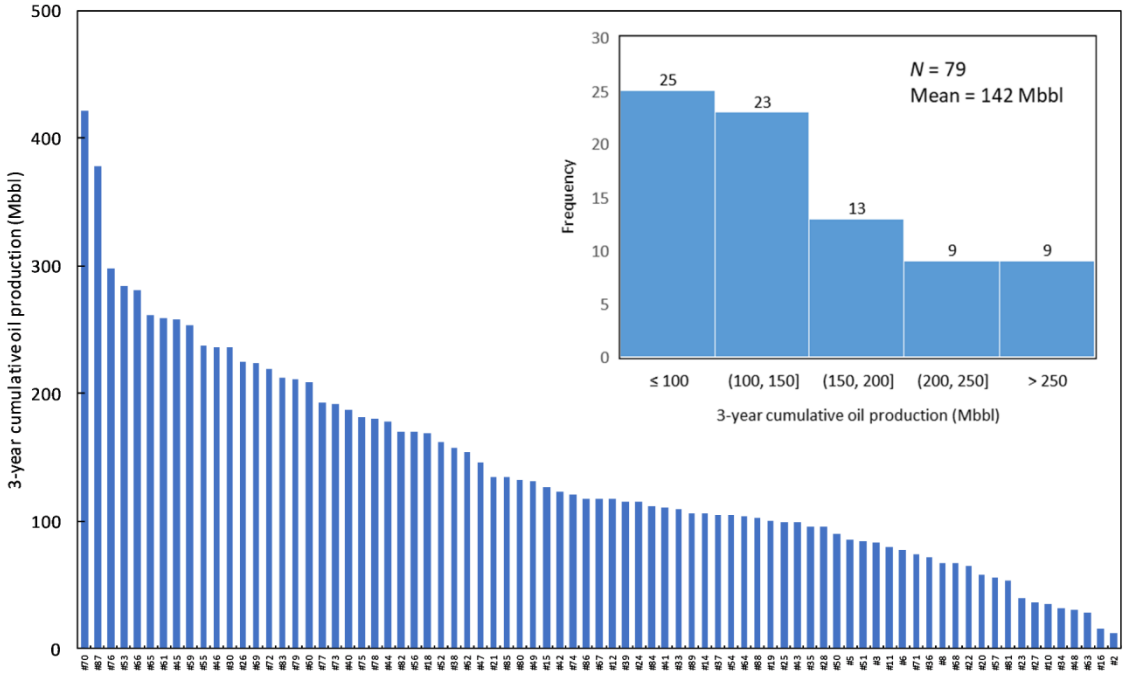


**Figure 1.8, Histogram of 3-year cumulative oil production of 79 TMS wells completed between 2011 and 2016.**

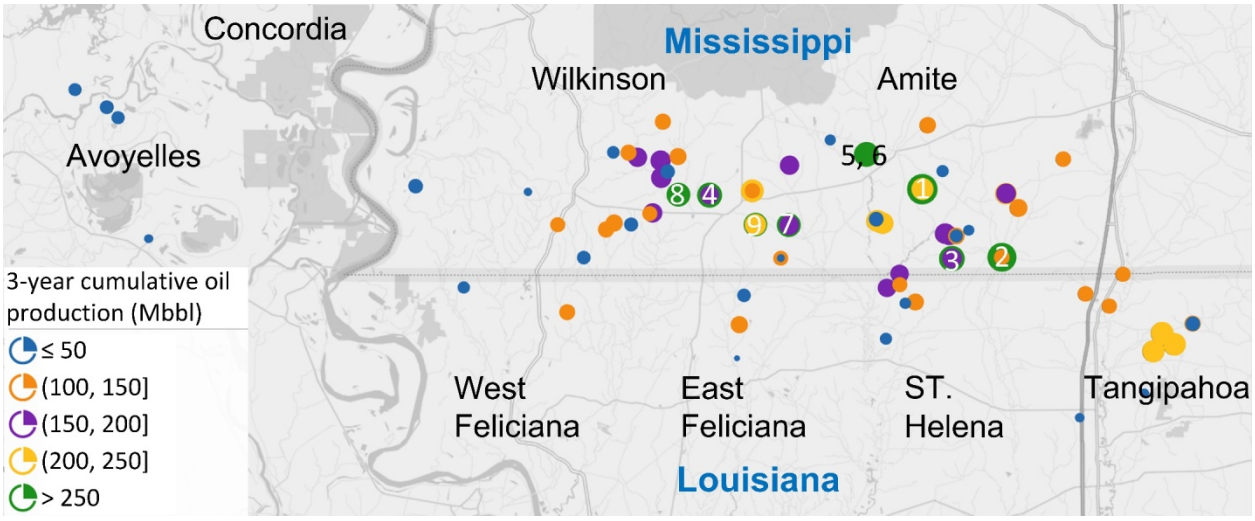


**Figure 1.9, Bubble map of 3-year cumulative oil production of 79 TMS wells completed between 2011 and 2016.** (The green bubbles represent the locations of the top 9 TMS wells with 3-year cumulative oil production of higher than 250 Mbbl, and the numbers represent their corresponding descending order of 3-year cumulative oil production.)

***Cumulative Gas and Water Production*** Figure 1.10 presents the statistical results of the 3-year cumulative gas and water production of TMS wells. The 3-year cumulative gas production was in the range of 8 to 642 MMscf, with an average of 88 MMscf. Six wells had produced more than 200 MMscf of gas at three years. The 3-year cumulative water production was between 6 and 343 Mbbl, averaged 131 Mbbl, eight of which eight had 3-year cumulative water production of higher than 200 Mbbl. Figure 1.11 shows the corresponding bubble map of the 3-year cumulative gas production of 79 TMS wells. The numbers in Figure 1.11 identify the five wells with the highest 3-year cumulative gas production. As can be seen, well #59 had the highest 3-year cumulative gas production. The well was completed with an effective lateral length of 7,066 ft. The peak production of well #59 was about 976 bbl/d of oil, 951 Mcf/d of gas (i.e., 1,134 boe/d). At three years of age, well #59 had produced 253,042 bbl of oil and 641,757 Mcf of gas (i.e., 360,001 boe). As of April 2020, it has produced 319,071 bbl of oil and 751,260 Mcf of gas (i.e., 444,281 boe) and is still producing at the rate of about 83 bbl/d of oil and 66 Mcf/d of gas (i.e., 94 boe/d, 88.2% oil). Besides, this well has also produced a large amount of water, as shown in Figure 1.12. Some geologists suspected that well #59 fractured into both a Lower Tuscaloosa hydrocarbon-bearing reservoir and a Lower Tuscaloosa saltwater-bearing reservoir. The 3-year cumulative water production was 339,143 bbl, ranking second among the 54 TMS wells in Mississippi. Well #65 had the highest 3-year cumulative water production of 343,099 bbl, as shown in Figure 1.11.

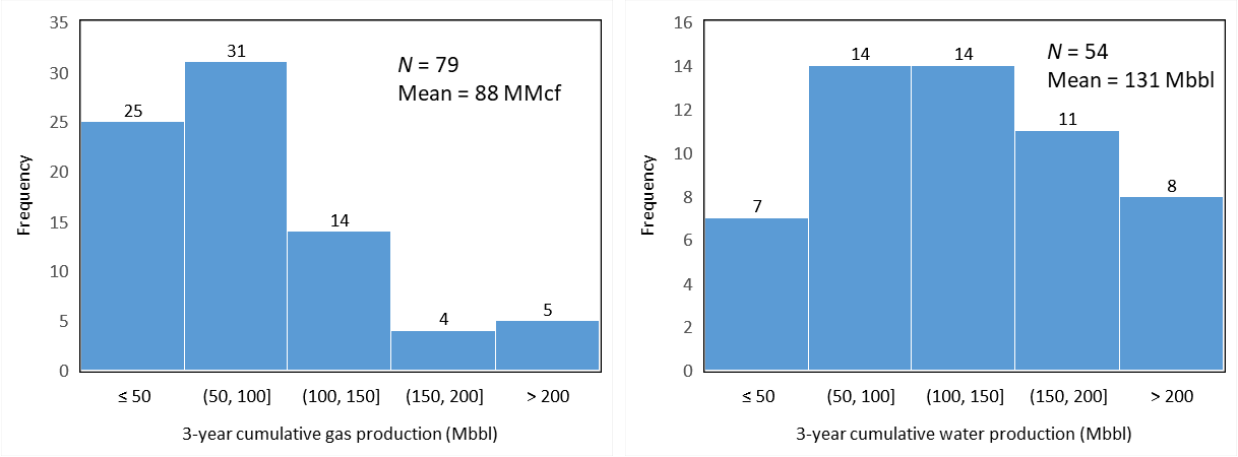


(a) 3-year cumulative gas production (b) 3-year cumulative water production

**Figure 1.10, Statistical results of 3-year cumulative gas and water production of TMS wells.**

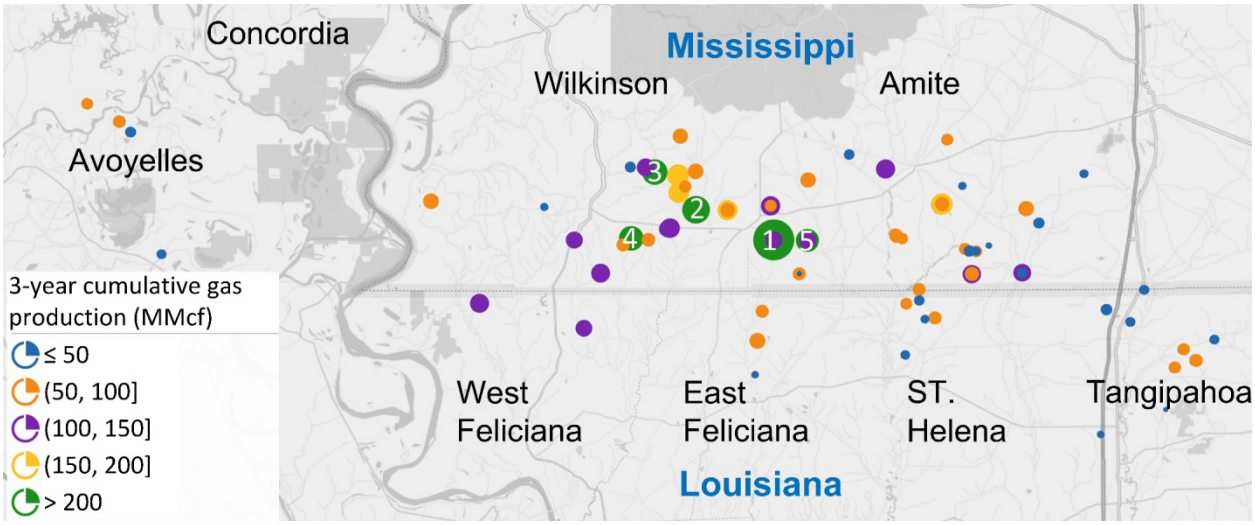


**Figure 1.11, Bubble map of 3-year cumulative gas production of 79 TMS wells completed between 2011 and 2016.** (The green bubbles represent the locations of the top 5 TMS wells with 3-year cumulative gas production of higher than 200 MMcf, and the numbers represent their corresponding descending order of 3-year cumulative gas production.)

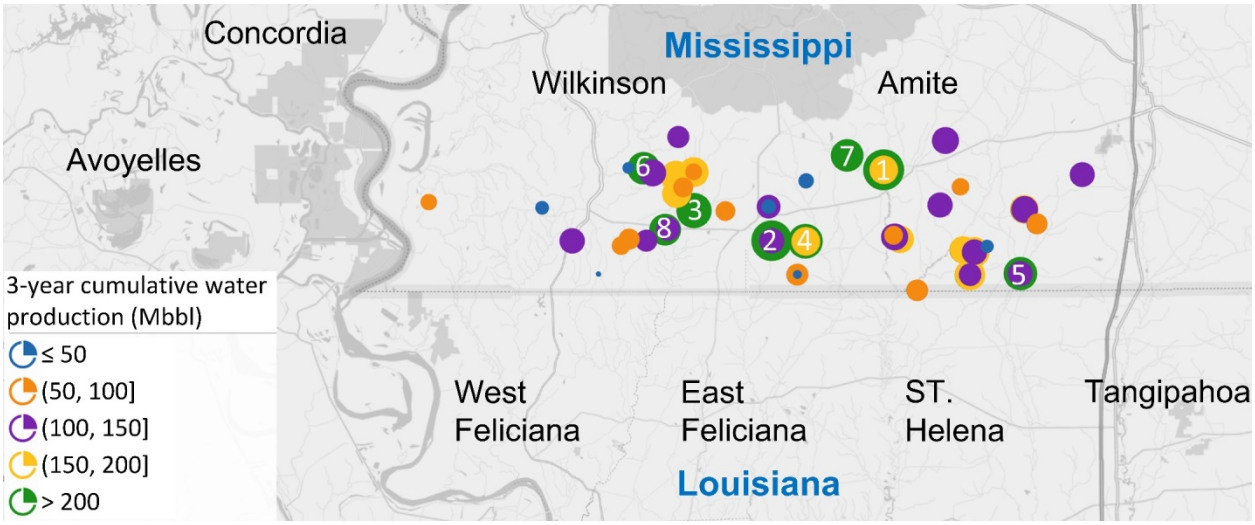


**Figure1.12, Bubble map of 3-year cumulative water production of 54 TMS wells in Mississippi that completed between 2011 and 2016.** (The green bubbles represent the locations of the top 8 TMS wells with 3-year cumulative water production of higher than 200 MMbbl, and the numbers represent their corresponding descending order of 3-year cumulative water production.)

***Cumulative GOR and Water Cut*** The 3-year GOR was calculated by dividing the cumulative gas production by cumulative oil production. As presented in Figure 1.13, the 3-year GOR was between 234 and 2,534 scf/bbl, averaged 645 scf/bbl. Compared with the initial GOR, the 3-year GOR increases slightly over time. The 3-year water cut was in the range of 0.07 to 0.80, with an average value of 0.44, which was higher than the average initial water cut of 0.37. Figure 1.14 shows the 3-year GOR bubble map of 79 TMS wells completed between 2011 and 2016. The green bubbles represent the locations of 11 TMS wells with the cumulative GOR of higher than 1000 scf/bbl. At three years, well #59 had the highest GOR of 2,534 scf/bbl. As stated before, this well also reported the highest 3-year cumulative gas production. Similar to the initial GOR, the 3-year GOR tends to decrease in the up-dip direction. Figure 1.15 presents the 3-year water cut bubble map of 54 TMS wells in Mississippi. Well #57 had the highest 3-year water cut of 0.80 among the 53 wells. As mentioned earlier, this well had the highest initial water cut of 0.66. At three years of age, this well had produced 55,565 bbl of oil, 41,749 Mcf of gas (i.e., 62,523 boe), and 217,151 of water. In April 2020, the production rate dropped to 7 bbl/d of oil, 3 Mcf/d of gas, and 14 bbl/d of water. Table 1.1 highlights some statistical results of the 79 TMS wells investigated in this study. Some information was collected from the website.

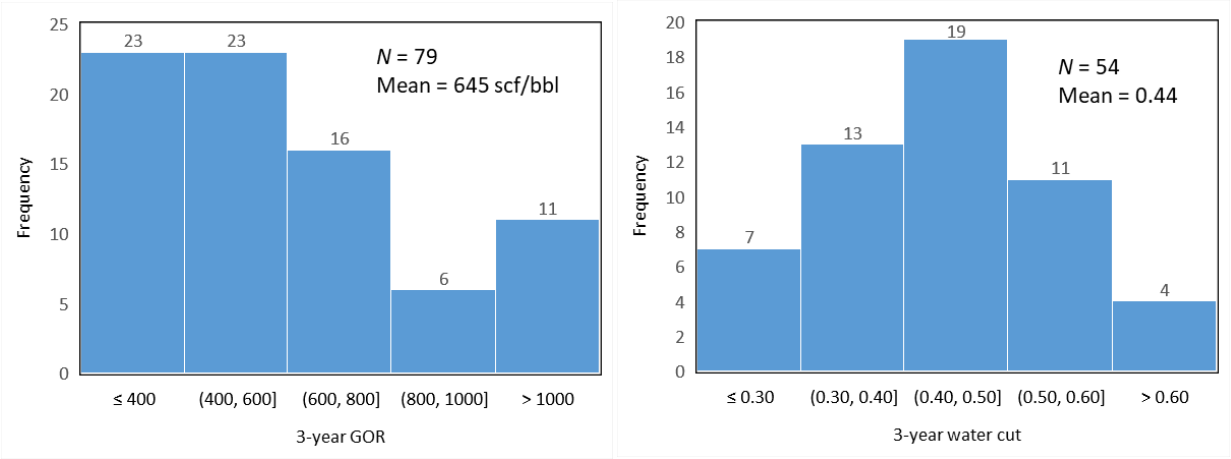


(a) 3-year GOR (b) 3-year water cut

**Figure 1.13, Histogram of GOR and water cut of TMS wells. (a) 3-year GOR; (b) 3-year water cut.**

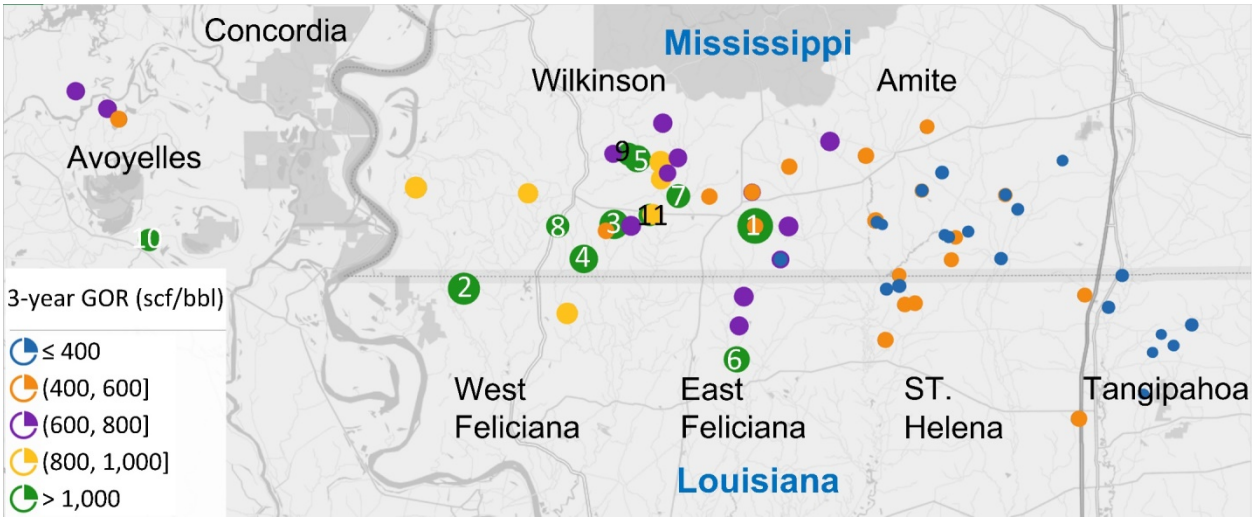


**Figure 1.14, Bubble map of 3-year GOR of 79 TMS wells completed between 2011 and 2016.**

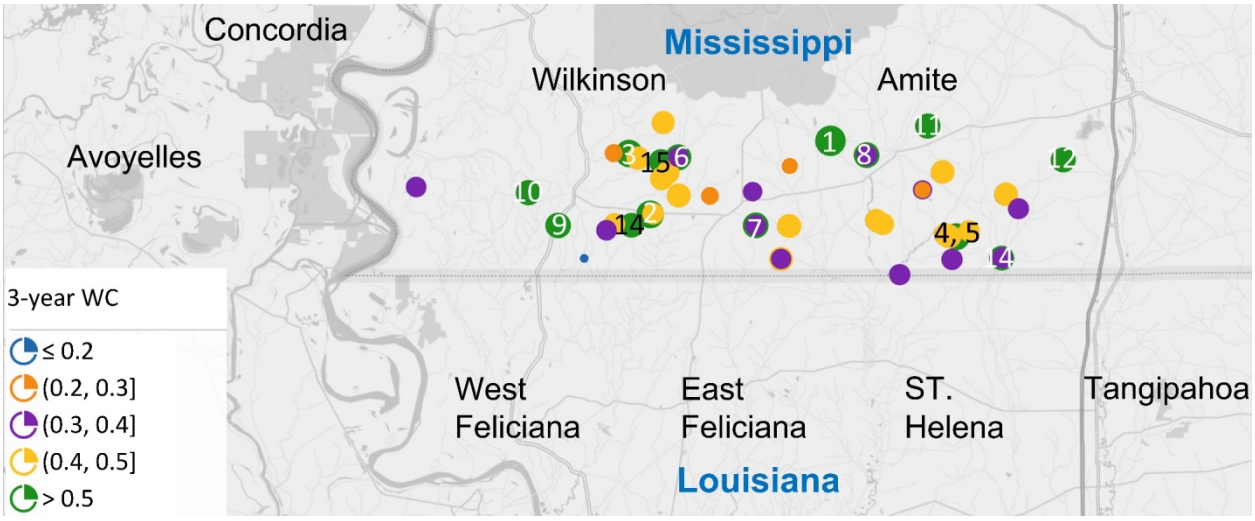


**Figure 1.15, Bubble map of 3-year water cut of 54 TMS wells in Mississippi completed between 2011 and 2016.**

**Table 1.1** Highlights of 79 TMS wells.

| Name | Well | Value |
|---|---|---|
| Highest initial oil production rate | #87 | 1,266 bbl/d |
| Highest initial gas production rate | #59 | 952 Mcf/d |
| Highest initial water production rate | #80 | 934 bbl/d |
| Highest initial production rate of oil equivalent | #70 | 1,298 boe/d |
| Highest 3-year cumulative oil production | #70 | 421,099 bbl |
| Highest 3-year cumulative gas production | #59 | 641,757 Mcf |
| Highest 3-year cumulative water production | #65 | 339,143 bbl |
| Highest 3-year cumulative production of oil equivalent | #70 | 449,843 boe |
| Highest initial gas/oil ratio | #51 | 1,050 scf/bbl |
| Highest 3-year gas/oil ratio | #59 | 2,534 scf/bbl |
| Highest initial water cut | #57 | 0.66 |
| Highest 3-year water cut | #57 | 0.80 |
| Longest effective lateral | #87 | 9,754 ft |
| Highest number of stages | #79 | 32 stages |
| Largest total proppant load pumped | #87 | 23,517,130 lbs |
| Highest average proppant load per stage pumped | #64 | 923,612 lbs/stage |

### *Performance of TMS Compared with Other Shale Plays*

Jacobs (2020) reported per-well production statistics of the largest unconventional oil resource plays in the United States, including Permian, Bakken, and Eagle Ford. This section compares the performance of TMS wells completed between 2011 and 2014 with these three shale plays at their five years of age. At five years, horizontal wells in the TMS see decline rates fall to an average of 23%, as listed in Table 1.2. The average 5-year-old horizontal in the Eagle Ford play shows an annual decline rate of 23% and an average oil production rate of 29 bbl/d. At ages five, the average well in the TMS completed between 2011 and 2014 produces about 20 bbl/d of oil. Therefore, horizontal wells in the Eagle ford and TMS share average decline rates of approximately 23%.

**Table 1.2** Comparison of annual decline rate at five years of age (Jacobs 2020).

| Name | Annual decline rate at 5 years | | | | Average daily production at five years (bbl/d) | | | |
|---|---|---|---|---|---|---|---|---|
| | Williston | Permian | EFS | TMS | Williston | Permian | EFS | TMS |
| 2011 Well | 17% | 19% | 22% | 27% | 54 | 24 | 27 | 26 |
| 2012 Well | 20% | 16% | 21% | 22% | 46 | 25 | 29 | 22 |
| 2013 Well | 14% | 18% | 24% | 24% | 49 | 28 | 28 | 17 |
| 2014 Well | 18% | 17% | 24% | 20% | 48 | 37 | 30 | 34 |
| Average | 17% | 18% | 23% | 23% | 49 | 29 | 29 | 20 |

The TMS is similar in composition and geological age to the Eagle Ford Shale formation in Texas (Dubiel et al., 2012). Therefore, this section further compares the performance of these two shale plays. The oil production rate data for the first 36 months of TMS wells and EFS wells are presented in Figure 1.16. Data for the EFS wells were obtained from ShaleProfile Analytics (2020). The 3-year cumulative oil production for TMS wells with the first production year of 2011, 2012, and 2013 are less than those for EFS wells. However, the 3-year cumulative oil productions of TMS wells that started production in 2014 and 2015 are higher than the cumulative production of EFS wells. The data in this figure indicates that the oil production rates of the TMS wells are comparable to that of the EFS wells in the first three years. However, drilling costs in TMS are much higher than in other shale plays due to deep drilling depths and high clay content. Between 2011 and 2015, the average drilling and completion cost in the EFS ranged from 6 million to 9 million dollars per well, while the corresponding average cost in the TMS was between 10 million and 13 million dollars per well. It should be mentioned that the TMS data represents a small dataset compared to EFS.

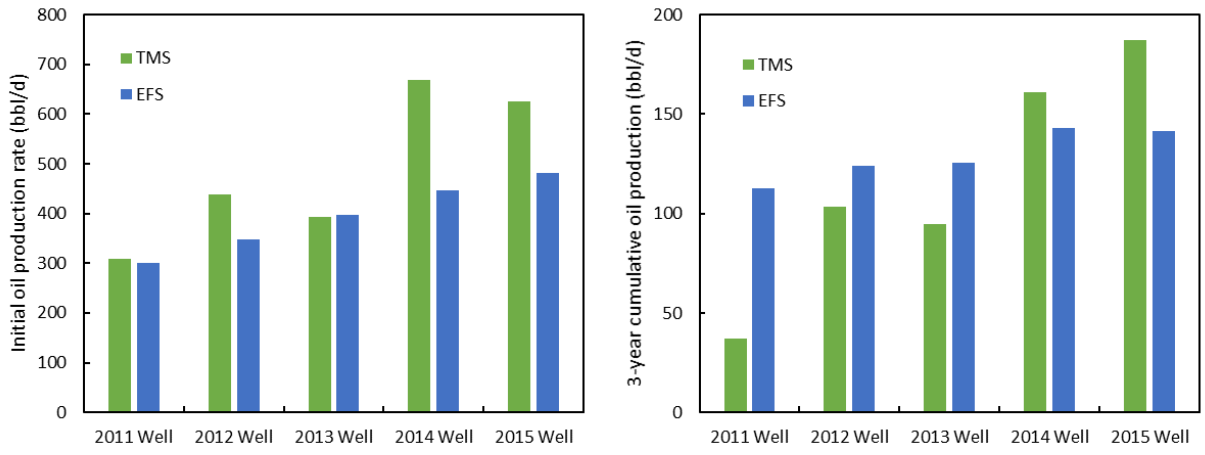


(a) Initial oil production rate

(b) 3-year cumulative oil production

**Figure 1.16, Comparison of the initial oil production and 3-year cumulative oil production between Tuscaloosa Marine Shale and Eagle Ford Shale.**

Table 1.3 presents the annual decline rates and the remaining production level during the first three years. The data in the column EFS are from ShaleProfile Analytics (2020). The annual decline rates of TMS and EFS wells in the first year were 77% and 69%, respectively. The average decline rates of horizontal wells in TMS and EFS at three years are 30% and 36%, respectively. After three years, the productivity of TMS and EFS accounted for only 9% and 10% of the initial production (IP) level, respectively. Wachtmeister et al. (2017) calculated the mean annual decline rate of 294 EFS wells based on the aggregate production data between 2010 and 2014. They precluded wells with cumulative oil production below 20 Mbbl, which were considered unsuccessful. Figure 1.17 shows the production decline curves based on the aggregate well production data (i.e., average value). The EFS data in the dashed curves are from ShaleProfile Analytics (2020). A hyperbolic model was used in the comparison because Wachtmeister et al. (2017) used the same model to predict Estimated Ultimate Recovery (EUR) of EFS wells. The EFS line shows results for the data from ShaleProfile Analytics (2020). The assumed cutoff value is 4 bbl/d (Wachtmeister et al., 2017). The 30-year cumulative oil productions of TMS and EFS wells are calculated to be 262 and 234 Mbbl, respectively. It is found that the long-term well performance in the TMS is very similar to that in the EFS based on the data of Wachtmeister et al. (2017).

**Table 1.3** Comparison of the mean annual decline rate for the 1st, 2nd and 3rd year of production.

| Production year | Mean annual decline rate (%) | | | Remaining production level (% of IP) | | |
|---|---|---|---|---|---|---|
| | TMS | EFS | EFS (Wachtmeister et al., 2017) | TMS | EFS | EFS (Wachtmeister et al., 2017) |
| Year 1 | 77 | 69 | 74 | 23 | 31 | 26 |
| Year 2 | 44 | 50 | 47 | 13 | 16 | 13 |
| Year 3 | 30 | 36 | 19 | 9 | 10 | 11 |

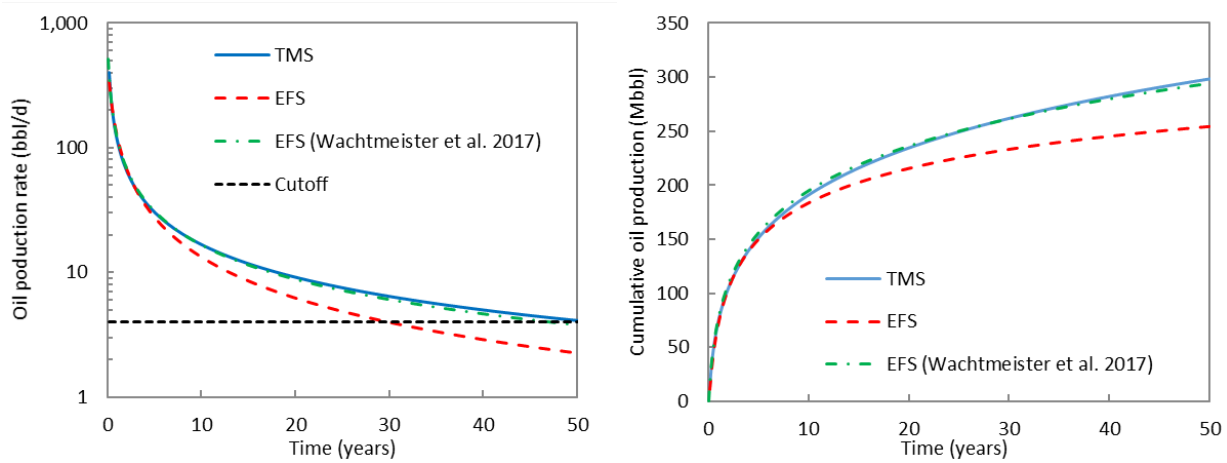


(a) average oil production rate (b) average cumulative oil production

**Figure 1.17, Hyperbolic decline curves for TMS and EFS wells based on aggregate production data.**

## 1.3 Data and Core Gathering for this Research

The Tuscaloosa Marine Shale (TMS) is an emerging shale play in central Louisiana and Southern Mississippi with significant oil reserve potential, yet its production rate is negligible and the shared knowledge on this shale play is rare compared to other shale plays. The University of Louisiana at Lafayette (the lead), the University of Oklahoma (OU), Missouri S&T, University of Southern Mississippi (USM) and Las Alamos National Laboratory (LANL) work together to address some critical gaps in the understanding of the TMS to make the development of this emerging shale more cost-efficient and environmentally sound. Six major objectives for this study have been recognized using scientific and technical approaches: 1. Improve the wellbore condition, drilling

and completion by better understanding the source of the wellbore instability issues and proposing innovative cement composition for the TMS. 2. Improve the estimation of TMS reservoir quality using advanced TOC calculation, water analysis and geophysical analysis. 3. Determine role of discontinuities on fracture growth and shale creep behavior using digital image correlation. 4. Improve fracturing of TMS using stable $CO_2$ foam and super-hydrophobic proppants. 5. Improve the knowledge on the nature of flow in such clay as well as organic rich TMS and water/fluid interaction using microfluidics system 6. Develop better socio-economic environment by community engagement in the development of TMS. This study works closely with industry members and has received significant support in terms of whole cores, slabbed cores, cuttings, produced water samples, well logs, drilling and completion reports, mud logging reports, and other well data. Goodrich Petroleum Corportation donated five whole cores which included the Tuscaloosa Marine Shale located in Mississippi and Louisiana. Cores from Lane 64-1 API# 17037201530000 included depths between 1540-15228.09 ft and Beech Grove Land 68H-1 API# 17037201510000 included depths between 13745-13924.83 ft were drilled in East Feliciana Parish, Louisiana. The core from Soterra 6H-1 API# 17105200390000 included depths between 12460-12642.1 ft was drilled in Tangipahoa Parish, Louisiana. The core from Eads Poitevent et al #1 API# 17103200620000 included depths between 12960 – 12963ft was drilled in St Tammany Parish, Louisiana. The core from Crosby Mineral 12-1H #1 API# 23157220371000 included depths between 12080 – 12195 ft was drilled in Wilkinson County, Mississippi (Fig. 1.18). Halcon Operating Co., Inc. donated two whole cores which included the Tuscaloosa Marine Shale located in Mississippi and Louisiana. The core from Broadway H1 API# 17079205390000 included depths between 13460 – 13769.9 ft was drilled in Rapides Parish, Louisiana. The core from SD Smith 1H API# 23157221021000 included depths between 13275 – 13478.3 ft was drilled in Wilkinson County, Mississippi. A modern TMSL Laboratory (Fig. 1.19) was designed and constructed in Petroleum Engineering Department at University of Louisiana at Lafayette and used for this study.

**Figure 1.18 Pictures of TMS core samples received from the industry partners.**

**Figure 1.19 A picture of designed laboratory for TMSL project.**

## References:


Borrok, D. M., Yang, W., Wei, M., & Mokhtari, M. (2019). Heterogeneity of the mineralogy and organic content of the Tuscaloosa Marine Shale, *Marine and Petroleum Geology*, *109*(June), 717–731.

Mancini, E.A., Obid, J., Badali, M., Liu, K.Y., Parcell, W. (2208). Sequence-stratigraphic analysis of Jurassic and Cretaceous strata and petroleum exploration in the central and eastern Gulf coastal plain, United States, *AAPG Bulletin* 92(12) 1655-1686.

John, C.J.; Jones, B.L.; Moncrief, J.E.; Bourgeois, R.; Harder, B.J. (1997). An unproven unconventional seven billion barrel oil resource – the Tuscaloosa Marine Shale", *LSU Basin Research Institute Bulletin*, 7 1-22.

Echols, J.B., 1997. Geochemical analyses of Tuscaloosa oils. The Basin Research Institute Bulletin, Baton Rouge, Louisiana, 7, 23–24.

Lu, J., Ruppel, S.C., Rowe, H.D., 2015. Organic matter pores and oil generation in the Tuscaloosa marine shale. *AAPG bulletin*, 99 (2), 333–357.

John, C.J., Jones, B.L., Harder, B.J. et al., 2005. Exploratory progress towards proving the billion barrel potential of the Tuscaloosa Marine Shale. *Gulf Coast Association of Geological Societies Transactions*, 55, 367–372.

Hoffmann, A. A., Borrok, D. M., 2020. The geochemistry of produced waters from the Tuscaloosa Marine Shale, USA. *Applied Geochemistry*, 116, 104568.

Jacobs T. 2020. Life after 5: how tight-oil wells grow old. *Journal of Petroleum Technology*, 72(2): 32–36.

Dubiel, R.F., Pearson, O.N., Pitman, J., et al., 2012. Geology and sequence stratigraphy of undiscovered oil and gas resources in conventional and continuous petroleum systems in the Upper Cretaceous Eagle Ford Group and related strata, U.S. Gulf Coast Region, *Gulf Coast Association of Geological Societies Transactions*, 62, 57–72.

ShaleProfile Analytics. 2020. The Major Tight Oil Basins: The Permian, Eagle Ford, Williston and the DJ-Niobrara. March 31st. https://shaleprofile.com/the-major-tight-oil-basins-update-march-2020/.

Wachtmeister, H., Lund, L, Aleklett, K., and Höök, M., 2017. Production Decline Curves of Tight Oil Wells in Eagle Ford Shale. *Natural Resources Research*. 26(3): 365–377.

# CHAPTER 2 Drilling and Well Integrity Investigation of the Tuscaloosa Marine Shale Formation

This section discusses different approaches to improve the drilling practices in the TMS formation. The objectives of this section include: i) Investigation of rock-fluid interaction in term of compatibility; ii) Development of more suitable drilling fluid systems for improving TMS drilling practices; and iii) Investigation and development of lost circulation mud systems for mitigating fluid loss.

## 2.1 Tuscaloosa Marine Shale Drilling

There has been a surge in tight oil and shale gas production over the past decade in the United States due to the high increase in oil and gas demand. This surge can be associated to the increased technological emphasis on production from unconventional reservoirs and improvement in drilling operations and practices. The production of shale gas and tight oil come from various shale plays including Haynesville, Barnett Shale and others. These major shale formations are attractive to operators because of their huge reserves. US Energy Information Administration (EIA) reported in 2018 that tight oil resources or plays accounted for 65 billion cubic feet per day (Bcf/d) of natural gas (accounting for 70% of total US dry gas) and 7 million barrel per day (bbl/d) of crude oil (60% of total US oil).

Despite the continuous increase in shale production, there are still major concerns over the drilling practices in these shale plays. There continue to be an increasing focus on efficient drilling of deep and tight shale formations. Despite their huge potential, shale drilling continues to be challenging for operators and usually lead to excessive expenses because of all the possible drilling problems encountered. Serious drilling problems continues to be associated with shale drilling especially in deep and high-pressure wells. Some common problems include bit balling, wellbore instability, and low drilling rates, all correlating to excessive drilling costs. Currently, drilling with polycrystalline diamond compact (PDC) bits and oil- or synthetic mud systems constitute the best practices for shale operations. However, stringent environmental regulations and high operating cost associated with using oil-based mud (OBM) systems limit the effectiveness of these systems. As a result, continuing investigations are still ongoing in industry to find ways to minimize these shale drilling problems and therefore the introduction of inhibitive muds and high-performance water-based muds (HPWBM).

In the design and development of drilling fluids, laboratory investigation of drilling fluid performance was carried out at consistent testing conditions to maintain consistency. The objective was to devise an economical, efficient, and more compatible drilling fluid systems as alternative to oil-based mud that can drill the deep high-pressure high-temperature (HPHT) Tuscaloosa Marine Shale formation.

### *2.1.1 Mineralogy Characterization*

The Tuscaloosa Marine Shale is characterized by its high concentration in clays. The FITR analysis revealed a clay content as high as 51 % in Crosby 12-1H well. The most common clays type include kaolinite, illite, and chlorite. These clays are highly detrimental to drilling due to their sensitivity to water. TMS formation is highly heterogeneous, which is reflected by the variation in mineralogy across the formation and at different depth. Figure 2.1 shows the FTIR analysis of a core samples obtained from Crosby 12-1H well.

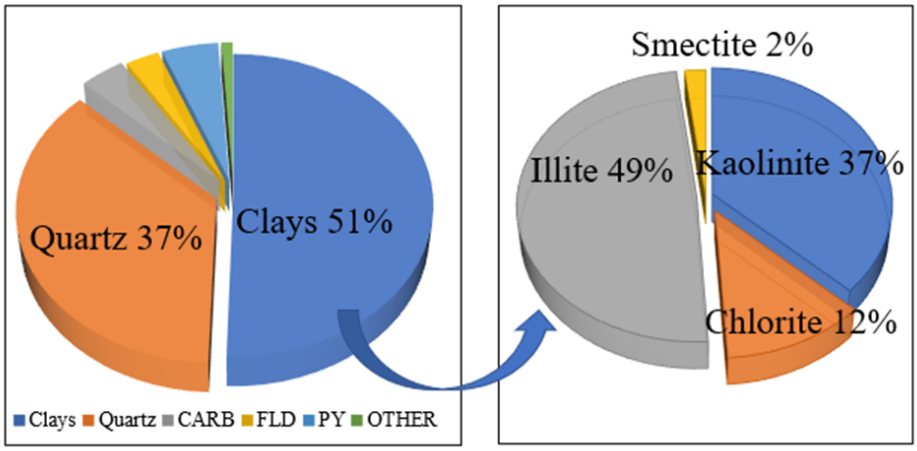


**Figure 2.1 Mineralogy composition of the TMS obtained using FTIR analysis.**

### *2.1.2 Swelling Characterization*

Shale swelling is very detrimental for drilling operations due all the concerns it engenders. Some related consequences of shale swelling include collapse, hole caving, and hole cleaning. The swelling index profile shows the effect of different drilling fluid systems on clay expansion during drilling operations. In this study, the swelling index was computed based on the change in volume after a certain period. It was obtained from the equation below.

$$\sigma = \frac{H_1 - H_0}{H_0} * 100 \quad \text{(1)}$$

Where $H_0$ represents the initial volume, $H_1$ is the final volume, and $\sigma$ indicates the shale swelling index.

The swelling index was obtained for all four (4) drilling fluid systems tested in this study for TMS while using freshwater as reference fluid. Figure 2.2a displays the different swelling indices obtained for twenty-four (24) hours. Among the drilling fluid, the conventional WBM showed the highest swelling index followed by the 1 wt% KCl, the 2 wt% KCl, and then the cesium formate.

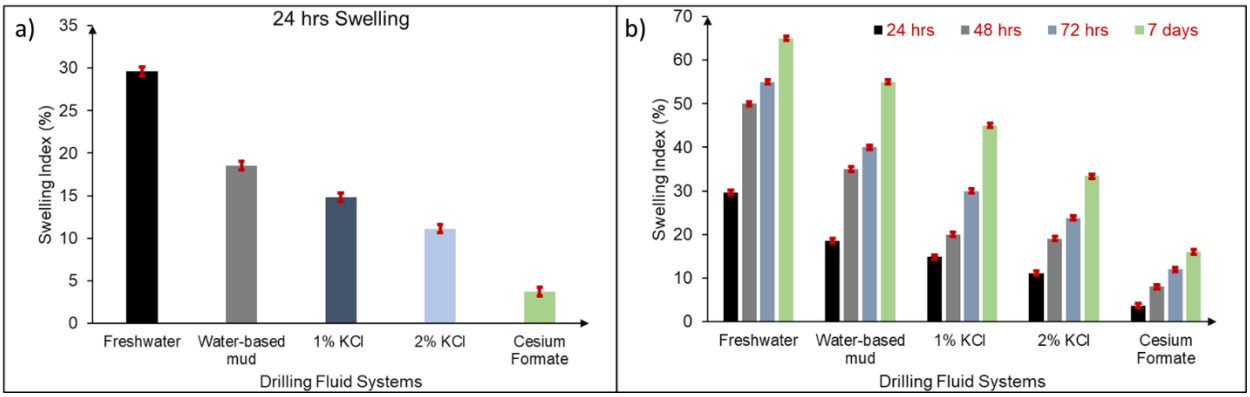


**Figure 2.2 a) Swelling index profile of the drilling fluid systems tested in this study with freshwater as reference fluid. b) Swelling index profile of the drilling fluid systems tested in this study with freshwater as reference fluid for different exposure times.**

Shale swelling is highly impacted by the time of exposure to the drilling fluid systems. Figure 2.2b shows the impact of exposure time on swelling indices for the tested drilling fluid systems. The profile shows an increase in swelling index as time increases for all fluid systems. The cesium formate and 2% KCl show the lowest increase in linear swelling index from 1 day to seven (7) days.

### *2.1.3 Cutting Dispersion Analysis*

The cutting recovery profile (Fig. 2.3) shows that the highest recovery rate is obtained using the cesium formate and 2% KCl with a recovery of 85.7% and 84.5% respectively. On the other hand, freshwater and WBM show the lowest cutting recovery with 65% and 75% respectively. These results imply better cutting stability with the inhibitive muds as opposed to the conventional WBM. The low dispersibility realized with the inhibitive mud systems show better cuttings integrity. The cutting recovery profile indicates that lower bit-balling is more likely to be achieved with the inhibitive mud systems as opposed to the conventional WBM. Cutting recovery is based on the following equation:

$$CR = \frac{Wf}{Wi} * 100 \quad \text{..... (2)}$$

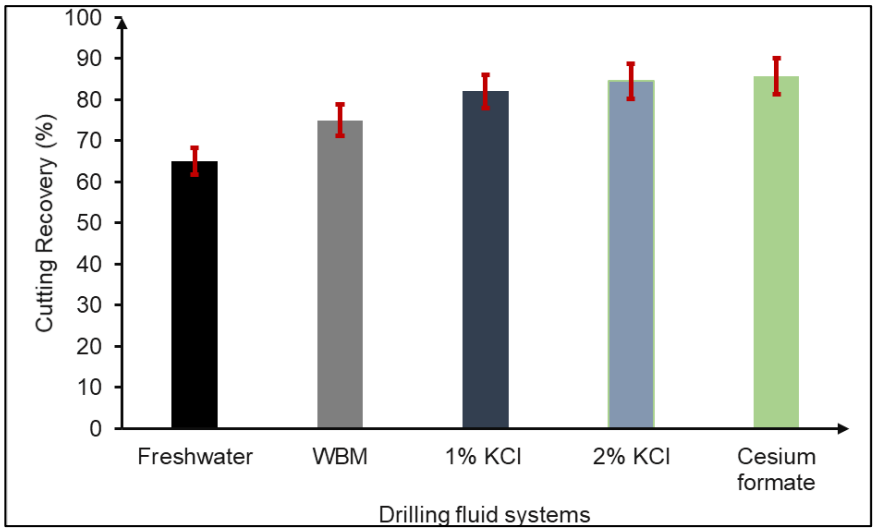


**Figure 2.3 Cutting recovery rate of different drilling fluid systems used in this study.**

### *2.1.4 Wellbore Strengthening*

Lost circulation during drilling is one of the major consequences of wellbore instability in shale. Figure 2.4 shows the effect of fracture width on cumulative dynamic fluid loss for different cedar fiber concentrations. Cedar fiber is used in this study due to its previous success in the formation.

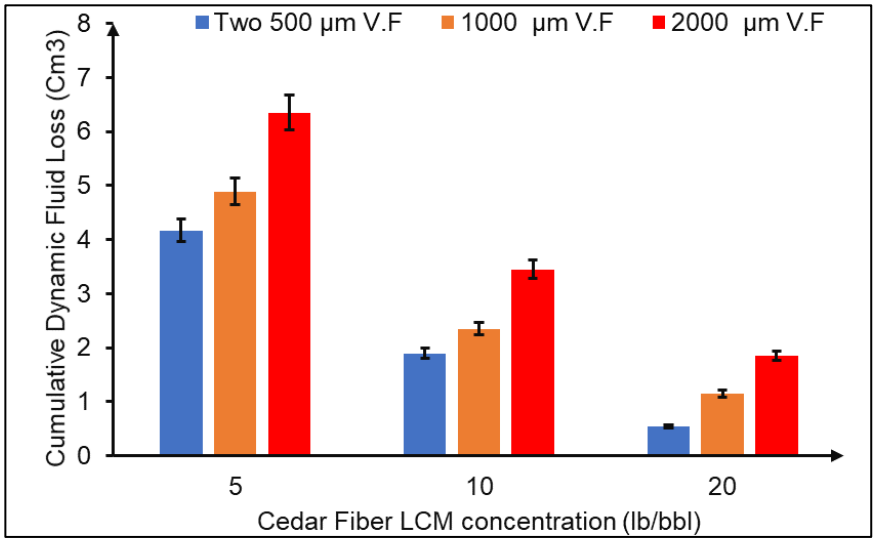


**Figure 2.4 Cumulative dynamic fluid loss for different fracture widths as function of cedar concentration.**

### *2.1.5 Torque and Friction Factor During Drilling*

Figure 2.5a and 2.5b show the torque and friction factor profiles, respectively. The profiles revealed an increasing relationship between both the torque and the friction factor and the weight on bit (WOB). The conventional WBM showed the highest torque and friction factor while the

cesium formate showed the minimum. The inhibitive mud systems showed a reduction of more than 50% in both torque and friction factor at higher WOB. All three inhibitive mud systems tested in this study provide better drilling performance as opposed to conventional WBM. The cesium formate brine provided the lowest friction factor and torque, which indicated better drilling performance compared to the KCl based systems.

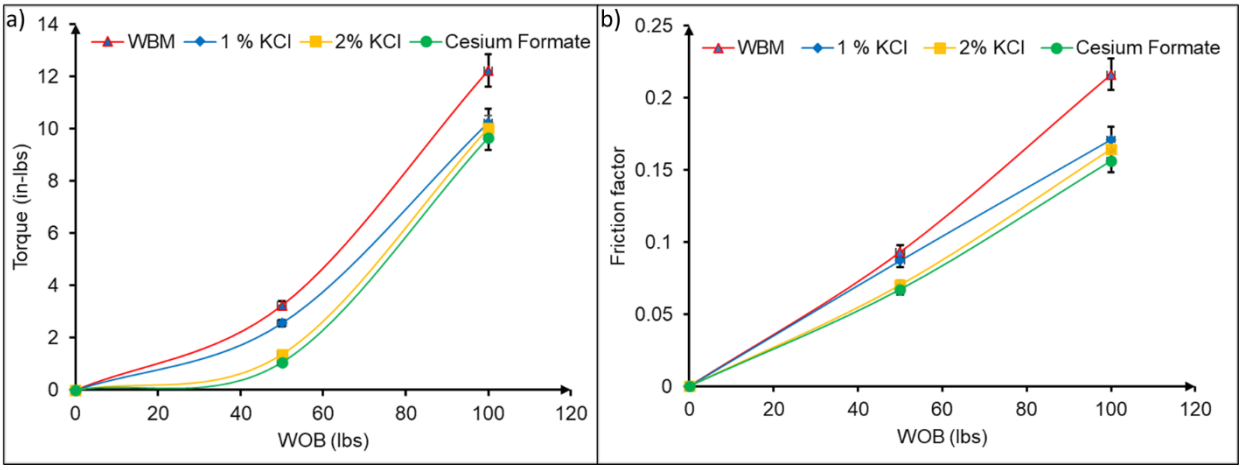


**Figure 2.5 a) Effect of the tested drilling fluid systems on torque during drilling. b) Effect of the tested drilling fluid systems on friction factor during drilling.**

### *2.1.6 Rate of Penetration (ROP) Optimization*

Most shale formations such as the TMS and the Eagle Ford are characterized by low drilling rate due to factors such as bit-balling, pipe hole sloughing that are caused by the incompatibility between the inappropriate fluid system and the formation. In this study, the effect of inhibitive mud systems (1 wt% & 2 wt% KCl, cesium formate), and the conventional WBM on the drilling rate was evaluated in the TMS. Figure 2.6 shows the ROP profile of the drilling fluid systems tested on TMS core samples. The results show an increasing correlation between the ROP and the WOB for all drilling fluid systems. Based on the ROP profile, conventional WBM showed the lowest ROP at various weight on bit (WOB) among the drilling fluid systems tested. This result was an indication of the incompatibility issues associated with WBM. The cesium formate showed the highest rates followed by the 2 wt% KCl, and finally the 1 wt% KCl, indicating cesium formate could constitute the most appropriate drilling fluid systems for reactive shale formations due to its elevated rate of penetration.

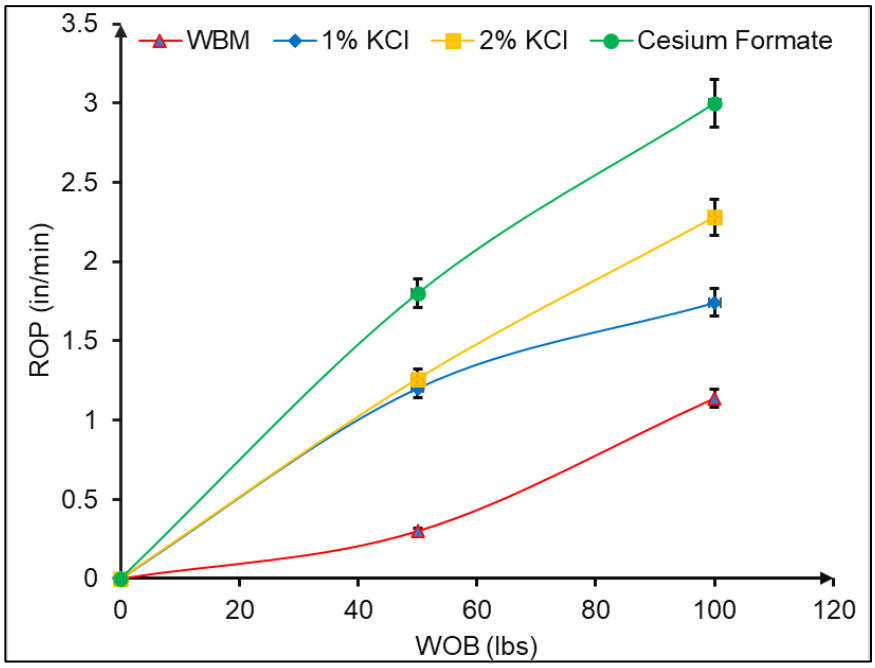


**Figure 2.6 ROP profile of the tested drilling fluid systems.**

## 2.2 Experimental Investigation of Well Integrity in the Tuscaloosa Marine Shale

Sustaining a long-term well integrity is crucial to the production life of well. There are various well components that ensure long-term of integrity. Well integrity provides technical, operational, and organization solutions for minimizing uncontrollable flow of formation fluid into the well throughout the lifetime of the well. There are both primary and secondary barriers that ensure no flow of formation fluid into the wellbore. Oilwell cement is a primary barrier during the lifetime of the well that is critical to well integrity. Oilwell cement plays a major role in the oil and gas industry, especially during the drilling and completion phase. Cement sealability helps maintain the integrity of the well and prevent subsurface fluid movement and migration to other formation and surface. The oilwell cement ability to withstand mechanical and chemical deterioration is known as durability. Cement durability and sealability is crucial to maintain long-term integrity. The durability and sealability is dependent on various cement properties such as permeability, unconfined compressive strength (UCS), rheology, Young's modulus, and Poisson's ratio. These properties are crucial for cement to generate an effective bond with the formation and/or the casing. The Tuscaloosa Marine Shale operations have been greatly limited by well integrity issues. The efficiency of cementing operations in the formation has been poor. The major cement issues during cementing involved poor bonding in all three sections of the wellbore: surface, intermediate and production. In the surface section, poor bonding was cited as a result of cementing around gumbo shale/weak formation where there was also some lost circulation. In the intermediate section, bonding issues were sited but the direct causes were not mentioned in the drilling reports. There were instances of cement contamination by mud which could have been a major influence on the bonding issues in this section. There were issues of lost circulation and weak formation in

cementing the production liner in place at required depth which also led to bonding issues. Additionally, there were instances of casing eccentricity as a result of poor mud displacement. Casing eccentricity refers to the degree to which the casing is off-center in another casing or open hole. Casing eccentricity issues increase the probability of poor cement bonding. During cementing, the cement slurry tends to flow through the larger portion of the hole much faster than through the smaller annulus leading to cement not reaching the layer of the formation to be sealed. A neat Portland cement is often thought of as been the primary barrier to prevent formation fluid influx during early setting phase. However, this is not completely certain considering the bonding and gas migration issues associated with its uses. The objectives of the tasks in this section include: (i) Investigate the effect of mud contamination of cement bonding mechanism; (ii) Evaluate the effect of lithology on cement bonding mechanism; (iii) Evaluate the effect of eccentricity on the cement bond with steel ("casing'); (iv) Evaluate the advantages of using nano-modified and geopolymer cement over Portland cement. This work effort includes the application of digital image correlation (DIC) strain mapping of neat class cement, nano-modified class H, and geopolymer bonding to steel ("casing") and subsurface formations.

### *2.2.1 Effect of Lithological*

Two lithologies (sandstone and shale) were used in this study. The base case for these experiments was neat Class H cement placed in a concentric annulus between steel and sandstone. This was compared to the same system but with shale as the formation. The nature of the two systems differs in that the vertical and horizontal strain occurs initially at the cement-steel interface (Fig. 2.7) while the initial strain in the shale sample occurs at the cement-shale interface (Fig. 2.8). There is no strain development along the cement-sandstone interface throughout the test.

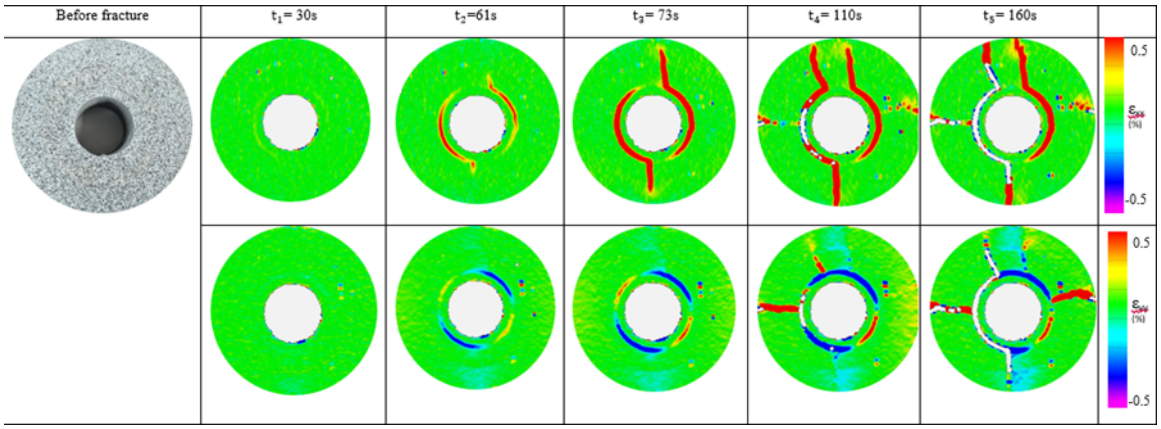


**Figure 2.7 Strain development ($\varepsilon_{xx}$ and $\varepsilon_{yy}$) for Sandstone Neat H concentric system.**

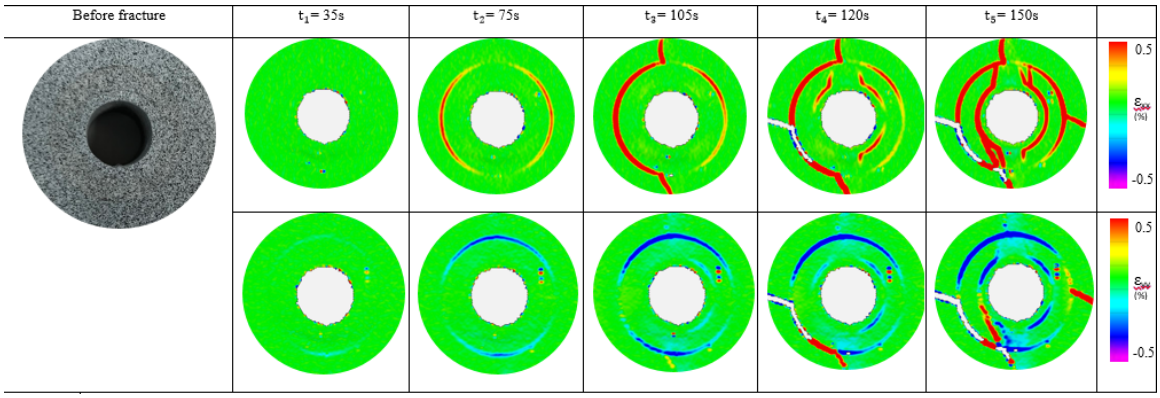


**Figure 2.8 Strain development ($\varepsilon_{xx}$ and $\varepsilon_{yy}$) for Shale Neat H concentric system.**

### *2.2.2 Effect of Mud Contamination*

From Fig. 2.9, it is evident that the strain development and progression of the mud-contaminated Neat H sample is very similar to the base case Neat Class H system (Fig. 2.7). The strain initiates at the cement-steel interface and results in the formation of a radial fracture which propagates through the cement and the sandstone finally leading to sample failure.

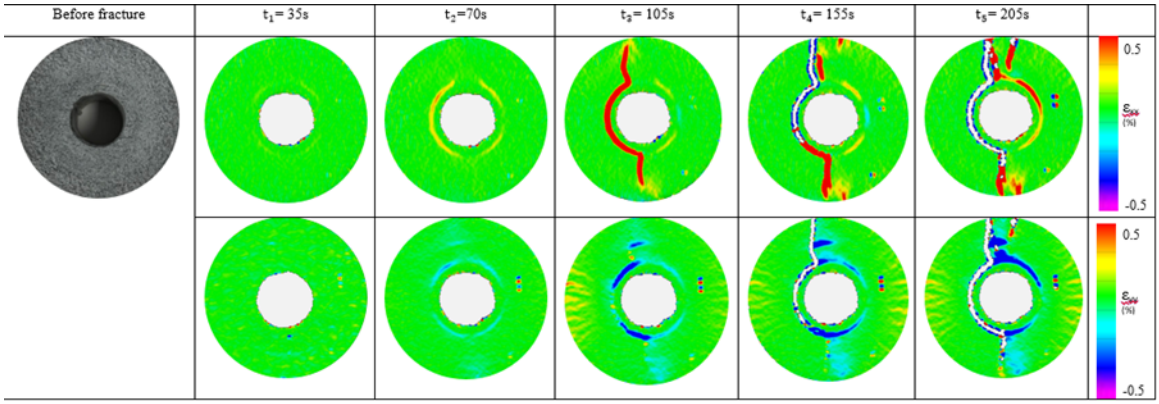


**Figure 2.9 Strain development ($\varepsilon_{xx}$ and $\varepsilon_{yy}$) for Sandstone mud-contaminated H concentric system.**

### *2.2.3 Effect of Casing eccentricity*

The effect of eccentricity in shale samples differed in terms of strain development to the sandstone samples. The compressive and tensile strain initiated along the cement-shale interface (Fig. 2.10) as in the concentric case. Specifically, for the concentric case, there was evidently strain development at the cement-steel interface as the load increased. Radial fractures were then developed from both interfaces parallel to the loading direction before both the hydraulic and shear bonds were disintegrated.

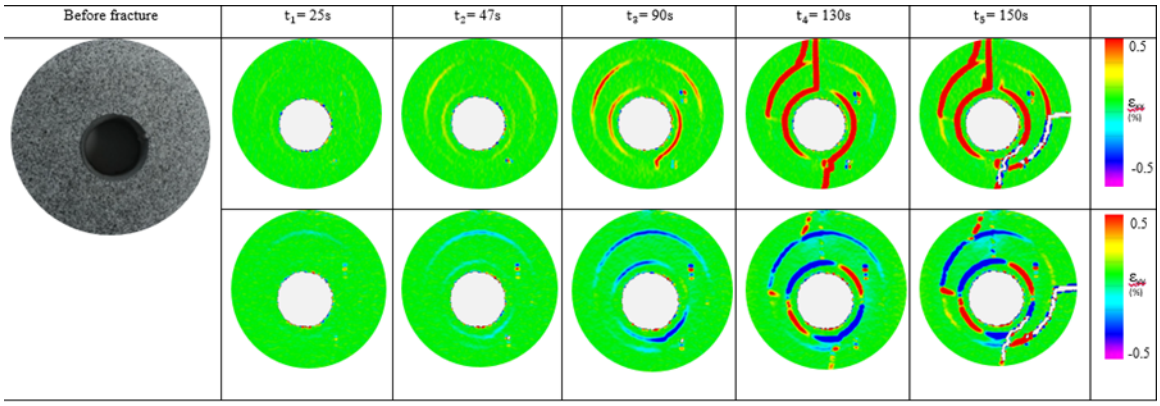


**Figure 2.10 Strain development ($\varepsilon_{xx}$ and $\varepsilon_{yy}$) for Shale Neat H eccentric system.**

### *2.2.4 Geopolymer Cement*

The strain deformation for this sample of the geopolymer case was very similar to that in the Neat Class H system. Strain initiated along the cement-steel interface and developed leading to the formation of radial fractures and finally sample failure (Figure 11).

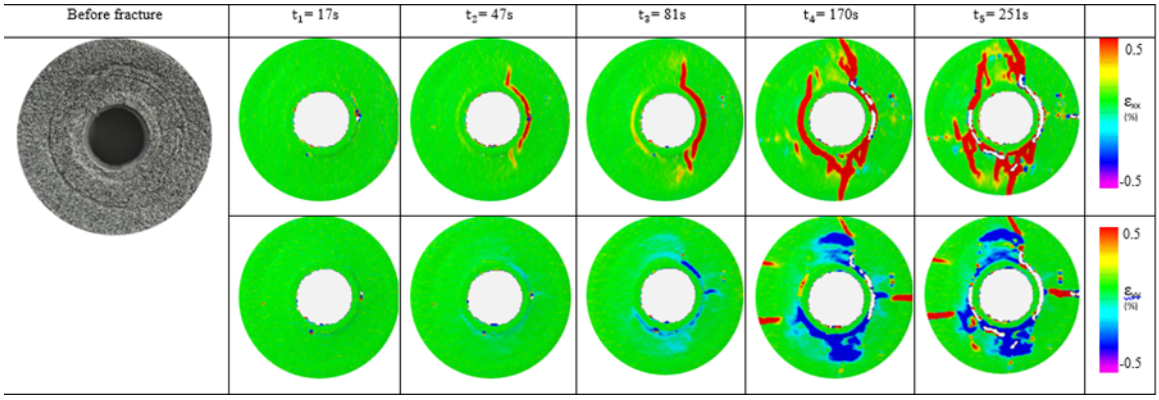


**Figure 2.11 Strain development ($\varepsilon_{xx}$ and $\varepsilon_{yy}$) for Sandstone geopolymer concentric system.**

### *2.2.5 Unconfined Compressive Strength (UCS)*

Even though it's recommended to perform indirect tensile strength of cement due to its likelihood to fail in tensile before compression, the Unconfined Compressive Strength (UCS) tests were conducted to investigate the compressive load that the designed cement samples can withstand. The three different cement recipes were cured under water at a temperature of 70°C ± 5°C (158°C ± 9°C) and their unconfined compressive strengths were tested as well. Three samples were prepared for each of the cement systems and for each curing time. The cement curing durations tested were 24 hours and 7 days. From Fig. 2.12, there is a clear increase in UCS with curing time. Geopolymer cement acquired a 44% lower UCS (10.3 MPa) after 24 hours than Neat Class H cement (18.6 MPa).

On the other hand, nano-modified Class H cement had a 41.5% lower UCS (10.8 MPa) than Neat Class H. UCS is only one of the cement properties that are required for a viable oil well cement in addition to bonding dynamics and flow behavior under different subsurface conditions. Based on these results it is evident that geopolymer cements should be field-tested and nano-synthetic graphite should be integrated in Portland cement designs.

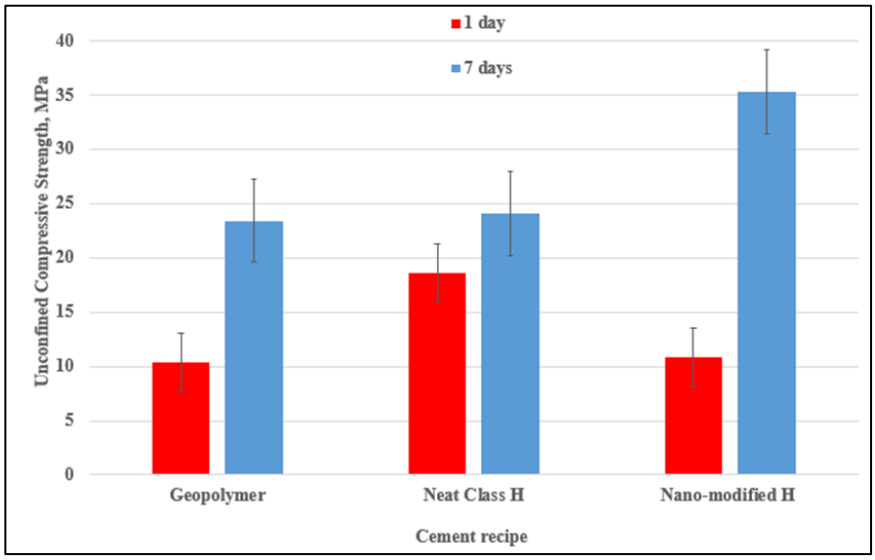


**Figure 2.12 Strain development ($\varepsilon_{xx}$ and $\varepsilon_{yy}$) for Sandstone geopolymer concentric system.**

## 2.3 Numerical and Computational Investigation of Well Integrity in the TMS

To prevent the formation of leakage pathways, cement sheath is a significant barrier, establishing zonal isolation for preventing fluid migration in the annulus, supporting casing and liner, and separating casing from corrosive fluids. Three types of mechanisms typically lead to the loss of cement integrity: hydraulic, mechanical, and chemical degradation (Bois et al., 2012). Hydraulic mechanism involves inefficient mud-cement displacement due to casing eccentricity or improper cement estimation, resulting in the channeling of cement at the wide side and slow-moving or immobile mud in the narrow region (Ermila et al., 2013). Mechanical degradation occurs when compressive or tensile loading on the cement is higher than limiting strength. Chemical degradation is the cement damaged because of interactions between cement and fluids such as muds (drilling fluids) and formation fluids. In the worst case, a cement is subjected to mechanical damage accelerated by chemical exposure leading to fluids penetrate deeper into cement sheath. Hence, it is essential to evaluate the integrity to prevent gas migration through annuli around the cement sheath. The five most common cement failure modes that damage well integrity are debonding, shear failures, radial cracks, axial cracks, and axial failures. Debonding is not only a result of tensile stresses exceeding contact strength at interfaces but also due to significant shear (or compressive) stresses that may take place. Debonding is a major issue in the Tuscaloosa Marine Shale (TMS) operations. Previous operations in the formation revealed that the primary cement

issue involved the poor bonding experienced in all three (3) sections of the wellbore: surface, intermediate, and horizontal.

This section investigates the effectiveness of cement to ensure long-term integrity using a computational and numerical method. The computational and numerical methods used in this study is an extension of the experimental investigation performed in the previous section..

### *2.3.1 Cement Integrity Under Diametric Compression Load*

The mechanical properties for each kind of rock formation are shown in Table 2.1. Effect of Cement Young's Modulus and Poisson's Ratio: The mechanical properties, Young's modulus (E) and Poisson's ratio (ν), are the most important parameters in the evaluation of cement sheath integrity. Previous studies on long-term well integrity risks showed that cement with lower E and higher ν reduce the risk of failures. These studies however were conducted for cement in liner-casing overlap. Present paper aims to evaluate the effects of cement Young's modulus and Poisson's ratio on the failure of the cement sheath bonded between casing and formation under diametric compression load. In this subsection, eight (8) different scenarios were simulated. Displacement boundary condition was kept constant at 0.18 mm. Stresses were evaluated along the three directions – x axis, y axis, and 45°. The results are presented in Fig. 2.13, Fig. 2.14, and Fig. 2.15. The compressive and tensile strength is considered as 25 and 1.4 MPa. Higher Poisson's ratio is better to maintain the cement integrity.

**Table 2.1** The mechanical properties of the rock formation.

| *Rock Properties* | *Elastic Formation* | *Normal Formation* | *Brittle Formation* |
|---|---|---|---|
| *Young's modulus (GPa)* | 5 | 10 | 25 |
| *Poisson's ratio* | 0.40 | 0.30 | 0.20 |

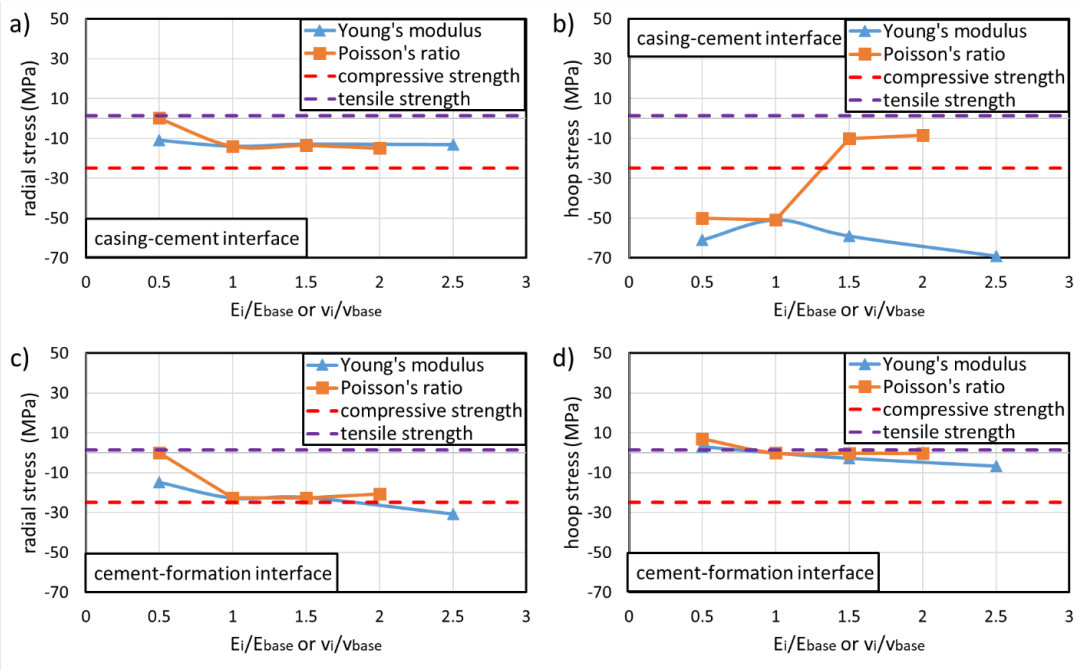


**Figure 2.13 The effects of Young's modulus and Poisson's ratio at 0° in the casing-cement and cement-formation interfaces. a) radial stress at casing-cement interface, b) hoop stress at casing-cement interface, c) radial stress at cement-formation interface, and d) hoop stress at cement-formation interface.**

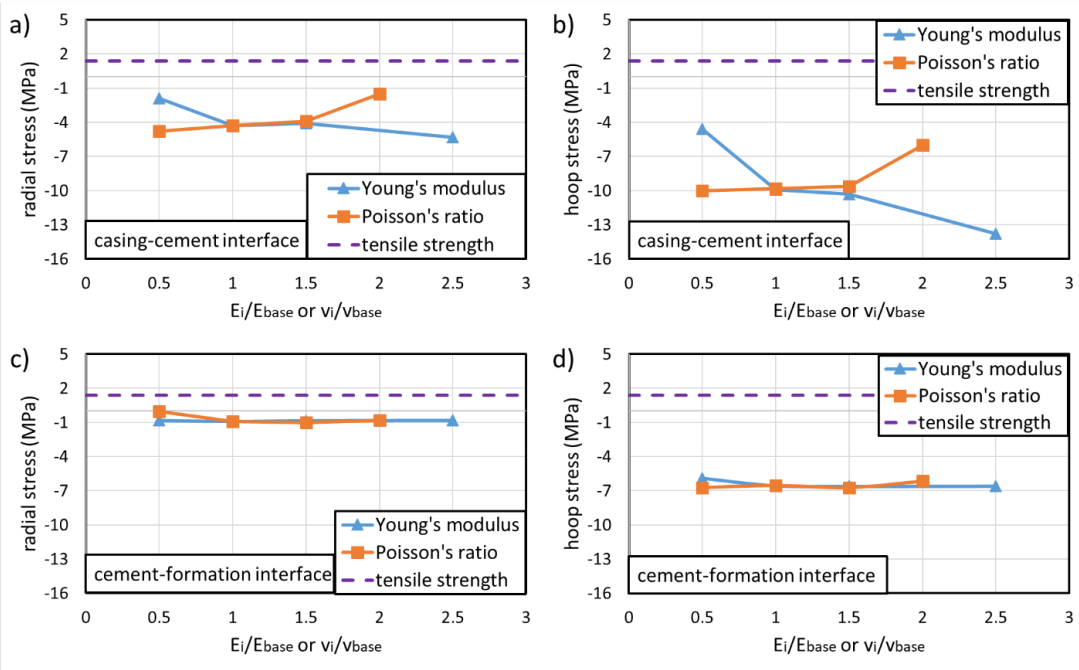


**Figure 2.14 The effects of Young's modulus and Poisson's ratio at 45° in the casing-cement and cement-formation interfaces a) radial stress at casing-cement interface, b) hoop stress at casing-cement interface, c) radial stress at cement-formation interface, and d) hoop stress at cement-formation interface.**

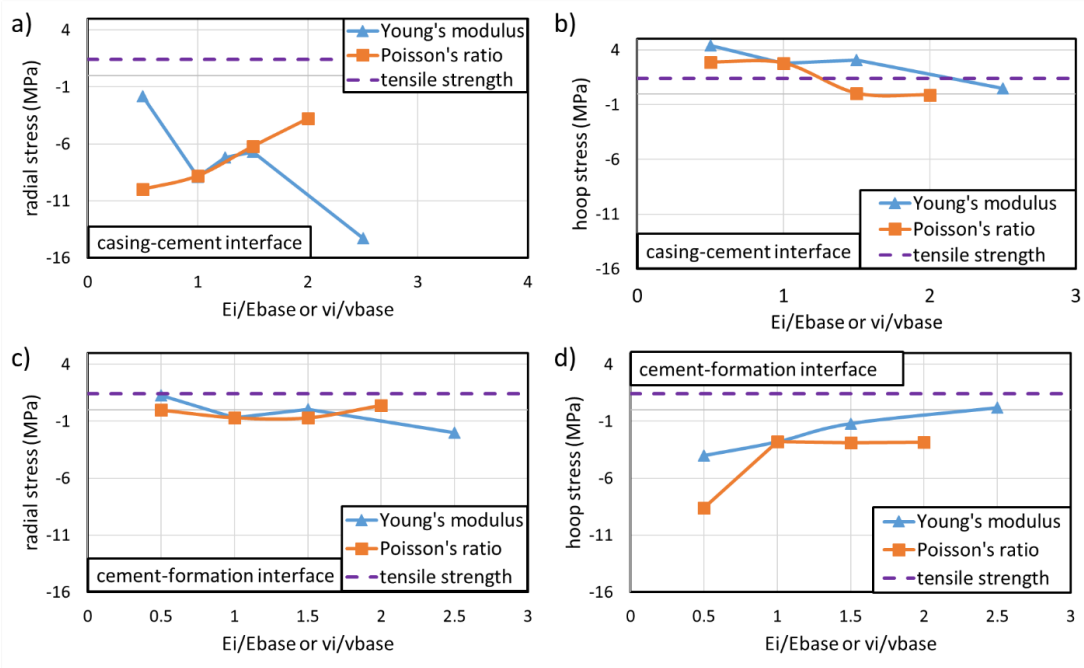


**Figure 2.15 The effects of Young's modulus and Poisson's ratio at 90° in the casing-cement and cement-formation interfaces a) radial stress at casing-cement interface, b) hoop stress at casing-cement interface, c) radial stress at cement-formation interface, and d) hoop stress at cement-formation interface.**

### *2.3.2 Thermal Considerations of Cement Integrity Under In-Situ Stresses*

Table 2.2 presents the comparison of mechanical stresses sensitivity to different parameters. Heat flow from formation to casing is representative of injection wells. For radial stress at 0° and 90°, differential temperature is the most sensitive parameter, followed by internal casing pressure and horizontal stress ratio. The other parameters such as thermal conductivity, expansion coefficient, Young's modulus, and Poisson's ratio do not exert a notable influence on the radial and hoop stresses. Increasing casing pressure raises compressive nature and the magnitude of radial and hoop stresses. On the other hand, an increase in differential temperature or horizontal stress ratio reduces the radial stress, making it more tensile. The tensile stress at 0° is larger than at 90°. For hoop stresses, thermal expansion coefficient is the most critical parameter, followed by differential temperature, horizontal stress ratio, and Young's modulus. Increasing temperature difference, horizontal stress ratio, and thermal expansion coefficient tend to reduce the hoop stress and make it more tensile. In general, hoop stress at 90° has a higher magnitude than 0°.

Casing temperature larger than formation temperature is a likely scenario in production wells. For radial stress, the effect of variates in parallel and perpendicular directions are similar. Compressive stress in perpendicular direction are larger than parallel. The most sensitive parameter to the radial stress is the differential temperature, followed by internal casing pressure, Young's modulus, and stress ratio. Young's modulus and stress ratio are more influential at low magnitude compared to higher magnitude. High differential temperature, casing pressure, Young's modulus, and low stress

ratio result in high compressive stress and increased the risk of cement crushing. Hoop stress has the highest sensitivity to change in Young's modulus. The other parameters, such as Poisson's ratio, differential temperature, and stress ratio also induce notable change. Similar to radial stress, compressive stress in perpendicular direction is slightly larger than parallel. Increasing Young's modulus, differential temperature, and Poisson's ratio result in higher compressive hoop stress. Contrary to this, an increase in stress ratio reduces compressive nature of hoop stress and pushes it towards tensile.

**Table 2.2** The comparison of mechanical stresses sensitivity to various parameters.

| *Direction* | *Radial stress ($\sigma_r$)* | *Hoop stress ($\sigma_\theta$)* |
|---|---|---|
| | $\Delta T < 0$ | |
| 0° | $\Delta T > P_i > N_R$<br>(α, K, E, and ν are not sensitive) | $\alpha > \Delta T > N_R > E$<br>(K, ν, and $P_i$ are not sensitive) |
| 90° | $\Delta T > P_i > N_R$<br>(α, K, E, and ν are not sensitive) | $\alpha > \Delta T > N_R > E$<br>(K, ν, and $P_i$ are not sensitive) |
| | $\Delta T > 0$ | |
| 0° | $\Delta T > P_i > E > N_R$<br>(K, α, and ν are not sensitive) | $E > \nu > \Delta T > N_R$<br>(K, $P_i$, and α are not sensitive) |
| 90° | $\Delta T > P_i > E > N_R$<br>(K, α, and ν are not sensitive) | $E > \nu > \Delta T > N_R$<br>(K, $P_i$, and α are not sensitive) |

## References


Bois, A. P., Garnier, A., Galdiolo, G. et al. 2012. Use of a Mechanistic Model to Forecast Cement Sheath Integrity. SPE Drilling & Completion, 27 (02): 303-314. SPE-139668-PA.

Ermila, M., Eustes, A. W. and Mokhtari, M. 2013. Improving Cement Placement in Horizontal Wells of Unconventional Reservoirs Using Magneto-Rheological Fluids. Unconventional Resources Technology Conference, Denver, Colorado, 12-14 August, 2013. URTec-1619212-MS.

# CHAPTER 3 Improving TMS Formation Evaluation

There is little published core data analysis for the TMS and so the reserve estimation in the TMS is heavily biased on well log analysis. On the other hand, due to the nature of inadequate wellbore conditions in the TMS, routine formation evaluation using well logs can be inaccurate and unreliable. In this chapter, TMS formation evaluation was performed as: (1) Characterization of brittleness and total organic carbon (TOC) of TMS with machine learning technique; (2) TMS properties from geophysical analysis; (3) Mineralogical composition, organic-richness and produced-water chemistry of TMS; (4) Ionic movement between TMS cores and water.

## 3.1 Geophysical characterization of brittleness and TOC of Tuscaloosa Marine Shale by using machine learning techniques

### *3.1.1 Characterization of the brittleness of TMS by using machine learning technique*

Our datasets come from Mississippi. The updip lower Tuscaloosa trend of southwest Mississippi occurs along the southern rim of the Mississippi Salt Basin. The lower Tuscaloosa formulation is found here at subsea depths of about 3000m to 4200m (Hersch, 1987) along gentle regional dip to the southwest. First generation fields within this part of trend (e.g, Cranfield, Brookhaven, Mallalieu, and Baxterville), discovered in the 1940's, are anticlinal and fault closures related to deep salt structures (Womack, 1950). Second-generation fields discovered in the late 1950's and early 1960's, are stratigraphic traps on broad structural noses with weak closure. Fields discovered during the latest round of drilling, including North Hustler and Thompson, are stratigraphic traps with updip and lateral sand pinch-outs; structural closure is essentially lacking. The location and delineation of this type of trap was pioneered by Shell Oil, which used seismic stratigraphic techniques to position exploratory wells, discovering Olive field in 1981 (Gruebel, 1985).

The Tuscaloosa formation comprises the basal formation of Gulf series of Upper Cretaceous ages (Fig. 3.1). An unconformity separates the Basal Tuscaloosa from the older Washita Fredericksburg formation of Lower Cretaceous ages. The sand has been described as having large amounts of chloritic materials and shaly materials in some areas. The Lower Tuscaloosa Formation has traditionally been divided into two members: a basal Massive Sand Member and a conformably overlying Stringer Sand Member, with informal local and field designations given to individual sands within these members. Spooner (1964) referred to the basal unit in northwest Louisiana as the Buckhorn sand and believed it to be younger than the Massive Sand of Mississippi. The TMS interval is highlighted with red dashed rectangle.

The 3D seismic data was recorded in 2007 with coverage area of about 25 square km, as shown as the yellow area in the Fig. 3.2 (c), where 23 wells (labeled as yellow triangle). Figure 3.2 shows the horizon slices of seismic amplitude extracted at the top and base of reservoir for both pre- and post- injection. A NW-SE directional fault goes through this area. The top negative amplitude

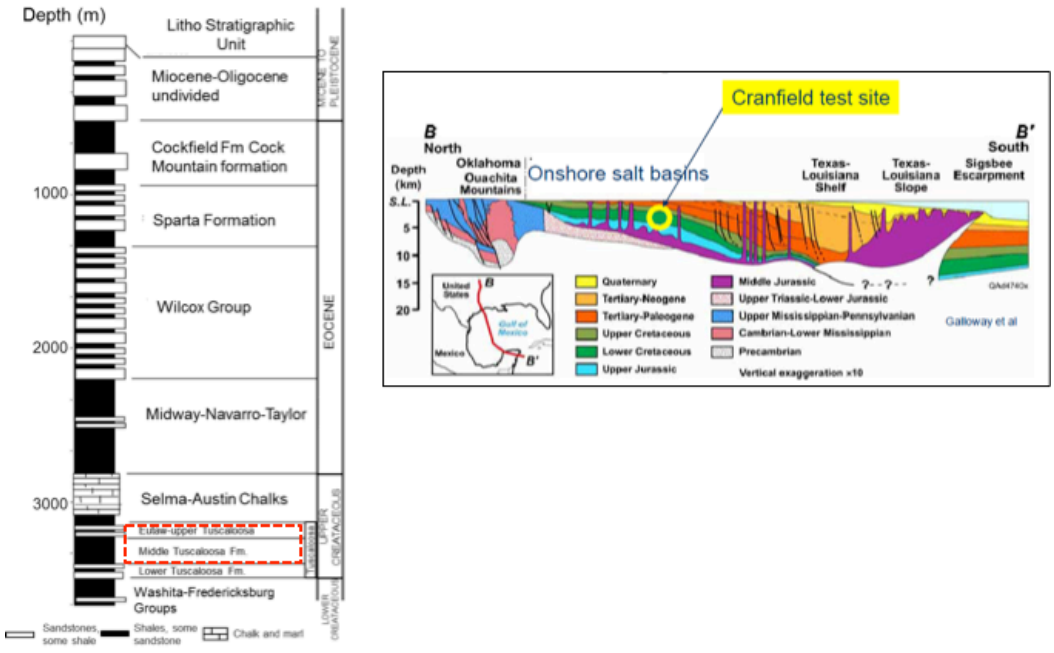


**Figure 3.1 Stratigraphy and geological section.**

(blue) represents the impedance drop transaction indicating the lower impedance of injection interval. The ellipse area shows change from white to blue from pre- to post- injection at the top slices, which can be interpreted as impedance decrease of injection interval. There is not obvious difference at the time-lapse base slices. The inline-1102 (red dash line) and well-28 (yellow triangle) will be used as 2D cross-section example and well-log validation.

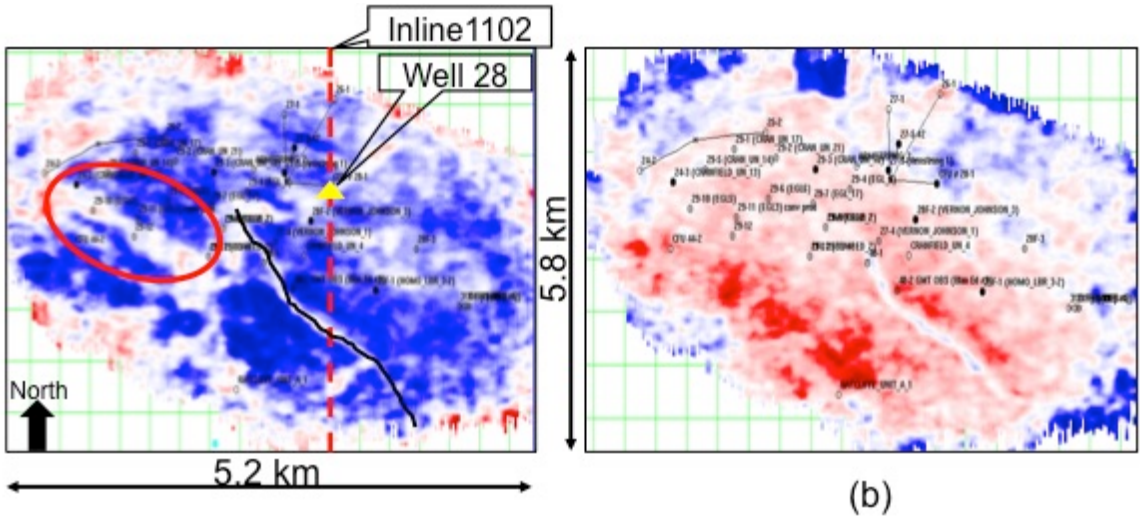


**Figure 3.2 Seismic datasets at top (a) and base (b) of lower Tuscaloosa sand.**

Well-logs from Well-28, where is yellow triangle located in Fig. 3.2 (a) are shown in Fig. 3.3. The preliminary interpretation of TMS is highlighted in yellow zone. The cross-correlation between synthetic and extracted pre-injection seismogram (along the deviation of well-28) is about 0.72, which demonstrates well feasibility for implementation of inversion method for improved resolution acoustic impedance. The wavelet (Fig. 3.3), which was extracted by calibrating seismic with well-log reflection coefficients. The peak frequency of the wavelet is about 30Hz and the phase is about 140 degree.

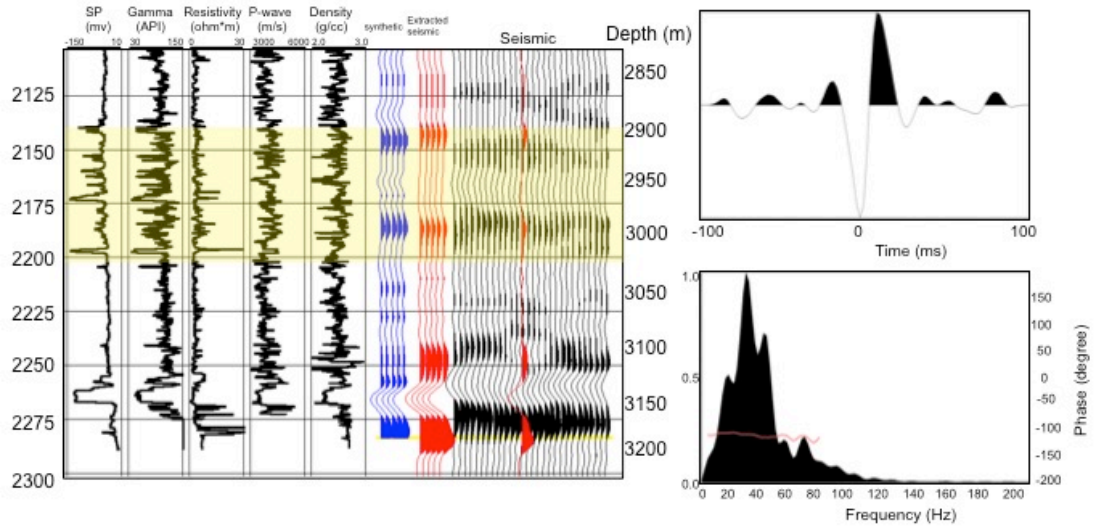


**Figure 3.3 Seismic well tie includes SP, Gamma ray, resistivity, P-wave velocity and density logs.** Synthetic seismogram (blue) and extracted seismogram from pre-injection seismic (red) have cross-correlation of 0.72. The wavelet in the left figure is extracted from seismic data.

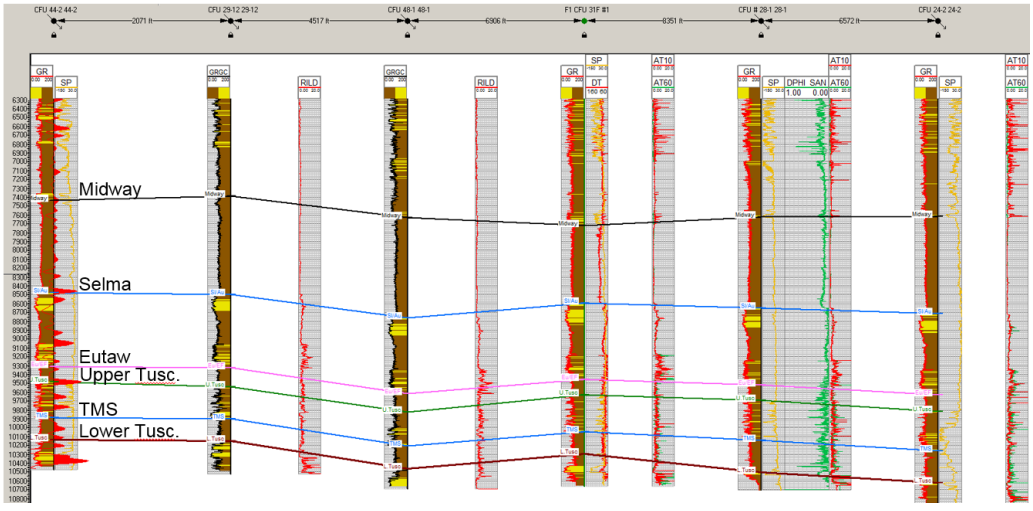


**Figure 3.4 Well-log correlation of wells in Cranfield, Mississippi showing formation top names across wells using gamma-ray log as a lithology indicator.**

Well-log correlation in Fig. 3.4 shows formations adjacent to the Tuscaloosa Marine Shale and the associated formation top name. The Midway formation in Southern Mississippi is mostly composed of marine clay and shale with minor sand and limestone beds. In Alabama, Mississippi, Louisiana, and eastern Texas, Midway Group overlies the Selma Group which was deposited during the Late Cretaceous and it consists of massive calcareous clays, marls, and chalky material (Cushing et al., 1964). The Eutaw Formation is separated into lower and upper units. The upper unit is referred to as the Tombigbee Sand Member and the lower unit is generally composed of glauconitic sand interbedded with dark to gray shales (Dowsett et al., 1989). The lower Tuscaloosa contains sandstone reservoirs that were deposited in a fluvial-deltaic system. On the other hand, sandstones from the Upper Tuscaloosa were deposited in an alternating transgressive and regressive shallow sea environment (Bearden et al., 2000). Between the Lower and Upper Tuscaloosa, lies the TMS which was deposited during Late Cenomanian to Turonian when there was a major rise in base level and a marine flooding event characterized by transgression sequences (Mancini and Puckett, 2002).

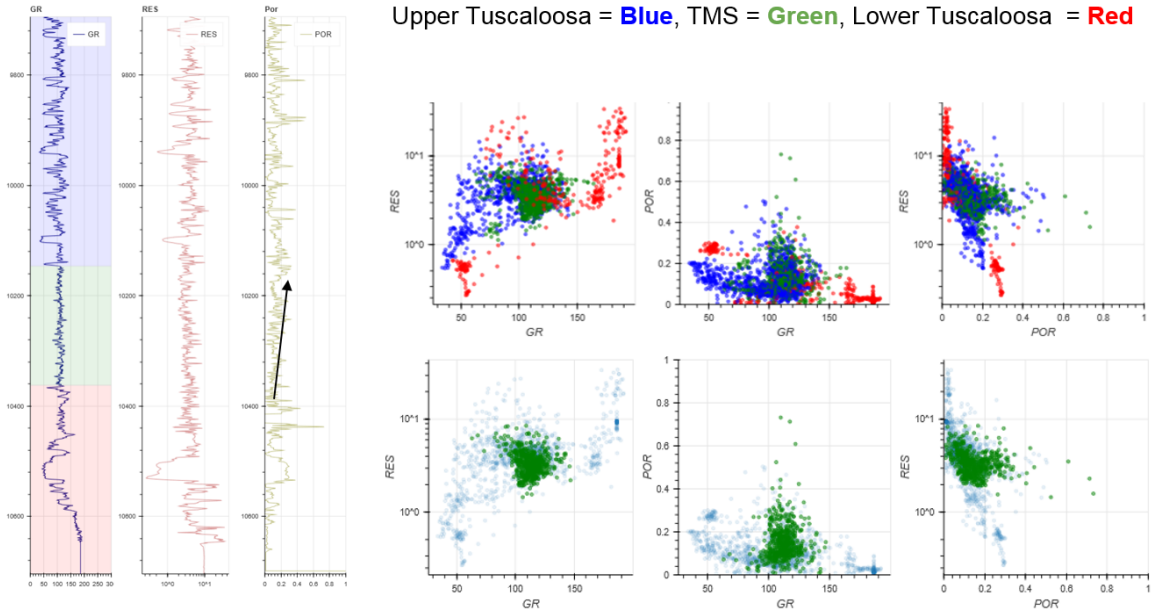


**Figure 3.5 Well-log data analysis at Well CFU-28.**

Figure 3.5 displays Well-log data analysis at Well CFU-28. The left three plots show the gamma-ray log, resistivity log, and porosity log. The top three of scatter plots show distribution of the Upper Tuscaloosa, TMS, and Lower Tuscaloosa. The bottom three scatter plots show the TMS distribution while the Upper and Lower Tuscaloosa are in the background with a faint blue color.

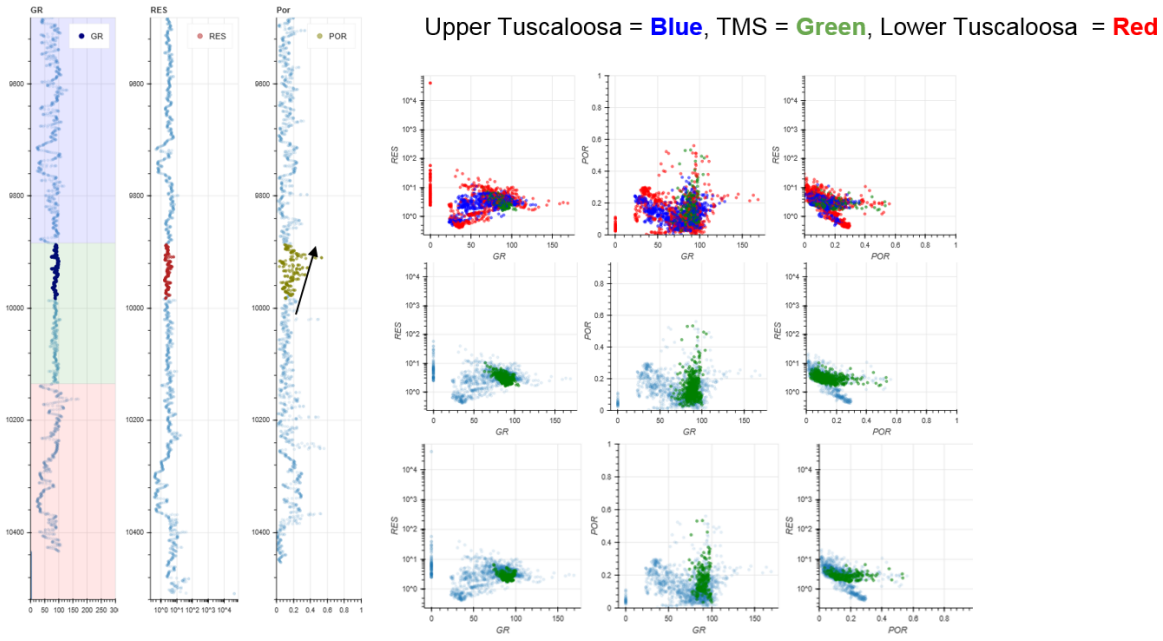


**Figure 3.6 Well-log data analysis at Well CFU-44-2.**

Figure 3.6 displays Well-log data analysis at Well CFU-44-2. The left three plots show the gamma-ray log, resistivity log, and porosity log (the log increases gradually from bottom to top of the formation). The top three of scatter plots show distribution of the Upper Tuscaloosa, TMS, and Lower Tuscaloosa. The middle three scatter plots show the TMS distribution while the Upper and Lower Tuscaloosa are in the background with a faint blue color. The bottom three scatter highlight a section of the TMS with high porosity values while the low porosity TMS, and the Upper and lower Tuscaloosa are in the background with a faint blue color.

*Theory and method*

Post-stack attributes (seismic hilbert transform, instantaneous frequency, and instantaneous phase) computed using OpendTect software are used as input features to an ANN model trained to predict four RPT labels derived using prestack data. Seismic hilbert transform, instantaneous frequency, and instantaneous phase, are used because of their ability to highlight geologic features within seismic data. The attributes facilitate understanding of seismic spatial and temporal variation which aid in providing insight of the depositional environment and reservoir characterization. Prestack compressional wave velocity (Vp) and shear wave velocity (Vs) and density inversion volumes were computed using Hampson Russell software which uses the Aki and Richards (1980) to approximate the Zoeppritz (1919) equations.

Alzate and Devegowda (2013) show that better production in unconventional reservoir can be explained using seismic lambda-rho and mu-rho crossplot RPT labels. This shows how RPT can be used to determine brittle and organic rich zones within seismic data. Shoemaker et al. (2019) has linked the lambda-rho and mu-rho crossplot clusters to ternary plot mineralogical facies

defined by the volume of quartz, carbonate, and clay. Moreover, Shoemaker et al. (2019) complemented the rock physics template with Hashin-Strikman bounds with mineralogical elastic constants.The predicted labels were grouped into zones by confining the RPT with projected seismic derived poison's ratio and young's modulus thresholds. Finally, Tensorflow machine learning framework was used to make an ANN trained to predict the RPT labels using poststack seismic attributes. To ensure optimal learning for the ANN, stochastic learning is used to train the ANN because it yields better results and allows the ANN to train faster as recommended by LeCun et al. (1998). The ANN was designed to have 3 hidden layers with 3 neurons in each layer. The trained ANN achieved a ninety percent accuracy.

*Data preprocessing*

Input data from seismic attributes are normalized between 0 and 1. This allows input data to have an equal range for a stable convergence of the ANN weights when training. Outlier data points in the lambda-rho and mu-rho crossplot were dropped since most were from the seismic data edge where the signal to noise ratio is low. Moreover, prior to training, labels with few data points were resampled randomly to match the labels with the highest frequency of occurrence within the area of interest. Resampling is crucial because the reservoir area of interest can be a low occuring RPT label, therefore strengthening the ANN by resampling will increase the chances of identifying similar areas during future predictions. Hence, up-sampling of the underrepresented label is best as opposed to down-sampling of the label with a high frequency which can increase the susceptibility of losing valuable information of the dominant label.

Four zones were obtained to highlight TOC content and brittleness distribution from well logs and seismic data Fig. 3.1. The seismic lambda-rho and mu-rho RPT was calculated using equation 1 and 2, then confined using poison's ratio and young's modulus, Fig. 3.7c and 3.7d, like in Altamar and Marfurt (2015) and Alzate and Devegowda (2013). Unlike the seismic RPT where four zones are defined, the well logs are TOC and brittleness are given as a trend because of well log data sparsity. Projection of the RPT label onto a horizon slice are shown in Fig. 3.9a.

$$\mu\rho = SI^2, \qquad (1)$$

$$\lambda\rho = AI^2 - 2SI^2, \qquad (2)$$

Well logs within the seismic data volume were used to compute lambda-rho and mu-rho RPT then colored using TOC and brittleness (Fig. 3.7a and 3.7b) values. Lambda-rho and mu-rho from well logs were computed using compressional and shear wave logs using equation 1 and 2. TOC from well logs was computed using the Passey's equation then fitted to TOC values measured from the well core. The obtained Passey's equation was used to determine TOC content in wells which had digital well logs but lacked TOC core measurements. Machine learning can aid in performing seismic data knowledge transfer across geologically localized seismic datasets. However, the

effect of difference in seismic band, phase, and temporal window between the training and prediction data should be put into account.

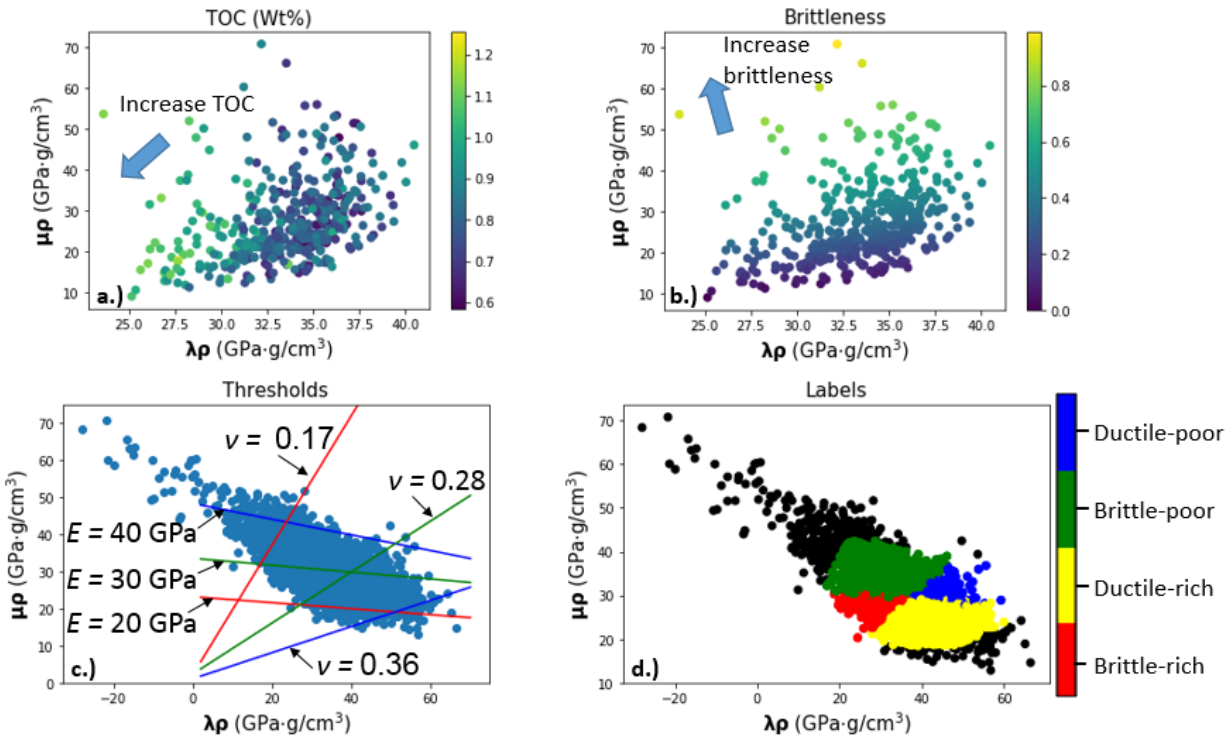


**Figure 3.7 TOC distribution and brittleness of TMS.**

Figure 3.7 (a) showa the TOC distribution trend increasing towards the zone with low lambda rho and mu rho. Figure 3.7 (b) shows the brittleness trend. Brittleness was calculated using the average of normalized poison's ratio and young's modulus as proposed in Grieser and Bray's (2007). c.) Showing poison's ratio and young's modulus thresholds set in order to obtain rock-physics labels. d.) Showing assigned labels set using thresholds in Fig. 3.7a. The black colored data points are a result of seismic low signal to noise ratio around the edge of the seismic data hence they were dropped.

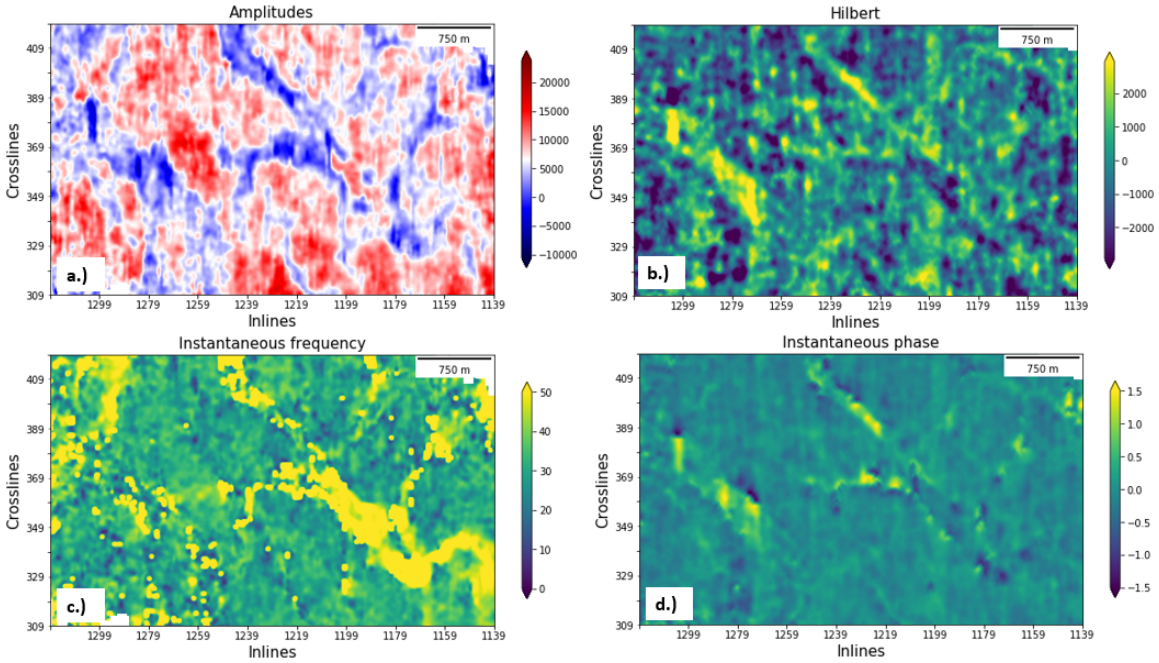


**Figure 3.8 The amplitude horizon slice and seismic attribute of horizon of TMS.**

Figure 3.8 displays; a.) showing amplitude horizon slice at the base of the TMS having a sinuous feature (channel); b.) Hilbert seismic attribute of horizon; c.) Showing instantaneous frequency seismic attribute of horizon. The seismic attribute highlights the channel, the southern end of the channel is seen to be more continuous. d.) Instantaneous frequency seismic attribute of horizon.

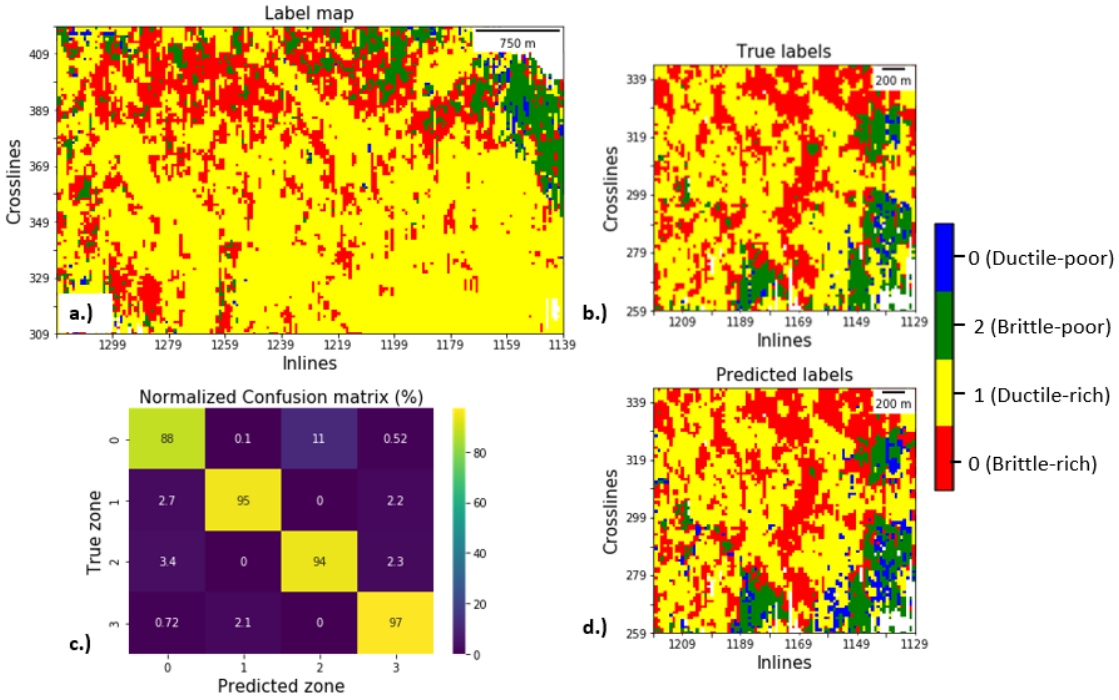

Figure 3.9 shows; a.) the label map of the RPT in Figs. 3.8 and 3.7. The northwest area appears to be dominated by a brittle rich zone (RPT label 1). On the other side, the channel appears to be filled with ductile rich zone (RPT label 2), the dominance of label 2 increases going south. b). the confusion matrix between the predicted labels and the true labels. c) Horizon slice RPT true labels from seismic data that was used for testing. d.) Horizon slice of predicted RPT labels after using the seismic data held for testing.

*Conclusions*

Geological interpretations are made better when they integrate seismic, rock physics, petrophysics, and other domain area data within the petroleum industry. Machine learning models like ANN can be used as the bridge between different domain data with non-linear relationships. Machine learning can aid in performing seismic data knowledge transfer across geologically localized seismic datasets. However, the effect of difference in seismic band, phase, and temporal window between the training and prediction data should be put into account.

### *3.1.2 Characterization of the TOC of TMS by using machine learning technique*

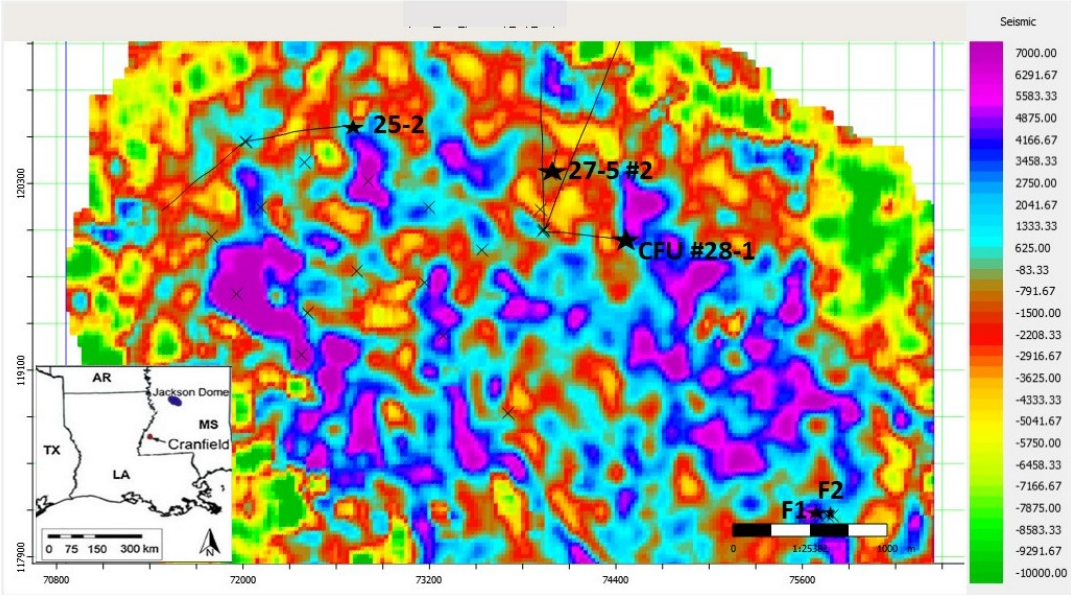


**Figure 3.10 Seismic map of Cranfield with the locations of specific wells** (Well CFU 44-2 is out of this survey area)

Six wells- CFU 44-2, 25-2, 27-5 #2, CFU 28-1, F1 and F2 as shown in Fig. 3.10 are used for this study. Figure 3.11 displays the structural cross section from west side to eastern flank of Cranfield structure. TOC values are also included for TMS section

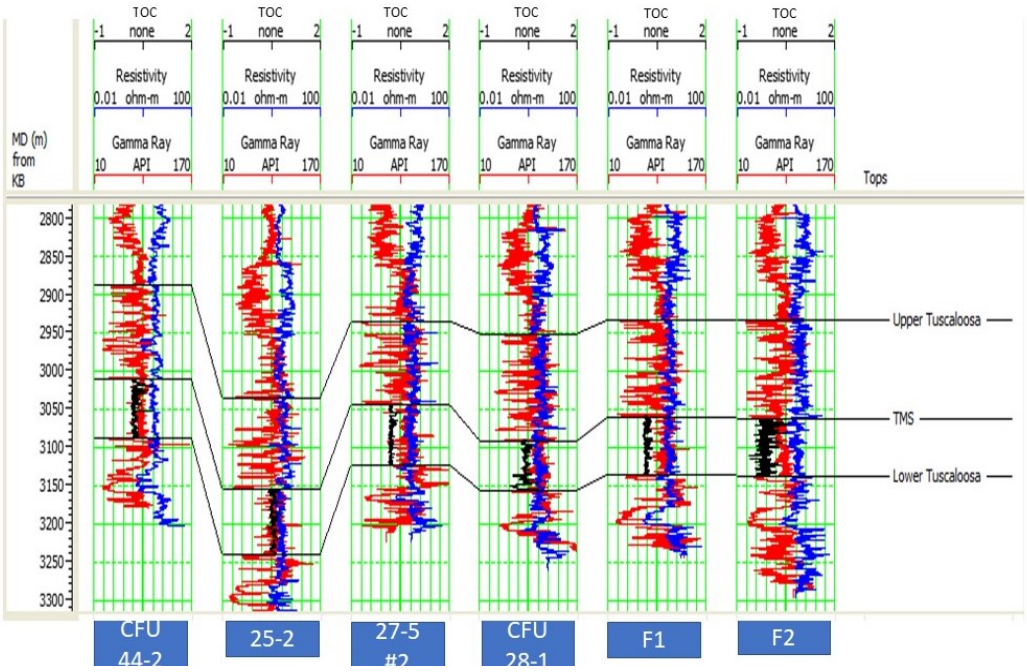


**Figure 3.11 the structural cross section from west side to eastern flank of Cranfield structure.**

TMS depth is varying with locations. The variation is higher in the west part than the east part. There is a huge fall of TMS depth between CFU 44-2 and 27-5 #2 well location. The TMS depth is getting deeper from the middle to the east of the Cranfield. The amount of organic carbon present in a rock is a determining factor in a rock's ability to generate hydrocarbons. The concentration of organic material in source rocks as represented by the weight percent of organic carbon. A value of approximately 0.5% total organic carbon (TOC) by weight percent is considered the minimum for an effective source rock.

Here, we use the Passey's "DlogR" method to calculate the TOC. Mainly Resistivity log and Density log are used to calculate the TOC. According to this method,

$$DlogR = \log\left(\frac{RESD}{RESD_{base}}\right) - 2.5 * (DENS - DENS_{base}) \quad (3)$$

$$TOC\ (\%\ weight) = SF1 * (DlogR * 10^{(0.297 - 0.1688 * LOM)}) + SO1 \quad (4)$$

Where,

$RESD$ = deep resistivity in any zone (ohm-m)

$RESD_{base}$ = deep resistivity baseline in non-source rock (ohm-m)

$DENS$ = density log reading in any zone (gm/cc)

$DENS_{base}$ = density corresponding to $RESD_{base}$ in lean shale interval (non-source rock)

$SF1$ = Scale Factor

$SO1$ = Scale Offset

$LOM$ = Level of Organic Maturity (unitless)

The TMS thickness and TOC range data for every well location have been gathered in the Table 3.1.

**Table 3.1** TMS thickness and TOC range.

| Wells Name | TMS top (meters) | TMS base (meters) | TMS thickness (meters) | TOC range |
|---|---|---|---|---|
| CFU 44-2 | 3012.7 | 3089.2 | 76.5 | 0.18 – 0.56 |
| 25-2 | 3156.4 | 3242.0 | 85.6 | 0.39 – 0.78 |
| 27-5 #2 | 3045.2 | 3124.2 | 79 | 0.15 – 0.43 |
| CFU 28-1 | 3092.7 | 3158.5 | 65.8 | 0.02 – 1.26 |
| F1 | 3061.6 | 3137.9 | 76.3 | 0.09 – 0.40 |
| F2 | 3063.9 | 3138.9 | 75 | 0.00 – 0.40 |

TOC values show a relatively higher values in the northern part of Cranfield than the southern part. Calculation with more wells will give us more clear idea.

*Multiple regression analysis*

The calculated TOC values are now tried to predict using seismic attributes and seismic inversion volumes. A multiple regression model has been developed. Using stepwise regression process for optimal attribute selection, multiple regression model determines the attributes based on minimal mean-squared prediction error. Stepwise regression automatically chooses the parameters which are linearly independent. (Hampson et al., 2001)
All attributes as well as the target TOC have been evaluated both in linear and non-linear forms. So, the predictive power of this method is very high. The target parameter can be written as a linear combination of attribute sample:

$$L^{(t)} = w_0 + w_1 A_1^{(t)} + w_2 A_2^{(t)} + w_3 A_3^{(t)} + \ldots$$

Here, A is any attribute and w is its weight.

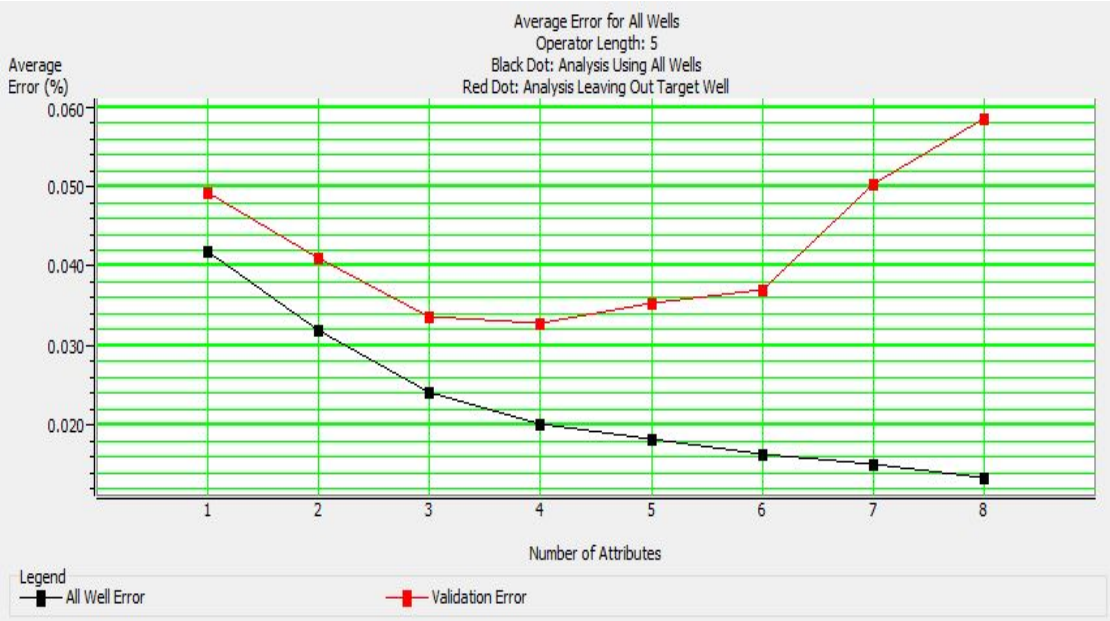


**Figure 3.12 Training and Validation curve showing average error percentage with increasing number of attributes.**

A list of three attributes- Dominant frequency, Instantaneous frequency, Apparent polarity proves to be the optimal input for TOC prediction analyzing this dataset. Using these attributes, the training accuracy shows 90% correlation and validation accuracy shows 81% correlation. The validation curve stops declining convincingly at three number attributes, which means the first three attributes give the best result in this case. An operator of length 5 is considered to produce the best result after several trial-and-error approach. Figures 3.13 and 3.14 show the prediction and validation results of our machine learning results.

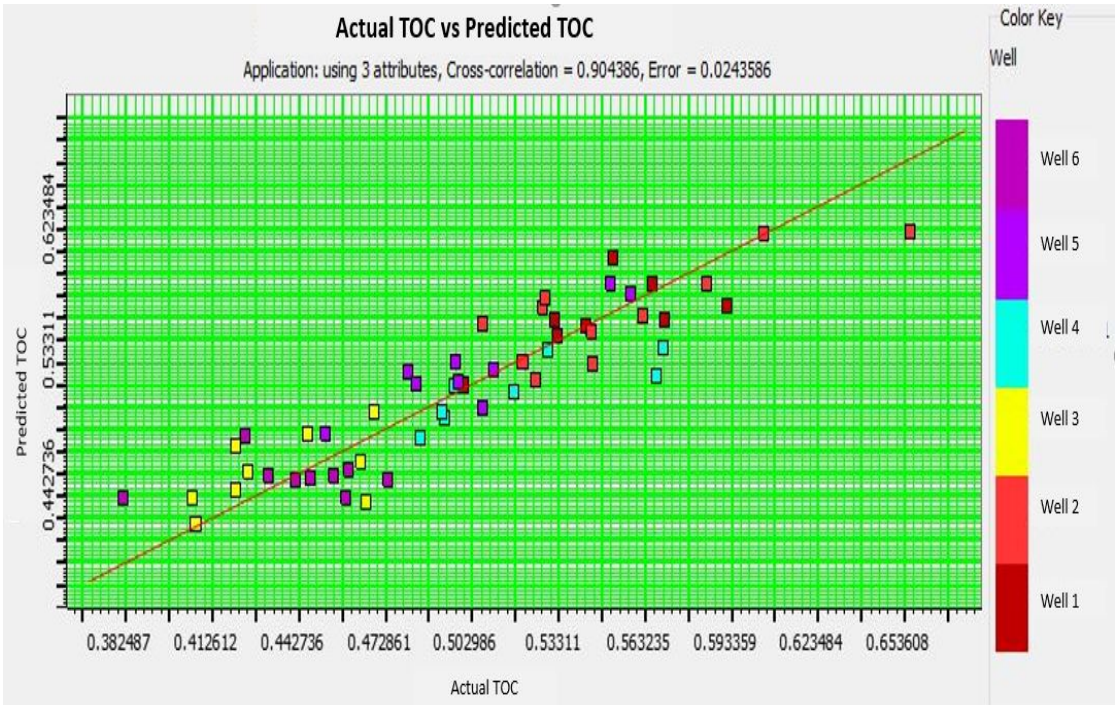


**Figure 3.13 Actual and Predicted TOC correlation for training data.**

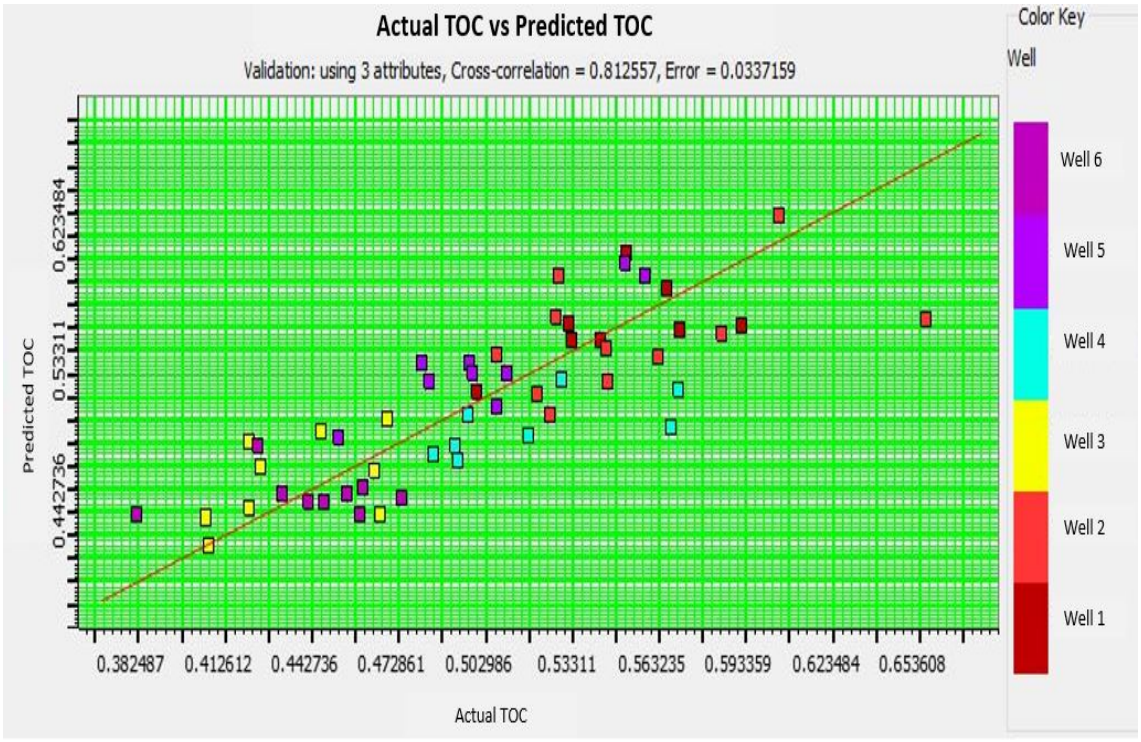


**Figure 3.14 Actual and Predicted TOC correlation for validation data.**

The established relationship between the seismic and target logs has now been applied to entire 3D volume. The work is done using Hampson-Russell software. It relates the multi-attribute relation to entire seismic zone of interest. A data slice is shown in Fig. 3.15. From Fig. 3.15, we can see the TOC values of the entire TMS zone in the survey region. It gives an overall idea about TOC value distribution in the entire zone.

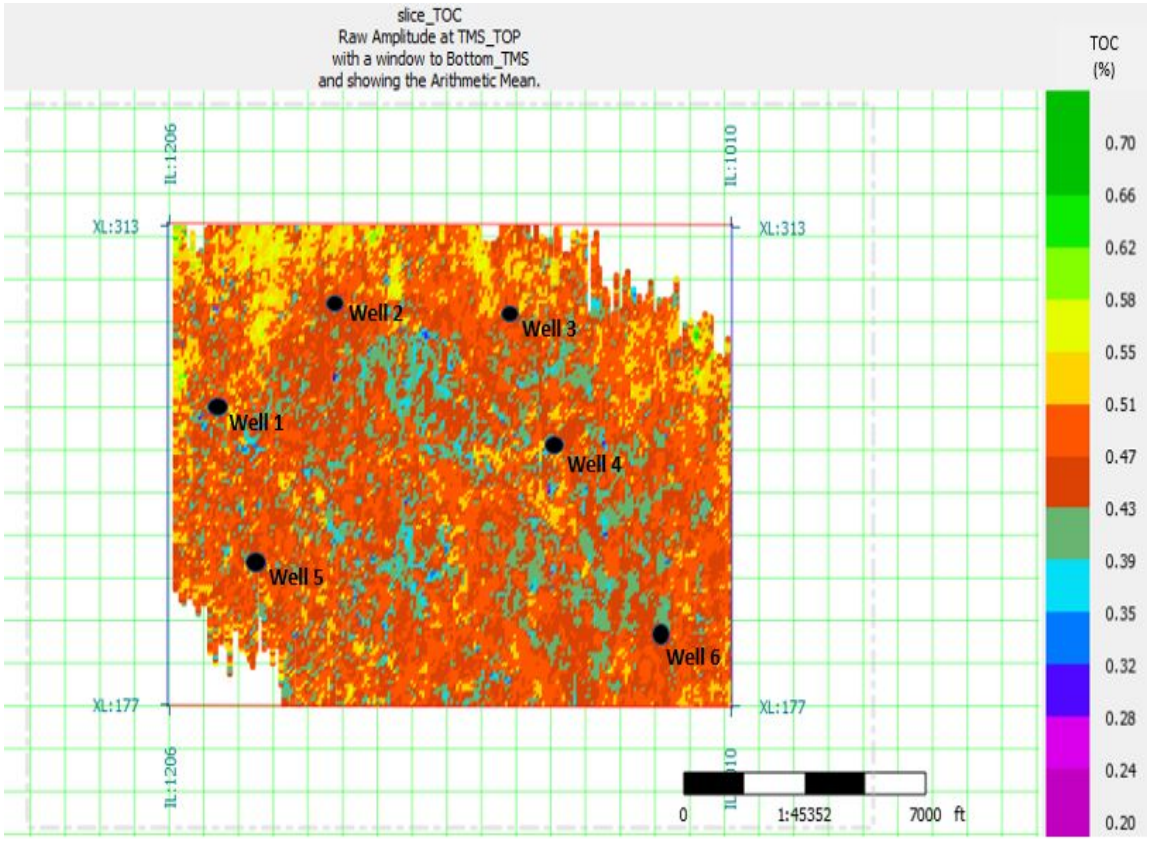


**Figure 3.15 Data slice of 3D volume. TOC distribution over the region.**

Correlation between seismic attributes and well logs of this region is showing consistent behavior. Multi-attribute regression establishes a relationship between them with a validation correlation of 81%. This relationship paves the way to apply seismic attributes (Dominant frequency, Instantaneous frequency, Apparent polarity) for TOC prediction over the region. From the map, we can see that the upper left corner region (Inline 1170, Crossline 305) would be a better place for petroleum extraction depending on TOC values. In this portion, a large area is showing relatively high value of TOC.

*Conclusions*

Though the result from neural network analysis is satisfiable, it cannot surpass the accuracy of our previous multiple regression analysis. In the multiple regression analysis, our training correlation was 90% and validation correlation was 81%. Comparing the results, multiple regression analysis should be applied for TOC prediction in our dataset.

To establish a robust relationship between different types of seismic attributes and many geomechanical properties is yet a challenging task. Trying to estimate the TOC with those features can pave the way to have more clear idea about those relationships. Different machine learning algorithms will help us to do that and the spatial distribution of TOC over the seismic survey area can also be established with higher confidence.

## 3.2 TMS properties from geophysical analysis

### *3.2.1 Characterization of the Elastic Mechanical Properties of the Tuscaloosa Marine Shale From Well Logs Using the VTI Model*

An empirical 1D geomechanical model was developed and used to evaluate the mechanical properties of the Tuscaloosa Marine Shale in Lane 64-1 and Smith SD 1H wells. The purpose of the model is to provide accurate Young's modulus and Poisson's ratio estimates for hydraulic fracturing design. Because vertical Poisson's ratio is less than the horizontal Poisson's ratio in the marine shale, the stiffness coefficients $C_{13}$ and $C_{11}$ were estimated using the relationships developed from the ultrasonic core data available for the two Tuscaloosa Marine Shale wells. Further, correlations between the static and dynamic properties from laboratory tests were used to improve minimum horizontal stress calculation. By using well logs and taking into account the VTI character of the formation, the proposed methodology offers reliable, continuous mechanical properties estimates.

For the two Tuscaloosa Marine Shale wells, core data comprised both static and dynamic mechanical properties. The static properties were obtained by axial and radial deformation, while wave propagation was used for the dynamic mechanical properties. The three-sample method was employed, and measurements were performed on samples cored normal, parallel, and at 45$^{o}$ to the bedding plane. For triaxial compression, the 19.05-mm or 25.40-mm diameter samples were installed in a triaxial pressure vessel and loading was applied using computer-controlled servo-hydraulics. The confining pressure was increased until it reached the value corresponding to the depth at which the sample was cored, after which it was maintained constant. This was followed by the application of an axial stress difference at a controlled axial strain rate of $1x10^{-5}$ /s. Loading continued until the sample failed and then all stresses were removed in a controlled manner. For the ultrasonic velocity measurements, end-caps containing 1 MHz transducers were used to measure P- and S-wave travel times of the vertically, horizontally, and 45$^{o}$ oriented core samples. VTI dynamic stiffness coefficients and dynamic properties are then calculated.

Because the vertical Poisson's ratio has smaller values than the horizontal Poisson's ratio in the Tuscaloosa Marine Shale formation, alternative relationships to the ANNIE equations were used. For the proposed 1D geomechanical model, the dynamic stiffness coefficients $C_{33}$ and $C_{44}$ were computed using the vertical compressional and shear velocity logs, while Stoneley velocity was used to compute $C_{66}$. Further, the ultrasonic core data were analyzed using linear regression, and all possible correlations to estimate $C_{13}$ and $C_{11}$ stiffness coefficients were developed. The highest R-squared (0.75) was obtained for the linear relationships in Figs. 3.16 and 3.17. $C_{13}$ is solved by the M-ANNIE equation, while M-ANNIE 2 assumption is adopted for $C_{11}$:

$$C_{13} = \tau C_{33} - 2C_{44}, \quad (5)$$

$$C_{11} = \varepsilon(2C_{66} - 2C_{44} + C_{33}), \quad (6)$$

where $\tau = 0.95$ and $\varepsilon = 1.03$. $C_{12}$ was then calculated using VTI symmetry:

$$C_{12} = C_{11} - 2C_{66}. \quad (7)$$

The stiffness coefficients were then used as inputs to estimate the dynamic vertical and horizontal Young's moduli, as well as the dynamic vertical and horizontal Poisson's ratios. Further, the dynamic mechanical properties were converted to static properties. The dynamic-to-static ratios are presented in Tables 3.2 and 3.3. The values of the ratios show that the dynamic Young's modulus is constantly higher than the static modulus. Alternatively, the ratios between the two Poisson's ratios consistently differ. Lastly, the minimum horizontal stress is computed.

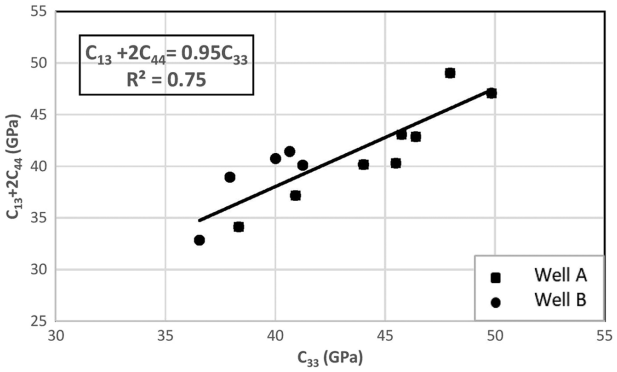


**Figure 3.16 M-ANNIE model assumption: $C_{13}$ + $2C_{44}$ versus $C_{33}$.**

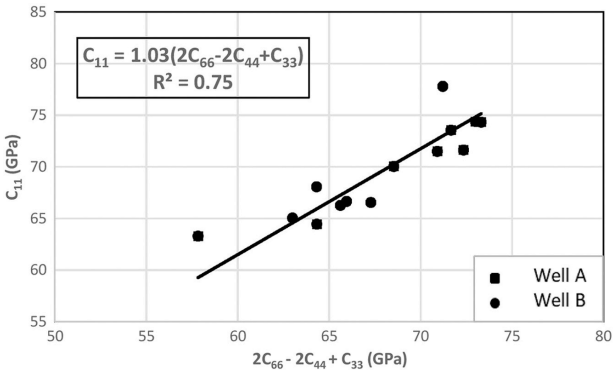


**Figure 3.17 M-ANNIE 2 model assumption: $C_{11}$ versus $2C_{66} - 2C_{44} + C_{33}$.**

**Table 3.2** Lane 64-1: orientation of the samples used along with the petrophysical properties and dynamic-to-static ratios at the analyzed depths.

| Sample no. | Avg. log depth (ft) | Orientation (deg.) | Avg. bulk density (g/cc) | Total porosity (% of BV) | Total water saturation (% of PV) | Total gas saturation (% of PV) | Total oil saturation (% of PV) | Pressure-decay permeability (nD) | $E_v(D)/E_v(S)$ | $E_h(D)/E_h(S)$ | $\nu_v(D)/\nu_v(S)$ | $\nu_h(D)/\nu_h(S)$ |
|---|---|---|---|---|---|---|---|---|---|---|---|---|
| 1 | 15,072.18 | 0, 45, 90 | 2.63 | 7.53 | 76.94 | 18.61 | 4.44 | 73.80 | 2.36 | 1.79 | 1.28 | 1.07 |
| 2 | 15,126.52 | 0, 45, 90 | 2.62 | 6.22 | 72.23 | 20.84 | 6.92 | 63.50 | 2.03 | 1.60 | 1.06 | 0.88 |
| 3 | 15,166.88 | 0, 45, 90 | 2.64 | 4.90 | 78.59 | 14.45 | 6.96 | 60.56 | 1.62 | 1.41 | 1.00 | 0.95 |
| 4 | 15,180.78 | 0, 45, 90 | 2.64 | 5.17 | 72.12 | 21.35 | 6.53 | 139.56 | 1.53 | 1.42 | 1.04 | 0.94 |
| 5 | 15,207.03 | 0, 45, 90 | 2.64 | 6.64 | 81.08 | 15.25 | 3.67 | 73.02 | 1.47 | 1.41 | 0.98 | 0.94 |
| 6 | 15,219.77 | 0, 45, 90 | 2.61 | 6.31 | 66.96 | 27.68 | 5.36 | 71.92 | 1.77 | 1.46 | 1.06 | 1.01 |
| 7 | 15,232.75 | 0, 45, 90 | 2.68 | 5.47 | 86.26 | 12.12 | 1.61 | 60.83 | 1.97 | 1.43 | 1.33 | 1.30 |
| 8 | 15,243.62 | 0, 45, 90 | 2.62 | 8.08 | 77.78 | 21.14 | 1.08 | 61.18 | 1.61 | 1.27 | 1.03 | 0.92 |

**Table 3.3** Smith SD 1H: orientation of the samples used along with the petrophysical properties and dynamic-to-static ratios at the analyzed depths.

| Sample no. | Avg. log depth (ft) | Orientation (deg.) | Avg. bulk density (g/cc) | Total porosity (% of BV) | Total water saturation (% of PV) | Total gas saturation (% of PV) | Total oil saturation (% of PV) | Pressure-decay permeability (nD) | $E_v(D)/E_v(S)$ | $E_h(D)/E_h(S)$ | $\nu_v(D)/\nu_v(S)$ | $\nu_h(D)/\nu_h(S)$ |
|---|---|---|---|---|---|---|---|---|---|---|---|---|
| 1 | 13,311.86 | 0, 45, 90 | 2.65 | 6.41 | 89.56 | 9.69 | 0.76 | 32.75 | 1.44 | 1.47 | 1.05 | 0.66 |
| 2 | 13,329.16 | 0, 45, 90 | 2.62 | 6.38 | 81.79 | 16.73 | 1.49 | 35.26 | 1.50 | 1.53 | 0.96 | 0.65 |
| 3 | 13,368.65 | 0, 45, 90 | 2.63 | 5.13 | 84.88 | 13.24 | 1.89 | 30.13 | 1.65 | 1.58 | 0.91 | 0.66 |
| 4 | 13,393.13 | 0, 45, 90 | 2.61 | 5.33 | 74.83 | 19.83 | 5.34 | 41.61 | 1.62 | 1.50 | 0.95 | 0.63 |
| 5 | 13,411.68 | 0, 45, 90 | 2.58 | 3.91 | 57.76 | 27.80 | 14.44 | 61.02 | 1.55 | 1.43 | 1.00 | 0.71 |
| 6 | 13,453.84 | 0, 90 | 2.62 | 6.13 | 74.60 | 22.30 | 3.11 | 51.33 | — | — | — | — |

The 45° sample at 13,453.84 ft (4100.73 m) was very different from the other two and was therefore not used for further computations.

The stiffness coefficients obtained from well logs using the VTI model for Lane 64-1 and Smith SD 1H wells were displayed in Figs. 318 and 3.19, respectively. The gamma ray (GR) and caliper (HCAL) logs are shown in Track 1, while resistivity measurements (AT90, AT60, AT30, AT20, and AT10) are displayed in Track 2. Track 3 shows neutron porosity (NPHI) along with the density (RHOZ) and the photoelectric effect (PEFZ), while Track 4 displays the vertical compressional slowness log (DTCO) together with the vertical (DTSM) and horizontal (DTSH_HORIZ) shear slownesses. The dynamic stiffness coefficients are displayed in tracks 5 through 10. The stiffness coefficients estimated from well logs (in grey) show a good match to the core data points (in black) corresponding to the coefficients computed using the experimental ultrasonic data from both wells.

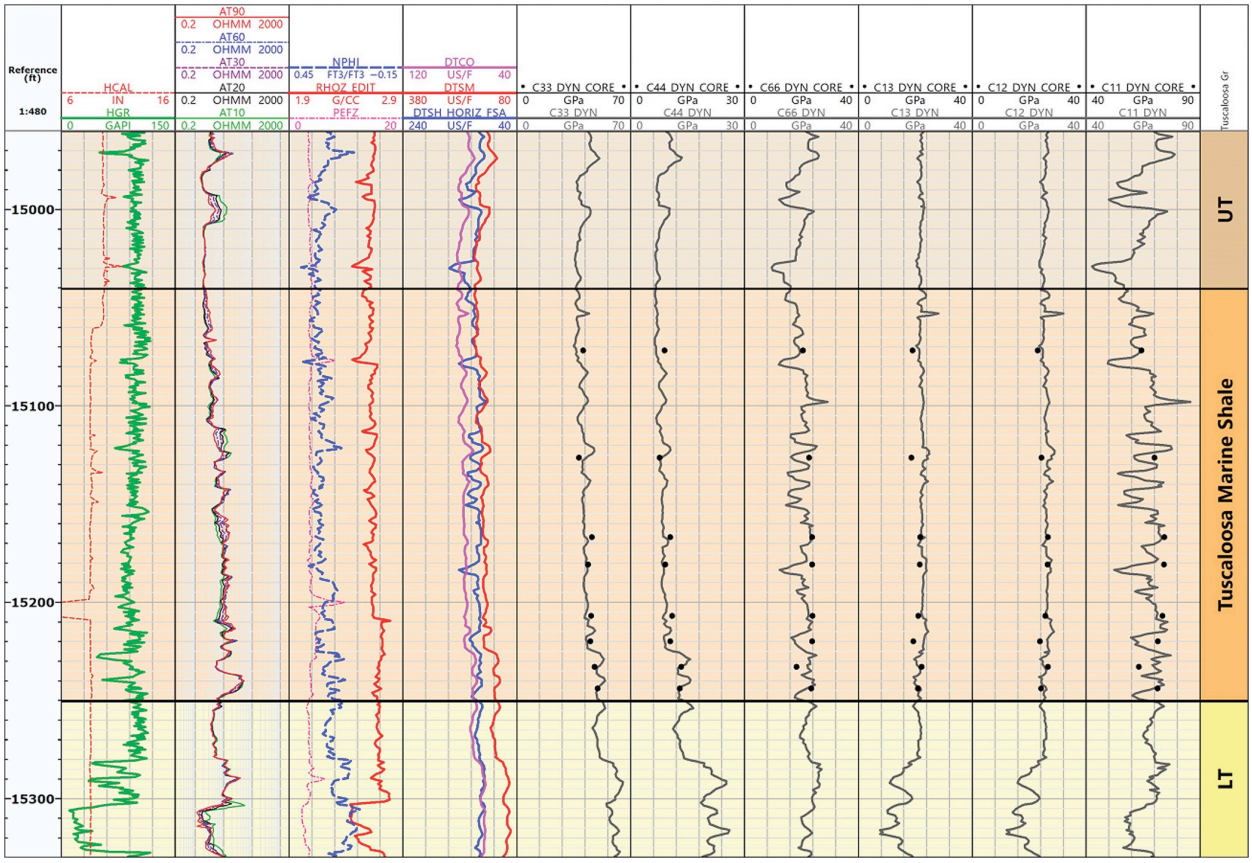


**Figure 3.18 Lane 64-1: dynamic elastic stiffness coefficients estimated for TMS using our proposed VTI model.** Track 1: GR, bit size (BS), and HCAL; Track 2: resistivity measurements (AT90, AT60, AT30, AT20, and AT10); Track 3: neutron porosity (NPHI), density (RHOZ), and photoelectric effect (PEFZ) logs; Track 4: vertical compressional slowness log (DTCO), vertical shear slowness (DTSM), and horizontal shear slowness (DTSH_HORIZ) logs; and tracks 5–10: The estimated dynamic stiffness coefficients (Cxy_VTI_DYN) are shown in dark gray, whereas the black dots represent dynamic core data.

Further, using the obtained stiffness coefficients, vertical and horizontal Young's moduli were calculated. In Figs. 3.20 and 3.21 (Track 3), both dynamic and static Young's moduli were compared with the isotropic solution. The plots for both Lane 64-1 and Smith SD 1H show that the horizontal Young's modulus is always higher than the vertical Young's modulus, which confirms the presence of horizontal lamination in the Marine Shale. In addition, static Young's moduli have lower values than the dynamic moduli. The static vertical Young's modulus and the isotropic Young's modulus show closer values. The static vertical Young's modulus shows values between 10.5 and 28.5 GPa, while the static horizontal Young's modulus is ranging from 18 to 48 GPa in Lane 64-1. In Smith SD 1H, the static vertical Young's modulus presents values between 16 and 33 GPa, while the static horizontal modulus has higher values (from 33 to 47 GPa). In both wells, the moduli steadily increase towards the base of the Tuscaloosa Marine Shale.

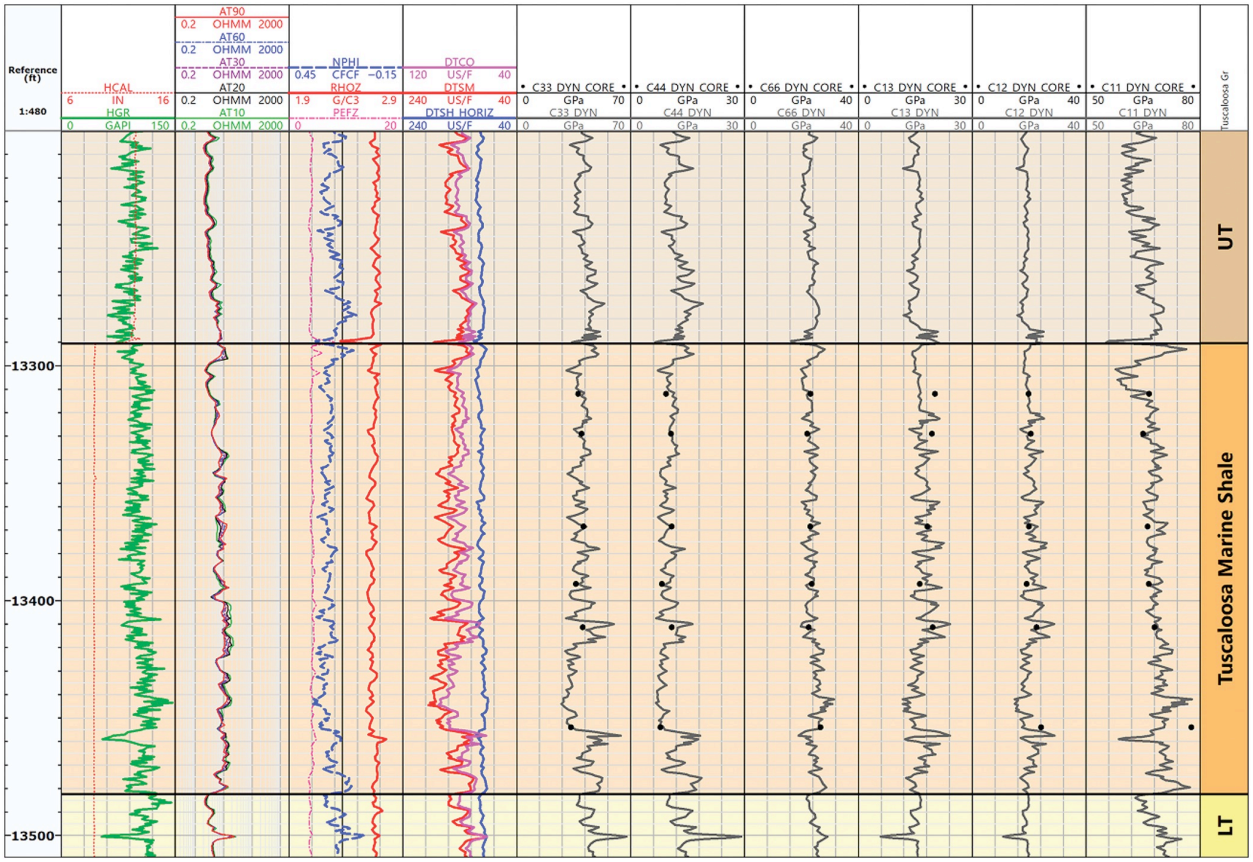


**Figure 3.19 Smith SD 1H: dynamic elastic stiffness coefficients estimated for TMS using our proposed VTI model.** Track 1: GR, bit size (BS), and HCAL; Track 2: resistivity measurements (AT90, AT60, AT30, AT20, and AT10); Track 3: neutron porosity (NPHI), density (RHOZ), and photoelectric effect (PEFZ) logs; Track 4: vertical compressional slowness log (DTCO), vertical shear slowness (DTSM), and horizontal shear slowness (DTSH_HORIZ) logs; and tracks 5–10: The estimated dynamic stiffness coefficients (Cxy_VTI_DYN) are shown in dark gray, whereas the black dots represent dynamic core data.

The results obtained for the Poisson's ratio are presented in Track 4 of Figs. 3.20 and 3.21. The same approach was utilized, and the dynamic and static vertical and horizontal Poisson's ratios were compared to the isotropic Poisson's ratio. It can be observed that in Lane 64-1 well, the isotropic Poisson's ratio presents significantly higher values than the VTI Poisson's ratios. In both wells, the vertical Poisson's ratio is less than the horizontal Poisson's ratio. However, in Lane 64-1, the static vertical Poisson's ratio shows values very close to the static horizontal Poisson's ratio. The difference between the two ratios varies from about 0.06 above UT/TMS boundary, 0.04 between the top of the Tuscaloosa Marine Shale and 15100 ft (4602.5 m), 0.07 in the 15100 - 15148 ft (4602.5 - 4617 m) interval, to less than 0.02 between 15148 and 15213 ft (4617 and 4637 m). The difference between the vertical and horizontal Poisson's ratios is higher in the lower interval of the Marine Shale, but still displays close values at the depths indicated in Fig. 3.20. In Smith SD 1H, the difference between the two ratios exceeds 0.1. The Tuscaloosa Marine Shale is characterized by an average PR_V_STAT of 0.21 and PR_H_STAT of 0.27 in Lane 64-1. In Smith

SD 1H, the formation presents an average static vertical Poisson's ratio of 0.22 and an average static horizontal Poisson's ratio of 0.32.

Lastly, the minimum horizontal stress was calculated using the VTI model. The Biot's coefficients ($\alpha_h$ and $\alpha_v$) are assumed equal to unity, as these are typically set to 1 when stress is computed for hydraulic fracturing simulation. A pore pressure gradient of 12.22 kPa/m is used, while vertical stress gradient varies, with an average of 24.88 kPa/m.

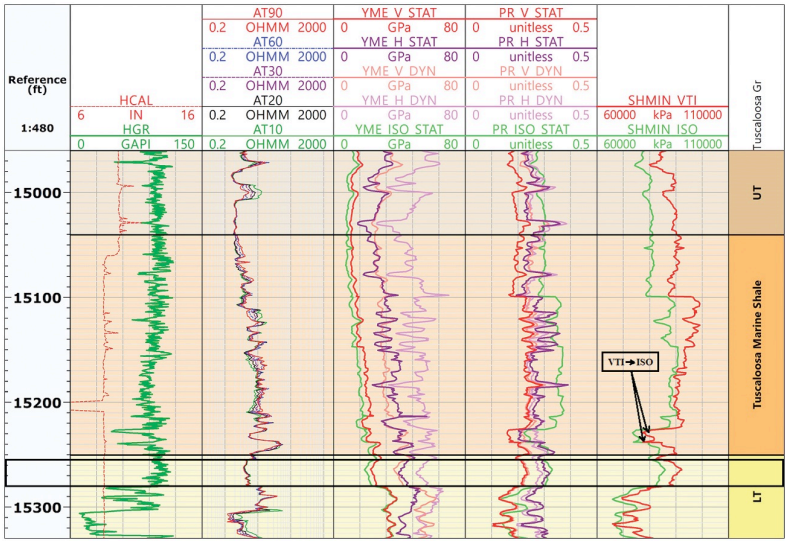


**Figure 3.20 Lane 64-1: comparison of the anisotropic properties with the isotropic model**. Track 3: VTI dynamic and static vertical and horizontal Young's moduli are compared with the isotropic Young's modulus; Track 4: VTI dynamic and static vertical and horizontal Poisson's ratios along with the isotropic Poisson's ratio; and Track 5: the VTI stress is compared to the isotropic stress. The highlighted 20 ft shale presents higher stress and lower Young's moduli values than the TMS target interval above.

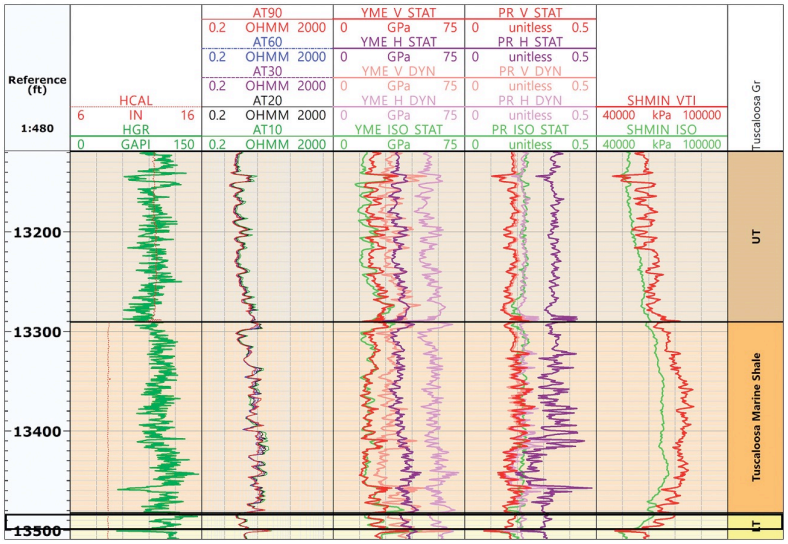


**Figure 3.21 Smith SD 1H: comparison of the anisotropic properties with the isotropic model.** Track 3: the VTI dynamic and static vertical and horizontal Young's moduli are compared with the isotropic Young's modulus; Track 4: VTI dynamic and static vertical and horizontal Poisson's ratios along with the isotropic Poisson's ratio; and Track 5: the VTI stress is compared to the isotropic stress. The highlighted 20 ft shale presents higher stress and lower Young's moduli values than the TMS target interval above.

The VTI minimum horizontal stress was further compared to the isotropic solution (Figs. 3.20 and 3.21 – Track 5). The minimum horizontal stress calculated with the proposed model is higher than the isotropic minimum horizontal stress in both wells. The Tuscaloosa Marine Shale shows values ranging from 77400 to 99400 kPa in Lane 64-1, while minimum horizontal stress presents slightly lower values in Smith SD 1H (between 66000 and 84000 kPa). However, while in Smith SD 1H

the VTI minimum horizontal stress is constantly 10000 kPa higher than the isotropic minimum horizontal stress throughout the central interval of the Tuscaloosa Marine Shale, in Lane 64-1, the two solutions present close values for the 15148 – 15213 ft (4617 – 4637 m) interval. The VTI minimum horizontal stress behavior in Lane 64-1 is a consequence of the small difference between the two Poisson's ratios. The anisotropic model starts converging to the isotropic solution, which assumes $\nu_h = \nu_v$. In addition, the rapid lateral variations in the mineralogical content of the Tuscaloosa Marine Shale may explain why the stress profiles corresponding to the two analyzed wells differ from one another. While the stress profile in Smith SD 1H seems to follow the calcite enrichment trend, the minimum horizontal stress in Lane 64-1 shows several zones characterized by distinct mechanical properties which may be the result of the significant vertical variation in the mineralogy of the formation.

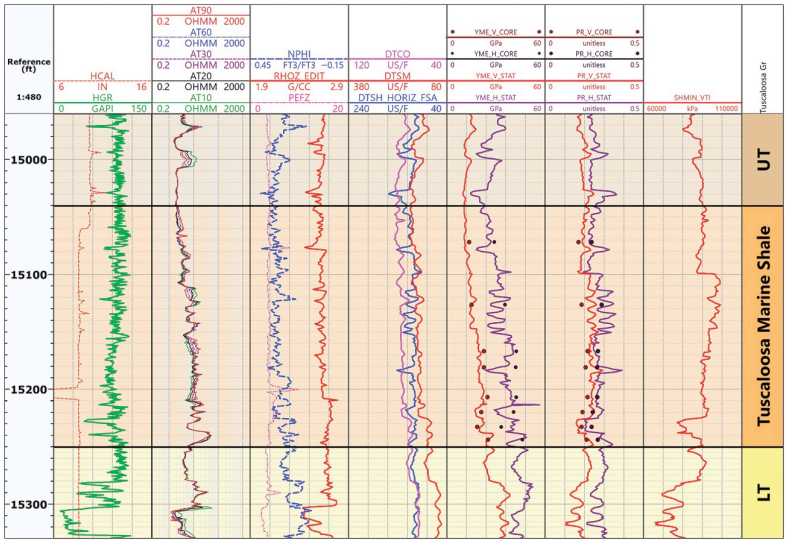


**Figure 3.22 Lane 64-1: Track 5: vertical and horizontal Young's moduli estimated using our proposed model along with the data points corresponding to the moduli measured using static triaxial tress tests**; Track 6: vertical and horizontal Poisson's ratios estimated using our proposed model along with the data points corresponding to the ratios measured using static triaxial stress tests; and Track 7: VTI minimum horizontal stress.

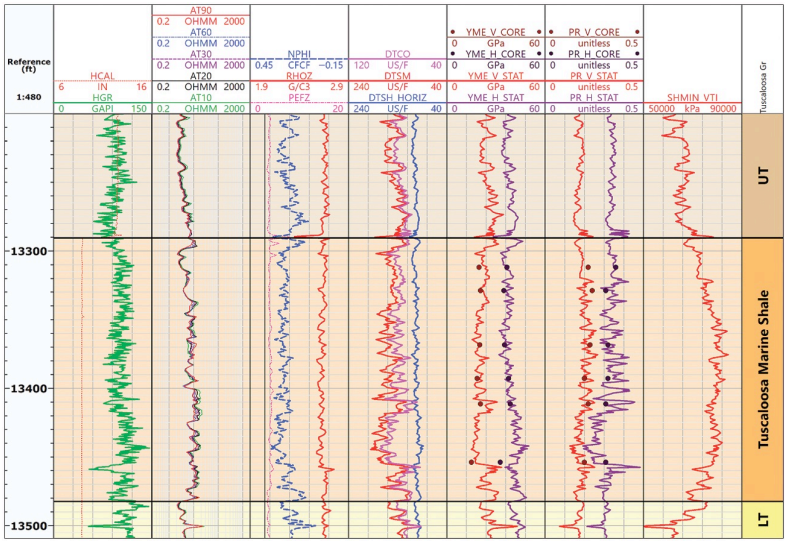


**Figure 3.23 Smith SD 1H: Track 5: vertical and horizontal Young's moduli estimated using our proposed model along with the data points corresponding to the moduli measured using static triaxial tress tests**; Track 6: vertical and horizontal Poisson's ratios estimated using our proposed model along with the data points corresponding to the ratios measured using static triaxial stress tests; and Track 7: VTI minimum horizontal stress.

The differences in Young's moduli and in situ stress between the target zone at the base of the Tuscaloosa Marine Shale and bounding layers can be further used to assess fracture containment. Fracture height control below the Tuscaloosa Marine Shale is of great importance, as penetrating into a possible water-bearing zone of the Lower Tuscaloosa is not desired. The results obtained show that the 20-foot shale has a distinct mechanical character and can be a potential frac barrier. There is an increase of up to 10000 kPa (Lane 64-1) and 6000 kPa (Smith SD 1H) in the minimum horizontal stress accompanied by a 10 GPa decrease in Young's moduli (YME_V_STAT = 20 GPa; YME_H_STAT = 40 GPa). In addition, Poisson's ratios increase at the boundary between the Tuscaloosa Marine Shale and Lower Tuscaloosa. The 20-foot interval is also characterized by higher gamma ray values than the lower interval of TMS, which indicates an increase in clay content, and, thus, confirms shale's ductility. This appears to be the most substantial potential frac barrier in both wells, however, fracturing tests are recommended to confirm the results.

For both wells, the values of the estimated elastic mechanical properties are compared to the static properties obtained using the triaxial test for the available core samples (Figs. 3.22 and 3.23). There is a good match between the estimated and measured elastic mechanical properties (tracks 5 – 7). Moreover, the minimum horizontal stress calculated with the proposed extension of the ANNIE model is shown in Track 8.

### *3.2.2 Natural Fracture Characterization in the Tuscaloosa Marine Shale Using Electrical Image Logs, Shear-Wave Splitting Analysis, and Core Data*

An integrated approach was used to characterize the natural fractures in the Tuscaloosa Marine Shale. Conventional well logs, borehole image data, shear-wave anisotropy, and slab analysis were used to study fracture development and orientation, fracture-bedding relationship, fracture filling, and stress direction in seven wells across the TMS play. The wells analyzed were Murphy 63H, Beech Grove 68-1, Lane 64-1, Denkmann 33 28H #2, Thomas 38H-1, Soterra 6H-1, and Eads_Poitevent_et_al_1. The goal of the study was to provide essential knowledge about natural fracture location and orientation in the Tuscaloosa Marine Shale that can be further used to avoid wellbore instability while drilling and improve well life, lateral well planning, and hydraulic fracturing design.

Borehole image and shear-wave splitting analysis were used to determine the main zones affected by fractures and then analyze the relationship between fracture orientation and corresponding paleostress direction. Fracture location was validated using the available slabs in Beech Grove 68-1, Lane 64-1, and Soterra 6H-1 wells. Moreover, the core analysis included a study of the fracture types, height, width, mineralization, and lithology influence on the fracture development in the Tuscaloosa Marine Shale. The mineralogical effect was also studied with the help of a petrophysical multi-mineral model which accounts for kerogen, calcite, pyrite, siderite, quartz, montmorillonite, illite, and chlorite presence in the formation. To reduce the evaluation risks of the multi-mineral petrophysical analysis, ECS logs were used.

For a quantitative formation evaluation with respect to lithology and fluids saturation, a petrophysical model with $\boldsymbol{M}$ components representing both solid and fluid volume fractions was

defined and applied to both conventional and ECS logs using a probabilistic approach. The theoretical response of the considered petrophysical model was used to compare the reconstructed logs to the original input logs with the help of the fitting errors. The iterative adjustment of the model with respect to its volume fractions is guided by the minimization of the error function **E = E(V, σ)** so as to obtain the best volumetric solution ***V*** for each depth interval.

Further, a workflow was created and applied to the electrical imaging data. The processing steps included correcting the orientation curves for magnetic declination, inclinometry QC, pad image creation, image based speed correction, histogram equalization, and pad concatenation and orientation. Buttons harmonization was also performed along with the image based speed correction so as to correct for differences between button responses. Histogram equalization helped map the distribution of borehole image data values to a user-specified range and was applied over a certain sliding window. A moving 1-meter depth window was used to generate a dynamic image. By applying the final step, the individual pad images were merged into a single array covering the entire borehole circumference. Both static and dynamic images were oriented relative to North, unfolded, and displayed from $0^o$ to $360^o$. Existing electrical contrasts were then interpreted on these images.

The natural fractures intersecting the borehole appear as sinusoids and their dip direction is given by the orientation of the sinusoid minimum:

$$dip\ angle = arctan\frac{h}{d} \tag{8}$$

where $h$ is the height of the sinusoid and $d$ is the diameter of the borehole. The dynamic images were visually analyzed to pick the fractures and determine both their dip angle and dip azimuth. Tadpole plots were used to display the results of the dip picking. Fracture orientation was further analyzed using azimuth frequency diagrams.

In addition, shear-wave splitting analysis was used to qualitatively assess the magnitude of the slowness anisotropy of the formation. In shear-wave splitting, the fast wave is polarized along the direction parallel to the fracture strike, while the slow wave is polarized perpendicular to it. Finally, to confirm maximum stress direction, the fast-shear azimuth was displayed on a rose plot.

*Natural Fracture in the Tuscaloosa Marine Shale*

Lane 64-1 (Fig. 3.24) presents a number of 11 open natural fractures distributed in two intervals with possible frac barriers in between. The 35-foot shale below the fractured interval located between 15170 and 15250 ft has no fractures and presents a substantial clay content, which points towards a more reliable frac barrier. Moreover, cores show well developed vertical fractures at the base of TMS and therefore, confirm the results of the borehole image analysis.

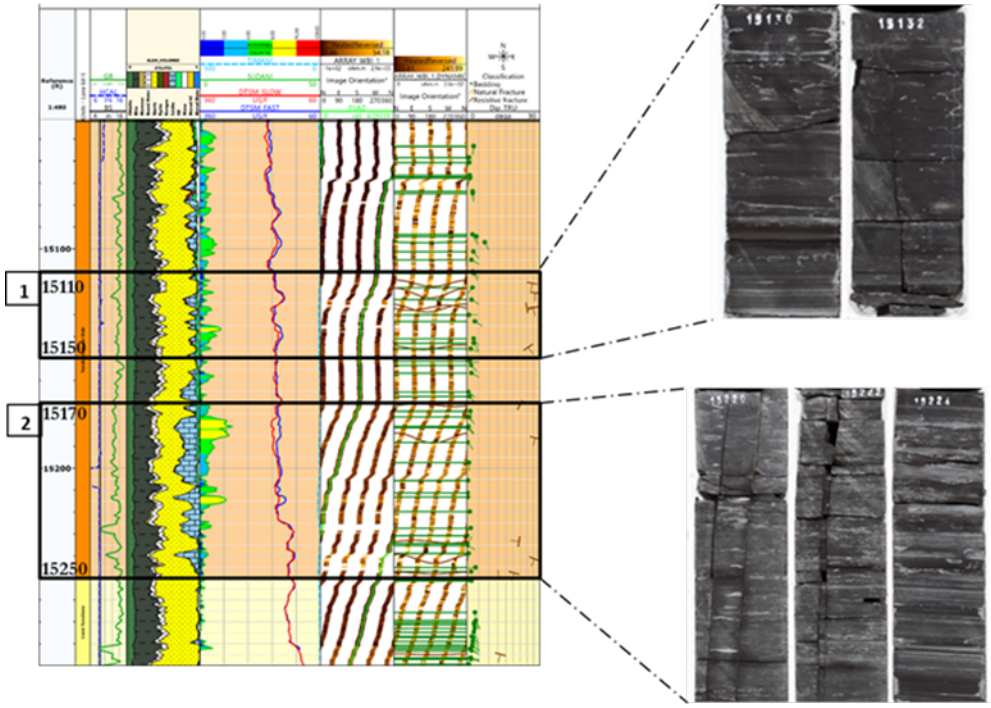


**Figure 3.24 Lane 64-1: Identification of two intervals presenting a significant number of fractures (brown sinusoids) on the image log (Track 5) and large slowness anisotropy (Track 3).** These zones have high calcite content (Track 2) and their location was further validated using cores.

For Murphy 63H well (Fig. 3.25), no slowness or core data were available, but the static image log revealed the occurrence of 14 cross-bedding fractures and 9 layer-bound fractures. A higher number of fractures is present in the upper fractured interval (14060 - 14140 ft) as a result of a higher calcite content compared to the lower zone, which makes the rock more brittle and prone to fracturing. Beech Grove 68-1 well in Fig. 3.26 displays two other zones with a total of 9 open cross-bedding natural fractures. The intervals located between 13740 - 13780 ft and 13800 - 13880 ft, respectively, are characterized by high calcite content and large slowness anisotropy, in addition to showing significant natural fractures in the cores.

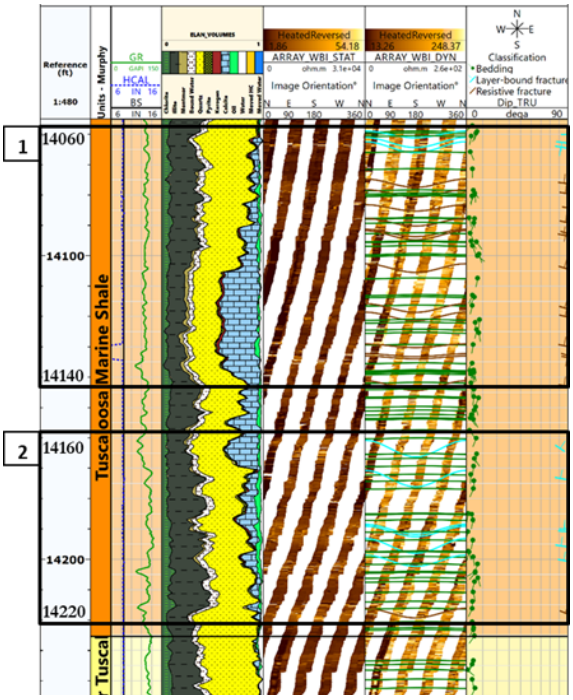


**Figure 3.25 Murphy 63-1H: Identification of two intervals presenting a significant number of fractures (brown sinusoids) on the image log (Track 4) and high calcite content (Track 2).**

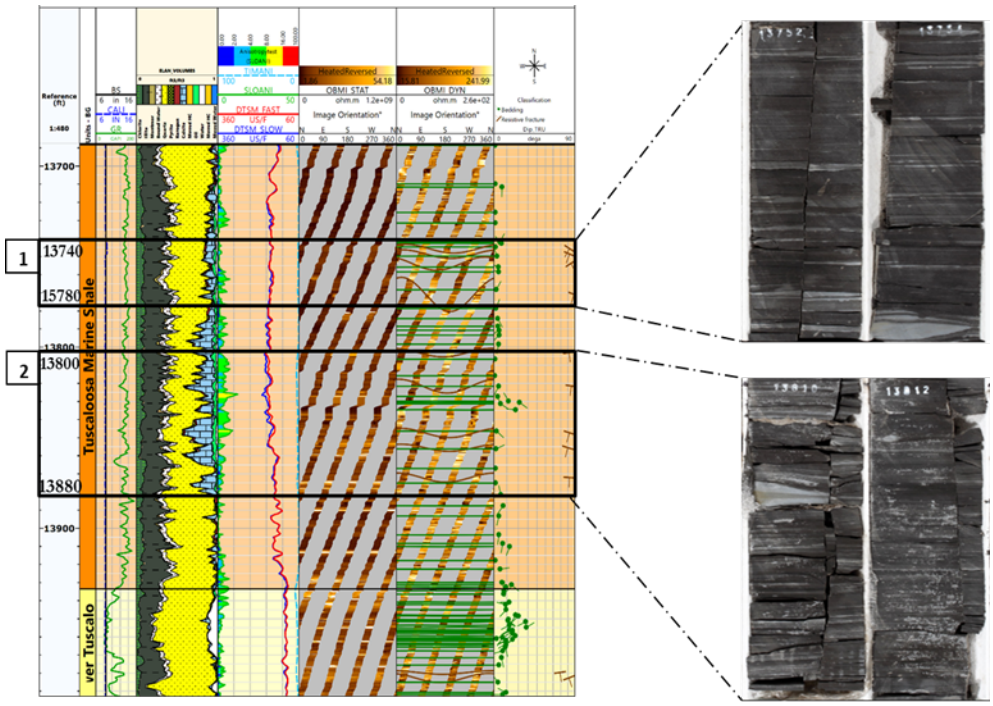


**Figure 3.26 Beech Grove 68H-1: Identification of two intervals presenting a significant number of fractures (brown sinusoids) on the image log (Track 5) and large slowness anisotropy (Track 3).** These zones have high calcite content (track 2) and their location was further validated using cores.

Fracture analysis was performed for each wellbore section of the Denkmann 33 28H #2 well. In the vertical interval, bedding has a mean dip magnitude of 4 degrees and strikes WNW-ESE (Fig. 3.27A), while open fractures show dip values ranging from 80 to 90 degrees, which points out that these are vertical or nearly vertical fractures perpendicular to the bedding. These occur along the E-W direction (Fig. 3.27B) and appear to terminate at an observable lithology contrast. In contrast, most of the closed fractures observed in this interval are continuous and their main orientation is E-W with a minor WNW-ESE orientation (Fig. 3.27C).

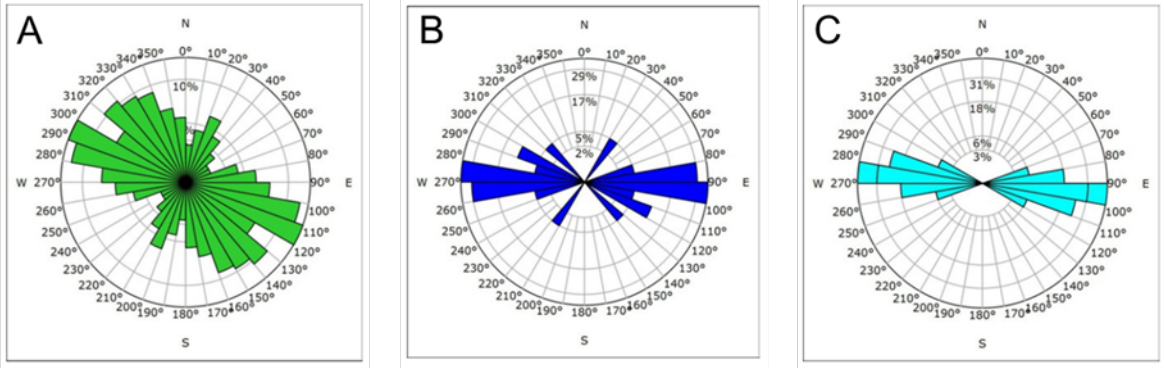


**Figure 3.27 Orientation of the bedding (A), open fractures (B) and closed fractures (C) in the vertical interval of the Denkmann 33 28H #2 well.**

Bedding in the curved interval has a mean dip magnitude of 6 degrees and is oriented WNW-ESE (Fig. 3.28A). Similarly, open fractures terminate at bedding interfaces, while the majority of the healed fractures transect the borehole continuously. According to the dip-strike analysis, these are sub-vertical and vertical fractures that strike E-W (Figs. 3.28B and 3.28C). Closed fractures also show a secondary WNW-ESE strike orientation.

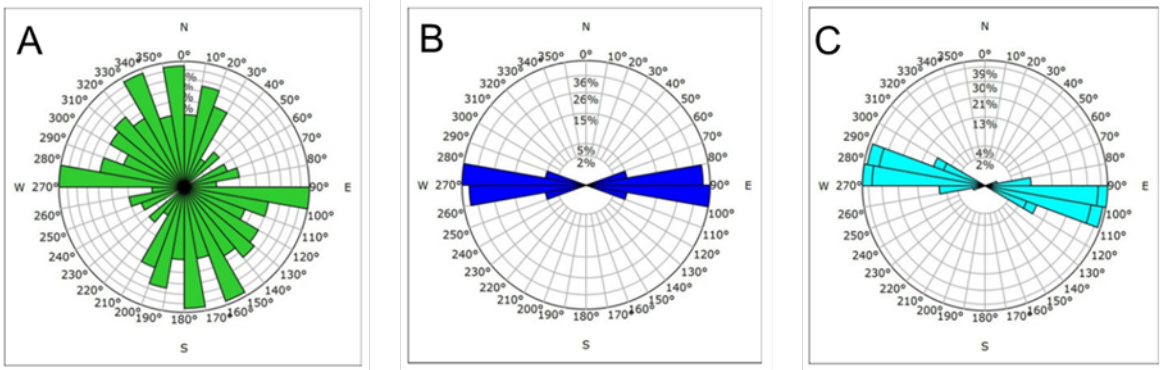


**Figure 3.28 Orientation of the bedding (A), open fractures (B) and closed fractures (C) in the curved interval of the Denkmann 33 28H #2 well.**

In the lateral section of the Denkmann 33 28H #2 well, bedding shows a mean dip magnitude of 4 degrees and strikes WNW-ESE (Fig. 3.29A). A total of 7 open litho-bound fractures oriented WNW-ESE (Fig. 3.29B) were identified throughout this interval. These represent sub-vertical and vertical natural fractures whose dip magnitude ranges from 80 to 90 degrees. Moreover, this

section is characterized by the presence of an important number of closed fractures (more than 500) that strike WNW-ESE (Fig. 3.29C). Most of these continuously transect the wellbore and were classified as continuous. Partial fractures were also picked. These grade in and out as lithology boundaries are crossed. More importantly, three faults striking ENE-WSW, ENE-WSW, and E-W, respectively, were identified in the lateral and could have further completion implications.

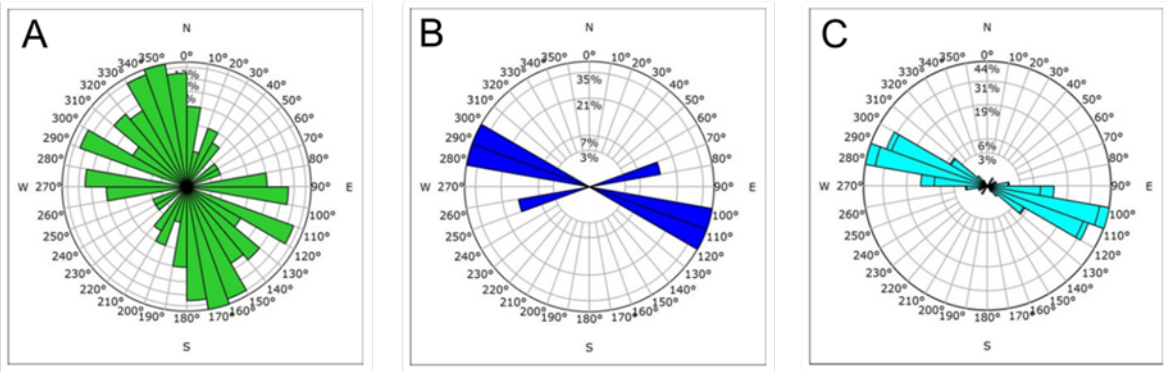


**Figure 3.29. Orientation of the bedding (A), open fractures (B) and closed fractures (C) in the lateral interval of the Denkmann 33 28H #2 well.**

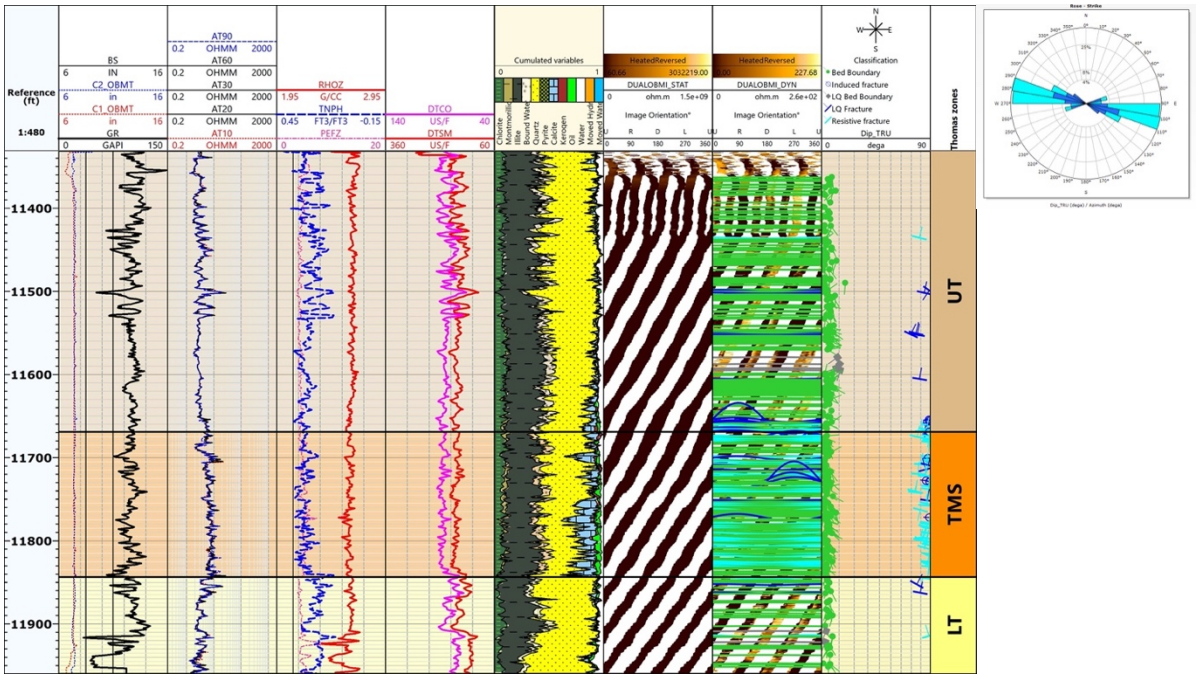


**Figure 3.30 Thomas 38H-1: Comprehensive layout used for fracture characterization.** Tracks 1-4: conventional well logs; Track 5: mineralogical and fluids model; Tracks 6-8: borehole image analysis. Top right: fracture rose plot showing that fractures trend E-W.

Besides conventional well logs, only electrical borehole image data were available for Thomas 38H-1 well. However, the high quality of the data allowed the identification of multiple resistive natural fractures intersecting the TMS bedding planes. A couple of induced fractures were also identified. Most of the fractures in the Thomas 38H-1 well show dip values ranging from 80º to 90º and can, therefore, be classified as vertical or nearly vertical fractures. Also, the rose plot (Fig. 3.30 - top right) confirms that the natural fractures in this well follow the general TMS fracture trend and occur along the E-W direction (90º - 110º E-W).

Due to the low coverage of the electrical borehole images in Soterra 6H-1, the identified structural features were classified as either possible fractures or bedding. However, the orientation of the fractures is still in good agreement with the general TMS trend. The possible fractures show a more inconsistent behavior, but the main development direction is 90º - 100º E-W (Fig. 3.31 – top right). Moreover, the fast shear azimuth plot (Fig. 3.31 – middle right) indicates that the maximum horizontal stress is oriented at 100º - 110º E-W. Slab analysis also confirmed fracture occurrence in the Soterra 6H-1 well and well-developed nearly vertical fractures were observed in the slabs.

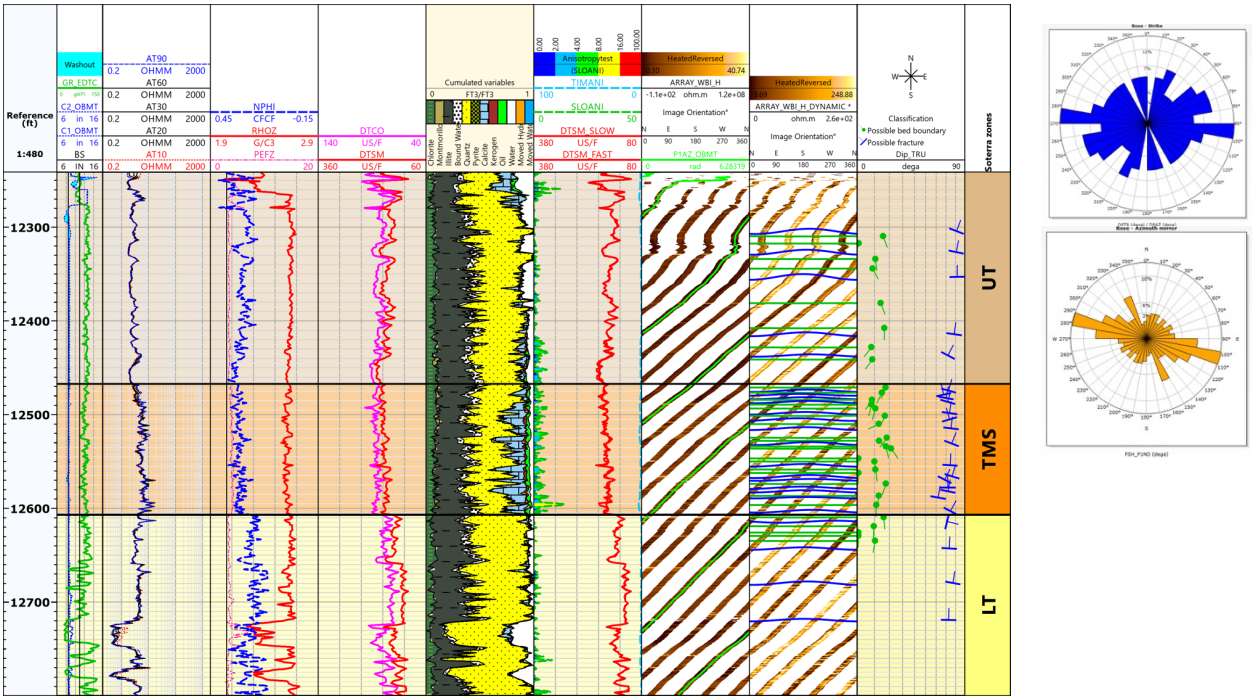


**Figure 3.31 Soterra 6H-1: Comprehensive layout used for fracture characterization. Tracks 1-4: conventional well logs;** Track 5: mineralogical and fluids model; Tracks 6: borehole anisotropy analysis, Tracks 7-9: borehole image analysis. Top right: fracture rose plot showing that fractures trend E-W. Middle right: rose plot showing that the $S_{hmax}$ is oriented at 100º-110º E - W.

For the Eads_Poitevent_et_al_1 well, the borehole image data available did not include all the variables necessary to process and interpret the images. Hence, fracture analysis was done based on the conventional well log data and borehole anisotropy analysis only. The results are displayed in Fig. 3.32. In the Eads_Poitevent_et_al_1 well, the base of the Tuscaloosa Marine Shale shows the deposition of a massive amount of calcite which increases the porosity and reservoir quality of

the formation. High slowness anisotropy values are observed throughout the intervals with a significant volume of calcite, which is most likely an effect of fracture occurrence in the formation. The direction of the maximum horizontal stress in this well (Fig. 3.32 - top right) agrees with the general TMS trend. $S_{hmax}$ is oriented at 90º - 100º E-W.

Moreover, the map in Fig. 3.33 shows that the orientation of the maximum horizontal stress is consistent throughout the formation. Murphy 63H, Beech Grove 68-1, and Soterra 6H-1 wells fall on the same paleostress line, while Eads_Poitevent_et_al_1 well shows a 10º counterclockwise rotation from South to North in the paleostress field.

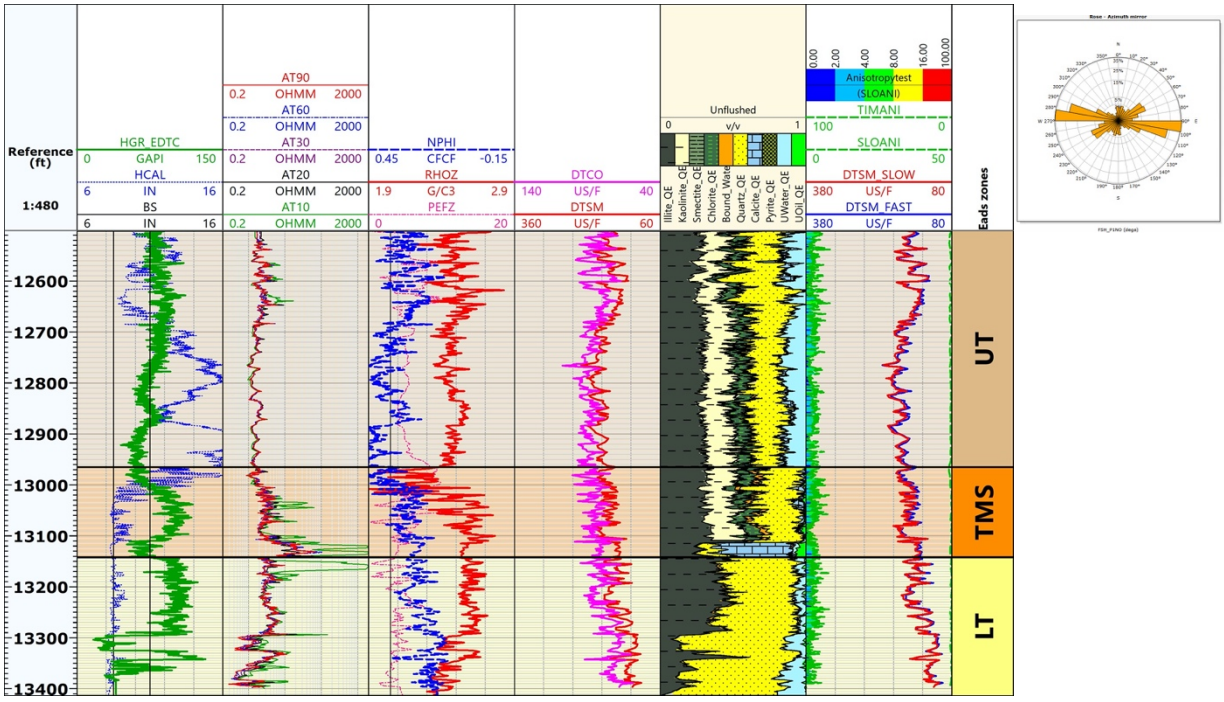


**Figure 3.32 Eads_Poitevent_et_al_1: Comprehensive layout used for fracture characterization.** Tracks 1-4: conventional well logs; Track 5: mineralogical and fluids model**;** Track 6: borehole anisotropy analysis. Top right: rose plot showing that the $S_{hmax}$ is oriented at 90º-100º E - W.


**Figure 3.33 Map showing paleostress evolution throughout the Tuscaloosa Marine Shale play.**

### 3.3 Mineralogical composition, organic-richness and produced-water chemistry of TMS

In this study, we report on TMS mineralogical and organic geochemical data from existing wells (where data have become available for the first time) and from cuttings from new wells that have not previously been analyzed. We additionally evaluated the relationships among mineralogy, geochemistry, and oil and gas production in the TMS.

The locations of the wells from which data were analyzed in this investigation are presented in Fig. 3.34 (taken from Beitel, 2020). Data from wells 14 through 20 were collected from samples of cuttings from the horizontal sections of these wells, which were completed in the basal portion of the TMS. The cuttings samples were analyzed at the University of Louisiana at Lafayette using XRD and Rock Eval™ Pyrolysis. Due to contamination from oil-based drilling muds, the cuttings were subjected to an extraction method that involves soaking the samples in a mixture of methanol and chloroform prior to pyrolysis. This process removes free hydrocarbons, including contaminants and any naturally occurring free hydrocarbons and bitumen. The mineralogical and organic content data for Well 21 was taken from the supplemental material provided in Enomoto et. al (2018).

Well and production data were collected for ninety-five TMS wells, including those for which we have mineralogical and geochemical data, using the drilling info database from Enverus™ (drillinginfo.com). Additional data for the wells in Louisiana were collected from the Louisiana

Department of Natural Resources. Additional data for the wells in Mississippi were collected from the Mississippi State Oil & Gas Board. In order to make valid comparisons of production for the wells, we chose to use total production amounts after 12 months. Wells that started producing after January 2019 did not meet the 12-month threshold prior to this compilation and were therefore not included.

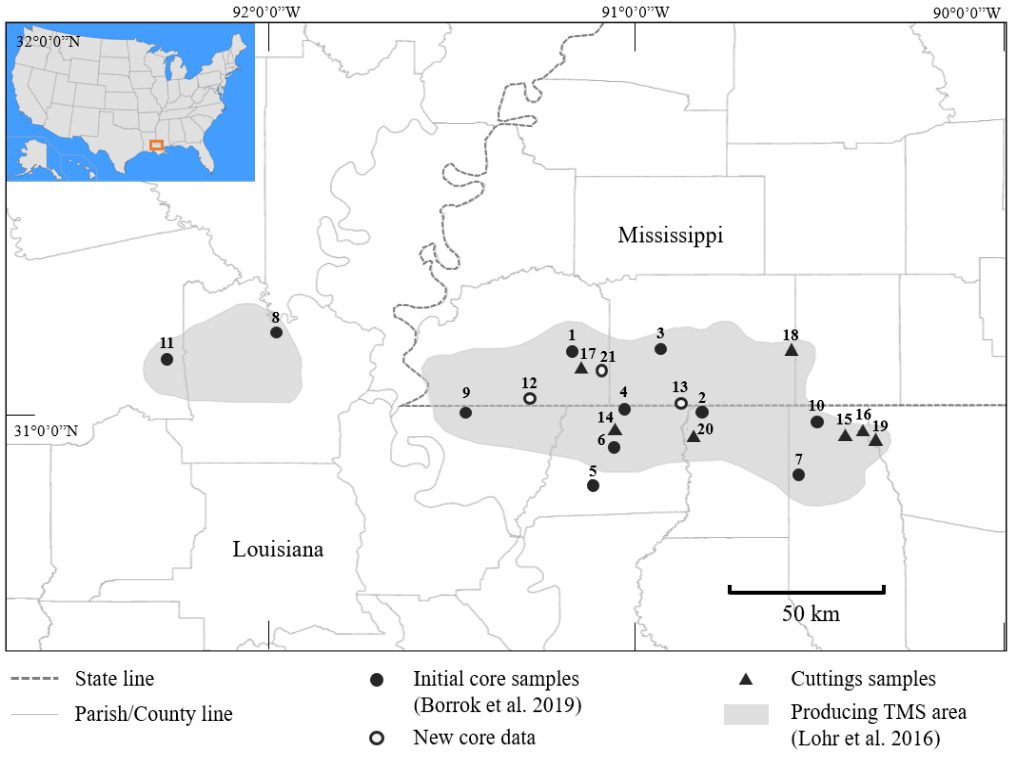


**Figure 3.34 Map showing the locations of wells from which mineralogical and geochemical data were collected.** The shaded region represents the producing area of the TMS.

### *3.3.1 Mineralogical composition of TMS*

The results from analysis of mineralogical data from the basal section of 21 wells in the TMS are summarized in Table 3.4. We chose the basal 18 m of the TMS for this compilation because this is the region where most data were available, it is the preferred landing zone for horizontals in the TMS, and it provided a basis of comparison among all the wells.

**Table 3.4** Statistical compilation for major mineral data in the basal section of the TMS.

| Well # | n samples | Avg. Quartz | Avg. Calcite | Avg. Total Clay | Avg. Plagioclase | Avg. Pyrite |
|---|---|---|---|---|---|---|
| | | (%) | (%) | (%) | (%) | (%) |
| 1 | 13 | 23.0 | 10.6 | 56.9 | 4.6 | 3.7 |
| 2 | 12 | 27.8 | 24.1 | 37.5 | 4.3 | 4.1 |
| 3 | 5 | 33.2 | 7.2 | 38.6 | 12.2 | 5.4 |
| 4 | 9 | 20.9 | 17.8 | 52.2 | 4.4 | 5.1 |
| 5 | 19 | 19.2 | 15.3 | 48.5 | 5.4 | 4.1 |
| 6 | 28 | 22.2 | 17.0 | 45.4 | 4.1 | 3.8 |
| 7 | 22 | 16.1 | 24.0 | 48.0 | 2.2 | 4.9 |
| 8 | 18 | 25.3 | 12.0 | 50.0 | 3.5 | 5.1 |
| 9 | 9 | 25.0 | 20.8 | 46.6 | 2.2 | 3.1 |
| 10 | 17 | 21.8 | 19.2 | 48.5 | 2.8 | 5.1 |
| 11 | 9 | 32.1 | 14.1 | 46.6 | 2.2 | 3.8 |
| 12 | 18 | 27.1 | 13.0 | 45.8 | 3.8 | 3.4 |
| 13 | 2 | 24.5 | 15.0 | 52.5 | 3.5 | 3.5 |
| 14 | 6 | 31.5 | 11.7 | 50.8 | 1.1 | 1.2 |
| 15 | 10 | 28.1 | 23.3 | 42.2 | 1.1 | 1.1 |
| 16 | 6 | 29.9 | 13.1 | 48.8 | 0.5 | 1.8 |
| 17 | 8 | 37.6 | 10.7 | 45.2 | 1.5 | 2.2 |
| 18 | 8 | 33.1 | 18.2 | 40.1 | 1.2 | 1.9 |
| 19 | 10 | 26.7 | 18.7 | 48.7 | 0.0 | 1.5 |
| 20 | 8 | 35.5 | 12.9 | 45.8 | 1.6 | 0.8 |
| 21 | 4 | 28.8 | 13.0 | 50.0 | 1.25 | 5.6 |
| Total | 241 | 25.2 | 16.8 | 47.0 | 3.2 | 3.7 |

The mineralogical results are additionally compiled in a ternary diagram in Fig. 3.35. Here data from the wells summarized in Borrok et al. (2019) are shown in gray, while the new data summarized in Beitel (2020) are colored. Table 3.5 summarizes the organic geochemical results from pyrolysis. The cuttings samples, highlighted in peach, could not be included for the average of the S1 peak or PI, which utilizes the S1 peak, as the free hydrocarbons from these samples were removed prior to analysis

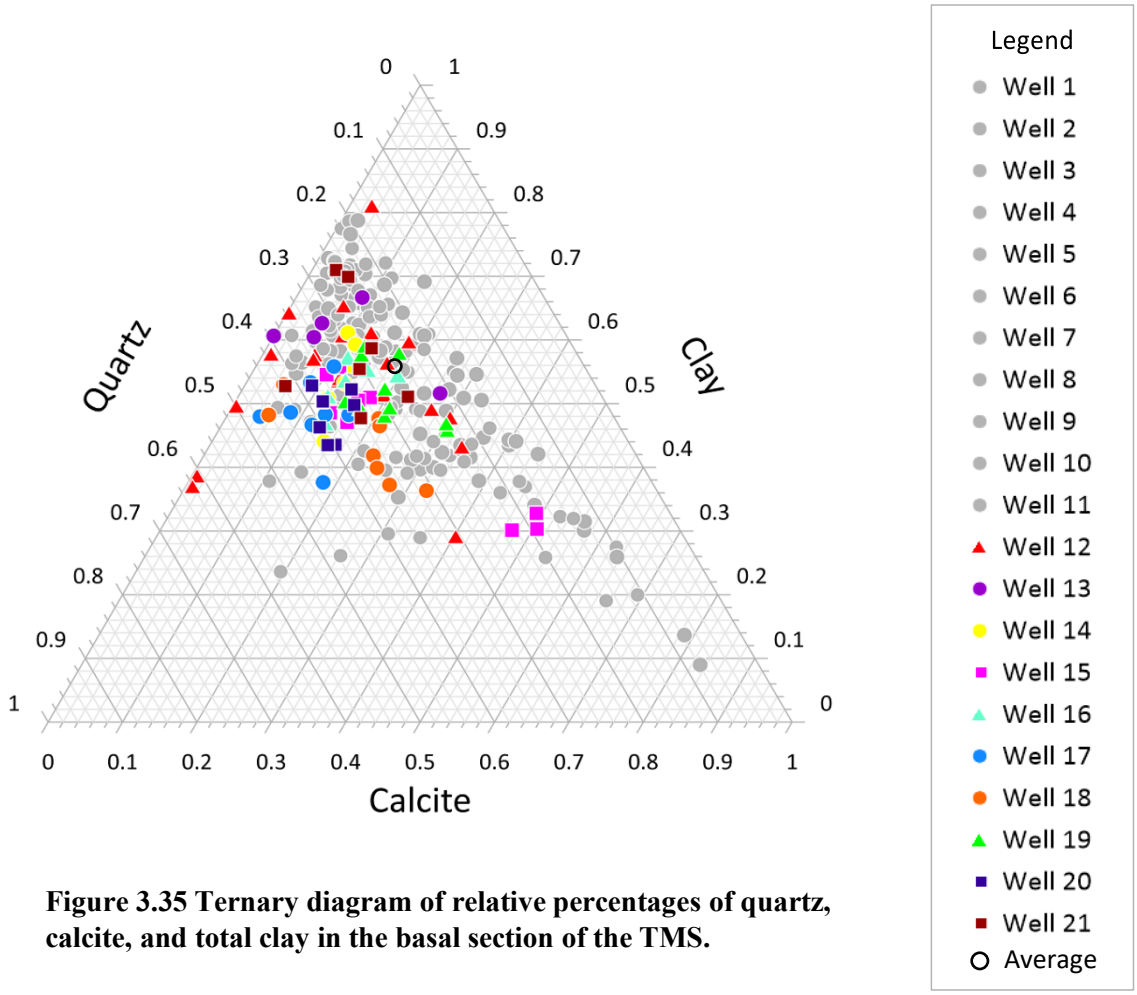


**Figure 3.35 Ternary diagram of relative percentages of quartz, calcite, and total clay in the basal section of the TMS.**

**Table 3.5** Statistical compilation of organic geochemical data in the basal section of the TMS.

| Well # | # of samples | Avg. S1 | Avg. S2 | Avg. Tmax | Avg. TOC | Avg. HI | Avg. OI | Avg. PI |
|---|---|---|---|---|---|---|---|---|
| | | (mg/g) | (mg/g) | °C | wt% | | | |
| 1 | 13 | 0.15 | 2.49 | 445 | 1.83 | 129 | 11 | 0.08 |
| 2 | 8 | 0.12 | 4.36 | 451 | 2.48 | 178 | 8 | 0.03 |
| 3 | 4 | 1.00 | 4.63 | 443 | 1.94 | 238 | 15 | 0.18 |
| 4 | 2 | 0.58 | 2.86 | 434 | 1.51 | 132 | 19 | 0.27 |
| 5 | 18 | 1.53 | 1.93 | 460 | 1.41 | 133 | 14 | 0.44 |
| 6 | 33 | 1.40 | 2.90 | 456 | 1.50 | 179 | 17 | 0.33 |
| 7 | 15 | 1.27 | 5.61 | 444 | 1.88 | 305 | 42 | 0.19 |
| 8 | 21 | 1.86 | 2.88 | 449 | 1.32 | 221 | 41 | 0.38 |
| 9 | 9 | 0.92 | 2.42 | 451 | 1.33 | 177 | 35 | 0.28 |
| 10 | 8 | 0.94 | 6.23 | 444 | 1.83 | 322 | 19 | 0.13 |
| 11 | 9 | 0.81 | 1.29 | 465 | 2.06 | 62 | 10 | 0.39 |
| 12 | 19 | 0.83 | 2.66 | 447 | 1.25 | 192 | 11 | 0.25 |

| | | | | | | | | |
|---|---|---|---|---|---|---|---|---|
| 13 | 7 | 0.29 | 2.77 | 452 | 1.55 | 126 | 12 | 0.11 |
| 14 | 6 | N/A | 2.25 | 439 | 1.13 | 198 | 36 | - |
| 15 | 10 | N/A | 1.83 | 435 | 1.72 | 106 | 66 | - |
| 16 | 6 | N/A | 3.01 | 433 | 2.33 | 122 | 54 | - |
| 17 | 9 | N/A | 3.14 | 437 | 1.56 | 202 | 37 | - |
| 18 | 8 | N/A | 4.24 | 434 | 1.70 | 244 | 48 | - |
| 19 | 10 | N/A | 7.25 | 436 | 2.22 | 324 | 19 | - |
| 20 | 7 | N/A | 1.90 | 441 | 1.09 | 171 | 36 | - |
| 21 | 17 | 0.65 | 3.44 | 445 | 1.45 | 218 | 17 | 0.16 |
| Total (without cuttings) | 183 | 1.00 | - | - | 1.58 | - | - | 0.25 |
| Total (with cuttings) | 239 | - | 3.26 | 447 | - | 191 | 25 | - |

In addition to the summary table, the HI and OI results are plotted in a pseudo Van Krevelen diagram in Fig. 3.36. As with the mineralogical results, data from the wells summarized in Borrok et al. (2019) are shown in gray, while the new data summarized in Beitel (2020) are colored.

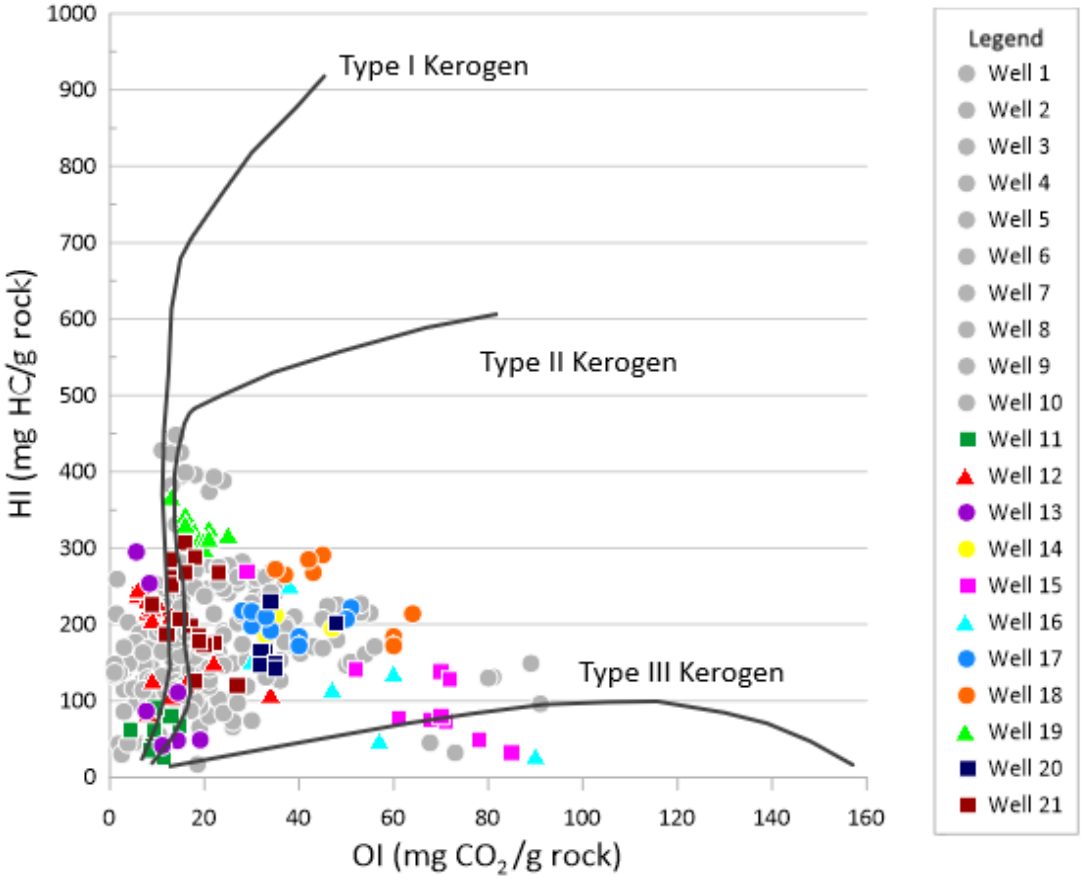


**Figure 3.36 Pseudo Van Krevelen diagram of samples from the basal section of the TMS.**

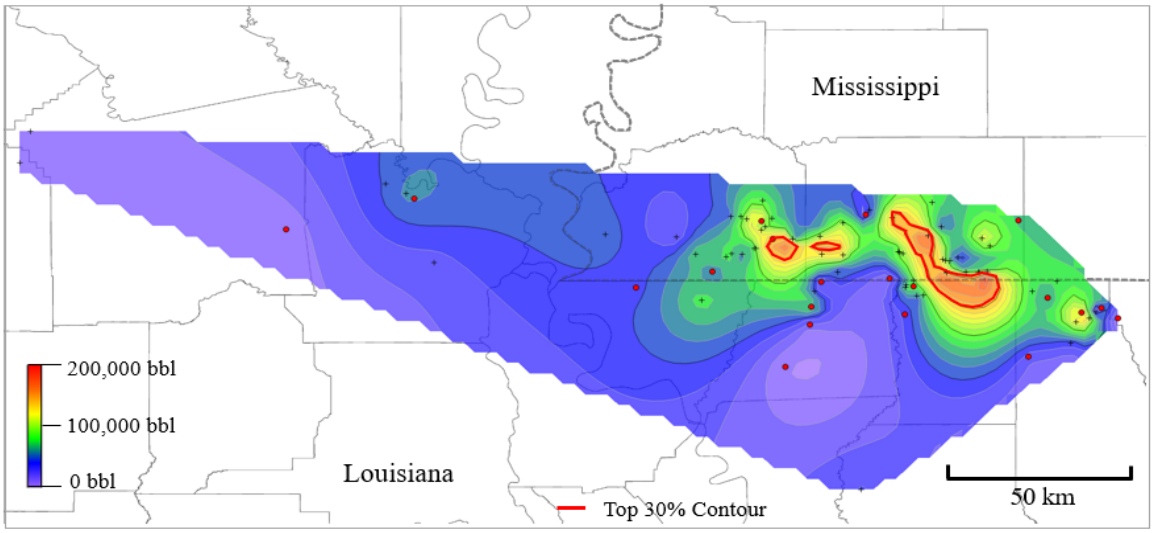


**Figure 3.37 Contour map of cumulative oil production for the first 12 months of TMS wells. Red dots indicate the 21 wells with mineralogical and geochemical data available.**

The distribution of the volumes of oil production (for the first 12 months of production) for TMS wells is illustrated in Fig. 3.37. The areas representing the top 30% of oil production are contoured with a thick red line. Figure 3.38 illustrates the relationships among oil and gas production and the amounts of quartz, calcite, clay, and TOC in the basal section of the TMS. Because the highest production values are only present in the eastern TMS region, this region was highlighted for the mineralogical and TOC contours. The areas representing the top 30% of oil production and gas production are contoured with thick red and purple lines, respectively.

Here we present a high-level discussion of our results. Finer details are available in previously published documents. Our mineralogical and geochemical analysis of the TMS highlighted the extremely heterogeneous nature of the formation both vertically (within individual wells) and horizontally (comparisons from well-to-well). Overall, the TMS is a clay/phyllosilicate-rich unit (average of 47% total clay in the basal section) with mixed type II (oil prone) and type III (gas prone) kerogen. The average TOC concentration in the basal section of the TMS was 1.6%, which is lower than most productive unconventional shale plays. However, despite the lower average, some wells in the TMS contained above 2% TOC with higher amounts of type II relative to type III kerogen in the basal section, suggesting that more limited regions of the TMS have enhanced economic potential.

Our attempts to correlate mineralogical and geochemical changes in the TMS with areas of oil and gas production had limited success. It appears that there are weak spatial correlations between regions of lower clay content (often with higher quartz content), areas of higher TOC, and regions with the most production of oil and gas. To verify these trends, the relationships would need to be further evaluated and refined through higher-density sampling. There was, however, a strong link between values for thermal maturity (measured as Tmax or via vitrinite reflectance) and areas of

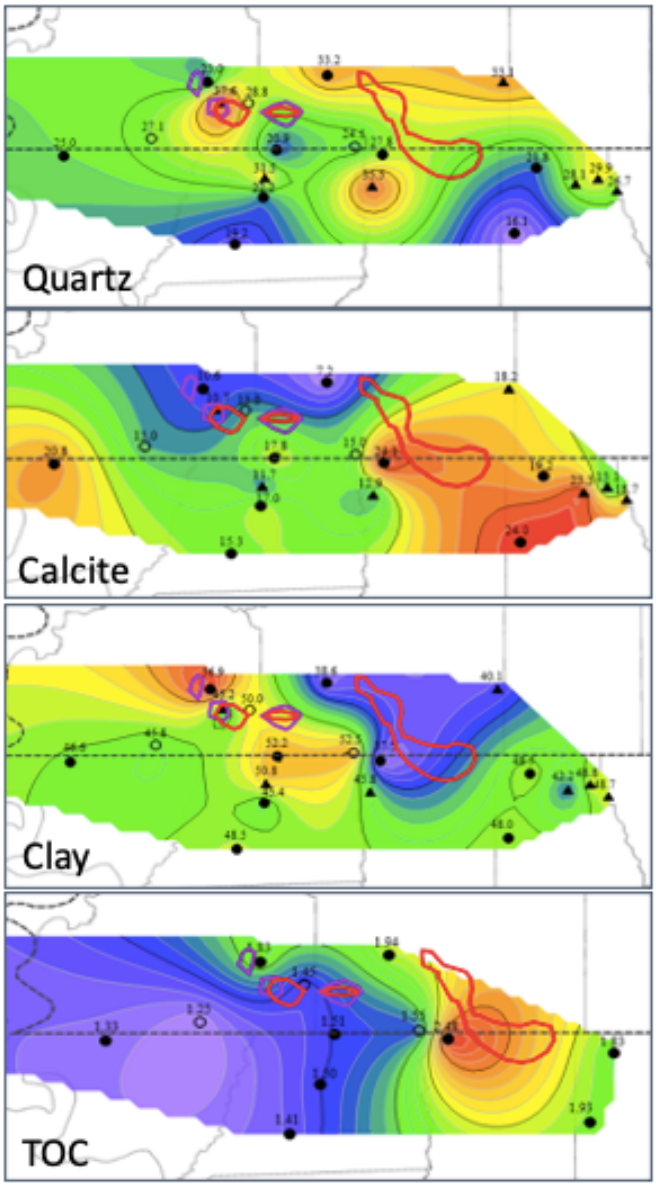


**Figure 3.38 Contour map of average quartz, calcite, clay, and TOC concentrations in the basal section of the TMS. The top 30% oil (red) and gas (purple) contours are shown for comparison.**

high oil production. There is a relatively narrow range of thermal maturity within the TMS play that seems to provide the opportunity for higher recovery of oil. Wells completed in areas of the TMS with lower or higher levels of thermal maturity were not able to reach the same levels of production. Clearly, this window of thermal maturity (about 435° to 445° Tmax) is indicative of the peak oil generation window for the TMS play. This observation also serves as further evidence that the TMS is a self-sourced oil field and that migration of oil from one area of the formation to another is very limited. Migration that did occur likely charged the underlying Lower Tuscaloosa sands and did not take place within the TMS unit itself.

A great deal of additional geological work needs to be done to place the mineralogical and geochemical data within a depositional and stratigraphic context. Initial work suggests that the variability of quartz, calcite and total clay in the base of the TMS within the eastern section of the study region indicates a paleo environment with enhanced clastic input and close proximity to the depocenter and fluctuations in sea level. In the western part of the TMS, the depositional environment changes to a lower energy setting where clay is increasingly dominant.

The overarching purpose of our work on these tasks was to provide new data and interpretations of those data to support future exploration efforts in the TMS. We are hoping that these new findings will spur further economic development in the region by helping petroleum companies reduce their risk by increasing their likelihood of success with new wells. We were successful in this regard, as we presented new average mineralogical abundances and organic geochemical data for the basal section of the TMS and demonstrated how they are related to oil and gas production.

We conclude that the most productive regions of the TMS occur in regions where lower clay contents are co-located with average TOC values near 2% and within a relatively narrow window of thermal maturity.

The heterogeneous distributions of physical and organic properties in the TMS serve as the primary challenge to more accurately predicting the locations of the highest hydrocarbon productivity. This problem is complex, as there are basin-wide heterogeneities superimposed (but also linked) with fine-scale heterogeneities. Based on our work we propose a new approach to evaluating petrophysical properties that moves away from sample-to-sample comparisons and instead focuses on quantifying how distributions of data within the TMS change using different scales and groupings. This statistical approach, when linked to stratigraphic insights from well log data, is likely the best pathway forward in further understanding the TMS geology and geochemistry.

### *3.3.2 Produced Water Chemistry of TMS*

An estimated 900 billion barrels of water are annually co-produced with oil and gas in the United States (Clark and Veil, 2009; Veil, 2012). Despite the well-understood practical water management problems posed by these fluids, produced waters also represent a relatively untapped pool of scientific information that could be used to further our understanding of fluid evolution and the plumbing of petroleum systems (e.g., Barnaby et al., 2004; Zhang et al., 2009; Engle et al., 2016; Saller and Stueber, 2018), as well as the influence of fracking water on water-rock geochemical processes (e.g., Kim et al., 2016; Kondash et al., 2017; Vengosh et al., 2017). These geochemical changes could influence porosity and permeability and ultimately oil and gas production. In this study, we examine the chemistries of produced waters from 24 operating petroleum wells in the Tuscaloosa Marine Shale (TMS) in Louisiana and southwest Mississippi. These results are summarized in Hoffmann and Borrok (2020). We also completed high-temperature water-rock interaction experiments to further understand the influence of fracking fluids on TMS rock properties.

The locations of the wells from which samples were collected for analysis of produced water compositions are presented in Fig. 3.39. Samples of produced water for this study were collected in Nalgene™ plastic bottles from the water stream of the oil-water separator at each well site. Samples were analyzed for pH in the field and filtered using 0.45-micron nylon syringe filters. Samples analyzed for cations were preserved with nitric acid, while samples for anion analysis were filtered but not acidified.

Major cations (Na, Ca, Mg, K, Sr, and Fe) and some elements that form anions (e.g., P and B) were analyzed in diluted samples (100 to 1000 times) using matrix-matched standards on a Perkin Elmer®Avio 200 ICP-OES instrument in the Center for Research in Energy and the Environment at Missouri S&T. Trace elements (Al, V, Cr, Co, Ni, Cu, Zn, As, Se, Mo, Cd, Pb, Tl, Mn, Ba) were analyzed in diluted samples (1000 times) on a Perkin Elmer® NexION 300 ICP-MS instrument. Major anions (Cl, $SO_4$, and Br) were analyzed in diluted samples (5000 times) using a Dionex® IC instrument. Concentrations of $HCO_3$ were determined using titration via Bromocresol Green and Methyl Red. Uncertainties for ICP and IC analyses were around ± 15% (calculated from

replicate analyses of samples that underwent different dilutions). This level of uncertainty is primarily attributable to the large dilution factors needed to analyze these highly saline waters.

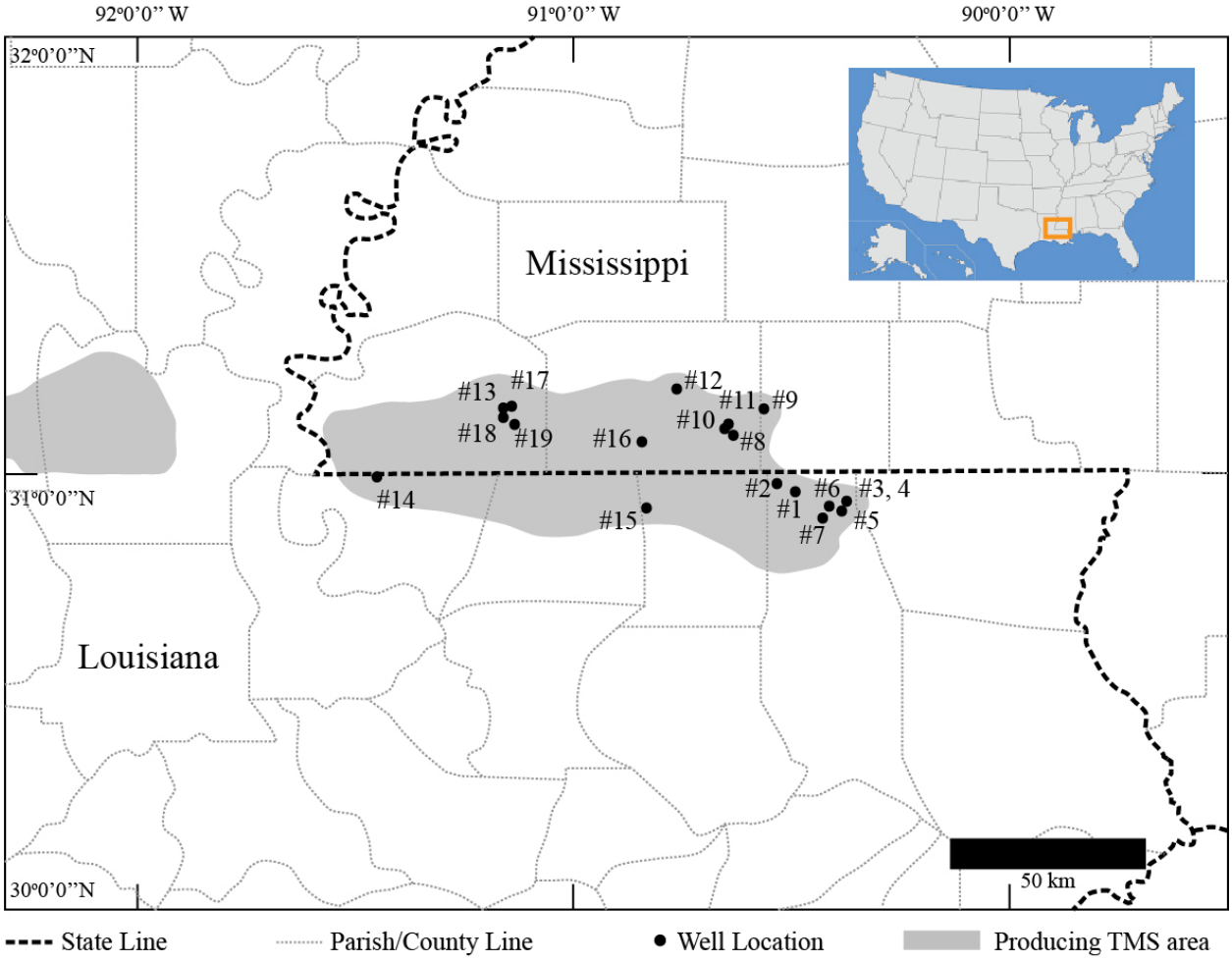


**Figure 3.39 Map showing the locations of wells from which samples of produced waters were collected.** The shaded region represents the producing area of the TMS.

In addition to analysis of produced waters, we conducted batch adsorption experiments with crushed TMS samples. Fluid conditions included compositions starting at pHs of 2, 4, and 6 and systems with distilled water (DIW), NaCl (Na), and Ca,Mg,Na,Cl (Mix) solutions. Both the Na and Mix fluids solutions we run at conditions of 3.2% salinity and 12% salinity. All experiments were conduction at 90°C. Experiments ran for approximately 2 months and samples were collected as a function of time to understand the evolution of the fluid chemistries. We also subjected polished chips of TMS samples mounted in epoxy to the same fluid conditions in separate experiments. The purpose of these experiments was to evaluate, using a scanning electron microscope (SEM), how the physical nature of the TMS samples changed during interaction with

the different fluid compositions. As with the produced waters, samples were analyzed using an ICP-OES or ICP-MS at Missouri S&T. Some were sent out to outside laboratories for analysis when our instrumentation was not available. TMS chip samples were evaluated using a Helios Nano Lab 600 instrument available in the Materials Research Center at Missouri S&T.

*Major anion and Cation in the water*

Major anion and cation concentrations in produced waters from the TMS are summarized in a box plot in Fig. 3.40. The relationships among total dissolved solids (TDS) in the produced waters and a) oil production, b) water production, and c) the ratio of water production to fracking water volume are presented in Fig. 3.41.

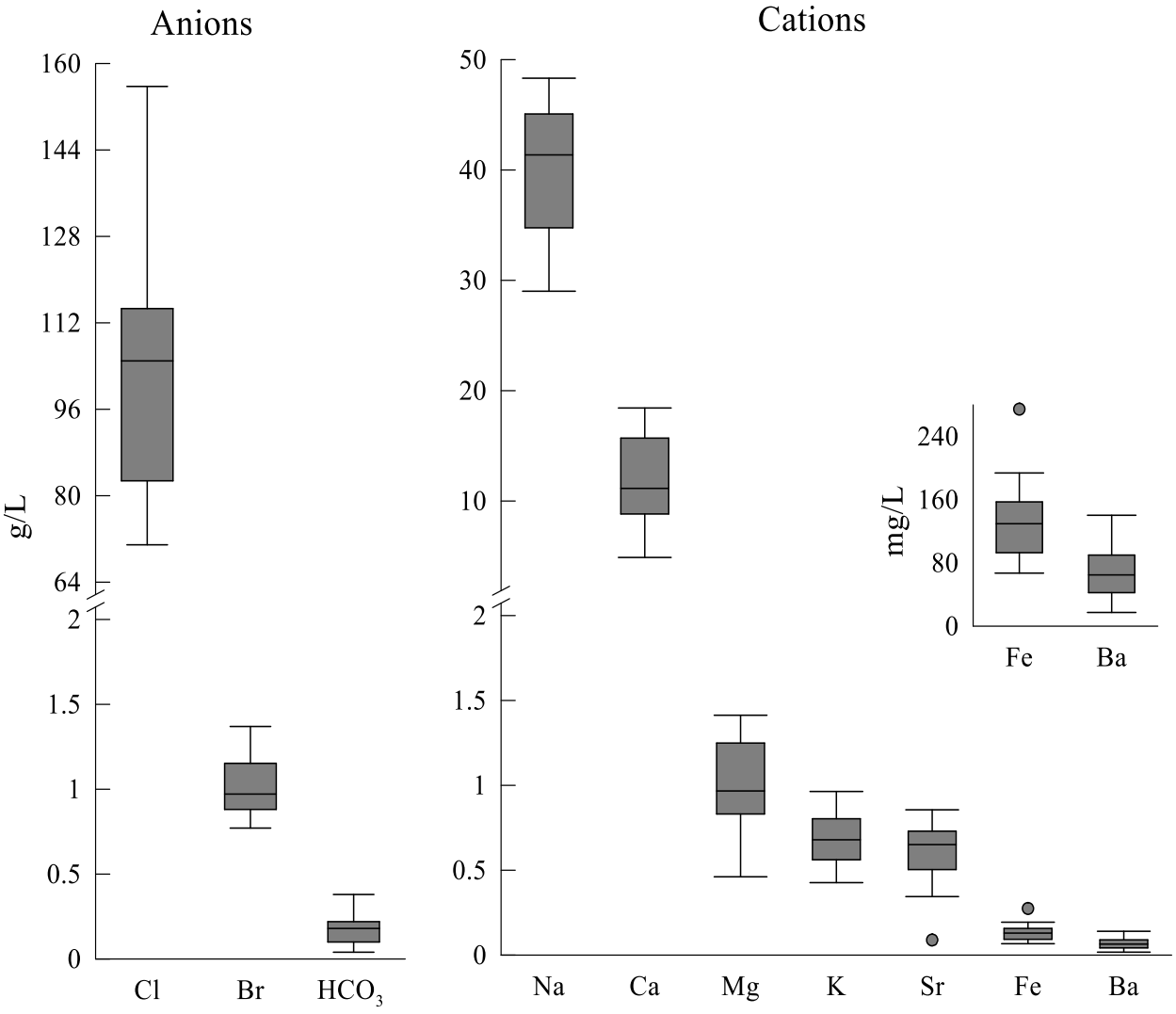


**Figure 3.40 Box plots of concentrations of major anions and cations in produced waters from the TMS.** Concentrations for $SO_4$ are not included, as they were largely below detection.

Finally, some initial results from high-temperature water-rock interaction experiments are highlighted in Figs. 3.42 through 3.44. Figure 3.42 illustrates how pH changed over time in the experiments with crushed TMS samples at starting pHs of 2, 4, and 6 using distilled water (DIW), NaCl (Na), and Ca,Mg,Na,Cl (Mix). For the Na and Mix fluids we ran experiments at 3.2% salinity and 12% salinity. The changes in pH are indicative of different geochemical weathering and precipitation pathways. Figures 3.43 and 3.44 are photomicrograph and SEM image examples of how the physical nature of the TMS changed during experiments with differing fluid compositions.

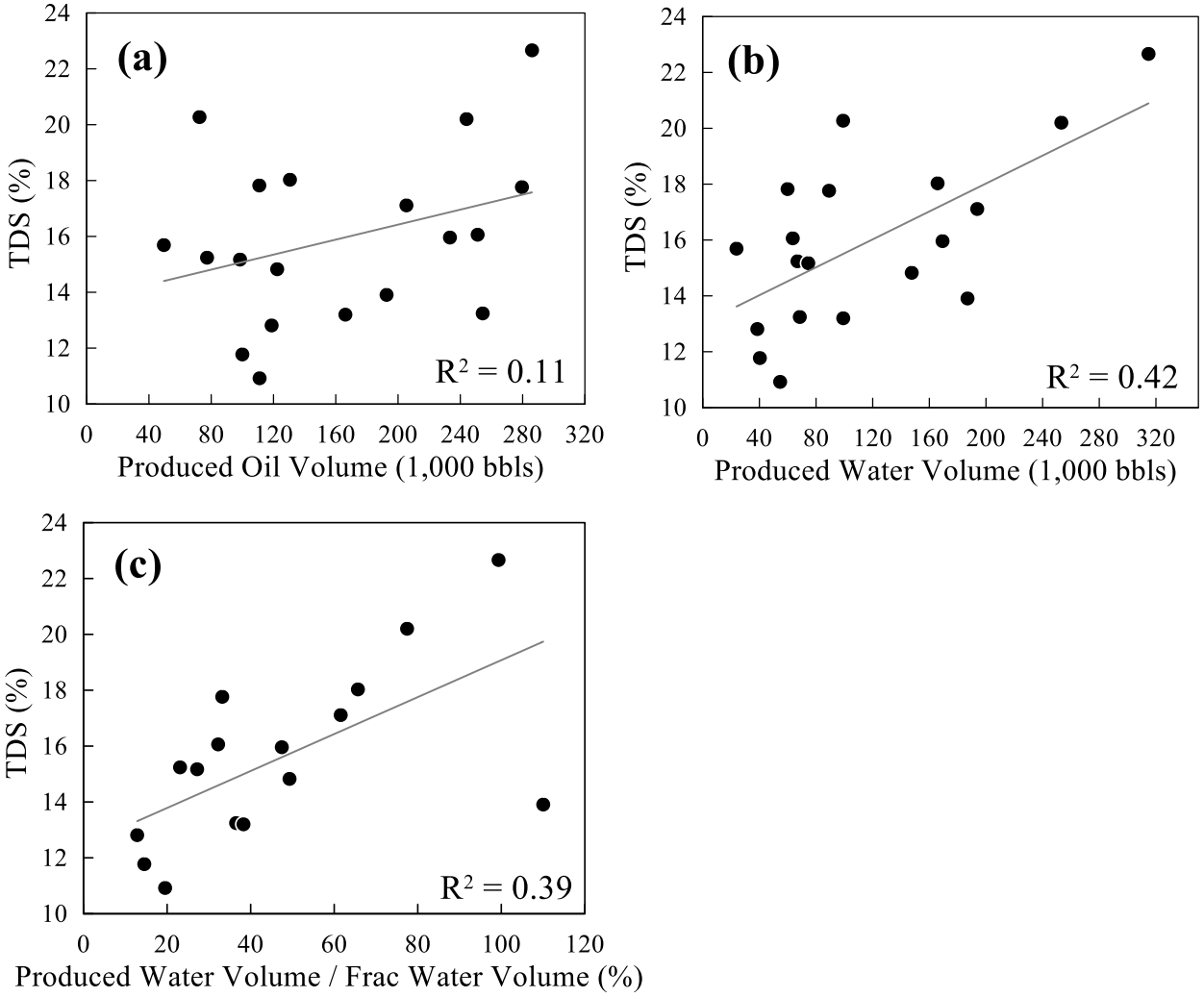


**Figure 3.41 Correlation plots comparing TDS with (a) produced oil volume, (b) produced water volume, and (c) produced water volume/fracking water volume for the TMS produced water samples.**

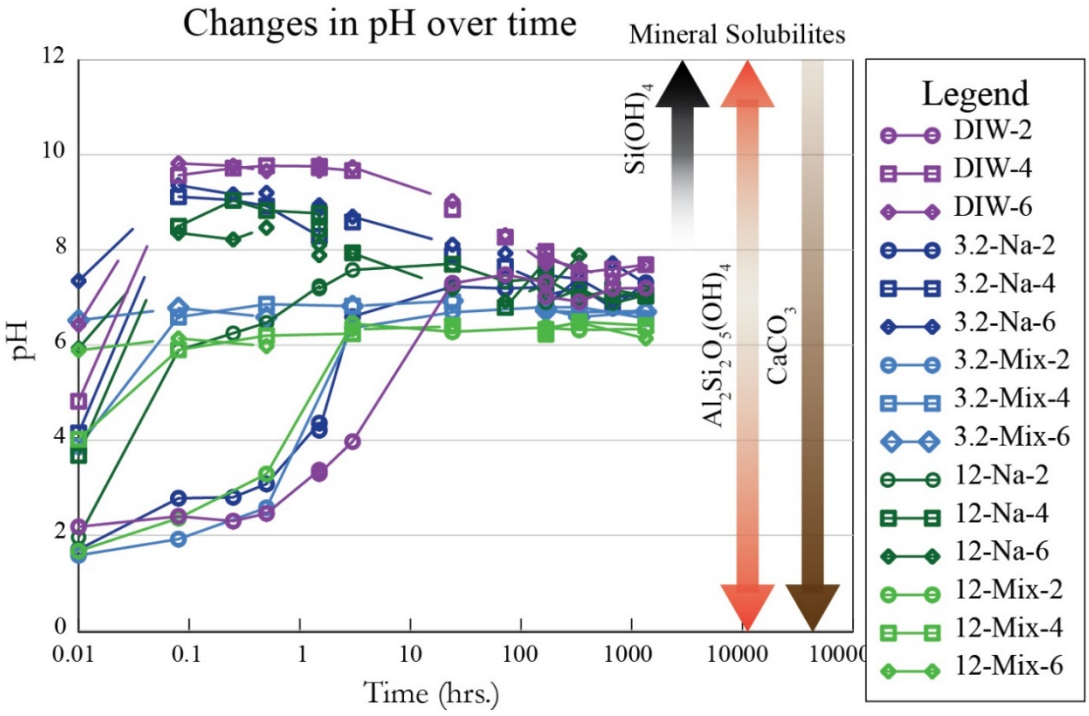


**Figure 3.42. Log Time vs. pH of experiment runs. Graded arrows indicate increasing relative mineral solubilities over pH ranges.** The water-rock interaction pathways change with changing starting pH and salinity.

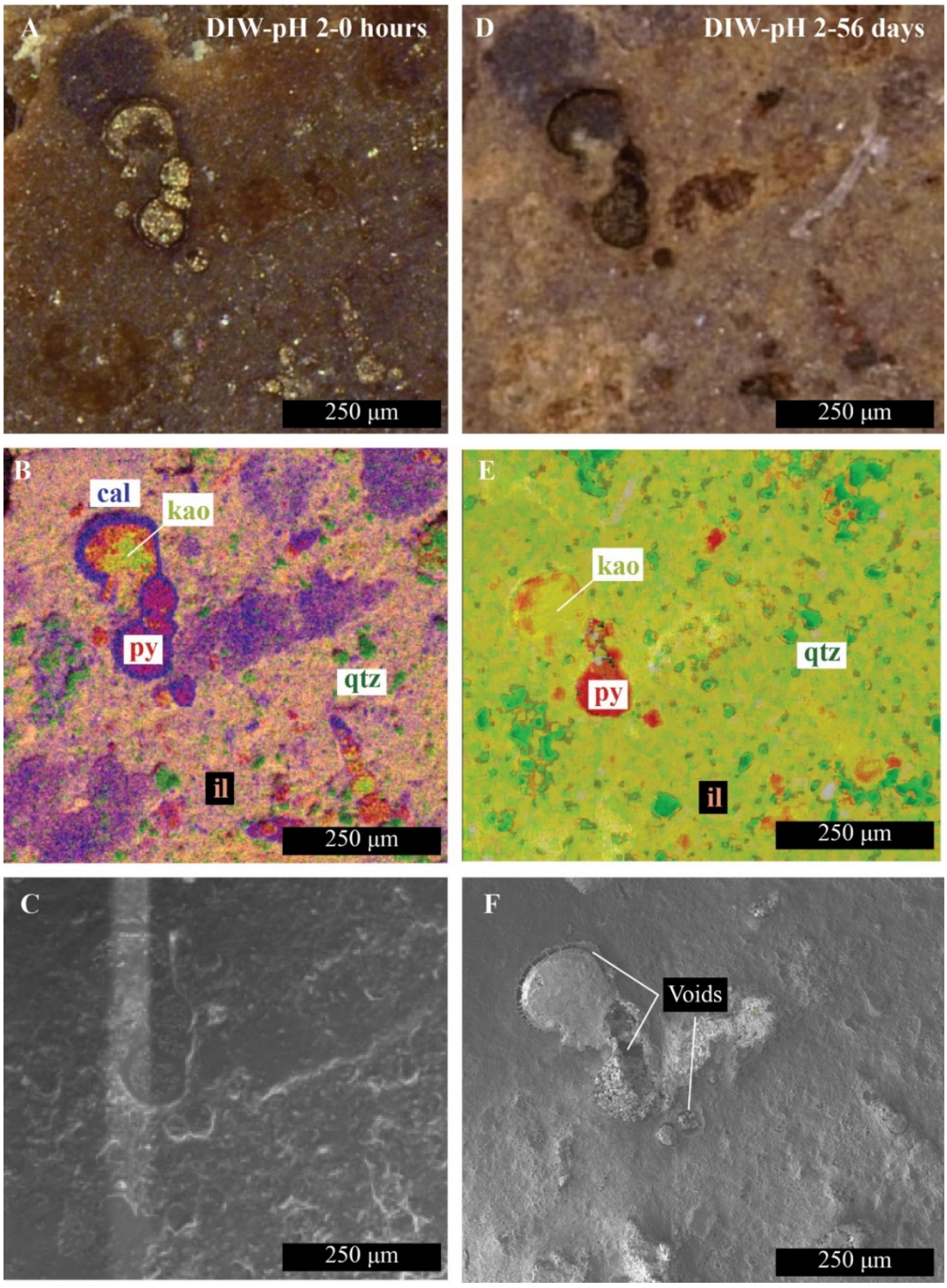


**Figure 3.43 Photomicrographs (A and D), EDS (B and E), and SE (C and F) images of mount before (DIW-pH 2-0 days) and after (DIW-pH 2-56 days) fluid-rock interactions.** Pyrite oxidation is observed from oxide staining in D. Carbonate dissolution is marked by the lack of calcite (blue) in E and void space seen in F after the reaction.

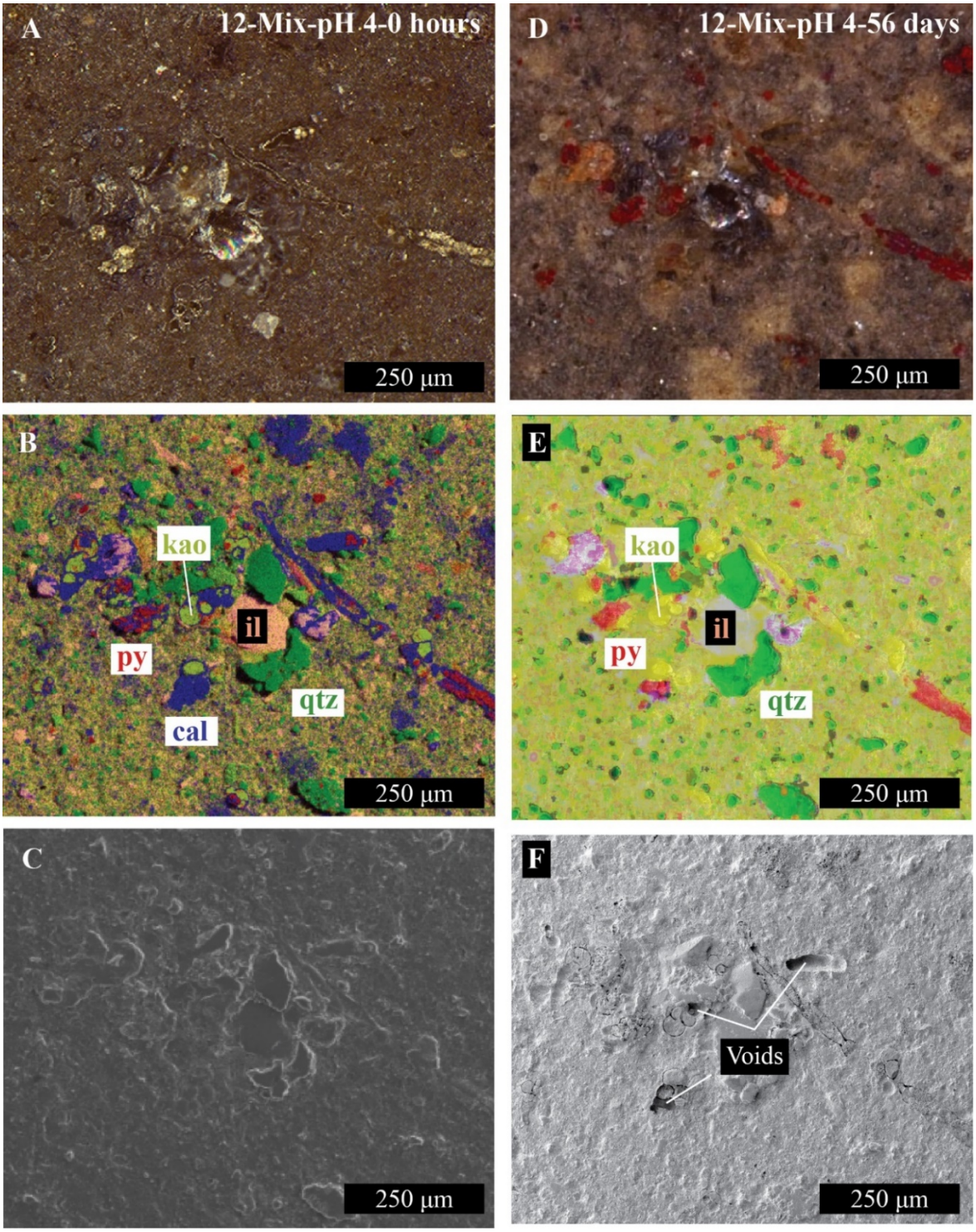


**Figure 3.44 Photomicrographs (A and D), EDS (B and E), and SE (C and F) images of mount before (12-Mix-pH 4-0 days) and after (12-Mix-pH 4-56 days) fluid-rock interactions.** Pyrite oxidation is observed from oxide staining in D. Carbonate dissolution is marked by the lack of calcite (blue) in E and void space seen in F after the reaction.

The dominant anion in all samples was Cl with a mean concentration of 103 g/L. The dominant cation in the samples was Na with a mean concentration of 40 g/L. Several lines of evidence, including comparisons to initial flowback water composition and changes in key elemental ratios (see Hoffmann and Borrok 2020 for more details) fit a scenario where the TMS formation brine endmember is progressively diluted by the original fracking fluid. For example, in Fig. 3.41c, there is a correlation between the produced water volume/the fracking water volume and TDS for the TMS wells. In other words, the wells with higher TDS values tended to be the wells where enough water was produced such that the influence of the original fracking water had diminished. Another important observation is that the ratio of produced water relative to fracking water was rarely above 1, which confirms that very little fluid flow is occurring in the TMS on time scales important for oil and gas production. In other words, this is indeed a tight formation with limited fluid flow potential without fracking. Additional work (described in Hoffmann and Borrok; 2020); however, demonstrates that the formation waters in the TMS were genetically similar to those in surrounding formations with the Gulf Coast Basin, which means that the formation waters did migrate through the TMS over geological time scales.

Initial results from the high-temperature water-rock interaction experiments, have highlighted at least three separate chemical evolution pathways for fluids in contact with TMS rock. These pathways are defined by differing degrees and timing of key dissolution, precipitation, and adsorption processes. The important dissolution processes include carbonate dissolution, which occurs rapidly in the low salinity solutions and in the low pH solutions with variable salinities and compositions. Another important dissolution process is sulfide oxidation, which occurred in all the experimental solutions. This resulted in the initial release of ferrous iron and some trace metals, which as rapidly followed by the precipitation of iron-oxide minerals and the loss of trace elements, presumably due to adsorption onto those precipitates. Dissolution of silicates such as feldspars was also important, particularly in the experiments where the pH increased to levels near 9.0. The precipitation of gypsum (a hydrated calcium sulfate mineral) also occurred in several of the experimental runs. This is a particularly important observation, as precipitation of gypsum during the introduction of fracking fluids could lead to plugging of fractures and flow pathways. Overall, the most dynamic chemical changes occurred in fluids with dilute compositions and NaCl compositions, while more subtle changes occurred in the Na, Ca, Mg, Cl systems. This demonstrates that fracking fluid compositions far from equilibrium with the host rocks will result in more and faster dissolution reactions, which could be followed by precipitation reactions. Fracking fluid compositions closer to those of the existing formation waters, which are in equilibrium with the host rock, tend to result in low dissolution rates and may delay or prevent precipitation.

The produced waters of the TMS are highly-saline Na-Ca-Cl brines that are typical of those found in other geologic units within the Gulf of Mexico Basin. The TMS brines appear to be diluted with varying amounts of the fracking water used in the completion of the wells. This influence of fracking water makes sense, as for most wells the total volume of water produced (at the time of sampling) was less than the volume of water used for fracking. The relatively small volumes of

produced water for TMS wells suggests that the TMS is a tight formation that allows for limited fluid flow over short time scales. However, evidence from Br and Cl systematics suggests that the brine fluids have migrated through the TMS over geologic time periods despite its low present-day permeability.

The high-temperature water-rock experiments with TMS samples provided new insights into how different fracking fluid chemistries interact with the TMS mineralogy. These insights may lead to the formulation of better fracking fluids, which can most effectively enhance porosity and permeability while limiting precipitation. These experiments can also be used to help predict the impact of using recycled produced waters in place of dilute freshwater for fracking operations.

## 3.4 Ionic Movement between TMS Cores and Water

The high clay content of TMS leads to drilling, wellbore instability, and fracturing performance issues, which is costly. Therefore, it is imperative to design drilling and fracturing fluids with effective clay inhibitor to mitigate swelling and increase in shale stability. The objective of this study is the screening of the clay stabilizers such as KCl, and NaCl inorganic brines and providing the baseline for TMS treatment utilizing well established methodologies such as capillary suction time (CST) and roller oven (RO) tests.

### *3.4.1 Experimental Procedures*

*Capillary Suction Time*

To investigate the relative sensitivity of Tuscaloosa Marine Shale to different concentrations of KCl and NaCl clay stabilizers and distinguish the efficient inhibition case scenario for this formation, the capillary suction time (CST) method is applied. This test measures the relative flow capacity of a ground formation rock slurry. During the experiment, 2.5g of shale is ground and sieved through 70 mesh. Then, the specimen is mixed with 50 ml of the prepared fluid by a magnetic stirrer for 2 hours. After the stirring, a 5ml sample is set into the cylindrical cast resting on the chromatography paper. The CST timer starts recording once the fluid reaches the electrode at the distance of 0.25" diameter boundary from the center of the cylinder and stops at 1". A shale with a high concentration of swelling or dispersible clays has a lower permeability, which provokes higher fluid retention time.

*Roller Oven Test*

To determine the Tuscaloosa Marine shale stability, the Roller Oven test is applied to evaluate the recovery ratio of shale when it is exposed to the fluid. The principal behind it involves a circulation of the tested drilling fluid around the shale specimen. Over 16-24 hours at the desired temperature, this test determines how mechanically shale weakens and reacts in contact with the water-based drilling fluid. The procedure involves grinding the shale to 10 mesh and more extensive than 40 mesh. Then, the ground particles are split evenly into 10g samples. Generated samples are mixed with 50ml of the prepared fluid and placed in the bottle to be rolled. Later, after the rolling is finished, the specimens are sieved through 70 mesh and adequately cleaned with fresh water. After,

the sample is dried. Once the drying of the tested specimen completed, it is reweighted. The mass of the sample recovered and sieved recognized as a measure of shale stabilization. The higher percentage of the tested particles recovered through sieving after the test, the better stabilization drilling fluid provides to the shale.

*Digital Image Correlation*

The experimental setup and DIC procedures are represented in Chapter 5. A front surface of the specimen, on which deformation was monitored, was covered with a thin layer of white spray paint (Rust-Oleum Flat White, SKU 249,126), forming a speckled pattern. Each of the specimens from the core has been assigned to the following fluids, where HC1 and LC1 were exposed to DI and high salinity (6 wt.%) brines, and HC2 and LC2 were exposed to DI and low salinity (2 wt.%) brines. A total volume of 1.5 liter of fluid was prepared for each of the experiments. After the preparation stage, the shale specimens are placed on the plastic mesh stand in the thin glass fluid container filled with a respective brine, with the painted surface facing the digital camera (3072 × 2048 pixels). The mesh stand mitigated the contact restriction of the bottom surface area exposure to the tested fluids. Images of the immersed specimen were taken during the deformation process. The DIC software (Aramis 2019) was used to analyze the changes in the speckle pattern of the specimen and derive the displacement and strain data across the entire specimen surface. A subset size of 45 pixels and a step size of 12 pixels was used in the DIC analysis. In order to calculate the average orthogonal or longitudinal strains' development in the tested specimens as a function of time, two planes were manually placed to segregate the desired area of study. In the case of the vertical strain being the main tension of interest, these boundaries are placed on the top and bottom of the tracked region. The average strain of the region was calculated by the following formula:

### *3.4.2 Sensitivity of the TMS to Water and Effect of Moisture*

In the work on the sensitivity of TMS to water, during the preparation of specimens for experimental work, we noticed a lamination that was self-induced in the full core from Crosby well 12-1H#1. Since we identified the lamination region, we concurrently identified the depth where the core "disking" occurred, which was 12,118.1 ft. A close look at the core sample reveals the micro laminas. We selected this interval to continue our investigation. We picked a small part of the core from the same depth that clearly showed more than six laminas and targeted it for visual inspection of TMS sensitivity to water. When water was placed on the surface of the specimen, the reaction was apparent to the naked eye; that is, water was absorbed rapidly from the surface of the specimen into the interior of laminas. We attribute the rapid absorption of water and drying up of TMS specimen to the simple hydrophilic nature of shale material and its strong capillary suction forces in the laminae. During the specimen preparation work, we estimated the laboratory RH was about 95% at 80 F.

After experimentation with the effect of water on TMS, we continued with the effect of time and changes in RH of the laboratory by changing the temperature from 80 F to 70 F. In 40 minutes from opening the full core box and exposing the TMS full core to the RH of PEI laboratory, we observed that a third self-induced fracture revealed itself without use of water. It was at the TMS

core depth of 12,117.771ft. We learned that TMS sensitivity to water and RH might not be deniable from these simple observations. In addition, we believe that the cementing material between the TMS lamina faces, which could be Chlorite and other material such as Calcite and Iron Dolomite, were dissolved in contact with probably acidic water so that it weakened the cement, causing a significant reduction in tensile strength of "shale." Due to shale anisotropy, the "weakly cemented" shale laminae generate a fracture, perhaps through the shearing mechanism.

### *3.4.3 Visual Deformation of the TMS in Contact with Swelling Inhibitors*

The reaction of TMS specimens to the different clay inhibitors has been examined and analyzed after it is immersed in the fluids. The solution such as: $K_2CO_3$ (10%), NaCOOH (10%), $NH_4Cl$ (10%), $NH_4Cl$+KCl(5%+5%), KCl (10%) and DI $H_2O$ have been prepared. First of all, the specimens were dried in the temperature chamber until the change in weight loss couldn't reach more than 0.05 mg. After it was determined that the weight of the specimens stabilized according to the weight constraint, each of the cores has been immersed into bicker with an assigned inhibitor. The results showed that the best performance among the described fluids was shown by $K_2CO_3$ (10%). It is suggested that the initial increase of weight for all of the specimens is due to water adsorption to the surface of the shale due to electric charge where the high concentration of negatively charged clay surface attracted positively charged hydrogen atoms. The continued increase of weight can be attributed to the capillary suction, due to which the water that was adsorbed to the surface, which then progressed into the molecular structure of clay that yielded in clay expansion and potential shale dispersion. As for NaCOOH (10%), $NH_4Cl$ (10%), $NH_4Cl$+KCl (5%+5%), DI $H_2O$, the abrupt weight loss can be seen from Fig. 3.45. This weight loss can be attributed to clay expansion and shale deformation that was caused by poor clay inhibitor performance. According to the preliminary results, fluids, where the dominant cation was represented in $K^+$, showed better performance than others.

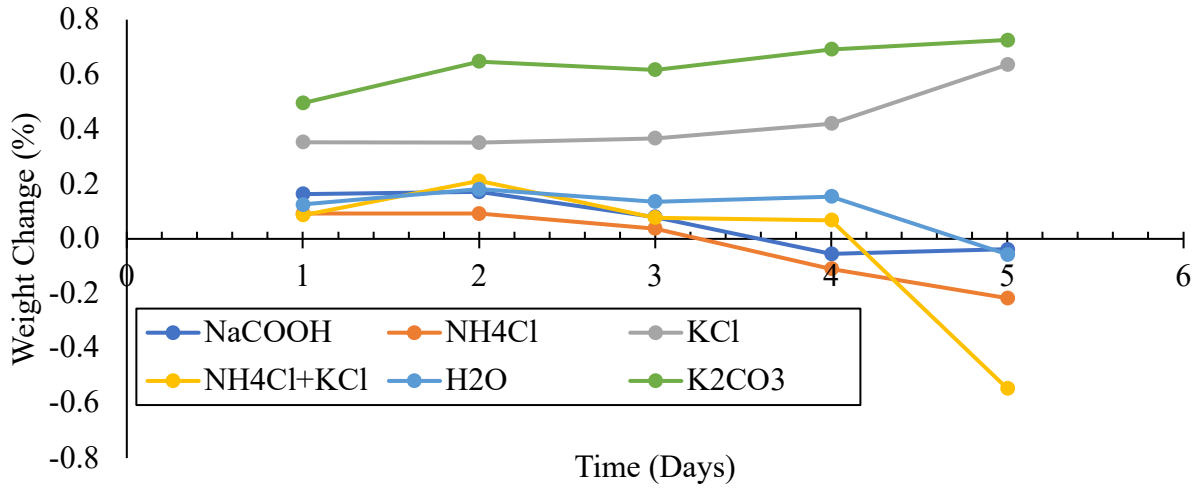


**Figure 3.45 Weight Change of the TMS Specimens Immersed into Cation Fluids.**

### *3.4.4 Evaluation of Tuscaloosa Marine Shale Stability Using Capillary Suction Time and Roller Oven Tests*

Three depths from CB well have been analyzed in this section. Figure 3.46 represents the CST data response measured for each of the targeted depths. The freshwater was used as a constrained reference to which the KCl and NaCl fluids are compared. As expected, the significant sensitivity of all of the samples has been observed in contact with the freshwater. It showed that the time taken for the freshwater to pass through the grounded shale is much longer, which is caused by water capillary absorption into the clay structure from the pack's surface that causes long fluid retention and CST response.

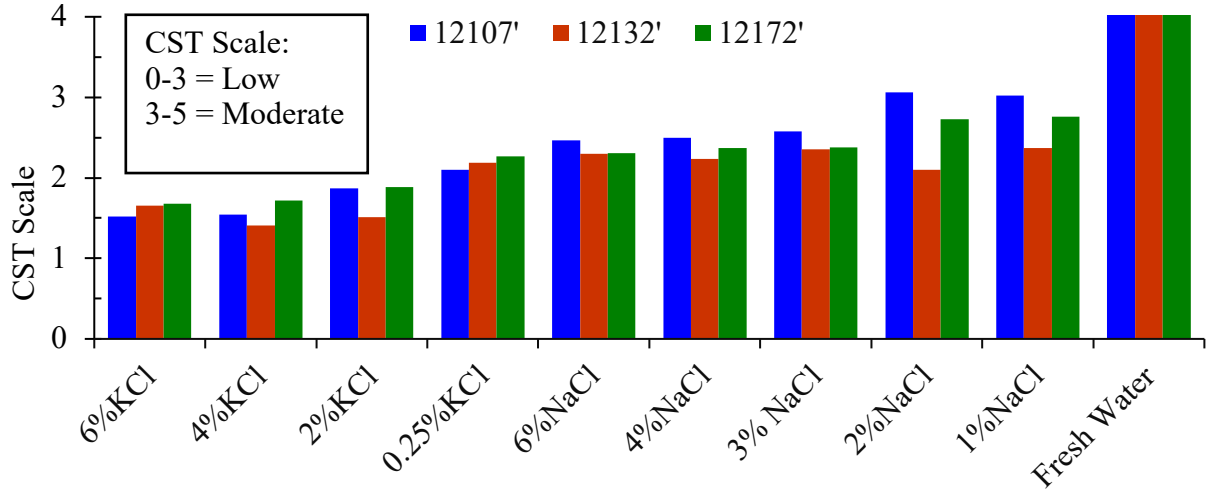


**Figure 3.46 Capillary Suction Time Results for CB Well Specimens.**

As can be seen, not in all of the studied cases, an increase of ionic strength of the fluid guarantees the proportional improvement of the shale-fluid interaction. This effect was explained by van Oort (2003) and examined by Griffin et al. (1986). For the depth of 12107′, the best clay stabilizer was found to be 6%KCl, outperforming 4%KCl, 2%KCl, and 0.25%KCl brines, respectively. However, it cannot be unnoticed that the dominance of 6%KCl over 4%KCl is insignificant, so it may be suggested to utilize second-grade brine that would yield less expenditure for this region. At the same time, for NaCl, which showed poorer inhibition performance compared to any grade of KCl, the response decreased until the concentration reached 4%, at which the stabilization potential was measured to be lower than 6%KCl. A similar CST response pattern is followed by the specimen from 12172′, where 6%KCl surpasses 4%KCl. However, looking at the 12132′ specimen's sensitivity, the results show that potassium brine with 6% strength is deficient compared to 4%KCl, which provides more excellent inhibition by 18%. Overall, there is no correlation found of the clay mineral concentrations to the magnitude of the shale response by the CST test.

The results of the Roller Oven test support to a limited extent the findings from the CST tests, which represented in Fig. 3.47. For 12107′ specimen 4%KCl and 2%KCl, which was not the case

during the CST test, outperformed 6%KCl. Specimen from 12132′ was found to be more stabilized in contact with 4%KCl and 2%KCl as well, in which 2%KCl grade excelled 6%KCl and 4%KCl. For 12172′ specimen, results showed that 6%KCl provided stabilization better than 4%KCl and 2%KCl. As it can be seen the magnitude of the response from the RO test of the specimen from 12172′ comparing to 12107′ and 12132′ is doubled. It was found from the XRD analysis that the concentration of Illite & Mica clay minerals in 12172′ zone is 27% and 29% higher than from 12107′ and 12132′ depths, respectively. Since illite has a high potential to disperse and migrate when in contact with the water-based fluid, it could be responsible for significant destabilization and higher attrition of the shale specimen.

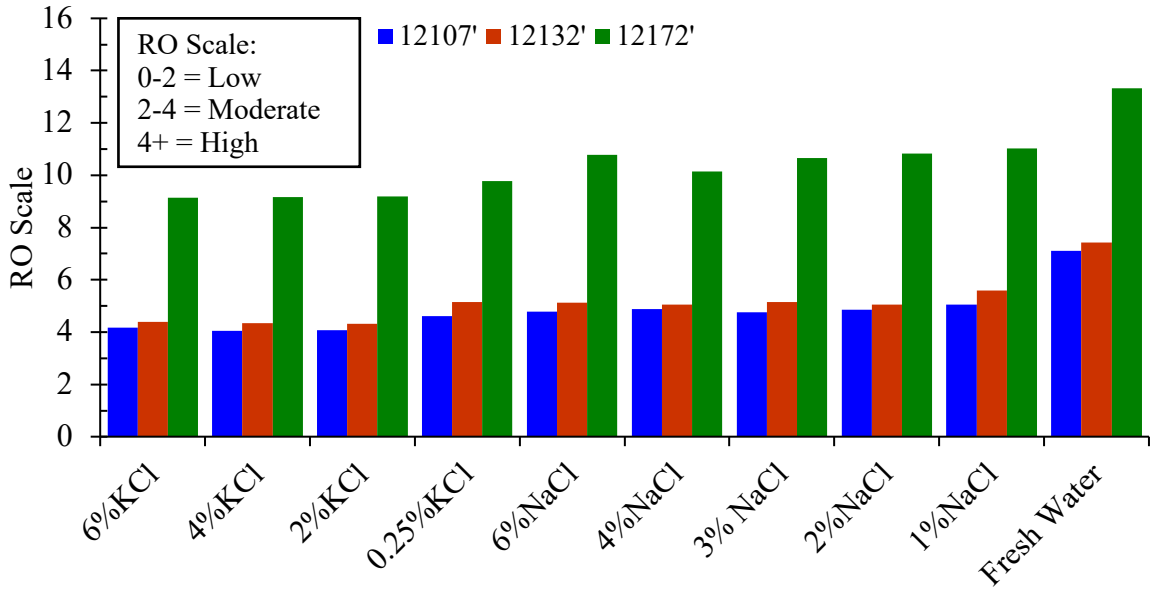


**Figure 3.47 Roller Oven Test Results for CB Well Specimen.**

The specimen from BG well exhibits high sensitivity to water that supports the clay mineralogical data with high clay content.

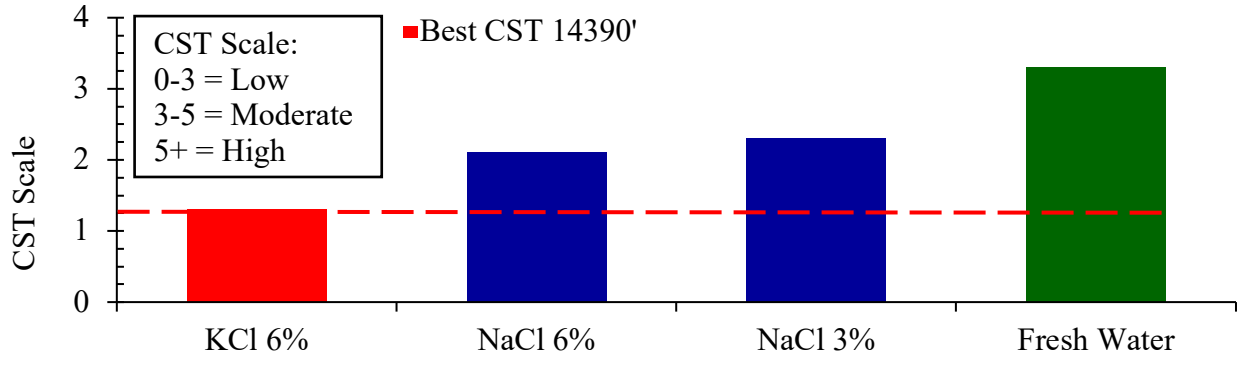


**Figure 3.48 Capillary Suction Time Test Results for BG Well Specimen.**

Reactivity results showed (Fig. 3.48) that better inhibition of the shale could be provided by 6%KCl, outperforming 6%NaCl and 3%NaCl by 61% and 76%, respectively. Based on that, it can be stated that NaCl provides much less chemical support to the mitigation of clay swelling and dispersion of this TMS shale specimen.

Similar conclusions can be drawn from the RO test results, which can be found in Fig. 3.49. The shale was less destabilized when the KCl clay control agent was applied. Interestingly, in this case, the 3% NaCl was almost the same magnitude as freshwater, providing practically no stabilization to the shale at all.

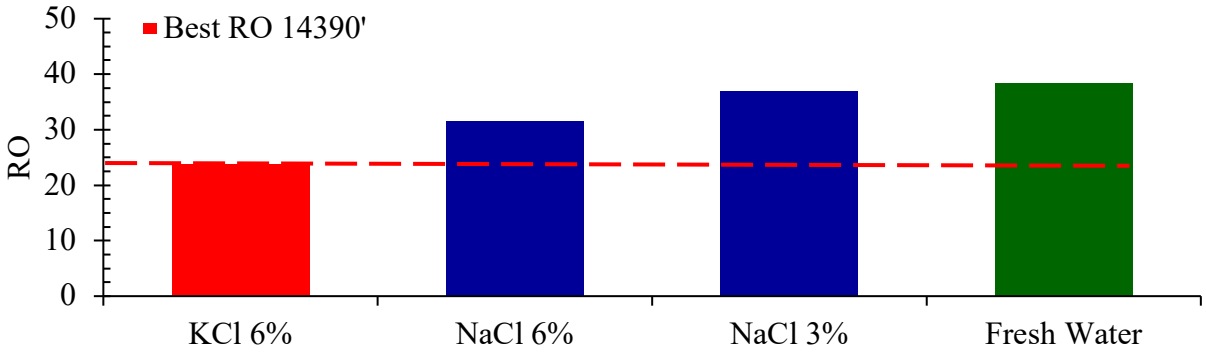


**Figure 3.49 Roller Oven Test Results for BG Well Specimen.**

### *3.4.5 Using Digital Image Correlation for Evaluating the Impact of Brine on Swelling of TMS*

A total of twelve experiments have been conducted to measure and characterize the swelling behavior of the TMS utilizing DIC during the shale interaction with DI water, KCl, and NaCl brines of various concentrations for 88 hours. The findings from the DIC results extended the current understanding of shale/fluid interaction by capturing the heterogeneous alteration of the shale during exposure to the water and brine systems. As such, the hydration of the matrix and propagation rate with the pattern of induced fractures were discovered to be affected diversely by the fluid networks as seen in the full field strain images. The severe alteration of the shale by matrix hydration and fracture openings was observed in all specimens in contact with DI water. In the case of diluted NaCl, fewer fractures were formed with a relatively lower average matrix strain. Opposite to all, KCl brine shows the best inhibition of the shale matrix by mitigating the significant matrix expansion, whereas a more considerable amount of fractures are stimulated when compared to NaCl solution.

As shown on the full-filled strain maps in Figs. 3.50 and 3.51, if the microcracks are identified on the surface of the specimens before the immersion, they exhibit and reach high strain first. Some of the horizontal micro-fractures in the specimen occurred during their production from the carrier cores while some might be drilling-induced. In order to evaluate the influence of the preexisting microcracks on the average strain, each of the high strain/fractured regions can be investigated individually. In the other work focused on the swelling of TMS, it was found that most of the cracks, either the ones that exist before the experiment or induced during the immersion through

the weak laminations by the imbibed water, reach the same average strain within the same time interval from the swelling initiation of those regions (Parrikar et al. 2021). Therefore, it may be suggested that the preexisting microcracks may only significantly influence the average strain at the initial stage of the shale-fluid interaction, which later is reduced and is dominated mainly by the fracture propagation through the possible interconnection of the pores, and matrix expansion at vicinity. In addition, these findings imply that there could be a similarity in the composition of the stimulated swelling regions.

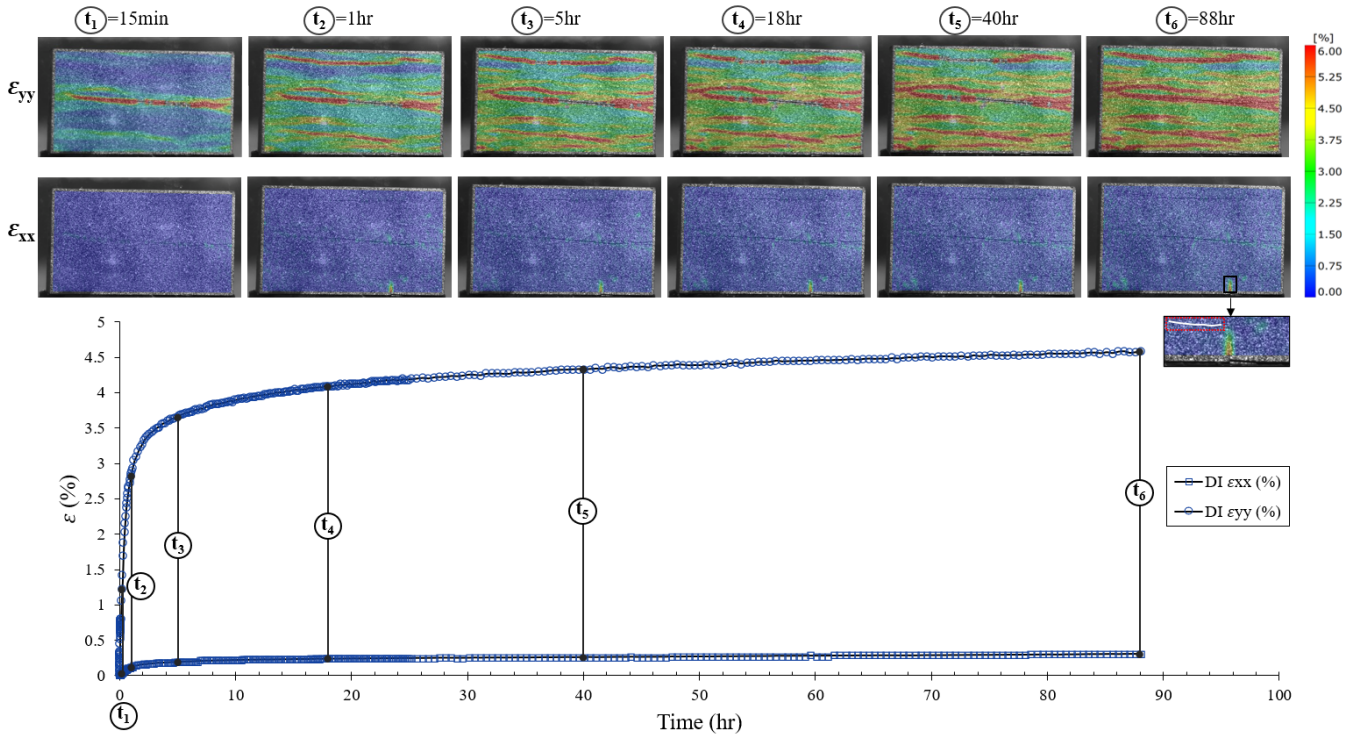


**Figure 3.50 Development of vertical ($\varepsilon_{yy}$) and horizontal ($\varepsilon_{xx}$) strains of $HC_2$ specimen immersed in DI water with the integrated full-field DIC Images at the six time stages 0.25,1,5,18,40 and 88hr.**

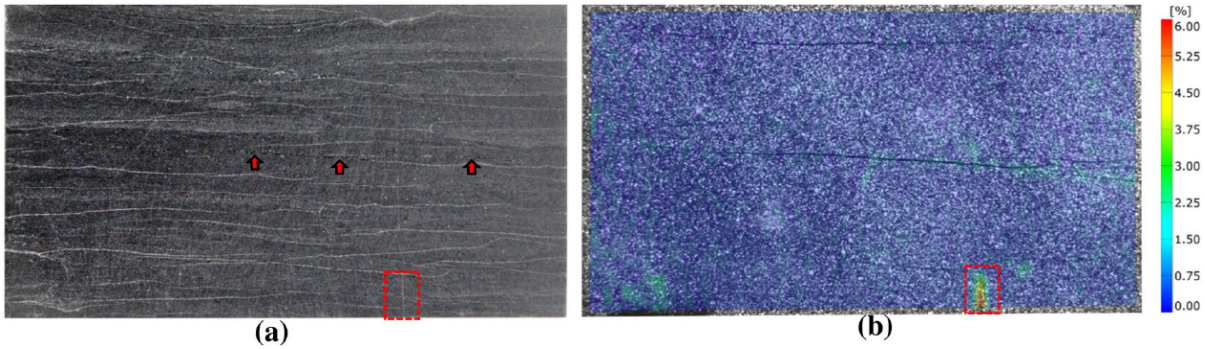


**Figure 3.51 The front surface of the HC2 specimen before the immersion in DI water with the highlighted sealed vertical fracture and arrows pointing out to the microfracture identified before the immersion (a) and full-field horizontal strain (εxx) map of this surface during the exposure to DI water at 88 h with the highlighted fractured region in vertical direction (b).**

The clay-rich intervals were found to swell more than the coarse-grained intervals, such as quartz layers presented in Fig. 3.52. Relatively higher permeability in the matrix of coarse-grained intervals may contribute to water volume uptake. However, since higher permeability conveys higher porosity, the expansion may be expected to be lower since the porosity is in the inverse relationship with clay concentration that is tightly filling the void in the shale. Our results show that some of the coarse grain regions exhibit low to no swelling strain in contact with all tested fluids. The finding supports the results that the quartz concentration in shale is in inverse correlation to the imbibed water. However, in the presence of lamination in such a region, focused on in Fig 16, we observe swelling followed by the occurrence of the delamination caused by all tested fluids. This deformation propagates, leading to a low-moderate, moderate, and high vertical strain in the samples immersed in KCl, NaCl brines, and DI water, respectively. Whereas the surrounding coarse-grained region in the vicinity remains unaltered, exhibiting low to no strains in all of the cases.

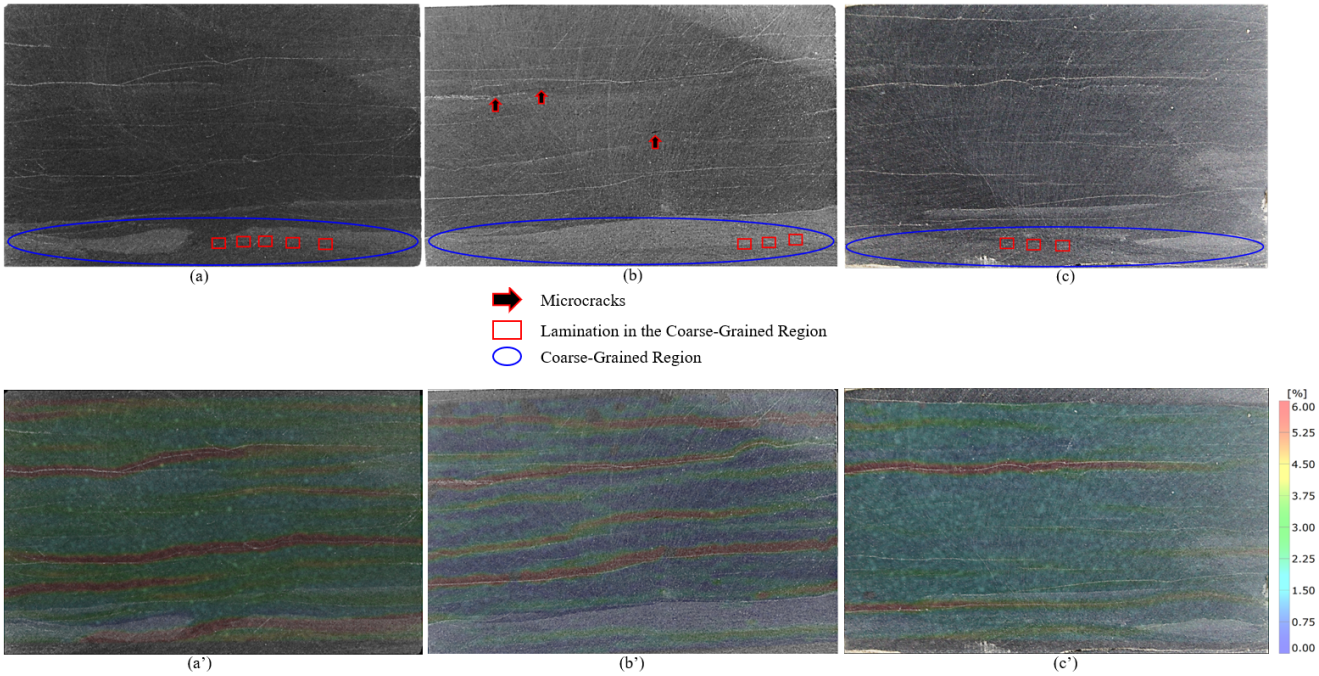


**Figure 3.52 The surface of the $HC_1$ specimens before the immersion into DI water, KCl and NaCl brines** presented in images a, b, c respectively, with circled coarse-grain regions, highlighted lamination in these regions, and visible micro-cracks identified on the surfaces of the specimens. The images a', b', c' represent the same surface of the specimens but with a DIC full-field vertical strain map mask overlay acquired at 88hr of the experiment. To observe the swelling strain in the coarse-grained region and identify which lamination was stimulated and which remained unaltered during interaction with the fluids.

The inhibition effect on shale swelling provided by NaCl brine is significantly lower in comparison to KCl brine. This might be attributed to the difference in the size of the hydration radius of these cations. The process of cation's hydration from the electrolyte compounds, which in our case are NaCl and KCl brines, can be described as follows. The partial negative end of the dipole water molecule, which is O-, attracted to the vicinity of the positively charged $K^+$ and $Na^+$ owing to the ion-dipole forces. The potassium is more prone to lose its hydration shell between these two cations and, consequently, be bonded with the clay surface due to its lower hydration energy. Since the surface charge of the ion has a strong inversely proportional relationship to the adsorption, the adsorption and neutralization of the clay's negative layer charge are much weaker for Na ion. In addition, the K tends to substitute the Na in smectite's structure in I/S clay, thus mitigating the clay hydration and reducing the interlayer space in the clay structure (Whitley et al. 2004). Respectively to these statements, if only Na ions are present in the fluid, the potential for swelling mitigation is significantly reduced since it might be ejected from the Stern layer. Therefore, the water molecules tend to adsorb to the clay surface between the clay flakes, causing an increase in shale expansion. In addition, the findings point to the conclusion that the ionic strength of the fluid significantly affects the rate of swelling and its progression. It was determined that the increase of KCl and NaCl concentration from 2 to 6% may reduce the shale swelling by 39 and 43%, Fig. 3.53, Table 3.6. In the case of fluid activity being lower than the formation fluid in the inter-clayey pores preserved during the shale preparation method, the water is forced from the shale by the osmosis. On the other hand, there is no evidence of the significant influence of the brine concentration on shale fracturing - laminae stimulation.

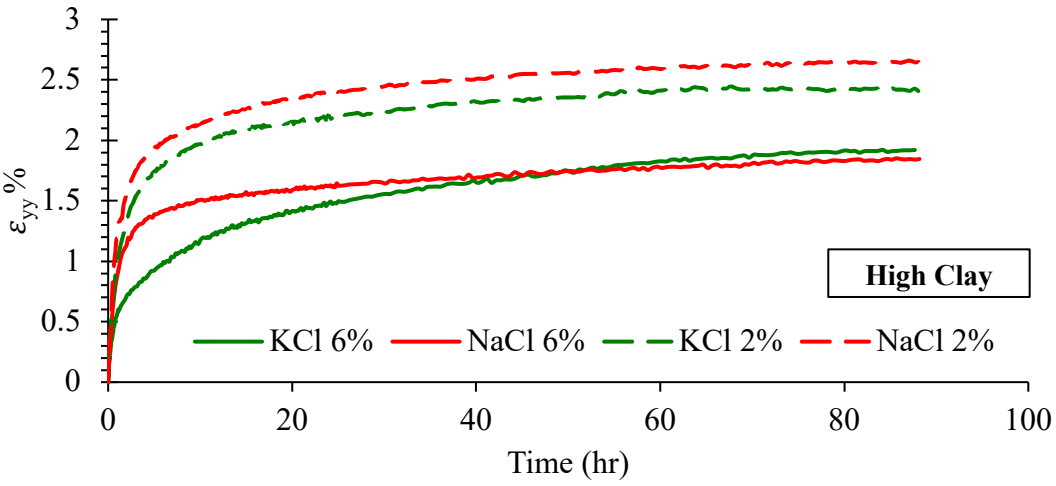

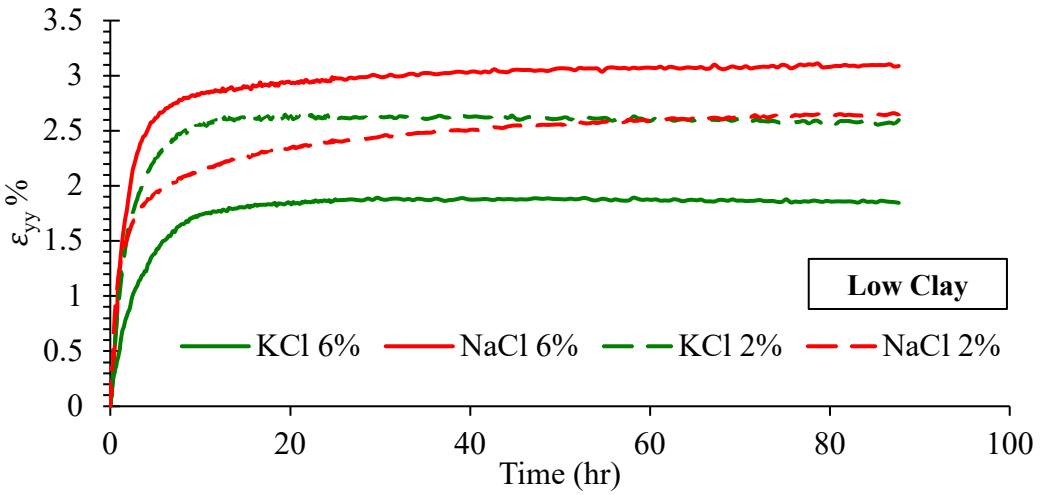


**Figure 3.53 Comparison of the vertical strain ($\varepsilon_{yy}$) development in HC and LC specimens immersed in 2 and 6 wt% KCl and NaCl brines for 88hr.**

**Table 3.6** Swelling Change % with an increase of the salt concentration.

| Sample ID | Depth | $\varepsilon_{yy}$ % in NaCl | $\varepsilon_{yy}$ % in KCl | Salt Concentration wt.% | Swelling % Change | NaCl | KCl |
|---|---|---|---|---|---|---|---|
| LC1 | 12192 | 3.08 | 1.84 | 6 | | -14% | 39% |
| LC2 | 12183 | 2.66 | 2.56 | 2 | | | |
| HC1 | 12137 | 1.84 | 1.92 | 6 | | 43% | 25% |
| HC2 | 12081 | 2.65 | 2.4 | 2 | | | |

## References

Aki, K, and PG Richards (1980). Quantitative Seismology: Theory and Methods. WH Freeman and Co.

Barnaby, R.J., Oetting G.C., and Gao, G., 2004. Strontium isotopic signatures of oil-field waters: Applications for reservoir characterization. *American Association of Petroleum Geologists Bulletin*, 88, 1677-1704.

Bearden, B. L., Mancini, E. A., & Puckett, T. M., 2000. Salt Anticline Play in the Mississippi Interior Salt Basin.

Clark, C.E., and Veil, J.A., 2009. Produced water volumes and management practices in the United States, ANL/EVS/R-09/1. Prepared for the U.S. Department of Energy, National Energy Technology Laboratory, September, 64.

Cushing, Elliott Morse, Ernest H. Boswell, and R. L. Hosman., 1964. General geology of the Mississippi embayment.

Dowsett, Harry J., 1989. Documentation of the Santonian-Campanian and Austinian-Tayloran stage boundaries in Mississippi and Alabama using calcareous microfossils. No. 1881-1884. US Government Printing Office.

Engle, M.A., Reyes, F.R., Varonka, M.S., Orem, W.H., Ma, L., Ianno, A.J., Schell, T.M., Xu, P., and Carrol, K.C., 2016. Geochemistry of formation waters from the Wolfcamp and "Cline" shales: Insights

into brine origin, reservoir connectivity, and fluid flow in the Permian Basin, USA. *Chemical Geology*, 425, 76-92.

Enomoto, C.B, Hackley, P.C., Valentine, B.J., Rouse, W.A., Dulong, F.T., Lohr, C.D., and Hatcherian, J.J., 2017. Geologic characterization of the hydrocarbon resource potential of the Upper Cretaceous Tuscaloosa Marine Shale in Mississippi and Louisiana, U.S.A., Gulf Coast Association of Geological Societies Transactions article #00193, 67, 95-109.

Enomoto, C.B., Lohr, C.D., Hackley, P.C., Valentine, B.J., Dulong, F.T., and Hatcherian, J.J., 2018. Petroleum geology data from Mesozoic rock samples in the eastern U.S. Gulf Coast collected 2011 to 2017: U.S. Geological Survey data release,

Griffin, J.M., Hayatdavoudi, A., and Ghalambor, A. 1986. Design of Chemically Balanced Polymer Drilling Fluid Leads to a Reduction in Clay Destabilization. *SPE Drilling Engineering*, 1, 31-42.

Gruebel, R. D. G., 1985. Exploring the lower Tuscaloosa in southwest Mississippi. *Gulf Coast Association of Geological Societies Transactions* 35, 87–96.

Hersch, J. B., 1987. Exploration methods-lower Tuscaloosa trend, Southwest Mississippi. *Gulf Coast Association of Geological Societies Transactions* 37, 105–111.

John, C.J., Jones, B.L., Moncrief, J.E., Bourgeois, R., Harder B.J. (1997) An unproven unconventional seven billion barrel oil resource—The Tuscaloosa marine shale: Louisiana State University Basin Research Institute Bulletin 7, Baton Rouge, 22

Kim, S., Omur-Ozbeck, P., Dhanasekar, A., Prior, A., and Carlson, K., 2016. Temporal analysis of flowback and produced water composition from shale oil and gas operations: Impact on frac fluid characteristics. *Journal of Petroleum Science and Engineering* 147, 202-210.

Kondash, A.J., Albright, E., and Vengosh, A., 2017. Quantity of flowback and produced waters from unconventional oil and gas exploration. *Science of the Total Environment*. 574, 314-321.

Mancini, E. A., Mink, R. M., Payton, J. W., & Bearden, B. L., 1987. Environments of deposition and petroleum geology of Tuscaloosa Group (Upper Cretaceous), South Carlton and Pollard fields, southwestern Alabama. *AAPG Bulletin*, 71(10), 1128-1142.

M. T. Taner, F. Koehler, and R. E. Sheriff, (1979), Complex seismic trace analysis, *GEOPHYSICS* 44: 1041-1063.

Parrikar, P., Mokhtari, M., Saidzade, A., 2021. Measurement of Deformation Heterogeneity During Shale Swelling Using Digital Image Correlation. *Journal of Energy Resources Technology*, 144(6), 063002.

Q. Passey, S. Creaney, J. Kulla, F. Moretti, and J. Stroud (1990) A practical model for organic richness from porosity and resistivity logs, *AAPG Bulletin*, 74 1777-1794.

R. Zhang, R. Ghosh, M.K. Sen, S. Srinivasan, 2013. Time-lapse thin-bed seismic inversion for $CO_2$ sequestration: a case study from Cranfield, Mississippi. *International Journal of Greenhouse Gas Control* 18 430-438.

Saller, A.H. and Steuber, A.M., 2018. Evolution or formation waters in the Permian Basin, United States: Late Permian evaporated seawater and Neogene meteoric water. *American Association of Petroleum Geologists Bulletin*, 102 (3), 401-428.

Spooner, H. V., 1964. Basal Tuscaloosa sediments, east-central Louisiana. *AAPG Bulletin* 48 (1), 1–21.

Van Oort, E. 2003. On the physical and chemical stability of shales. *Journal of Petroleum Science and Engineering*, 38 (3-4), 213-235.

Veil, J., 2012. U. S. produced water volumes and management practices in 2012. Prepared for the Ground Water Protection Council, Veil Environmental, LLC, April, 119

Vengosh, A., Kondash, A., Harkness, J., Lauer, N., Warner N., and Darrah, T.H., 2017. The geochemistry of hydraulic fracturing fluids. *Procedia Earth and Planetary Science*, 17, 21-24.

Whitley H.D., Smith D.E., 2004. Free energy, energy, and entropy of swelling in Cs–, Na–, and Sr–montmorillonite clays. *Journal of Chemical Physics*, 120, 5387.

Womack, R., 1950. Brookhaven oil field, Lincoln County, Mississippi. *AAPG Bulletin* 34 (7), 1517–1529.

Zhang, Y., Gable, C.W., Zyvoloski, G.A., and Walter, L.M., 2009. Hydrogeochemistry and gas compositions of the Uinta Basin: A regional-scale overview. *American Association of Petroleum Geologists Bulletin*, 93 (8), 1087-1118.

Zoeppritz, Karl (1919). "VIIb. Über Reflexion und Durchgang seismischer Wellen durch Unstetigkeitsflächen."

# CHAPTER 4 Characterization TMS with Digital Image Correlation (DIC) System

## 4.1 Introduction

Strain is one of key parameters in the evaluation of rock mechanical properties. To measure the strain, the typical method in the petroleum industry is the application of strain gauges. Attachment of strain gauges is the routine procedure in petroleum rock mechanics or in oilfield cementing laboratories. However, there are several shortcomings with this technique. The quality of data from such sensitive sensors largely depend on the quality of attachment. Anybody having experience with strain gauges knows what challenging work is the preparation and the attachment of strain gauges and at the end, the quality of data might be questionable with a minor attachment issue. Moreover, the data collection is restricted to the point of strain gauge attachment rather than full-field measurement.

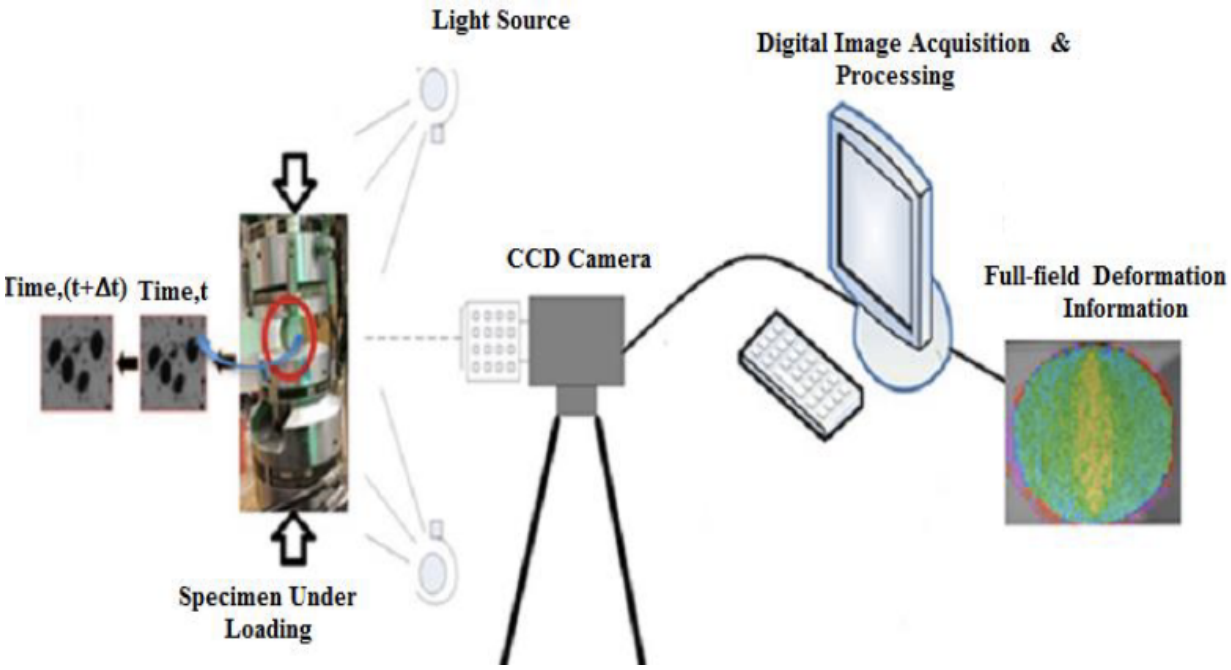


**Figure 4.1 Digital Image Correlation System.**

To overcome these challenges, optical methods for strain measurement have recently gained significant attention in mechanical engineering. Digital Image Correlation (DIC) is based on high-speed camera recording of object monitoring the random contrast speckle pattern painted at facing surface of the specimen (Fig. 4.1). Camera captures images depending on the speed of the camera. The stereoscopic camera set up provides a series of virtual strain gauges. Stereo-correlation between the images allows calculation of the sample position and deformation U/V/W (measured

in mm or pixels) as crack opening occurs. Local derivative calculations provide Lagrangian strain tensor profiles $\sigma_{xx}/\sigma_{yy}/\sigma_{zz}$ (measured in micro-strain, mm/mm, or %) across the entire surface under analysis. In this study, a digital image correlation system is constructed in our laboratory and is used to characterize TMS properties such as geomechanical properties, fracture toughness, and fracture creep.

## 4.2 Uniaxial Compression tests on TMS using Digital Image Correlation

Uniaxial tests are widely used to measure the strength of shale in compression. Uniaxial Compressive Strength (UCS) and elastic constants are measured in these tests. The strains are usually measured using conventional measurement techniques like LVDT and strain gauges. However, these measurements cannot provide any measurement of deformation distribution in the specimen. In this study, we employed digital image correlation (DIC) to measure specimen deformation during uniaxial compression. DIC is a versatile non-contact measurement technique developed for capturing deformations over the surface, providing deformation measurement and spatial variations in deformation of specimens in this study.

### *4.2.1 Experimental setup*

13 specimens were prepared from two TMS wells. Two specimen orientations, bedding plane-parallel, and perpendicular with respect to loading direction were investigated. Specimens with nominal dimensions of 1″ × 1″ cross-section and 2″ length were prepared. The exact dimensions of all specimens along with their mineralogy and depth are shown in Table 4.1. Figure 4.2 shows some of the specimens and their distinct laminar nature.

**Table 4.1** Specimen orientation, depth and mineralogy.

| Specimen No. | Orientation | Depth (ft) | Width (in) | Breadth (in) | Height (in) | Carbonate (wt. %) | Tectosilicate (wt. %) | Clay (wt. %) |
|---|---|---|---|---|---|---|---|---|
| 1 | Parallel | 12553.1 | 0.86 | 0.953 | 1.997 | 38 | 27 | 35 |
| 2 | Parallel | 12559.8 | 1.03 | 1.19 | 2.1 | 14 | 23 | 63 |
| 3 | Parallel | 12501.5 | 0.85 | 0.96 | 1.66 | 23 | 21 | 56 |
| 4 | Parallel | 12198.4 | 0.965 | 0.976 | 1.995 | 15 | 30 | 55 |
| 5 | Parallel | 12561.7 | 0.84 | 0.97 | 2.17 | 4 | 41 | 55 |
| 6 | Parallel | 15223 | 0.79 | 0.96 | 2.09 | 6 | 32 | 62 |
| 7 | Parallel | 15049.44 | 0.75 | 0.89 | 1.94 | 9 | 33 | 58 |
| 8 | Parallel | 15196.5 | 1.033 | 0.955 | 1.994 | 3 | 36 | 61 |
| 9 | Perpendicular | 12552 | 1.021 | 0.898 | 1.7 | 2 | 34 | 64 |
| 10 | Perpendicular | 12591.6 | 1 | 0.9 | 1.5 | 29 | 31 | 40 |
| 11 | Perpendicular | 12592 | 0.94 | 0.966 | 1.7 | 29 | 31 | 40 |
| 12 | Perpendicular | 15206.3 | 0.84 | 0.9 | 1.59 | 55 | 29 | 16 |
| 13 | Perpendicular | 12553.1 | 0.936 | 0.947 | 1.746 | 17 | 23 | 60 |

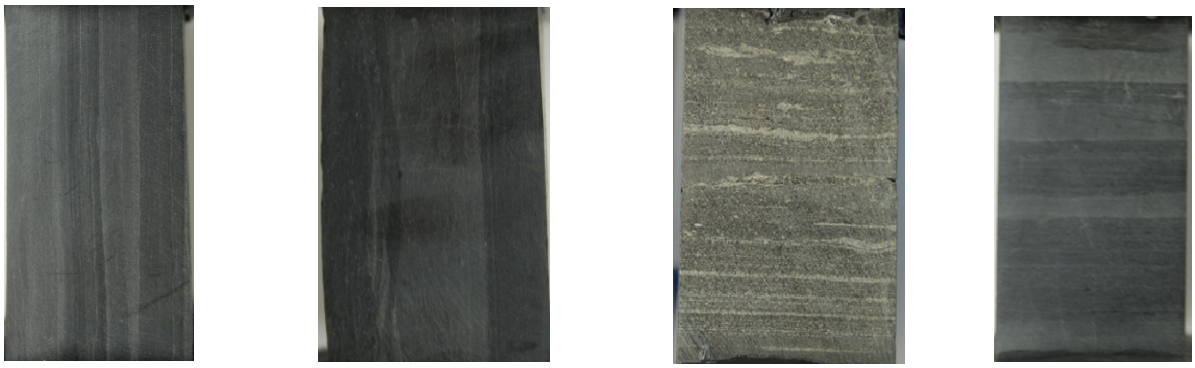

(a) (b) (c) (d)

**Figure 4.2 Specimen pictures showing laminar nature of TMS**

**(a) Specimen 4, (b) Specimen 8, (c) Specimen 9, (d) Specimen 12**

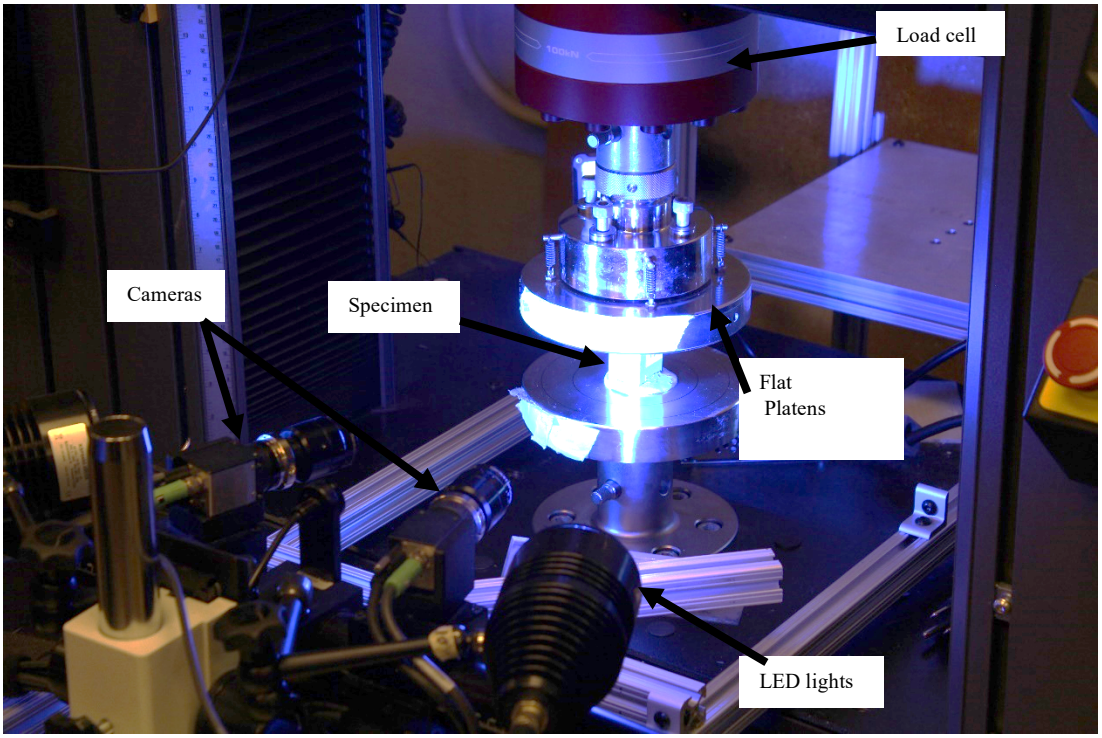


**Figure 4.3 Loading equipment and DIC setup.**

Instron 5982 (100 KN load cell) was used to apply compressive loading during the experiment. Flat loading platen with top platen equipped with a universal ball joint was used to compress the specimens. To ensure the flatness of the specimen surface during compression, a Sulphur capping compound was applied to the specimen ends. The specimens are compressed at a constant rate of 0.15 mm/min. The effect of the orientation of bedding planes on compressive properties was investigated. The DIC system consists of two 12 MP digital cameras connected to a computer and blue LED lights (Fig. 4.3). A random black and white speckle pattern were applied to the specimen surface using flat paint. The cameras captured deformation images of these painted faces of the specimen at 1 Hz frequency. The images were analyzed using commercial DIC software (ARAMIS 2019). The DIC analysis was conducted using a subset size of 40 pixels and a point distance of 15 pixels. Field of view used was 76 mm × 56 mm. Displacement accuracy of 0.2 µm was achieved in these experiments.

### *4.2.2 Tensile and Uniaxial Compressive Strength of TMS Cores*

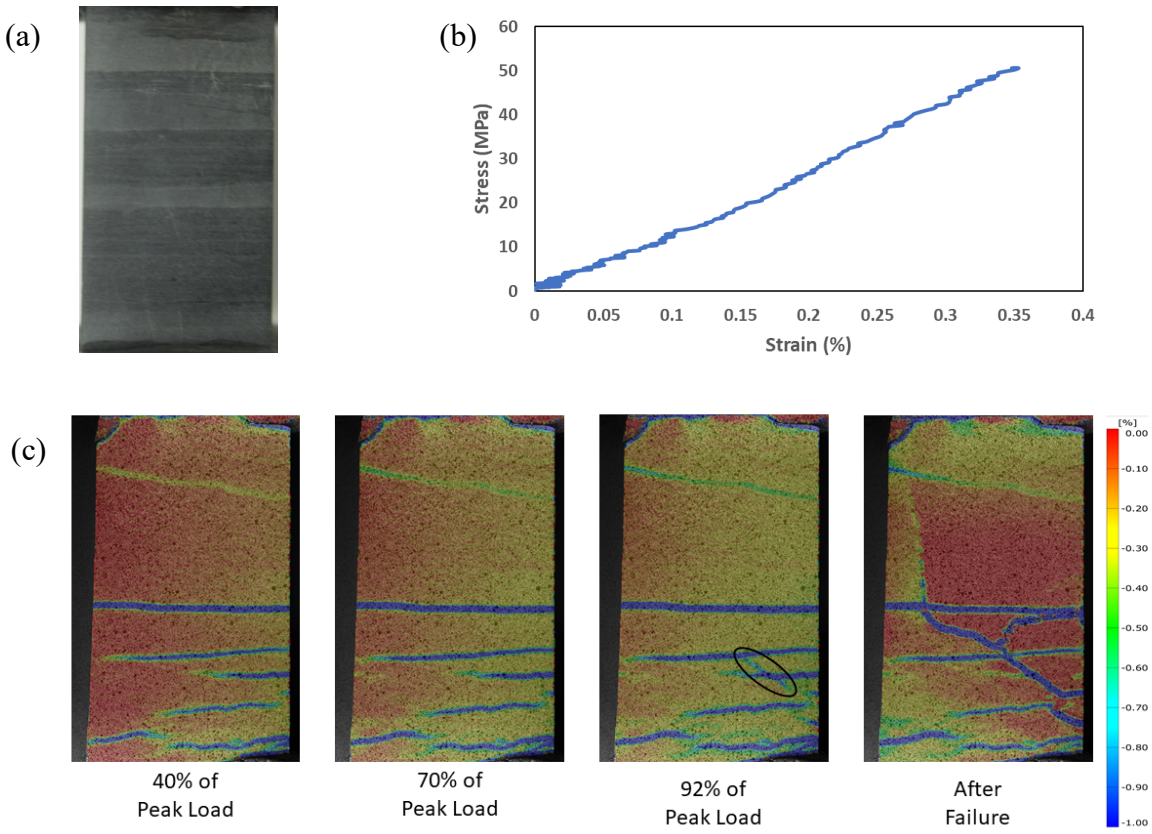


**Figure 4.4 Compression of a bedding perpendicular specimen (a) picture of specimen laminations (b) Stress-strain curve (c) Full field pictures of vertical normal strain using DIC.**

Uniaxial compression experiments were performed on TMS specimens. DIC images were analyzed to obtain full-field strains on the specimen surface. TMS specimens are very heterogeneous and their deformation is governed by the features present in the specimen. Figure 4.4 shows deformation analysis conducted on a specimen with laminations perpendicular to the loading axis. The stress was calculated using the load measure in the Instron machine. The strain presented in the stress-strain curve is the average strain computed over the specimen surface using DIC. The full field images of vertical normal strain show spatial strain variation and influence of mineralogy variations in the laminations. The blue regions indicate soft laminations that compress to large strains with red regions indicating stiff laminations that undergo lower deformation. The strain increases in all the layers with increasing load. In this specimen, at 92% load, additional localization of deformation was captured near the interface of one of the soft laminations (marked in a bubble). This localized deformation arises from the incompatibility of high and low strain region interface and then developed into a crack that leads to specimen failure. Other bedding perpendicular specimens displayed similar strain localizations arising near stiff and soft lamination interfaces, which then led to the specimen failure.

Figure 4.5 shows deformation analysis conducted on a specimen with laminations parallel to the loading axis. The stress in the stress-strain plot was calculated using applied load and the strain presented is the average vertical normal strain measured on the specimen surface using DIC. The full-field strain map of horizontal and vertical normal strains is also shown. The vertical normal strain is very uniform in the specimens with bedding planes parallel to the loading axis. The image of horizontal normal strain shows localization of tensile strain along lamination boundaries at low loads while vertical normal strain remains uniform. At peak load, multiple sites of high localized tensile strains along lamination boundaries can be seen. After this point, the specimen undergoes failure by delamination. All specimens with bedding planes parallel to the loading axis exhibited delamination failure during uniaxial loading.

The peak loads during the uniaxial compression test were used to calculate UCS and the slopes of the stress-strain plot were used to measure Young's modulus. The obtained values are shown in Table 4.2. Clay content is considered to have a large impact on material strength and properties. The UCS and modulus were plotted against clay content and also as a function of orientation in Fig 4.6.

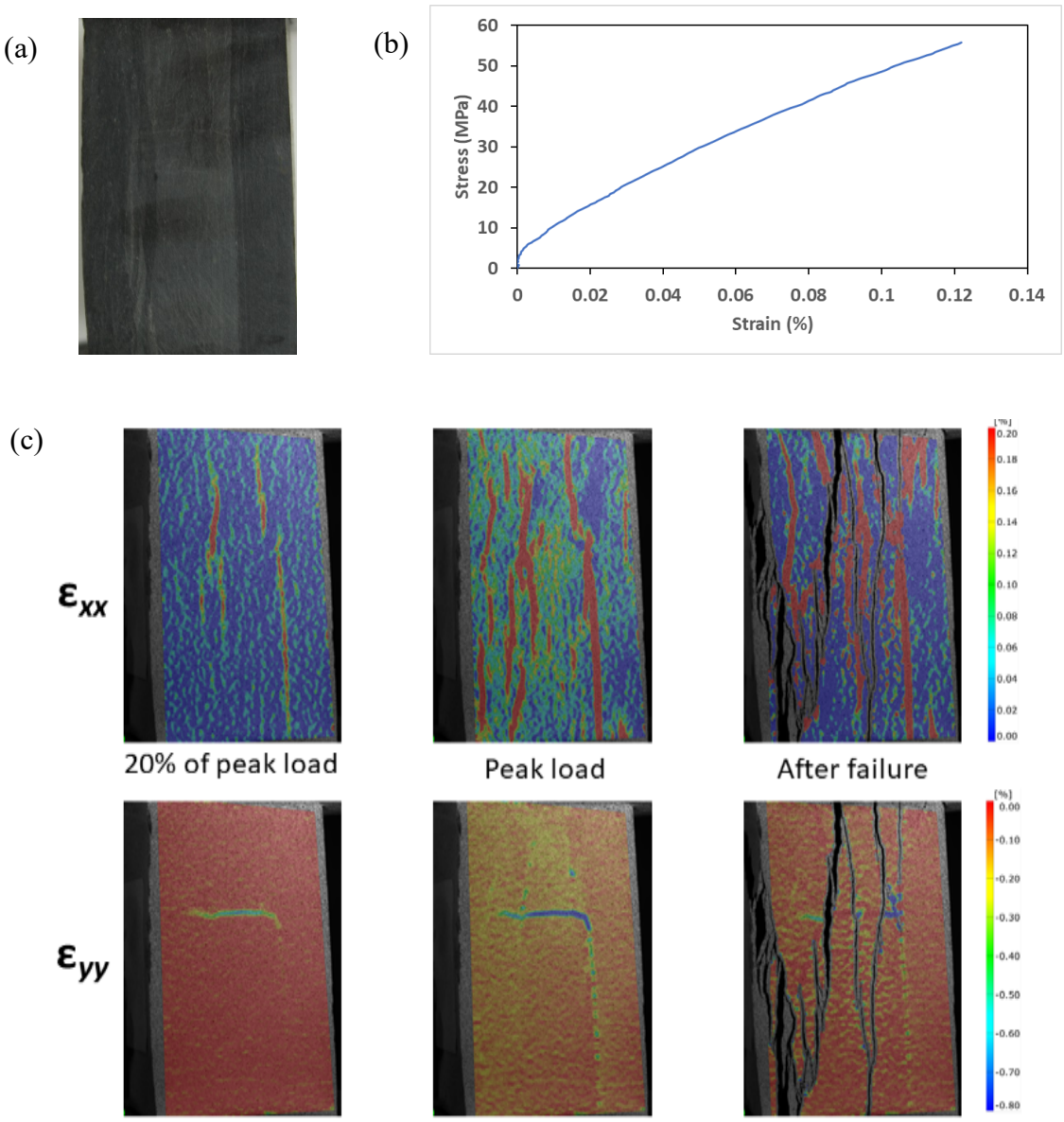


**Figure 4.5 Compression of a bedding parallel specimen (a) picture of specimen laminations (b) Stress-strain curve (c) Full field pictures of horizontal normal strain and vertical normal strain using DIC.**

**Table 4.2** Measured UCS and Young's Modulus.

| Specimen No. | Orientation | UCS (MPa) | Young's Modulus (GPa) |
|---|---|---|---|
| 1 | Parallel | 49.77 | 41.80 |
| 2 | Parallel | 27.52 | 29.31 |
| 3 | Parallel | 64.10 | 45.85 |
| 4 | Parallel | 48.52 | 34.99 |
| 5 | Parallel | 41.98 | 45.78 |
| 6 | Parallel | 47.43 | 49.31 |
| 7 | Parallel | 43.30 | 47.38 |
| 8 | Parallel | 55.71 | 47.72 |
| 9 | Perpendicular | 37.71 | 28.38 |
| 10 | Perpendicular | 27.07 | 28.77 |
| 11 | Perpendicular | 50.68 | 14.31 |
| 12 | Perpendicular | 103.34 | 31.28 |
| 13 | Perpendicular | 52.37 | 17.91 |

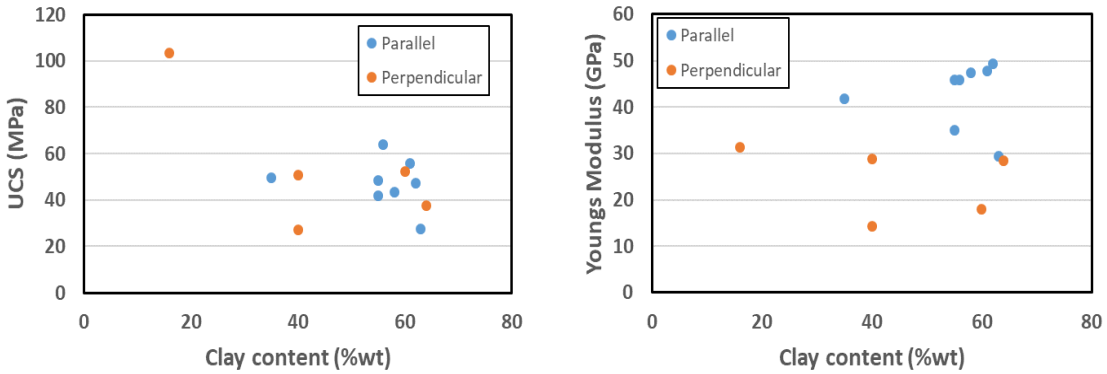


**Figure 4.6 UCS and Modulus as a function of clay content and specimen bedding plane orientation.**

The average UCS in bedding parallel specimens was 47.29 MPa and in bedding perpendicular specimens was 54.24 MPa. The amount of clay content does not affect UCS significantly. This may be because soft and stiff layer distribution is relatively similar in all the specimens. The orientation of bedding planes also does not affect the UCS. The modulus in specimens with bedding planes perpendicular to the loading was lower than the specimens with bedding planes parallel to loading. The average Young's modulus in bedding perpendicular specimens was 24.13 GPa and in bedding parallel specimens was 42.77 GPa. This can be attributed to the orientation of clay particles at the microscopic level as well as the presence of cracks along bedding planes that are easy to compress. The Young's modulus was not sensitive to clay content in specimens with bedding planes perpendicular to the loading axis.

### 4.3 Measurement of Fracture Toughness in TMS with DIC

Fracture toughness it the ability of material to resist propagation of preexisting cracks or flaws. Studies have shown that fracture toughness can vary greatly with respect to specimen size and configuration. In this case, it is referred to as critical Stress Intensity Factor (SIF) or the apparent fracture toughness of material. The dependency of the apparent fracture toughness on specimen size is caused by the presence of Fracture Process Zone (FPZ) at the crack tip. Theoretically, measuring intrinsic fracture toughness using equations derived based on Linear Elastic Fracture Mechanics (LEFM) requires an infinitely large sample to eliminate the effect of the FPZ. Fracture process zone (FPZ) is a zone of microcracking that surrounds a tip of the crack and it develops with an increase in load. This phenomenon causes inelastic softening deformation of the sample; thus it cannot be accurately described by the Linear Elastic Fracture Mechanics (LEFM). For that reason, standard LEFM fracture toughness equations that are based on peak load ($P_{max}$) are not efficient in estimating fracture toughness of samples that are affected by the FPZ.

In this work, DIC is integrated with the semi-circular bend test (SCB) to measure Mode I fracture toughness of TMS. Then, FPZ length is quantified using DIC, and Irwin's approach is utilized to obtain fracture toughness values from the SCB test that account for nonlinear behavior. Also, the full-field displacements obtained by the DIC are utilized to calculate fracture toughness using Williams' expansion series and over-deterministic least square method. Two sets of fracture toughness values are then compared, showing a good match for TMS samples.

#### *4.3.1 Semi-circular Bend Test*

SCB test is used to determine Mode I fracture toughness (Fig. 4.7). During the Mode I test, the tensile stress field develops ahead of the crack tip. $K_I$, or Mode I stress intensity factor (SIF), is a term that describes the stress field state around the tip of the notch. Under quasi-static conditions and pure Mode I deformation, the critical value of the SIF is the Mode I fracture toughness. For the semi-circular bend test, $K_{IC}$ can be measured using Equation 1

$$K_{IC} = \frac{Y' P_{max} \sqrt{\pi a_0}}{2RB} \qquad (1)$$

Where $P_{max}$ is peak load, R is radius, B is thickness, $a_0$ is initial notch length, S is support span and Y' is non-dimensional stress intensity factor defined as (Kuruppu et al. 2013):

$$Y' = -1.297 + 9.516\left(\frac{S}{2R}\right) - \left(0.47 + 16.457\left(\frac{S}{2R}\right)\right) * \frac{a_0}{2R} + \left(1.071 + 34.401\left(\frac{S}{2R}\right)\right)\left(\frac{a_0}{2R}\right)^2$$

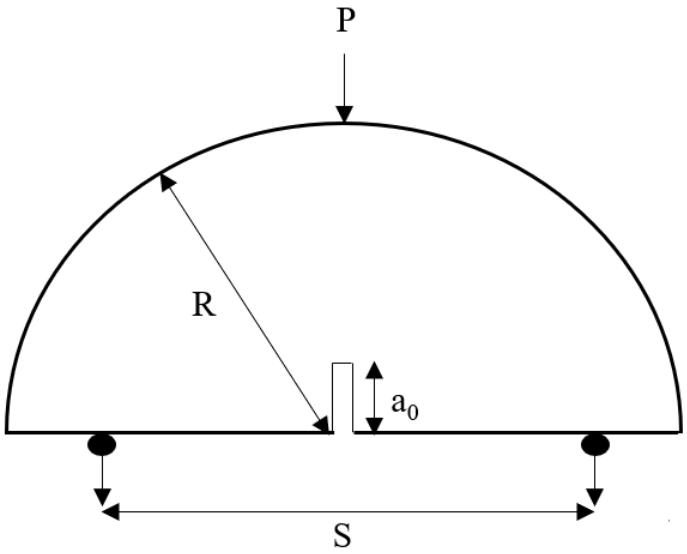


**Figure 4.7 Schematics of the SCB test.**

Because presence of nonlinear behavior affects fracture toughness results, Irwin (1961) proposed to use a term "effective notch length" to correct the values. For the SCB test, fracture toughness solution with Irwin's correction becomes:

$$K_{IC}^{IRW} = \frac{Y' P_{max}\sqrt{\pi a_{eff}}}{2RB} \quad (2)$$

$$a_{eff} = a_o + r_y \quad (3)$$

where $r_y$ is plastic zone size. For rocks, $r_y$ is the length Fracture Process Zone (FPZ), because nonlinear behavior in geologic materials is caused by subcritical cracking and not by plasticity. $r_y$ is determined using DIC and used to correct fracture toughness using Equation 2. Subsequently, non-dimensional stress intensity factor $Y'$ is calculated using $a_{eff}$. Fracture toughness calculated using Equation 2 is the inherent fracture toughness.

Digital Image Correlation (DIC) is a non-contact measurement technique, in which pixel intensity is measured before and after deformation. This allows for visualization of a full-field displacement during rock testing. Using speckling technique, groups of pixels are united into subsets. After material undergoes deformation, the subset from the reference image is matched with a subset from the deformed image. After subsets are matched, relative displacement between the center of a subset from reference image and the center of the subset from deformed image is calculated by

DIC. This allows for a full-field displacement and strain calculations. Equations 4 and 5 are used to measure displacement of each subset.

$$x' = x_0 + \Delta x + u + \frac{\partial u}{\partial x}\Delta x + \frac{\partial u}{\partial y}\Delta y \quad (4)$$

$$y' = y_0 + \Delta y + v + \frac{\partial v}{\partial x}\Delta x + \frac{\partial v}{\partial y}\Delta y \quad (5)$$

The horizontal ($u$) and vertical ($v$) displacement of any point near the crack tip can be described using Williams' series solution shown in Equations 6 and 7.

$$u = \sum_{n=1}^{N} \frac{A_{In}}{2G} r^{\frac{n}{2}} \left\{\kappa cos\left(\frac{n}{2}\theta\right) - \frac{n}{2} cos\left(\frac{n}{2} - 2\right)\theta + \left\{\frac{n}{2} + (-1)^n cos\left(\frac{n}{2}\right)\theta\right\} - \right. \quad (6)$$

$$\left. - \sum_{n=1}^{N} \frac{A_{IIn}}{2G} r^{\frac{n}{2}} \left\{\kappa \sin\left(\frac{n}{2}\theta\right) - \frac{n}{2} sin\left(\frac{n}{2} - 2\right)\theta + \left\{\frac{n}{2} - (-1)^n\right\} * sin\left(\frac{n}{2}\theta\right)\right\} + T_x - Ry \right.$$

$$v = \sum_{n=1}^{N} \frac{A_{In}}{2G} r^{\frac{n}{2}} \left\{\kappa \sin\left(\frac{n}{2}\theta\right) + \frac{n}{2} sin\left(\frac{n}{2} - 2\right)\theta - \left\{\frac{n}{2} + (-1)^n sin\left(\frac{n}{2}\right)\theta\right\} - \right. \quad (7)$$

$$\left. - \sum_{n=1}^{N} \frac{A_{IIn}}{2G} r^{\frac{n}{2}} \left\{-\kappa cos\left(\frac{n}{2}\theta\right) - \frac{n}{2} cos\left(\frac{n}{2} - 2\right)\theta + \left\{\frac{n}{2} - (-1)^n\right\} * cos\left(\frac{n}{2}\theta\right)\right\} + T_y + Rx \right.$$

Where G is Shear Modulus, ν is Poisson's ratio, $r$ and θ are polar coordinates of the point with respect to crack tip and $n$ is the number of terms in solution. $A_{I1}$and $A_{II1}$ are unknowns that depend on loading conditions. Because plain stress conditions require extremely thin samples, for rocks it is easier to achieve conditions that are similar to plain strain. For this reason, plain strain κ of 3-4ν is used. Terms $T_x$, $T_y$ and $R$ are added to account for horizontal and vertical translation, and rotation respectively.

Terms $A_{I1}$ and $A_{II1}$ can be related to Mode I ($K_I$) and Mode II ($K_{II}$) stress intensity factors through Equations 8 and 9.

$$A_{I1} = \frac{K_I}{\sqrt{2\pi}} \quad (8)$$

$$A_{II1} = -\frac{K_{II}}{\sqrt{2\pi}} \quad (9)$$

Equation 10 is a condensed form of Equation 6 and 7 for a particular point $k$ with polar coordinates $r_k$, $\theta_k$ (shown in Fig 3),where $f_I$, $f_{II}$, $g_I$ and $g_{II}$ are known functions of a point $k$.

$$u_k = \sum_{n=1}^{N}(A_{In}f_{In}(r_k,\theta_k)) - \sum_{n=1}^{N}(A_{IIn}f_{IIn}(r_k,\theta_k)) + T_x - Ry_k$$

$$v_k = \sum_{n=1}^{N}(A_{In}g_{In}(r_k,\theta_k)) - \sum_{n=1}^{N}(A_{IIn}g_{IIn}(r_k,\theta_k)) + T_y + Rx_k \quad (10)$$

These equations can be rewritten in a matrix form to account for multiple points at the time. Assuming that M is a number of points and N is a number of terms used, Equation 11 is obtained.

$$h = b * \Delta, \quad (11)$$

Where

$$h = \begin{bmatrix} u_1 \\ \vdots \\ u_m \\ v_1 \\ \vdots \\ v_m \end{bmatrix}, \quad b = \begin{bmatrix} f_{I1}(r_1\theta_1) & \cdots & -f_{II1}(r_1\theta_1) & \cdots & 1 & 0 & -y_1 \\ \vdots & \ddots & \vdots & \ddots & \vdots & \vdots & \vdots \\ f_{I1}(r_M,\theta_M) & \cdots & -f_{II1}(r_m,\theta_m) & \cdots & 1 & 0 & -y_M \\ g_{I1}(r_1\theta_1) & \cdots & -g_{II1}(r_1\theta_1) & \cdots & 0 & 1 & x_1 \\ \vdots & \ddots & \vdots & \ddots & \vdots & \vdots & \vdots \\ g_{I1}(r_M,\theta_M) & \cdots & -g_{II1}(r_m,\theta_m) & \cdots & 0 & 1 & x_M \end{bmatrix}, \Delta = \begin{bmatrix} A_{I1} \\ \vdots \\ A_{II1} \\ \vdots \\ T_x \\ T_y \\ R \end{bmatrix}$$

Equation 12 shows a least square solution to solve for the unknown Δ and evaluate $A_{In}$ and $A_{IIn}$.

$$[\Delta] = \left[[b]^T[b]\right]^{-1}[b]^T[h] \quad (12)$$

The full-field displacements obtained from the DIC are used in William's series solution to measure mode I SIF of the samples. Subsequently, full-field displacements taken at the peak load, provide critical value of the SIF, denoted in this work as $K_{IC}^{DIC}$. In this work, only Mode I fracture toughness is discussed. It is important to note that the length of the FPZ is not incorporated in the DIC solution, i.e., original crack tip location is used in the calculations of fracture toughness using DIC displacements.

### *4.3.2 Experimental Setup*

11 Tuscaloosa Marine Shale specimens with notches in Arrester orientation were prepared from cores provided by Goodrich Petroleum. Dimensions of all samples are shown in Table 4.3. Figure 4.8 show some of the tested samples.

**Table 4.3** Dimensions and depths of TMS samples.

| Tuscaloosa Marine Shale | | | | | |
|---|---|---|---|---|---|
| Sample | D(mm) | B(mm) | R(mm) | a(mm) | Depth (ft) |
| TMS-1 | 36.98 | 24.59 | 18.59 | 6.81 | 15135 |
| TMS-2 | 36.63 | 24.89 | 16.05 | 4.95 | 15135 |

| | | | | | |
|---|---|---|---|---|---|
| TMS-3 | 36.58 | 21.59 | 17.53 | 6.60 | 15140 |
| TMS-4 | 36.83 | 21.34 | 17.53 | 6.99 | 15140 |
| TMS-5 | 36.45 | 29.29 | 17.53 | 5.44 | 15148 |
| TMS-6 | 37.74 | 24.43 | 17.22 | 5.21 | 15161 |
| TMS-7 | 37.34 | 20.85 | 18.06 | 6.10 | 15194 |
| TMS-8 | 37.16 | 20.08 | 17.06 | 5.60 | 15194 |
| TMS-9 | 36.58 | 20.83 | 17.02 | 5.08 | 15214 |
| TMS-10 | 36.58 | 25.40 | 17.02 | 6.35 | 15216 |
| TMS-11 | 36.83 | 23.37 | 17.53 | 6.60 | 15216 |

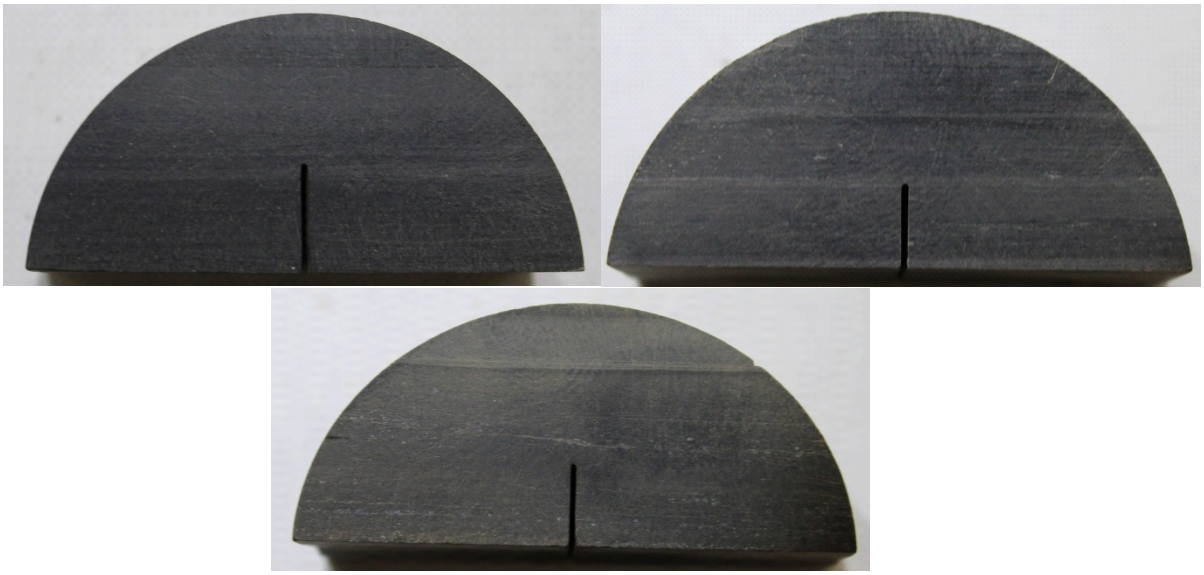

**Figure 4.8 Tuscaloosa Marine Shale samples.**

Shear Modulus was determined using Equation 14**.**

$$G = \frac{E}{2(1+\nu)} \tag{14}$$

For TMS samples, dynamic E and $\nu$ were obtained from sonic logs provided by Goodrich Petroleum. These values were normalized to obtain static values of these parameters. Shear Modulus was determined using Equation 14**.** Shear Modulus and Poisson's ratio for tested TMS samples is presented in Table 4.4.

**Table 4.4** Shear Modulus and Poisson's ratio values for TMS samples.

| Sample | G (GPa) | ν |
|---|---|---|
| TMS-1 | 7.774 | 0.229 |
| TMS-2 | 7.774 | 0.229 |
| TMS-3 | 7.684 | 0.235 |
| TMS-4 | 7.684 | 0.235 |
| TMS-5 | 8.531 | 0.225 |
| TMS-6 | 7.801 | 0.256 |
| TMS-7 | 9.770 | 0.240 |
| TMS-8 | 9.770 | 0.240 |
| TMS-9 | 8.485 | 0.172 |
| TMS-10 | 8.521 | 0.169 |
| TMS-11 | 8.521 | 0.169 |

### *4.3.3 Visualization and Development of Fracture Process Zone*

DIC is used to visually track development of FPZ during loading. In most of the samples, FPZ starts to develop almost at the peak load. Figure 4.9 shows FPZ development of sample TMS-5. FPZ is not observed on image "a" that was taken at 1356 N which is 87% of peak load. It starts developing at 1546 N which is 98% of peak load, depicted on image "b". Image "c" shows sample TMS-5 at 99.5% of peak load, showing fully developed FPZ. The sample does not fail completely right after reaching peak load, show on image "d" taken at 1523 N, or 97% of post peak load. After that, the sample fails, but the load does not immediately go to zero. Figure 4.10 presents load-displacement behavior of sample TMS-11. The sample does not exhibit FPZ at any point of the experiment. Absence of FPZ means sample has undergone no plastic deformation, or softening, meaning that it is extremely brittle, more brittle than the sample discussed above. Samples TMS-

5 and TMS-11 prove that TMS has a large degree of heterogeneity, and specimens that are located less than 70 ft apart can show different displacement behavior with respect to load.

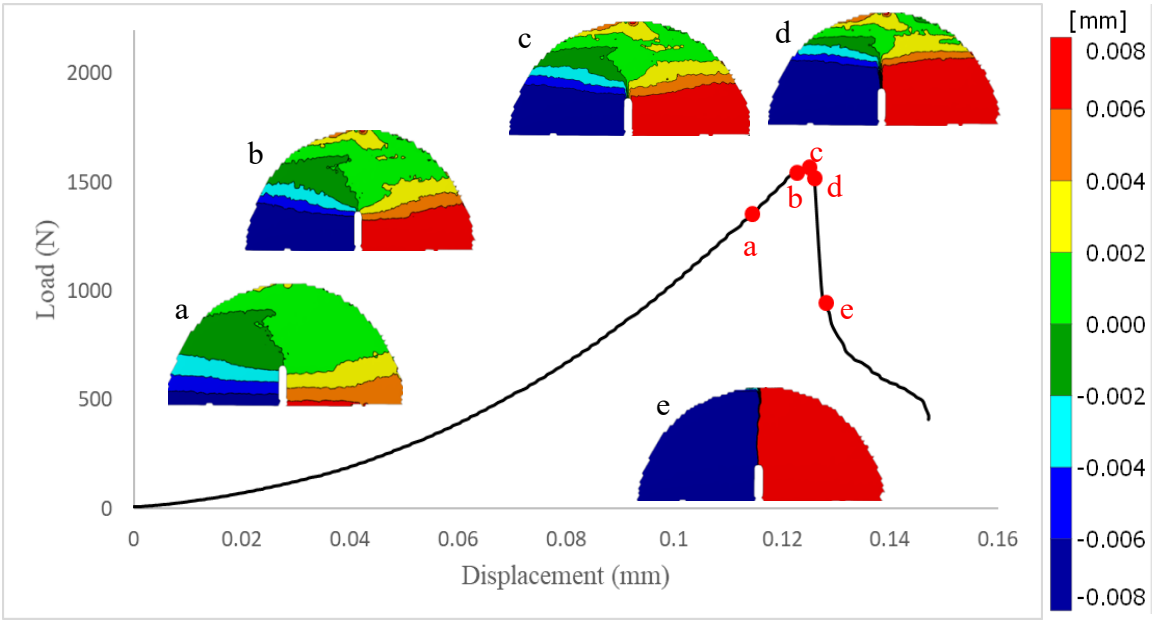


**Figure 4.9 Development of FPZ of sample TMS-5 during testing.**

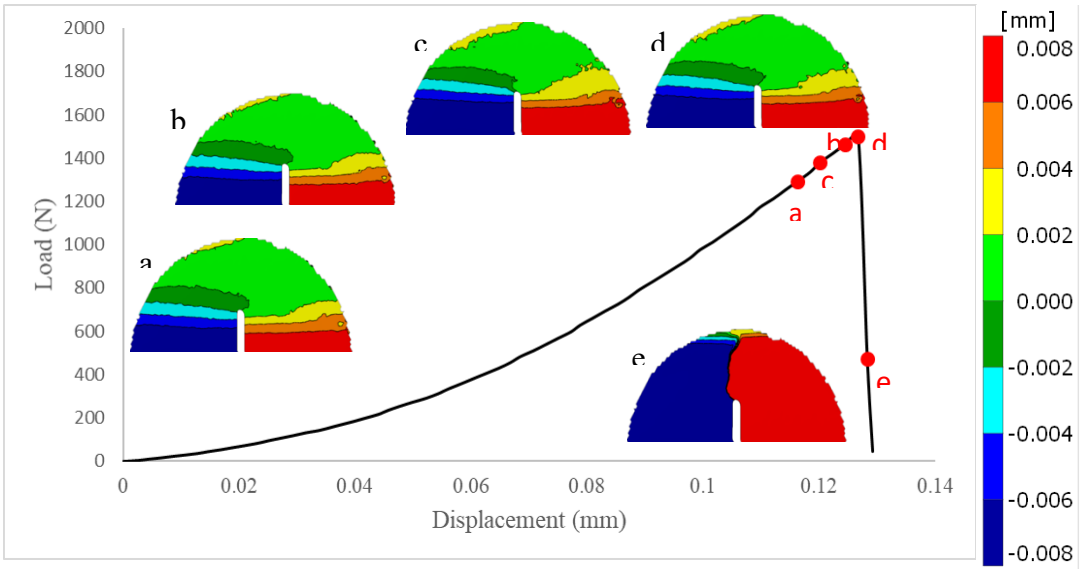


**Figure 4.10 Development of FPZ of sample TMS-11 during testing.**

Fully developed FPZ of Berea Sandstone, Mancos Shale and TMS samples with different notch orientation is presented in Fig. 4.11. TMS samples show a large variation in developed FPZ's: in some samples it is relatively straight, in some samples it deviates and it some samples it does not exist. The reason for deviation of FPZ in some samples is extreme heterogeneity of TMS. Difference in mechanical properties of materials can cause deviation of the FPZ. To measure crack tip opening displacement (CTOD), two points, 2 mm apart across the FPZ, are selected on the horizontal section right above the tip of the notch. The change in distance between these two points is CTOD. Measured length of FPZ's and CTOD's for each sample are listed in Table 4.5.

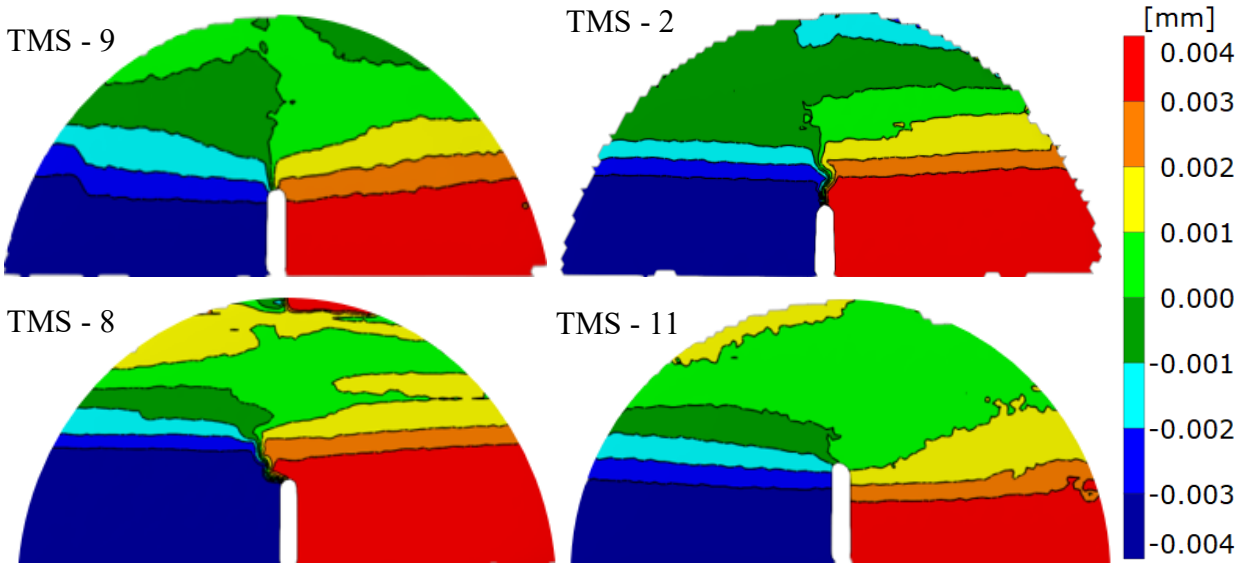


**Figure 4.11 Fully developed FPZ of samples TMS-9, TMS-2, TMS -8 and TMS-11.**

**Table 4.5** FPZ length and CTOD of Tuscaloosa Marine Shale.

| Tuscaloosa Marine Shale | | |
|---|---|---|
| Sample | FPZ (mm) | CTOD(mm) |
| TMS-1 | 3.0 | 0.006 |
| TMS-2 | 3.9 | 0.005 |
| TMS-3 | 0.3 | 0.009 |
| TMS-4 | 2.5 | 0.008 |
| TMS-5 | 3.4 | 0.009 |
| TMS-6 | 3.2 | 0.008 |
| TMS-7 | 3.5 | 0.008 |

| | | |
|---|---|---|
| TMS-8 | 3.0 | 0.009 |
| TMS-9 | 2.6 | 0.010 |
| TMS-10 | 1.7 | 0.009 |
| TMS-11 | 0.0 | 0 |
| Mean | 2.46 | 0.011 |
| SD | 1.29 | 0.006 |

### *4.3.4 Fracture Toughness Values*

Fracture toughness values were calculated using Irwin's approach of "effective notch length" shown in Equation 2. Figure 4.12 shows a comparison between original values (SCB), corrected values (SCB(c)) and values obtained from DIC solution for TMS. The average difference between corrected values and values obtained from numerical solution is 19.8%. In all cases, an improvement in relative matching accuracy is seen by using effective notch length. The difference between corrected values and values obtained by the DIC, can be explained by a few factors. Firstly, values for Shear Modulus and Poisson's ratio were obtained from normalized dynamic logs which could provide misleading readings. Secondly, extreme heterogeneity within samples implies that using a single Shear Modulus and a single Poisson's ratio for each sample might not be sufficient. Finally, presence of microfractures could provide discrepancies in displacements readings that could lower the accuracy of the DIC solution. All $K_{IC}$ values from the charts are presented in Table 4.6. All cases prove that nonlinear deformation affects results of SCB test and the values need to be corrected. On average, original SCB values are underestimated by 14.8% for Tuscaloosa Marine Shale in comparison to corrected SCB values. For some samples, this correction is more than 25%; because $K_{IC}$ values in downhole conditions are much larger, this difference could have a significant impact on hydraulic fracturing design.

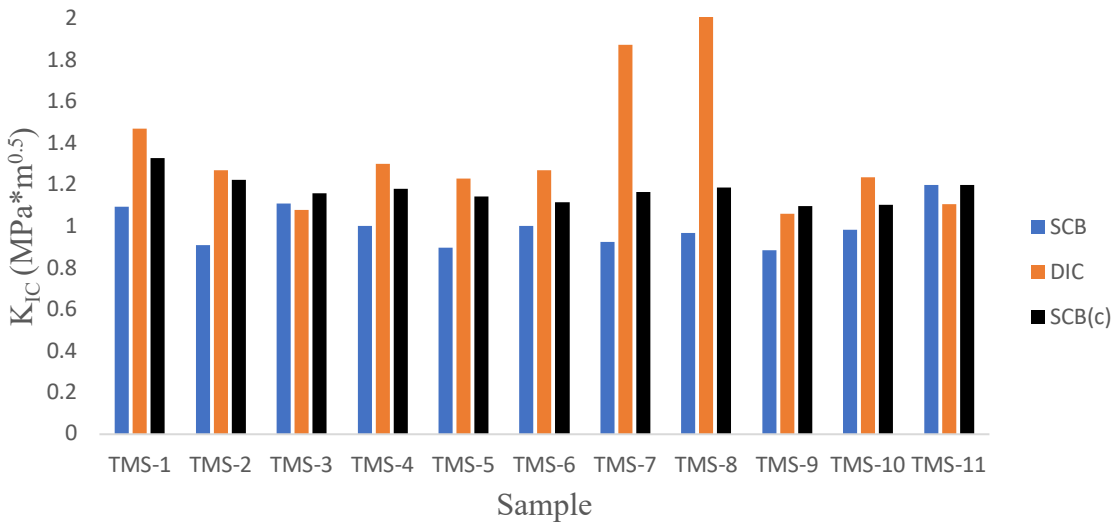


**Figure 4.12 Comparison between original $K_{IC}$ values obtain from SCB (SCB), corrected SCB values (SCB(c)) and values obtained using DIC solution for the TMS.**

**Table 4.6** Comparison of initial $K_{IC}$ values, corrected $K_{IC}$ values and $K_{IC}$ values obtained using DIC solution for Tuscaloosa Marine Shale.

| | SCB ($MPa*m^{0.5}$) | SCB(c) ($MPa*m^{0.5}$) | DIC ($MPa*m^{0.5}$) |
|---|---|---|---|
| TMS-1 | 1.10 | 1.33 | 1.47 |
| TMS-2 | 0.91 | 1.22 | 1.27 |
| TMS-3 | 1.11 | 1.16 | 1.08 |
| TMS-4 | 1.00 | 1.18 | 1.30 |
| TMS-5 | 0.90 | 1.14 | 1.23 |
| TMS-6 | 1.00 | 1.12 | 1.27 |
| TMS-7 | 0.93 | 1.16 | 1.87 |
| TMS-8 | 0.97 | 1.19 | 2.03 |
| TMS-9 | 0.89 | 1.10 | 1.06 |
| TMS-10 | 0.98 | 1.10 | 1.24 |
| TMS-11 | 1.20 | 1.31 | 1.11 |

### *4.3.5 Relation of Fracture Toughness and Fracture Process Zone to Mineralogy of the TMS*

Fracture toughness burst results (hollow cylinder), along with fracture toughness values obtained from the DIC and from corrected SCB test are plotted against the depth of the well, as shown in Fig. 4.13. All values are in Arrester Orientation. While most of the values lie withing the range of 0.8 MPa$*$m$^{0.5}$ to 2 MPa$*$m$^{0.5}$, some of the hollow cylinder test results exceed 4 MPa$*$m$^{0.5}$. Large variations in $K_{IC}$ results obtained from this test are caused by the variability in the magnitude of confining pressure applied to the specimens during the test. No clear relation between the depth of the sample and fracture toughness values is seen.

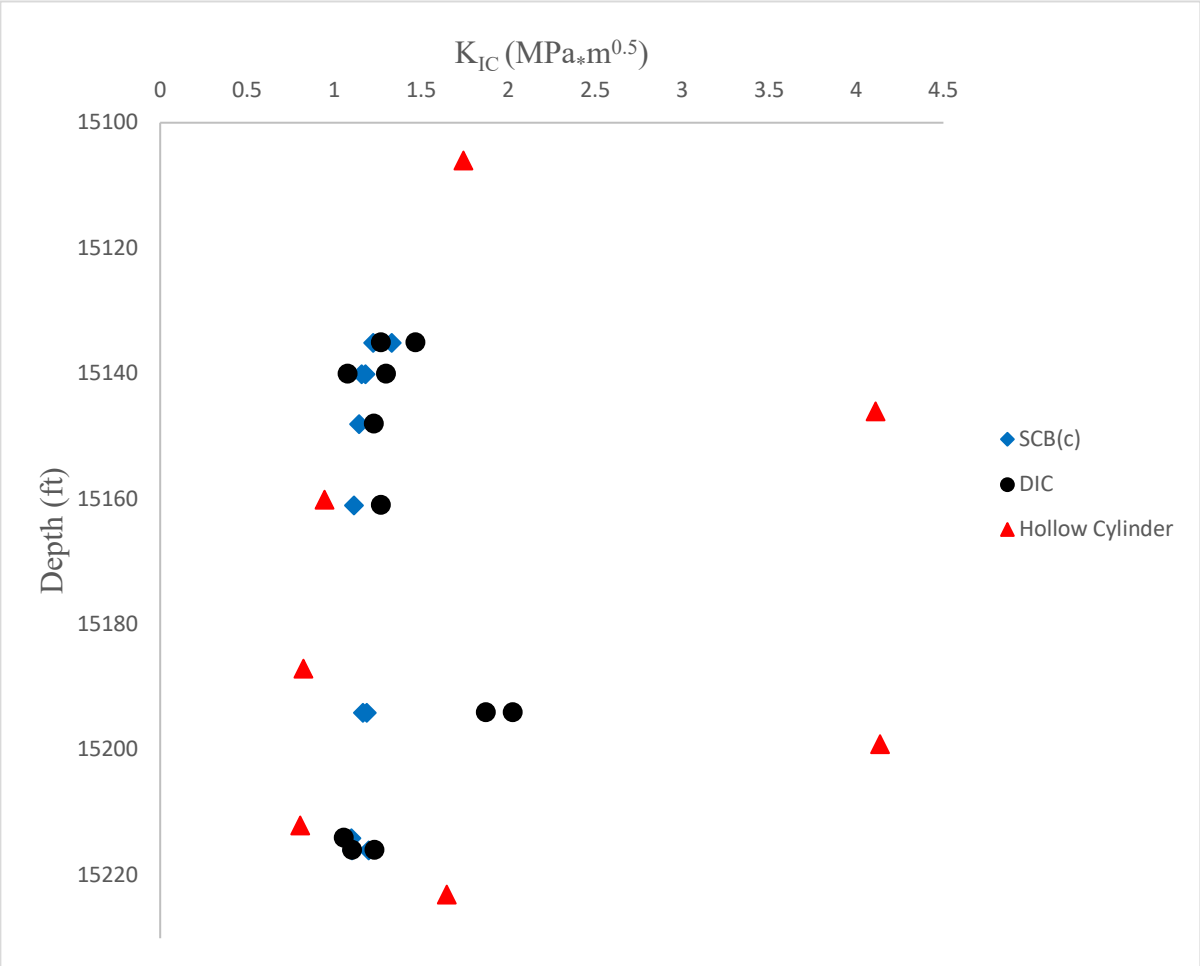


**Figure 4.13 $K_{IC}$ values of TMS using corrected SCB test, DIC and Hollow Cylinder test.**

To enhance understanding of fracture toughness and fracture properties of the TMS, $K_{IC}$ values and length of the FPZ are correlated to weight concentrations of quartz, calcite, clay and TOC. Some of the samples used in this study are extracted from the same depth. In this case, the average value is used. Overall matrix plot is shown in Fig. 4.14. Mineralogy for each depth is shown in Table 4.7.

Corrected $K_{IC}$ values have weak positive relation with weight concentrations of quarts and clay (r value ~ 0.25) and a stronger negative relation with calcite content with an r value of -0.605. It is expected to observe a negative relation with calcite for two reasons. Firstly, it is a brittle mineral and it will compress less under loading conditions than more ductile minerals like clay. Secondly, it is a weaker mineral than quartz and it requires smaller force to fracture. For these reasons, it is reasonable that calcite lowers fracture toughness of the specimens. $K_{IC}$ values obtained from DIC have some negative relation with weight concentrations of quartz and calcite (r value ~ -0.5 and -0.7) and some positive relation with clay content and TOC with r values of 0.64 and 0.6 respectively. DIC solution is based on horizontal and vertical displacements of the sample. Because both quartz and calcite are brittle they undergo smaller displacements, it may in lower $K_{IC}$ results. Clay and kerogen are more ductile, thus they contribute to larger displacements of the sample, which increases values obtained from the DIC solution. Both of the methods agree that calcite lowers $K_{IC}$ of the sample. Hollow cylinder test results have some positive relation with weight concentrations of quartz, calcite and TOC with r values ~ 0.53, and some negative relation with clay content with r value of -0.47. However, fracture toughness obtained from this test is dependent on the confining pressure applied to the sample. Because final confining pressures were different and the variation in $K_{IC}$ values is large, more experimental data is required to make a clear conclusion. Overall, results obtained from the DIC have stronger relation with the mineralogical composition, thus can be better described by it. Length of the FPZ shows a good correlation with clay content with r value of 0.697 and negative correlations with quarts and calcite content (r value of -0.323 and -0.560). It proves that clay increases ductility of the rock, increasing plastic deformation, or softening of the sample. In contrary, quartz and calcite make the specimen more brittle, reducing plastic deformation of the sample. Exact values of r for each correlation are listed in Table 4.8.

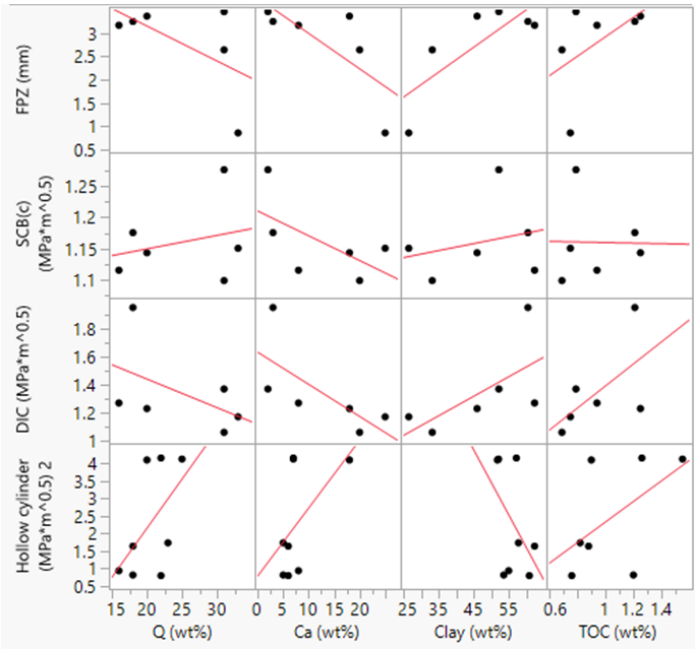


**Figure 4.14 Matrix plot showing relations of $K_{IC}$ and FPZ with mineralogy.**

**Table 4.7** Mineralogical composition at different depths.

| Depth (ft) | Q (wt%) | Calcite (wt%) | Clay (wt%) | TOC (wt%) |
|---|---|---|---|---|
| 15052 | 22 | 7 | 57.2 | 1.26 |
| 15106 | 23 | 5 | 57.8 | 0.82 |
| 15135 | 31 | 2 | 52.2 | 0.79 |
| 15146 | 20 | 18 | 51.8 | 0.9 |
| 15148 | 20 | 19 | 46 | 1.25 |
| 15160 | 16 | 8 | 60 | NA |
| 15161 | 16 | 8 | 62.4 | 0.94 |
| 15187 | 18 | 5 | 53.6 | 1.2 |
| 15194 | 18 | 3 | 60.5 | 1.21 |
| 15199 | 25 | 7 | 52.1 | 1.55 |
| 15212 | 22 | 6 | 60.9 | 0.76 |
| 15214 | 31 | 20 | 33.2 | 0.69 |
| 15216 | 33 | 25 | 26.5 | 0.75 |
| 15223 | 18 | 6 | 62.4 | 0.88 |

**Table 4.8** Correlation coefficients of weight content of minerals with respect to $K_{IC}$ and length of FPZ.

| | SCB(c) | DIC | Hollow cylinder | FPZ |
|---|---|---|---|---|
| Q (wt%) | 0.262 | -0.494 | 0.542 | -0.323 |
| Ca (wt%) | -0.605 | -0.699 | 0.531 | -0.560 |
| Clay (wt%) | 0.258 | 0.643 | -0.468 | 0.697 |
| TOC (wt%) | -0.017 | 0.601 | 0.539 | 0.158 |

## 4.4 Creep Behavior of TMS Core Sample Monitored with DIC Technique

### *4.4.1 Experimental Preparation*

The specimens were chosen based on their orientations and mineralogy as described in table 4.9 from the available core of two distinct wells A (Soterra) and B (Lane). The samples were all originated from the base of the Tuscaloosa formation.

**Table 4.9** TMS core samples for creep test.

| Orientation | Name | Carbonate (%) | Tectosilicate (%) | Clay (%) |
|---|---|---|---|---|
| Parallel | TMS A-1 | 14 | 23 | 63 |
| | TMS A-2 | 29 | 31 | 40 |
| | TMS A-3 | 23 | 21 | 56 |
| | TMS B-1 | 8 | 30 | 62 |
| | TMS B-2 | 15 | 30 | 55 |
| | TMS B-3 | 6 | 28 | 66 |
| Perpendicular | TMS A-4 | 27 | 31 | 42 |
| | TMS B-4 | 6 | 25 | 69 |
| | TMS B-5 | 17 | 23 | 60 |

Specimen preparation for creep tests followed the ISRM (International Society of Rock Mechanics) suggested methods for the creep characteristics of rock and the ASTM D7070 (American Society for Testing and Materials) standard test methods for creep of rock core under constant stress and temperature. Due to the low success rate of specimen preparation, the samples' shape was changed from cylindrical to cuboid and maintain the standard dimensions of height/length $\geq 1.7$ and $\leq 2.1$. After cutting, the loading faces of the samples needed to be flat to $\pm 0.001$ inch and parallel on both sides. To do that, capping was done those sides. The front face of the specimen with the better lamination was polished. Then, black and white flat paint was used

to spray white and black speckle patterns on that same front face for the image processing technique in DIC.

Multistage Uniaxial Compressional Compliance Creep Tests were performed on specimens in perpendicular and parallel direction. Prior to these tests, the peak load or ultimate strength of the specimens was determined at 46 MPa for the sample oriented in parallel direction and 69 MPa for the sample oriented in perpendicular direction. The peak loads were determined to have a general idea of where the ultimate strength of the specimens is. For the multistage creep test, the deviatoric stress was applied from 10 MPA to failure of the sample with an increment of 10 MPA for both directions. For the first step (10MPA), the sample was compressed at a constant rate of 0.6 MPa for 1 min until it reached 10 MPA and was held constant for 5 hours. Similarly, the other step followed the same method as the first until reaching the specimen failure. The displacement caused by the compressive force before and after deformation of the sample was recorded. Those displacement measurements are essential in the calculation of the strain determined by the software.

The multistage uniaxial compressional compliance creep test was used to get ample information about the creep behavior of the rock specimen. Constitutive equations have been developed to determine the stress and strain subject to creep. First, a law has been established to describe the creep curves approximately from their tangent lines (Fig. 4.15).

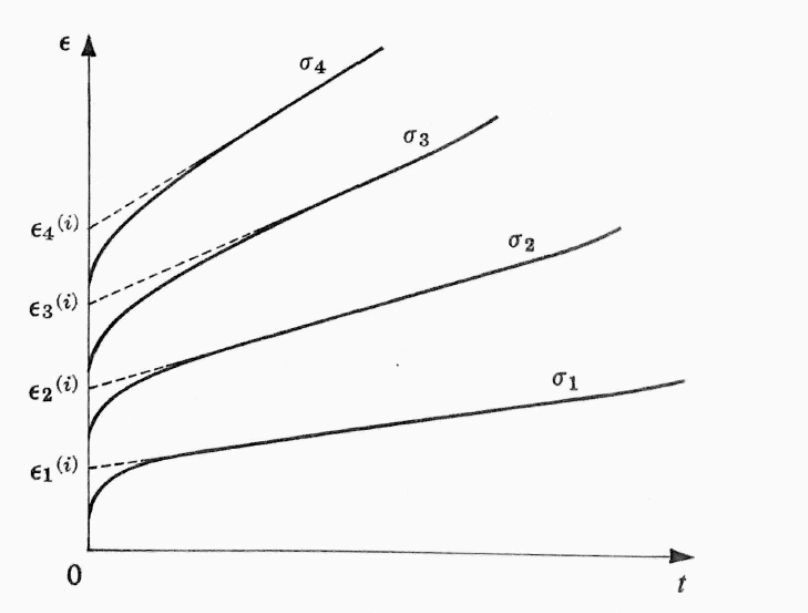


**Figure 4.15 Linearized creep curves (Hult, 1966).**

With those types of deductions, several errors were made because this law does not express properly the first stage of the creep process. However, those errors would be reduced greatly during continuous creep. Thus, the intercepts $\varepsilon^{(i)}$ and slopes $\frac{d\varepsilon}{dt}$ with σ as parameter will define the straight creep lines by:

$$\varepsilon = F(\sigma) + tG(\sigma)` \quad (1)$$

Where $\varepsilon^{(i)} = F(\sigma)$ and $\frac{d\varepsilon}{dt} = G(\sigma)$

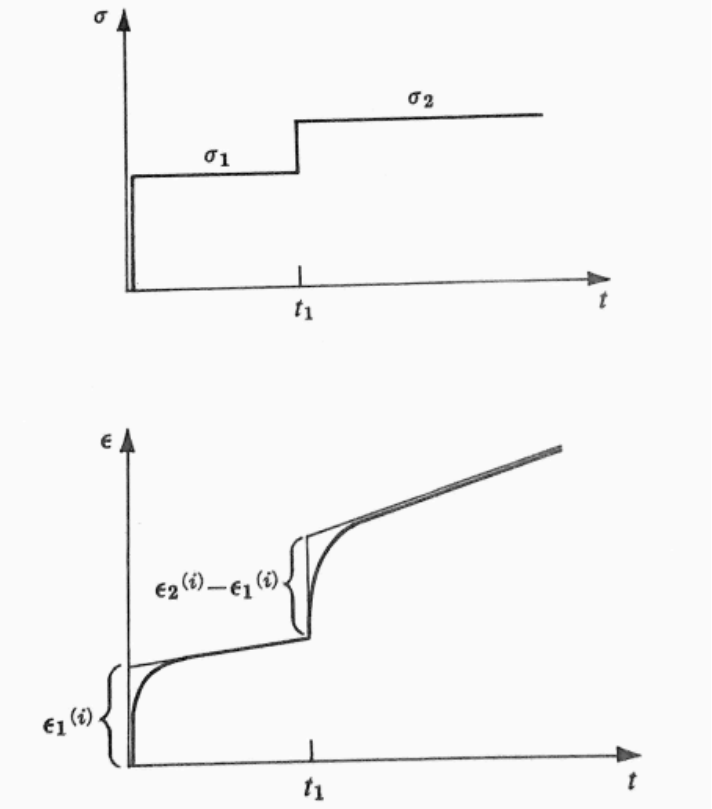


**Figure 4.16 Creep curve during multistage uniaxial compressional compliance creep test (Hult, 1966).**

As Hult presented in Fig. 4.16, during a test, when a stress level is increasing from $\sigma_1$ to $\sigma_2$ at a period $t_1$, the incremental strain theory can be expressed as:

$$\Delta\varepsilon \backsimeq \Delta F(\sigma) \quad (2)$$

Where $\Delta F$ is the change F corresponding to $\Delta\sigma$.

Therefore, (1) will be:

$$\Delta\varepsilon = \Delta F(\sigma) + t_1 \Delta G(\sigma) \quad (3)$$

From Fig. 4.16, it could also be predicted that the total strain developed in any rock specimen can be written as a sum of instantaneous elastic strain and creep strain.

$$\varepsilon = \varepsilon^{(i)} + \varepsilon^{(c)} \quad (4)$$

Where $\varepsilon$ is defined as the total strain in the specimen

$\varepsilon^{(i)}$ is defined as the instantaneous elastic strain
$\varepsilon^{(c)}$ is defined as the creep strain

Thereby, to calculate the increment of strain at the beginning of the second step loading, there exists a need to reduce the instantaneous elastic strain from the second step loading from the instantaneous elastic strain obtained from the first step loading. Similarly, the same method will be followed for all the other steps of the creep experiment and the total creep strain for all of these steps will be calculated for the total strain observed minus the sum of all the increments in elastic strain. Regarding the creep strain in equation (4), it is composed of the primary and steady state creep strain. As Omar Aydan (2017) mentioned, since the creep laws are generally concerned with the secondary stage, which is called the steady state creep stage, Norton's Law empirical model was found to best fit the model of the steady-state creep (Rassouli et al., 2012). The model is of the following form:

$$\dot{\varepsilon}_{SS} = A\sigma^n \tag{5}$$

Where $\dot{\varepsilon}_{SS}$ is the steady state creep rate
*A* and *n* are the empirical constants
σ is the applied axial stress.
Taking the logarithm DIC of the previous equation, it will become:

$$\log \dot{\varepsilon}_{SS} = \log A + n \log \sigma \tag{6}$$

The primary or transient creep stage was not included in the coefficient calculation. The empirical constants *A* and *n* were found using the data by fitting a straight line to the data in a $\log(\dot{\varepsilon}_{SS}) - \log(\sigma)$ space.
However, the creep strain in equation (4) composed of the primary and steady state creep strain could be directly estimated using a power-law function of time (t) (Sone and Zoback, 2013; Rassouli and Zoback, 2018; Zoback and Kohli, 2019). The model is of the following form:

$$J = \frac{\varepsilon}{\sigma} = Bt^n \tag{7}$$

Where J is the creep compliance
ε is strain of the sample
σ is the applied stress on the sample
*B* and *n* are the empirical constants
and t is the time

The empirical constants *B* and *n* can be determined from the DIC data by fitting a straight line to the data in a log(time) − log(J) space. As stated by Rassouli and Zoback (2018), the slope of the linear fit and the intercept of the linear fit at t = 1 s give respectively the power exponent *n* and the logarithm of the constant *B*

### *4.4.2 Results of Multistage Uniaxial Compressional Compliance Creep Test*

The stress level was calculated using the original cross-sectional area of each specimen. As for the axial strain, it was calculated by taking the variation of the axial deformation of the specimen over the original length of the sample. To have a better accuracy of the result, the DIC data were used to calculate the average strain value for each specimen versus time. Thus, we obtained this typical average axial strain against time plots for the parallel and perpendicular direction (Figs. 4.17 and 4.18).

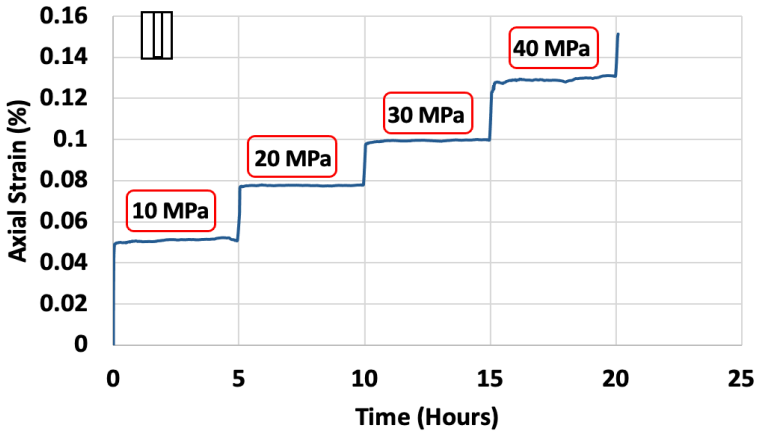


**Figure 4.17 Typical average axial strain against time for a parallel sample.**

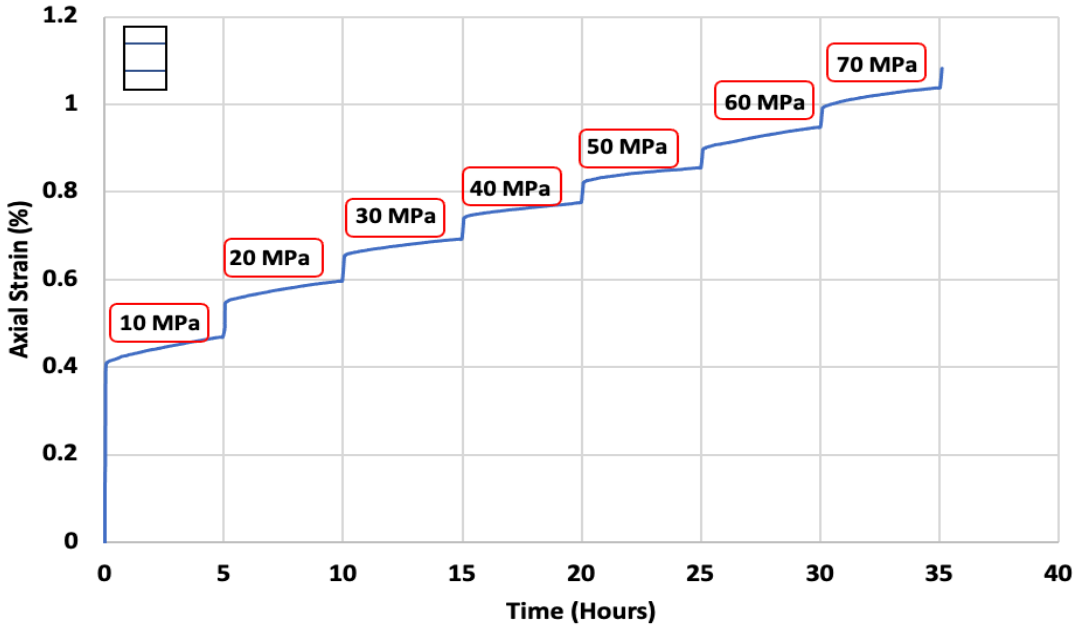


**Figure 4.18 Typical average axial strain against time for a perpendicular sample.**

Table 4.10 also provides the summary of the results obtained during the multistage uniaxial compressional compliance creep tests conducted on nine TMS specimens. All specimens from both bedding orientations display the first and secondary creep stage but did not reach the tertiary stage. The specimens failed to reach the tertiary stage as they would break in pieces during the loading period before the axial stress became constant. Thus, the conclusion which can be derived from these results is that the best way to reach the tertiary creep time is to either reduce the axial stress to be applied on the sample to be near the peak load of the given sample or to reduce the time for each stress level. In addition to that, all specimens reached the secondary creep stage 1.18 hours after the stress started being applied on the said specimen. In other words, every stress increment exhibited similar first and secondary creep stage. As shown in the table above, most TMS parallel samples break after completing their fourth stress level at 40 MPa. On the other side, the TMS perpendicular samples exhibit a higher stress level which could go up to the seventh step before breaking. Table 4.11 presents the summary of the investigation of the total strain for a couple of specimens. The perpendicular samples have in average three times higher total strain value than the parallel ones. In addition to that, the creep strain for both samples orientation is decreasing and increasing proportionally with the stress level (Fig. 4.19). That increase and decrease can be related to the fact that cracks, pore closure of the specimens and other characteristics of the rock microstructure such as the porosity, thermal maturity or the distribution and morphology of organic matter can be contributed to the creep deformation.

**Table 4.10** Details of multistage uniaxial compressional creep experiments.

| Orientation | Name | Stress (MPa) | Time to reach failure (Hours) | Carbonate (%) | Tectosilicate (%) | Clay (%) |
|---|---|---|---|---|---|---|
| Parallel | TMS A-1 | 10 | 20.08 | 14 | 23 | 63 |
| | | 20 | | | | |
| | | 30 | | | | |
| | | 40 | | | | |
| | TMS A-2 | 10 | 20.04 | 29 | 31 | 40 |
| | | 20 | | | | |
| | | 30 | | | | |
| | | 40 | | | | |
| | TMS A-3 | 10 | 25.08 | 23 | 21 | 56 |
| | | 20 | | | | |
| | | 30 | | | | |
| | | 40 | | | | |
| | | 50 | | | | |
| | TMS B-1 | 10 | 10.05 | 8 | 30 | 62 |
| | | 20 | | | | |
| | TMS B-2 | 10 | 15.06 | 15 | 30 | 55 |
| | | 20 | | | | |
| | | 30 | | | | |
| | TMS B-3 | 10 | 20.09 | 6 | 28 | 66 |
| | | 20 | | | | |
| | | 30 | | | | |
| | | 40 | | | | |
| Perpendicular | TMS A-4 | 10 | 35.14 | 27 | 31 | 42 |
| | | 20 | | | | |
| | | 30 | | | | |
| | | 40 | | | | |
| | | 50 | | | | |
| | | 60 | | | | |
| | | 70 | | | | |
| | TMS B-4 | 10 | 35.14 | 6 | 25 | 69 |
| | | 20 | | | | |
| | | 30 | | | | |
| | | 40 | | | | |
| | | 50 | | | | |
| | | 60 | | | | |
| | | 70 | | | | |
| | TMS B-5 | 10 | 20.08 | 17 | 23 | 60 |
| | | 20 | | | | |
| | | 30 | | | | |
| | | 40 | | | | |

**Table 4.11** The total strain for a couple of specimens.

| Orientation | Name | Stress (MPa) | Instantaneous Elastic Strain (%) | Creep Strain (%) | Total Strain of Specimen (%) |
|---|---|---|---|---|---|
| Parallel | TMS A-1 | 10 | 0.050 | 0.0032 | 0.33 |
| | | 20 | 0.071 | 0.0010 | |
| | | 30 | 0.091 | 0.0018 | |
| | | 40 | 0.11 | 0.0076 | |
| | TMS B-1 | 10 | 0.066 | 0.010 | 0.17 |
| | | 20 | 0.089 | 0.006 | |
| Perpendicular | TMS A-4 | 10 | 0.413 | 0.064 | 3.49 |
| | | 20 | 0.426 | 0.050 | |
| | | 30 | 0.494 | 0.037 | |
| | | 40 | 0.493 | 0.034 | |
| | | 50 | 0.508 | 0.032 | |
| | | 60 | 0.411 | 0.050 | |
| | | 70 | 0.434 | 0.045 | |
| | TMS B-4 | 10 | 0.433 | 0.058 | 3.86 |
| | | 20 | 0.507 | 0.018 | |
| | | 30 | 0.550 | 0.020 | |
| | | 40 | 0.482 | 0.052 | |
| | | 50 | 0.502 | 0.044 | |
| | | 60 | 0.547 | 0.037 | |
| | | 70 | 0.573 | 0.037 | |

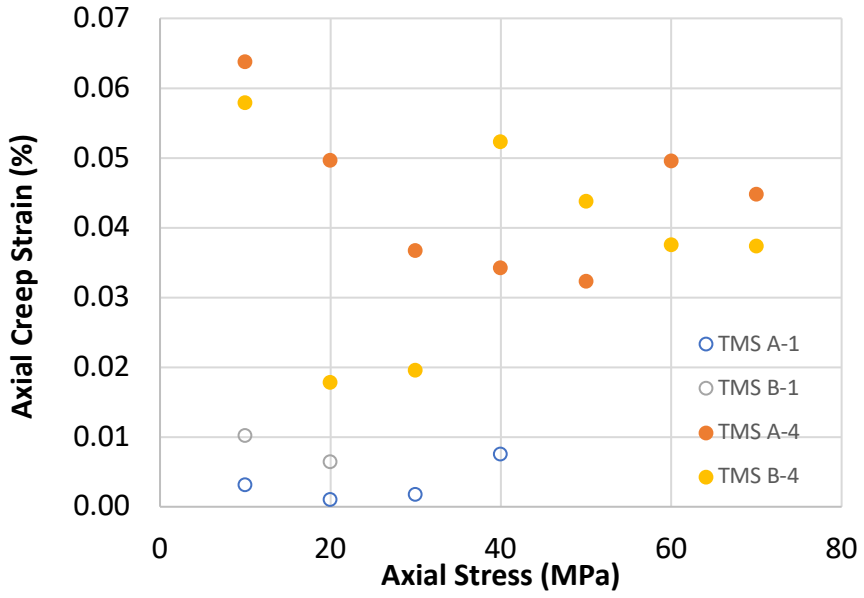


**Figure 4.19 Axial creep strain versus axial stress for couple of specimens.**

### *4.4.3 Norton's Law Creep Model*

The sample TMS B-2 and TMS B-3 were not included in the coefficient calculation because the DIC software crashed during the test. In addition to that, new parameters were implemented using the DIC full field view. The sample is failing when the parallel sample has a normal strain in horizontal direction $\varepsilon_{xx}$ value of 1%. Using that rule, the specimen TMS A-1, TMS A-2, and TMS A-3 were failed before/at the fourth stage (40MPa), respectively.

**Table 4.12** Values for the steady state creep law for the parallel tested samples.

| Orientation | Name | Stress (MPa) | Steady State Creep Rate ($s^{-1}$) | Log(Stress) | Log(Creep Rate) | A ($MPa^{-1}s^{-1}$) | n | $R^2$ |
|---|---|---|---|---|---|---|---|---|
| Parallel | TMS A-1 | 10 | 4.27E-07 | 1.00 | -6.37 | 1.23E-07 | 0.546 | 0.992 |
| | | 20 | 6.51E-07 | 1.30 | -6.19 | | | |
| | | 30 | 7.72E-07 | 1.48 | -6.11 | | | |
| | TMS A-2 | 10 | 2.61E-07 | 1.00 | -6.58 | 1.32E-08 | 1.299 | 1.000 |
| | | 20 | 6.55E-07 | 1.30 | -6.18 | | | |
| | | 30 | 1.08E-06 | 1.48 | -5.97 | | | |
| | TMS A-3 | 10 | 5.56E-08 | 1.00 | -7.26 | 1.38E-09 | 1.745 | 0.844 |
| | | 20 | 4.72E-07 | 1.30 | -6.33 | | | |
| | | 30 | 5.59E-07 | 1.48 | -6.25 | | | |
| | | 40 | 5.98E-07 | 1.60 | -6.22 | | | |
| | TMS B-1 | 10 | 4.34E-07 | 1.00 | -6.36 | 1.81E-08 | 1.380 | 1.000 |
| | | 20 | 1.13E-06 | 1.30 | -5.95 | | | |

**Table 4.13** Values for the steady state creep law for the perpendicular tested samples.

| Orientation | Name | Stress (MPa) | Steady State Creep Rate ($s^{-1}$) | Log(Stress) | Log(Creep Rate) | A ($MPa^{-1}s^{-1}$) | n | $R^2$ |
|---|---|---|---|---|---|---|---|---|
| Perpendicular | TMS A-4 | 10 | 6.06E-07 | 1.00 | -6.22 | 4.28E-07 | 0.324 | 0.377 |
| | | 20 | 1.84E-06 | 1.30 | -5.73 | | | |
| | | 30 | 1.59E-06 | 1.48 | -5.80 | | | |
| | | 40 | 1.48E-06 | 1.60 | -5.83 | | | |
| | | 50 | 1.40E-06 | 1.70 | -5.85 | | | |
| | | 60 | 1.43E-06 | 1.78 | -5.84 | | | |
| | | 70 | 1.46E-06 | 1.85 | -5.84 | | | |
| | TMS B-4 | 10 | 9.66E-07 | 1.00 | -6.01 | 7.34E-07 | 0.199 | 0.503 |
| | | 20 | 1.72E-06 | 1.30 | -5.76 | | | |
| | | 30 | 1.55E-06 | 1.48 | -5.81 | | | |
| | | 40 | 1.54E-06 | 1.60 | -5.81 | | | |
| | | 50 | 1.53E-06 | 1.70 | -5.81 | | | |
| | | 60 | 1.60E-06 | 1.78 | -5.79 | | | |
| | | 70 | 1.60E-06 | 1.85 | -5.79 | | | |
| | TMS B-5 | 10 | 1.19E-06 | 1.00 | -5.92 | 2.18E-07 | 0.731 | 0.789 |
| | | 20 | 2.14E-06 | 1.30 | -5.67 | | | |
| | | 30 | 1.90E-06 | 1.48 | -5.72 | | | |
| | | 40 | 3.96E-06 | 1.60 | -5.40 | | | |

Figure 4.20 presents a fitting of linear trend line in log (creep rate) against log (stress) for the TMS A-1 specimen. The points are fitted with a straight line generating the coefficient values which are shown in the equation coefficient. The values for the parameters of the steady state creep law for the TMS A-1 are the following: $A$ is equal to $1.23 \times 10^{-7}$ $MPa^{-1}$ $s^{-1}$ and $n$ is equal to 0.55.

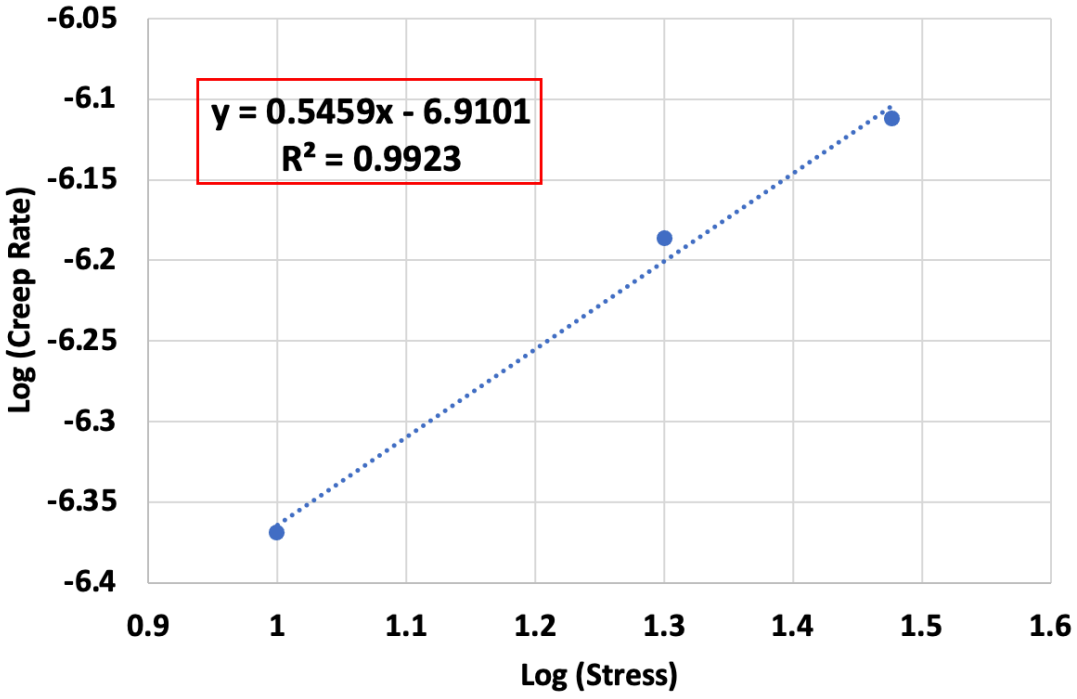


**Figure 4.20 Fitting of linear trend line in log (creep rate) against log (stress) for the TMS A-1 specimen.**

Similar procedure was adopted for all the other samples as indicated in Tables 4.12 and 4.13 to determine the coefficient values of $A$ and $n$ and the results ended up being a good fit to the experimental data with $R^2$ value greater than 0.8 for the parallel samples. On the other hand, the results for the perpendicular sample for most of the tested samples do not present a good fitting line with the experimental data with $R^2$ value between 0.38 to 0.79. The parameters $A$ and $n$ found do not exhibit a good fit to the experimental data for all the tested samples. In addition to that, Omar Aydan (2017) mentioned that the $n$ value typically ranges from a bit less than 2 to 8. Thus, based on our n value found, these results may not be appropriate for the modeling of the actual parameters for each stress level. Therefore, it is suspected that the Norton's law was not a good fit because the microstructure was changing as the load increased. Indeed, other than pores getting closed, it was seen on the DIC full field map view that some cracks were closing and new ones getting formed. All those reactions happening may be contributing to the creep rate changing over time and stress level increase. Another model was then established to fulfill that purpose.

### *4.4.4 Power-Law Creep Model*

Since each stress step was applied over a finite duration (60 s), Zoback and Kohli (2019) presented that the strain data was not an actual representation of the creep compliance function. Thus, to account for this lag in the strain data compared to a true impulse response, Lakes' approach, first used in 1999, was employed. In this approach, the initial portion of the strain data was discarded,

and the remaining data was used to do the calculation. As the stress level increases, only a time shifting was implemented in the linear regression because the exact mechanism of the creep that has to be removed in each stress level is still lacking full understanding. Figure 4.21 presents the linear regression performed in a log–log space of the specimen TMS A-4 to determine *n* and *B* constants. In that figure, the power law did not best fit the first regression line at 10 MPa because upon the application of load, the micro pores and cracks would close due to the increase of stress. Following the closure of all the cracks, the rocks start behaving more elastically hence the power law equation started to best fit the linear regression at different stress level application.

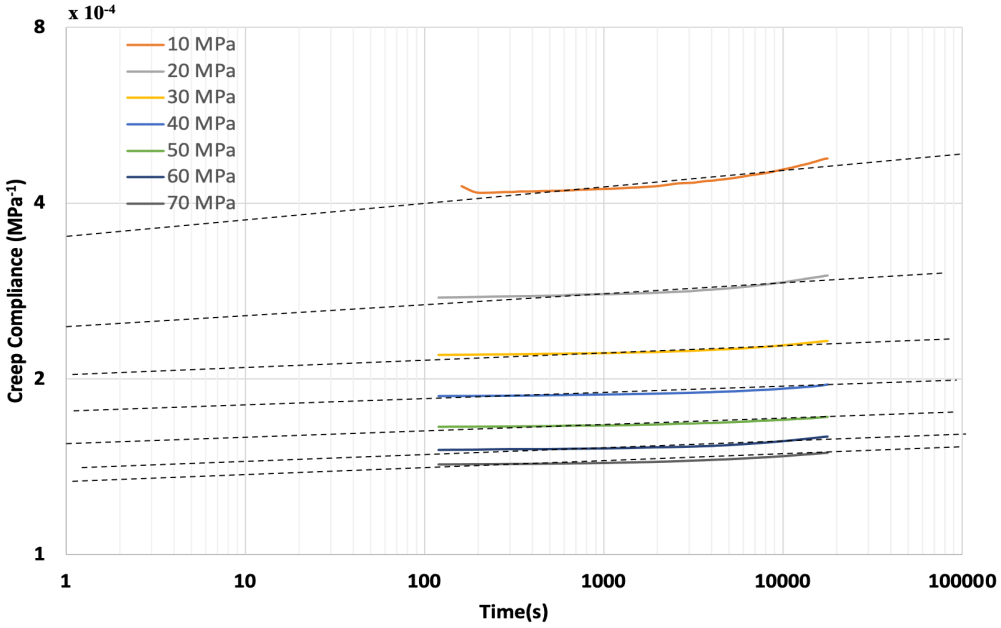


**Figure 4.21 Linear regression performed in a log–log space of the specimen TMS A-4.**

Table 4.14 and Fig. 4.22 provide the recapitulative table and plot for the *n* and *B* value for each stress level for the specimen TMS A-4.

**Table 4 .14** Recapitulative table for the *n* and *B* value for TMS A-4.

| Name | Stress (MPa) | B | n |
|---|---|---|---|
| TMS A-4 | 10 | 3.51E-04 | 0.029 |
| | 20 | 2.47E-04 | 0.018 |
| | 30 | 2.05E-04 | 0.012 |
| | 40 | 1.77E-04 | 0.009 |
| | 50 | 1.58E-04 | 0.008 |
| | 60 | 1.41E-04 | 0.011 |
| | 70 | 1.35E-04 | 0.010 |

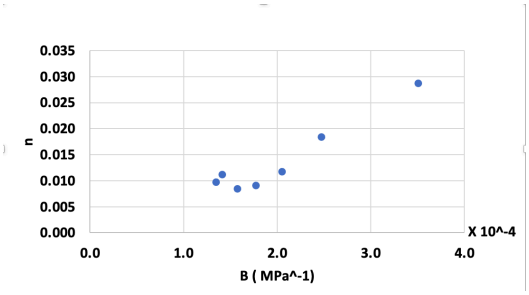


**Figure 4.22 Plot of *n* and *B* value for TMS A-4.**

As the creep time increased, the *B* value decreased presenting the fact that the sample was getting stiffer after each stress step (Fig.4.22). Concerning the *n* value, it was made clear that the *n* value is decreasing and increasing at different stress level. This fact can be explained as an undergoing of the time-dependent deformation by the rock and collapsing of pores over time. Using this procedure, the *B* value may be a little overestimated because some creep error may be adding on the next creep stage each time that the stress level was increased. Indeed, in our studies, the plastic strain was not considered during our analysis which is an instantaneous permanent deformation of rocks. However, that viscoplastic deformation is related to the creep permanent deformation (Rassouli and Zoback, 2018). To counter that effect, it was supposed that whatever effect that contributed to the creep happening was only predominant during the first hour of the experiments. Thus, as the stress level increases that reaction may require less time. Therefore, the power law model used in that condition still provided a good fitting. The same method was applied for all the other samples and the coefficients *n* and *B* were found for all the samples to determine the *n* and *B* parameters (Tables 4.15 and 4.16**).**

**Table 4.15** The coefficients *n* and *B* for all the parallel tested samples with their mineralogy.

| Orientation | Name | Stress (MPa) | B | n | Carbonate (%) | Tectosilicate (%) | Clay (%) |
|---|---|---|---|---|---|---|---|
| Parallel | TMS A-1 | 10 | 4.71E-05 | 1.18E-02 | 14 | 23 | 63 |
| | | 20 | 3.93E-05 | 1.60E-03 | | | |
| | | 30 | 3.30E-05 | 3.90E-03 | | | |
| | TMS A-2 | 10 | 2.03E-05 | 2.86E-02 | 29 | 31 | 40 |
| | | 20 | 2.35E-05 | 7.00E-04 | | | |
| | | 30 | 2.18E-05 | 7.20E-03 | | | |
| | TMS A-3 | 10 | 1.17E-06 | 1.93E-01 | 23 | 21 | 56 |
| | | 20 | 8.85E-06 | 3.19E-02 | | | |
| | | 30 | 1.20E-05 | 2.01E-02 | | | |
| | | 40 | 1.41E-05 | 1.51E-02 | | | |
| | TMS B-1 | 10 | 5.65E-05 | 2.41E-02 | 8 | 30 | 62 |
| | | 20 | 5.12E-05 | 1.28E-02 | | | |
| | TMS B-2 | 10 | 2.62E-04 | 4.90E-02 | 15 | 30 | 55 |
| | | 20 | 1.86E-04 | 4.80E-03 | | | |
| | | 30 | 1.55E-04 | 6.30E-03 | | | |
| | TMS B-3 | 10 | 7.90E-04 | 2.30E-03 | 6 | 28 | 66 |
| | | 20 | 4.53E-04 | 2.20E-03 | | | |
| | | 30 | 3.39E-04 | 1.40E-03 | | | |
| | | 40 | 2.78E-04 | 2.60E-03 | | | |

**Table 4.16** The coefficients *n* and *B* for all the perpendicular tested samples with their mineralogy.

| Orientation | Name | Stress (MPa) | B | n | Carbonate (%) | Tectosilicate (%) | Clay (%) |
|---|---|---|---|---|---|---|---|
| Perpendicular | TMS A-4 | 10 | 3.51E-04 | 2.87E-02 | 27 | 31 | 42 |
| | | 20 | 2.47E-04 | 1.84E-02 | | | |
| | | 30 | 2.05E-04 | 1.17E-02 | | | |
| | | 40 | 1.77E-04 | 9.10E-03 | | | |
| | | 50 | 1.58E-04 | 8.40E-03 | | | |
| | | 60 | 1.41E-04 | 1.12E-02 | | | |
| | | 70 | 1.35E-04 | 9.70E-03 | | | |
| | TMS B-4 | 10 | 3.65E-04 | 2.59E-02 | 6 | 25 | 69 |
| | | 20 | 2.65E-04 | 7.10E-03 | | | |
| | | 30 | 1.99E-04 | 6.70E-03 | | | |
| | | 40 | 1.56E-04 | 1.62E-02 | | | |
| | | 50 | 1.47E-04 | 1.17E-02 | | | |
| | | 60 | 1.40E-04 | 9.60E-03 | | | |
| | | 70 | 1.32E-04 | 8.30E-03 | | | |
| | TMS B-5 | 10 | 4.63E-04 | 1.98E-02 | 17 | 23 | 60 |
| | | 20 | 2.96E-04 | 1.81E-02 | | | |
| | | 30 | 2.45E-04 | 1.09E-02 | | | |
| | | 40 | 2.12E-04 | 7.20E-03 | | | |

### *4.4.5 Effects of Mineral Composition and Anisotropy*

To better analyze the effects of mineral composition and anisotropy in the TMS samples, more parameters were implemented on the DIC data. Besides the specimen TMS A-1, TMS A-2, and TMS A-3 which failed before and at the fourth stage (40MPa), the initial stress level of 10 MPa is referred as the outliner to prepare the samples to be in situ conditions for the main experiment. A plot for the second and third loading stage was generated to facilitate the comparison (Figs. 4.23 and 4.24). The samples TMS A-3, TMS B-1 and TMS B-3 were not represented in the graph because TMS A-3 and TMS B-3 were acting like outsiders and TMS B-1 failed during the third stage loading. Figures 4.23 and 4.24 were given a nomenclature PL A or PL B to express the sample from well A and B in the parallel direction to the bedding. Similarly, a nomenclature PD A or PD B was given to present the sample from well A and B in the perpendicular direction to the bedding.

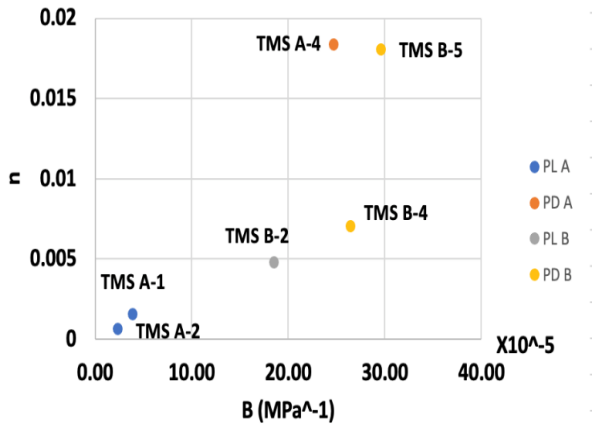


**Figure 4.23 *B* and *n* value comparison plot at 20 MPa.**

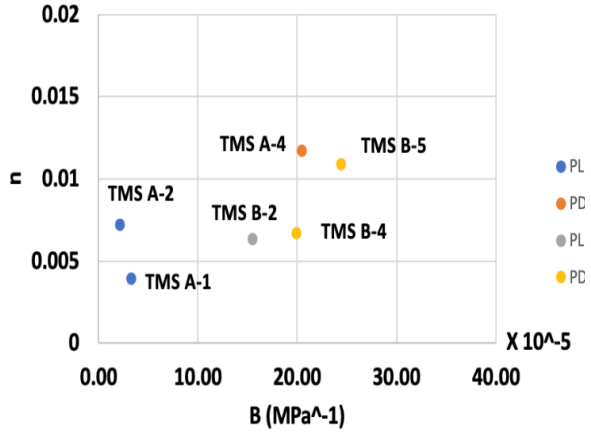


**Figure 4.24 *B* and *n* value comparison plot at 30 MPa.**

As is made evident by the data, both value of the parameters *B* and *n* in the perpendicular samples TMS A-4, TMS B-4, and TMS B-5 are in average twice higher than those for the parallel samples TMS A-1, TMS A-2, TMS B-2. This observation proves that the samples exhibit a higher creep compliance when loading in the direction normal to the bedding than in the direction parallel to the bedding. Even though the samples TMS B-4 and TMS B-5 were loading in the same direction and from the same well B, the specimen TMS B-4 has a lower *B* and *n* value than the sample TMS B-5. This result is possible because of their different mineralogy composition. Indeed, TMS B-4 has on average a lower composition value than TMS B-5 in both clay and carbonate content. In fact, the samples were tested as received. Apparently dry, an oven dry test was not performed; therefore, as Moore and Lockner (2004) explained the clay rich samples with clay bounded water may affect at room temperature the creep behavior of the sample by allowing the grain to slide between the grain rich in clay and other minerals. In addition to that, the samples from well B (TMS B-2, TMS B-4 and TMS B-5) have higher clay content, more than 64% on average, than the samples from well A (TMS A-1, TMS A-2 and TMS A-4) which display more than 40 % on average for the clay content; therefore, it can be deduced that on average the higher amount of clay minerals will result in higher and more prominent creep behavior. Concurring with Sone and Zoback (2013) explaining that the shale with high clay content will result to higher porosity value which will definitively affect the creep reaction in shale sample. However, since the gaps between the well A and B value for the parameters *B* and *n* is not huge, a conclusion can be made that both well will exhibit the same creep reaction on average.

### *4.4.6 Effect of Strain Distribution in the Different Layers*

To have a better understanding of what was happening during the creep deformation, the study of the strain distribution in the different layers was investigated using DIC. In Fig. 4.25, layer 1 presented a higher compressional strain; therefore, it is considered as a soft layer which is supposed to be composed of clay and kerogen content. The range of strain value for the soft layer was between -0.8 and -1. Similarly, layer 2 exhibited a lower compressional strain; therefore, it is considered as a stiff layer which is supposed to be composed of quartz, feldspar, pyrite, and carbonates. The range of strain value for the stiff layer was between 0 and -0.40. A range strain value of -0.4 to -0.8 was defined as a combination of both soft and stiff component.

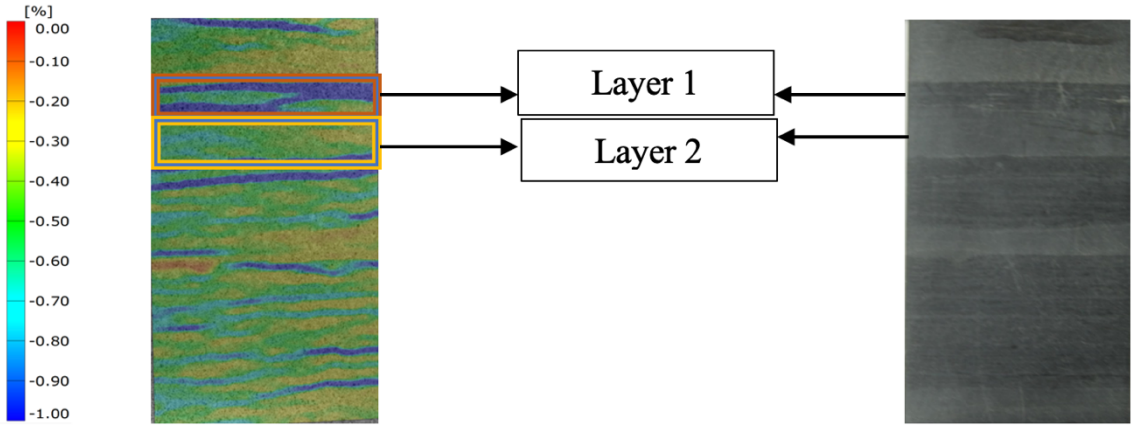


**Figure 4.25 Soft and stiff layers determination for TMS A-4.**

The average axial against time for the specimen TMS A-4 was investigated in Fig. 4.26. As it is seen, the whole sample, soft and stiff layers present the same increasing trend. As for the soft layer, it exhibits higher average axial strain over time as the stress level increases. While the stiff layer is presenting the lowest average axial strain throughout the experiment. As for the whole sample, the average axial strain over time is leaning more towards the soft layer behavior.

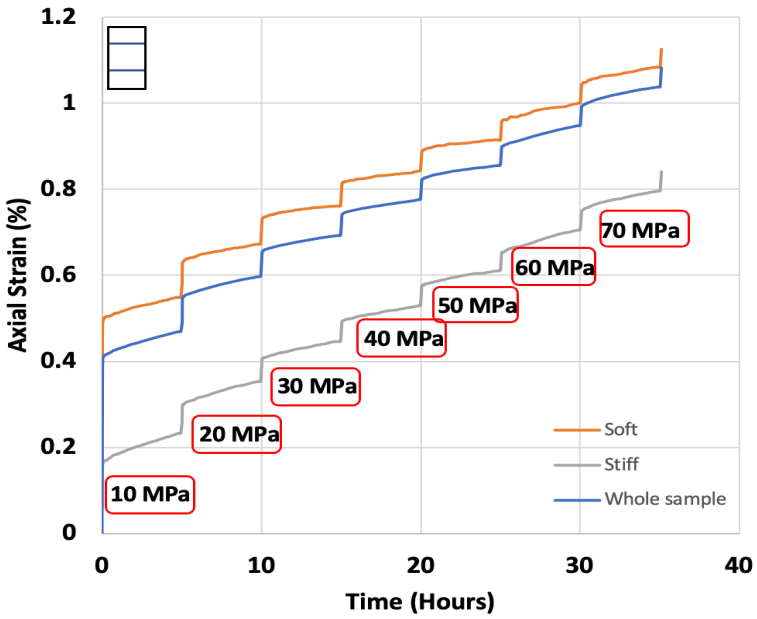


**Figure 4.26 Average axial strain against time for TMS A-4.**

Therefore, for a better understanding of what was happening during each stage, the average axial creep strain was calculated. Thus, it was observed that the creep strain followed a decreasing, increasing, and decreasing trend as the stress level increase over time for the whole sample, soft and stiff layer (Fig. 4.27). Regarding the stiff layer, its average creep strain was a little bit higher than the soft and the whole sample respectively throughout the experiment. However, the thickness of the soft layer being experimented on is way lower than that of the stiff layer (Fig. 4.25). Therefore, it is safe to assume that the creep behavior is happening more in the soft layer than in the stiff ones.

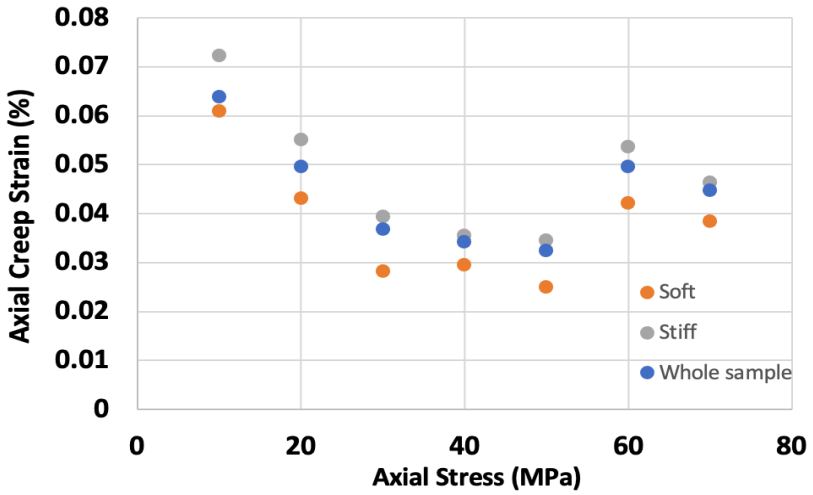


**Figure 4.27 Axial creep strain versus axial stress for TMS A-4.**

The power law creep modeling was done on each of the distinct layer (1 and 2) of the specimen TMS A-4 as designed in the picture above. The parameters *B* and *n* were determined as presented in Table 4.17.

**Table 4.17** *B* and *n* value for the entire and distinct layer of TMS A-4.

| Name | Region | Stress (MPa) | B (x10$^{-4}$) | n |
|---|---|---|---|---|
| TMS A-4 | Layer 1: Soft | 10 | 4.45 | 0.021 |
| | | 20 | 2.93 | 0.014 |
| | | 30 | 2.34 | 0.009 |
| | | 40 | 1.98 | 0.007 |
| | | 50 | 1.73 | 0.006 |
| | | 60 | 1.53 | 0.009 |
| | | 70 | 1.44 | 0.008 |
| | Layer 2: Stiff | 10 | 1.06 | 0.075 |
| | | 20 | 1.21 | 0.036 |
| | | 30 | 1.21 | 0.020 |
| | | 40 | 1.14 | 0.014 |
| | | 50 | 1.07 | 0.013 |
| | | 60 | 0.99 | 0.017 |
| | | 70 | 1.00 | 0.013 |
| | Whole sample | 10 | 3.5067 | 0.029 |
| | | 20 | 2.4734 | 0.018 |
| | | 30 | 2.0487 | 0.012 |
| | | 40 | 1.7721 | 0.009 |
| | | 50 | 1.5763 | 0.008 |
| | | 60 | 1.4116 | 0.011 |
| | | 70 | 1.3487 | 0.010 |

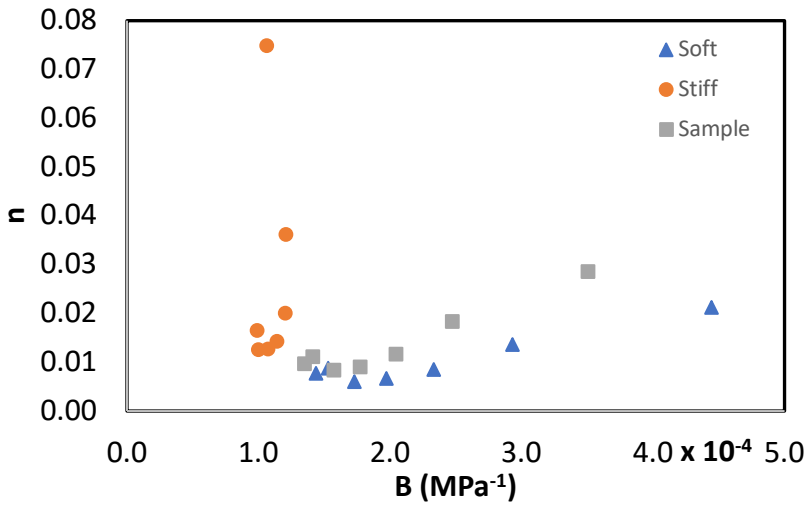


**Figure 4.28 *B* and *n* value plot for the entire and distinct layer of TMS A-4.**

The *B* value for the soft layer was ranging from $4.45\times10^{-4}$ to $1.44\times10^{-4}$ while the *n* value was ranging from 0.021 to 0.008. For the stiff layer, the *B* value was varying from $1.06\times10^{-4}$ to $0.99\times10^{-4}$ while the *n* value was varying from 0.075 to 0.013. The soft layer exhibited higher value for *B*

than the stiff layer due to its softness allowing more compression while the stiff layer being already rigid is not compressing anywhere as much. As for the *n* value, it is also higher for the soft layer than the stiff layer as seen in Fig. 4.28. In addition to that, observations show that the n value for the entire TMS A-4 sample is following the stiff layer trend but is clearly influence by the soft ones. Therefore, this finding is conformed with the idea that the creep deformation is happening in the soft components more so than the stiff components as claimed by Sone and Zoback (2013), and Zoback and Kohli (2019) findings for other shale formations.

### *4.4.7 Comparison of TMS with Other Shale Formations*

Sone and Zoback (2013) and Rassouli and Zoback (2018) conducted a series of triaxial creep experiments on Barnett, Haynesville, Eagle Ford, and Fort St. John shale and on Haynesville and Eagle Ford shale formations respectively. The samples were picked based on their mineral composition and the anisotropy was also addressed in their respective studies by having both vertical and horizontal samples for all formations. The triaxial tests were performed at an axial differential stress of 30 MPa and 40 MPa respectively. As a result, a power-law model fitting the data obtained provided the two parameters *B* and *n* of those samples. Therefore, a comparison could be made between the results found by Sone and Zoback (2013), Rassouli and Zoback (2018) and these conducted TMS experiments. The recapitulative Tables 4.18 and 4.19 present the summary of the results obtained during Sone and Zoback (2013) and Rassouli and Zoback (2018) experiment and this creep experiment on TMS on those differential stress level.

**Table 4.18** Results from Sone and Zoback (2013) experiments.

| | Differential Stress | 30 MPa | |
|---|---|---|---|
| **Formation** | **Orientation** | **B (x 10^-5)** | **n** |
| **Barnet** | Horizontal | 2.6 | 0.018 |
| | Vertical | 3.5 | 0.020 |
| **Haynesville** | Horizontal | 1.6 | 0.021 |
| | Vertical | 5.2 | 0.046 |
| **Eagle Ford** | Horizontal | 2 | 0.044 |
| | Vertical | 3.7 | 0.048 |
| **Fort St. John** | Horizontal | 2.6 | 0.038 |
| **TMS** | Horizontal | 9.9 | 0.008 |
| | Vertical | 21.6 | 0.010 |

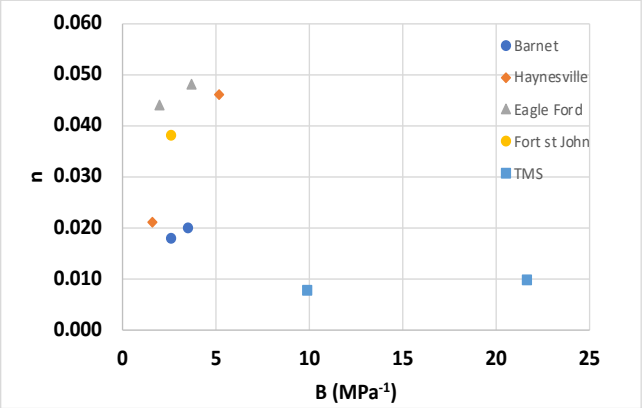


**Figure 4.29 TMS vs Sone and Zoback (2013) experiments.**

**Table 4.19** Results from Rassouli and Zoback (2018) experiments.

| | Differential Stress | 40 MPa | |
|---|---|---|---|
| Formation | Orientation | B (x 10^-5) | n |
| Haynesville | Horizontal | 2.4 | 0.010 |
| | Vertical | 4.8 | 0.048 |
| Eagle Ford | Horizontal | 3.7 | 0.014 |
| | Vertical | 3.9 | 0.030 |
| TMS | Horizontal | 14.6 | 0.009 |
| | Vertical | 18.2 | 0.011 |

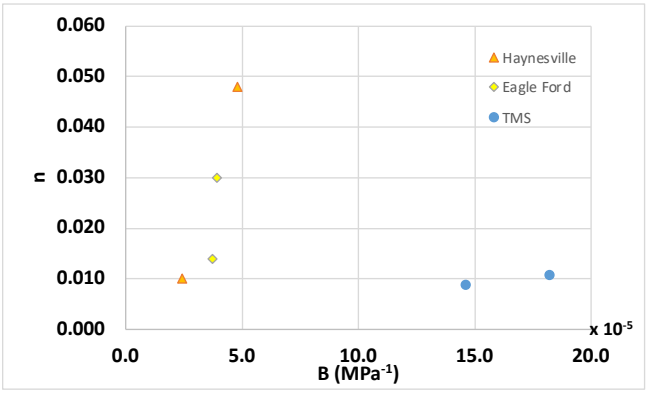


**Figure 4.30 TMS vs Rassouli and Zoback (2018) experiments.**

Based on both Figs. 4.29 and 4.30, since TMS samples have very high clay content on average, more than 50%, the *B* values are higher for both direction than the ones found in Barnett, Haynesville, Eagle Ford, and Fort St. John shale formations at the differential stress level of 30 MPa and 40 MPa. However, their *n* values are on average lower in both direction than the ones found in Barnett, Haynesville, Eagle Ford, and Fort St. John shale formations at the differential stress level of 30 MPa and 40 MPa. The lower *n* value for the TMS can be explained by the fact that TMS does not exhibit a lot of pore compaction as other shale formations do. Since TMS could be defined as a weak rock based on its multiple fractures, the formation of internal cracks could also be a reason for the earlier failure of the samples at differential stress level. Therefore, more experiments using the triaxial test should be investigated on the TMS samples by putting them more in the in-situ state conditions to accurately predict the time-dependent behavior of the rocks.

## 4.5 Thermal conductivity measurement of TMS

Thermal conductivity is the ability of a substance to conduct heat. The work in this subtask is to conduct a thermographic investigation on TMS core samples to analyze the thermal conductivity using a thermal imaging camera. Eight TMS core samples from Soterra and Lane wells were cut for this purpose. Tables 4.20 and 4.21 show the core samples depth and dimension.

**Table 4.20** Core samples from Soterra well.

| Depth | Length | Breadth | Height | Mass |
|---|---|---|---|---|
| 12501 ft | 0.025 m | 0.027m | 0.023m | 0.039 kg |
| 12583 ft | 0.022 m | 0.022 m | 0.022 m | 0.026 kg |
| 12584 ft | 0.019 m | 0.026 m | 0.026 m | 0.033 kg |
| 12589 ft | 0.029 m | 0.029 m | 0.023 m | 0.044 kg |

**Table 4.21** Core samples from Lane well.

| Depth | Length | Breadth | Height | Mass |
|---|---|---|---|---|
| 15085 ft | 0.033 m | 0.024m | 0.024m | 0.047 kg |
| 15169 ft | 0.027 m | 0.030 m | 0.019 m | 0.038 kg |
| 15176 ft | 0.026 m | 0.026 m | 0.025 m | 0.040 kg |
| 15186 ft | 0.029 m | 0.026 m | 0.020 m | 0.037 kg |

In order to measure the thermal conductivity, the core sample was heated to 150$^{o}$C on one side for 30 minutes. The temperature distribution along the core was recorded by a thermal camera FLIR T440. The thermal images of the camera were analyzed using FLIR thermal studio to get the exact values of temperature along the shale. On the other hand, simulation was carried out in ABAQUS CAE to perform transient heat transfer simulation with various thermal conductivity constant to match the temperature range obtained from the thermal camera images. The simulation was carried out for 10 minutes, 20 minutes and 30 minutes to compare with the temperature of thermal camera with specific time. After the simulation was carried out. The temperature data obtained from simulation as well as from the thermal camera were compared to get exact thermal conductivity of shale.

The thermal conductivity was also measured by hot rod method which consists of a probe with heater and temperature sensor inside (Fig. 4.31). As current passes through the heater, the system monitors the temperature of the sensor over time. Analysis of the time dependence of the sensor temperature determines the thermal conductivity.


**Figure 4.31, Picture of Tempos thermal analyzer.**

The results of thermal conductivity measurement are displayed in Tables 4.22 and 4.23. The results indicated that the depth of the core did not have direct relationship with the thermal conductivity. Core samples with orientation perpendicular to the bedding-plane have higher thermal conductivity comparing with those of bedding plane-parallel.

The clay content for Soterra used in the measurement were ranging from 14 percent to 51 percent. The lowest clay content in Soterra and Lane displayed the highest value of thermal conductivity. Similarly, the highest clay content in these wells had the lowest thermal conductivity.

**Table 4.22** Measured thermal conductivity in Soterra.

| **Depth** | **Hot Rod Method** | | **Thermal Camera Method** | |
|---|---|---|---|---|
| | Parallel | Perpendicular | Parallel | Perpendicular |
| 12501 ft | 1.33 W/mK | 1.85 W/mK | 1.35 W/mK | 1.80 W/mK |
| 12583 ft | 1.40 W/mK | 1.85 W/mK | 1.40 W/mK | 1.9 W/mK |
| 12584 ft | 1.38 W/mK | 2.10 W/mK | 1.45 W/mK | 2.20 W/mK |
| 12589 ft | 1.10 W/mK | 1.68 W/mK | 1.15 W/mK | 1.70 W/mK |

**Table 4.23** Measured thermal conductivity Lane.

| **Depth** | **Hot Rod Method** | | **Thermal Camera** | |
|---|---|---|---|---|
| | Parallel | Perpendicular | Parallel | Perpendicular |
| 15049 ft | 0.98 W/mK | 1.84 W/mK | 0.95 W/mK | 1.80 W/mK |
| 15085 ft | 1.15 W/mK | 2.10 W/mK | 1.20 W/mK | 2.10 W/mK |
| 15176 ft | 1.70 W/mK | 2.68 W/mK | 1.68 W/mK | 2.80 W/mK |
| 15186 ft | 1.35 W/mK | 2.32 W/mK | 1.35 W/mK | 2.25 W/mK |

## References


Aydan Ö (2016) Time-Dependency in Rock Mechanics and Rock Engineering , 1st ed. CRC Press.

Hult JAH (1966) Creep in engineering structures. Blaisdell.

Kuruppu MD, Obara Y, Ayatollahi MR, Chong KP, Funatsu T (2013) ISRM-suggested method for determining the mode I static fracture toughness using semi-circular bend specimen. *Rock Mech Rock Eng.* 47(1):267–274.

Rassouli FS, Mehranpour MH, and Moosavi M (2012) Study of Punch Tip Effect On Creep of Materials In Impression Creep Test. In Paper presented at the 46th U.S. Rock Mechanics/Geomechanics Symposium, Chicago, Illinois.

Rassouli FS, Zoback MD (2018). Comparison of short-term and long-term creep experiments in shales and carbonates from unconventional gas reservoirs. *Rock Mech Rock Eng*, *51*(7): 1995–2014.

Sone H, and Zoback MD (2013) Analysis of Intra-Reservoir Stress Variations in Shale Gas Reservoirs Based on the Variation of Viscoelastic Properties. In Paper presented at the 47th U.S. Rock Mechanics/Geomechanics Symposium, San Francisco, California, June 2013.

Zoback, M. D., & Kohli, A. H. (2019). Unconventional reservoir geomechanics: Shale Gas, tight oil and induced seismicity. Cambridge University Press.

# CHAPTER 5 $CO_2$ foam and Super-Hydrophobic Proppant to Improve Fracturing in TMS

This section relates to employed $CO_2$ foam as fracturing fluid. An important advantage of using $CO_2$ foam as fracturing fluids is their composition. Foams consist of 53-95% gas which cuts down on the amount of water used when comparing foams to traditional slickwater-based fluid. Nanoparticle-stabilized $CO_2$ foam is proposed in this study to improve the $CO_2$ foam stability, rheological properties, and fluid loss capabilities as fracturing fluid. Another method of improving fluid flow in shale fractures with the application of nano-coating on proppants is studied. The nano-coated proppant surface can act as super-hydrophobic surface (or super-oleophobic), thus contact angle between water and the surface reaches close to 180°. The nano-surface of proppant reduces the contact between the fluid and the surface, and hence affects the fluid flow through the facture.

## 5.1 Nanoparticle-Stabilized $CO_2$ foam as Fracturing Fluid

### *5.1.1 Nanoparticle-stabilized $CO_2$ foam generation*

The nanosilica used in this study was received from Nouryon Pulp and Performance Chemicals Inc. Details of the silica dispersion are listed in Table 5.1.

**Table 5.1** Specification of nanosilica**.**

| Chemical Composition | Physical Form | $SiO_2$ content | pH | Density | Viscosity | Average particle size |
|---|---|---|---|---|---|---|
| Water-based Epoxy Silane-modified colloidal silica | Dispersion | 28 wt.% | 8 | 1.2 g/mL | 5cp | 7 nm |

The equipment setup for $CO_2$ foam generation and foam properties measurement is shown in Figure 5.1. The two pumps used in the experiment were manufactured by Teledyne ISCO Inc. Both syringe pumps (Model: 500D) were wired to the controller, connected to the power supply, and refilled with distilled water. Two accumulators were installed for storing nanosilica and $CO_2$. Pressure transducers and indicators were assembled and wired to the Data Acquisition System (DAS). The data recording set was interfaced with Excel worksheet to automatically save pressure readings from transducers. Back Pressure Regulars (BPR) were prepared by pressurizing the BPR dome with nitrogen to designed pressure (1300psi at system outlet). The outlets of BPRs were connected to the stainless steel beadpack column where $CO_2$ foam was generated. A sapphire observation cell was installed after the beadpack column. The configuration of the beadpack is displayed in Table 5.2. Two Swagelok valves were installed before and after the sapphire tube. A 20 ft long, 1/16'' diameter stainless steel capillary was installed to record the pressure drop of the flow by a differential pressure transducer. After the capillary tube, another accumulator was

installed to dispose of foam. The last BPR at the outlet was used to maintain the experimental pressure. A fan heater and a thermal couple were used to control the operating temperature. Only the pumps and the data recording systems were placed outside the air bath chamber.

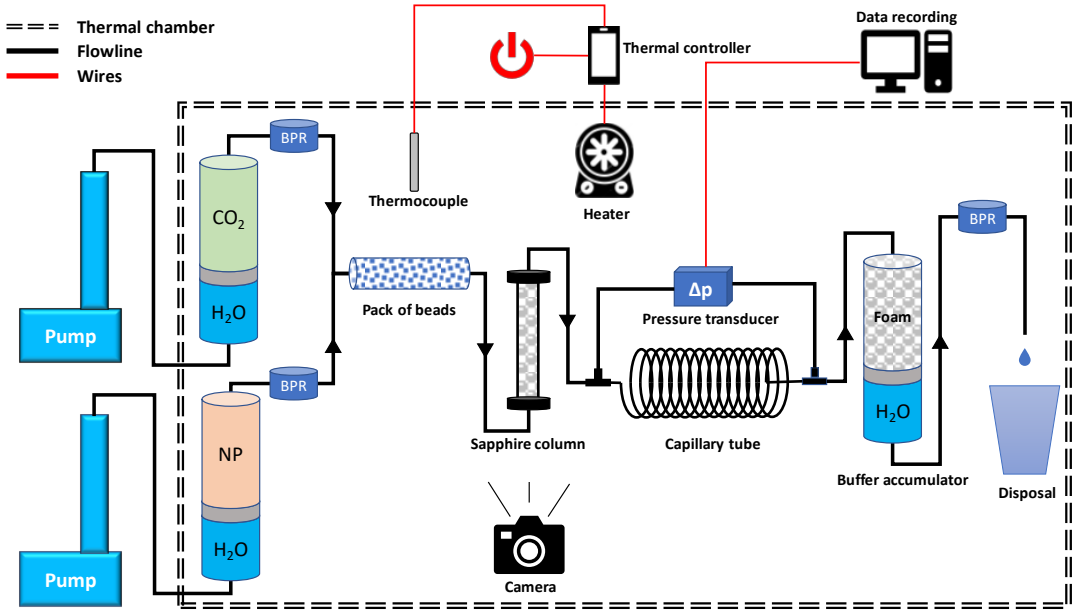


**Figure 5.1 Illustration of experiment setup.**

**Table 5.2** Properties of the beadpack.

| Sand mesh | Inner radius | Length | Porosity | Permeability |
|---|---|---|---|---|
| 70~140 | 4.5mm | 212.1mm | 33.4% | 14.16 Darcy |

The experiment procedure is described below:

1. Assemble and install the system setup as described above. Calibrate pressure transducers and indicators.
2. Load the prepared nanoparticle dispersion and $CO_2$ into the two accumulators, respectively. Set up the temperature on the thermal controller and heat up the system to the desired temperature.
3. Set the pump flow rate for the nanosilica dispersion and $CO_2$ based on foam quality and start the co-injection of both accumulators. At the same time, start pressure reading of the data acquisition system from the computer.
4. When the pressure drop along the "Capillary tube" is stabilized over time, stop the pump. Terminate the data acquisition system.
5. Record the foam heright change in the sapphire cell until all the foam in the cell is fully collapsed.
6. Cleanse the flowline for the next experiment.

The foam configuration and experiment conditions for each set of experiments conducted in this study is shown in Table 5.3. The flow rates were selected considering both the capability of laboratory equipment and a typical shear rate (up to $1000s^{-1}$) seen in hydraulic fracturing treatment (Barbati et al., 2016).

**Table 5.3** Experiment design.

| Foam quality | Nanosilica (ppm) | NaCl | Pressure (psi) | Temperature (°C) | Flow rate (mL/min) |
|---|---|---|---|---|---|
| 10% ~ 90% | 5000 | 5% | 1300 | 20 | 6 ~ 18 |
| 70% | 500 ~ 7000 | 5% | 1300 | 20 | 12 |
| 70% | 5000 | 3% ~ 11% | 1300 | 20 | 12 |
| 70% | 5000 | 5% | 1300 | 20 ~ 72 | 18 |

Different models have been applied to characterize foam rheology, but the results can differ owing to various factors such as the differences in foam configuration and experiment conditions, besides the nature of the model itself. A commonly-used model for foam characterization is the Hershel Bulkley model expressed as,

$$\tau = \tau_y + K\gamma^n \tag{1}$$

where $\tau$: shear stress; $\tau_y$: yield stress; $K$: consistency index, which is equal to the shear stress at a shear rate of $1s^{-1}$; $n$: flow index, which describes whether it is a Newtonian fluid ($n$=1) or non-Newtonian fluid ($n$<1 for shear-thinning and $n$>1 for shear-thickening); and $\gamma$: shear rate.
$\tau_y \approx 0$ for high shear rate conditions, thus equation (4) becomes,

$$\tau = K\gamma^n \tag{2}$$

Gu and Mohanty (2015) expressed the shear stress at the wall as,

$$\tau_w = \frac{d\Delta p}{4L} \tag{3}$$

where $\tau_w$: yield stress at the capillary wall; d: inner diameter of the capillary tube; $\Delta p$: pressure drop along the capillary tube; L: Length of the capillary tube.
The $\gamma_{wa}$ at the capillary wall is calculated as,

$$\gamma_{wa} = \frac{8v}{d} \tag{4}$$

where $\gamma_{wa}$: apparent shear rate at the capillary wall; v: fluid velocity in the capillary tube.
Since the shear stress in equation (2) gives the intrinsic shear stress at the wall, the shear rate should also be the intrinsic shear rate expressed as,

$$\gamma_{wi} = \frac{3n'+1}{4n'}\gamma_{wa} \tag{5}$$

where $\gamma_{wi}$: the intrinsic shear rate at the capillary wall; $n\ or\ n'$: the flow index.
By plotting $\tau_w$ and $\gamma_{wa}$ in a log-log plot, the flow index is obtained as,

$$n' = \frac{dlog(\tau_w)}{dlog(\gamma_{wa})} \tag{6}$$

The flow index n is believed to be equal to the fitted $n'$ in equation (6). Then the consistency index K is expressed as,

$$K = \frac{K'}{\left[\frac{3n'+1}{4n'}\right]^{n'}} \tag{7}$$

where $K'$ is the wall shear stress at $\gamma_{wa} = 1s^{-1}$.
At last, the apparent visocisty $\mu_a$ is related to the intrinsic shear rate as

$$\mu_a = \frac{\tau_w}{\gamma_{wi}} = K\gamma_{wi}^{n-1} \tag{8}$$

The indices of *K* and *n* can be determined by plotting the straight line of $log(\tau_w) \sim log(\gamma_{wa})$. First, *n'* is obtained by the slope of the line according to equation (6). *K'* is the intercept of the line, in which the wall shear stress $\gamma_{wa}$ is $1s^{-1}$. Then the value of *n* is equal to the fitted $n'$ and *K* is calculated by equation (7).

### *5.1.2 Different factors effect on the $CO_2$ foam rheology*

#### *5.1.2.1 Determination of model indices K and n*

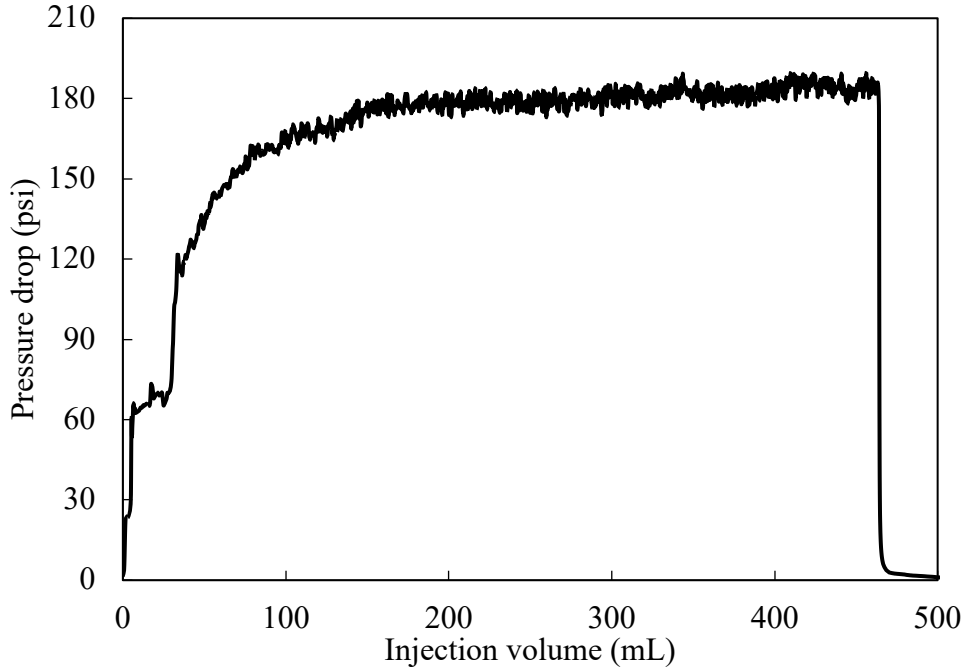


**Figure 5.2 Typical differential pressure over the capillary.**

Figure 5.2 shows a typical differential pressure along the capillary. This curve was obtained for 70% foam generated with 5000ppm nanosilica, 5% NaCl at 12mL/min total flow rate under room temperature. After the stabilization of the pressure readings, an average stabilized pressure value was used to calculate foam $\mu_a$. The $\tau_w$ and $\gamma_{wa}$ were calculated with the pressure drop and flow rate over the capillary tube. Figure 6.3 displays the *Log($\tau_w$) versus Log($\gamma_{wa}$)* for the foam quality of 70%. The slope and intercept of Fig. 5.3 are related to $n'$ and $K'$ values and are used to calculate $n$ and $K$ accourding to the equation (7). The $K$ and $n$ values obtained in Table 5.4 showed that all $n$>1, implying a shear-thickening behavior. Aroonsri et al. (2013) had generated nanosilica-stabilized $CO_2$ foams under high-pressure conditions and they obtained a consistency factor of 0.0039 Pa·s$^n$ and a flow index of 1.022, which is close to the results obtained here. However, due to the inherent complexity of foam rheology and the vastly differed experiment conditions, one needs to be cautious to compare the absolute values of the fitted $K$ and $n$. It is a case-by-case comparison in this study, but statistical tools might be needed to validate the effect of various foam configurations or experiment conditions on $K$ and $n$ when deemed necessary. Xiao et al. (2016) had investigated the effects of various variables on the power law parameters for nanosilica-stabilized $CO_2$ foams. According to their experimental results, the consistency index could fall at a magnitude of $10^{-6}$ for high-quality foams and $10^{-3}$ for lower quality foams. Table 5.4 shows that the $K$ values for foam qualities lower than 90% have a magnitude of $10^{-3}$ while the 90% foam shows a magnitude of $10^{-6}$. The absolute values of the $K$ and $n$ however did not show a clear pattern. Shear-thickening behavior had also been observed in their study and the flow index fell around $1.5 \pm 0.4$ with the low-end featuring low-quality foams and high-end featuring high-quality foams, which is consistent with the results obtained in this study.

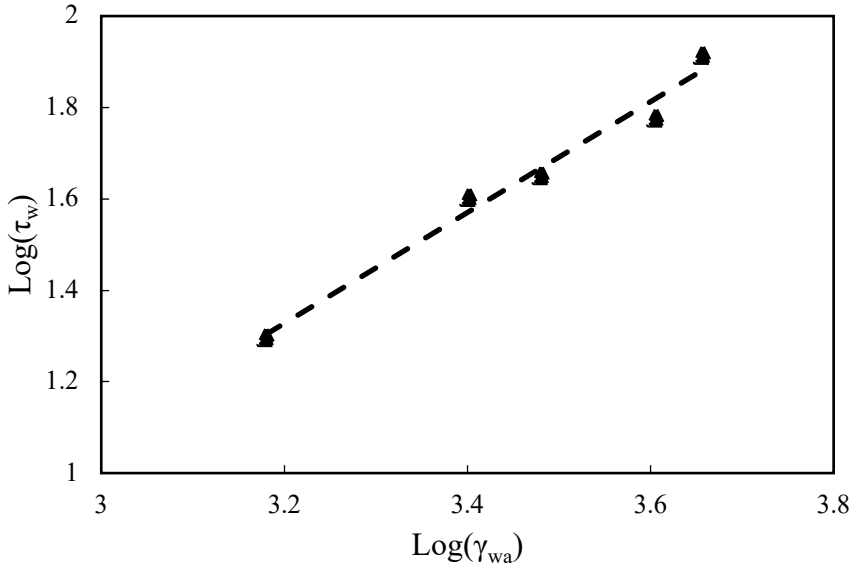


**Figure 5.3 Log($\tau_w$) versus Log($\gamma_{wa}$) for the foam quality of 70%.**

**Table 5.4** Rheological parameters for different Γ.

| Γ | Parameters estimated | | $R^2$ |
|---|---|---|---|
| | K (mPa·s$^n$) | n (Unitless) | |
| 10% | 0.0015131 | 1.211 | 0.997 |
| 30% | 0.0038828 | 1.126 | 0.994 |
| 50% | 0.0055802 | 1.124 | 0.980 |
| 70% | 0.0029623 | 1.213 | 0.981 |
| 90% | 0.0000052 | 1.866 | 0.974 |

*5.1.2.2 Foam quality effect on the foam rheology*

After the *K* and *n* values were determined, the $CO_2$ foam apparent viscosity, $\mu_a$, was calculated by $\mu_a = \frac{\tau_w}{\gamma_{wi}}$. At a specfic flow rate, intric shear rate is determined by equation (6) and shear stess, $\tau_w$, is calculated by measuring the pressure drop along the capillary tube. $CO_2$ foams with 10%, 30%, 50%, 70% and 90% qualities were generated with 5% NaCl and 5000ppm silica nanoparticle dispersion at 12mL/min and room temperature to study how Γ affected $\mu_a$. The $\mu_a$ of foams were plotted against foam qualities as shown in Fig. 6.4. As we can see, $\mu_a$ increases as Γ increases from 10% ~ 70%, and $\mu_a$ begins to drop as Γ continues increasing. The pattern of foam $\mu_a$ versus Γ is closely associated with the corresponding texture of the foam generated. As Fig. 5.5 shows, the generated $CO_2$ foam becomes finer-textured and appears denser with Γ increasing from 10% ~ 70%. Further increased the foam quality to 90% resulted in observable bubbles in the sapphire tube, which corresponded to the low apparent viscosity shown in Fig. 5.4.

It is believed that foam $\mu_a$ increased due to the generation of more liquid lamellae, the higher resistance to deform lamellae, and an increased surface tension gradient at the interfaces (Worthen, 2013). Finer textured foams have a higher density of lamellae and encounter more frequent deformation of bubbles. It is more difficult to deform bubbles with smaller radius according to the Young-Laplace equation, all of which could cause an increase in $\mu_a$. As shown in Fig. 5.4, the concave shape or the "mountain-shaped" curve of $\mu_a$ versus Γ has been found in several studies, but the corresponding Γ for the highest $\mu_a$ varies. The critical foam quality that leads to the peak $\mu_a$ varies across the literature, some of which are listed in Table 5.5.

**Table 5.5** Comparison of critical Γ corresponding to the peak $\mu_a$ in literature.

| Authors | Critical Γ value |
|---|---|
| Pang, 2010 | 85% |
| Zhu et al., 2017 | 74% |
| Mo and Yu, 2012 | 60% |
| Worthen et al., 2013 | 75% |
| Worthen and Mohanty, 2014 | 75% |
| This study | 70% |

Despite the differences in the critical foam quality values, the value generally should fall between 50% and 90% as pointed out by Worthen et al. (2013). This mountain-shaped curve is comprehensible from the point of lamellae transformation. As Γ increases in foam, an emulsion with dispersed bubbles is gradually transformed into packed bubbles supported by lamellae. The apparent viscosity of low-quality foams increases but only slightly, owing to the inadequate foam deformation. However, the $\mu_a$ of foams will stop increasing if further increase the foam Γ above a specific value (such as 70% in this study) since the bubble films get so thin that it does not require much energy to deform. Therefore, a typical curve of $\mu_a$ versus Γ displays a concave shape.

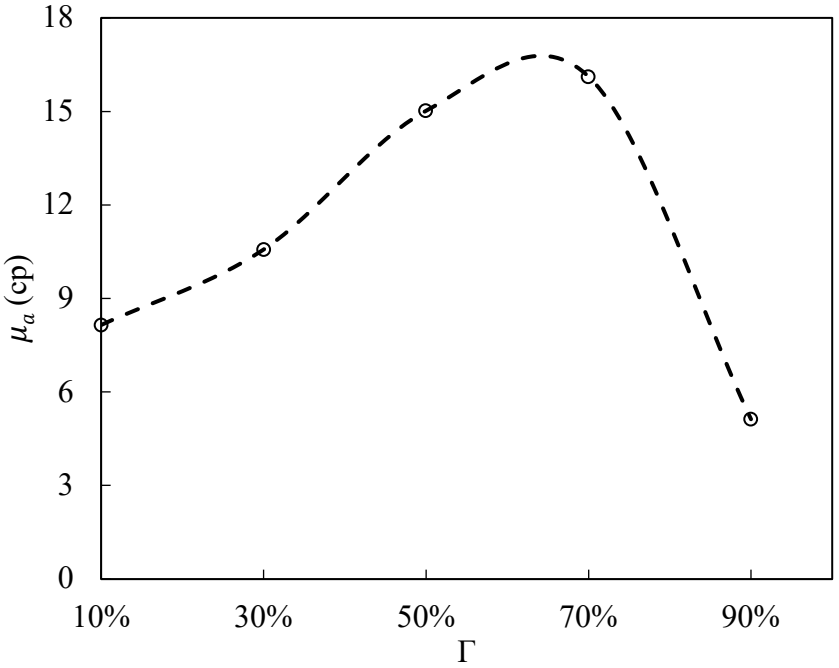


**Figure 5.4 The effect of Γ on $\mu_a$.**

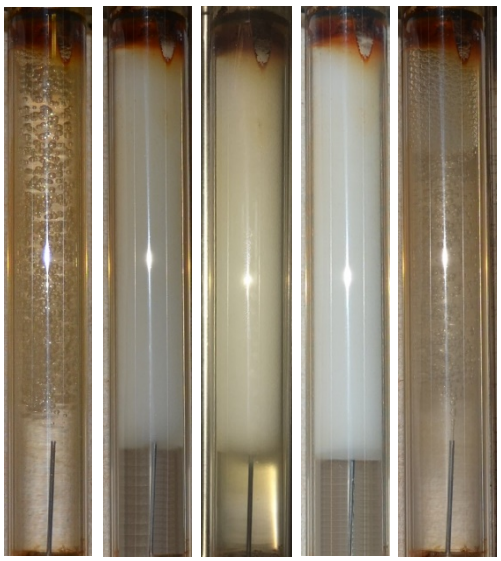


**Figure 5.5 $CO_2$ foam generation at different Γ.**

*5.1.2.3 Nanoparticle concentration effect on the foam rheology*

Nanoparticle concentration is another factor that affects foam stability and apparent viscosity. To investigate nanoparticle concentration effect on $CO_2$ foam apparent viscosity, $CO_2$ foams were generated with 70% quality under 5% NaCl and a flow rate of 12mL/min. The foam $\mu_a$ under different nanosilica concentrations were calculated and displayed in Fig. 5.6. When the nanosilica concentration increased from 500ppm ~ 3000ppm, the apparent viscosity kept increasing from 5.23 cp to 15.44 cp. For nanoparticle concentration above 3000ppm, the apparent viscosity was stabilized at around 16 cp. Further increase of the nanoparticle concentration above 3000ppm would no longer result in a higher $\mu_a$. The increase of foam apparent viscosity with the increasing nanosilica concentration might be attributed to a similar mechanism as in the analysis of Γ - the improvement of foam texture. Apart from more liquid lamellae and higher resistance to bubble deformation owing to the improved foam texture, the increase of nanoparticle concentration also improved the viscoelasticity of foam films, which increased the interfacial strength of the foam to resist external disturbance (Lv et al., 2015), thus consequently contributed to a higher foam $\mu_a$. However, there is a limit to this contribution to the interfacial viscoelasticity of foams. Nanoparticles will continue being absorbed into foam films during the initial increase of nanoparticle concentration. The distribution of nanoparticles was upgraded from deficiency to monolayer, to bilayer and to robust 3D network, which gradually improved the structural integrity of foam films. However, additional nanoparticles would no longer contribute to a significant improvement in viscoelasticity due to the limited interfacial area and would be diffused or proportioned within the interstice, which accounted for the stabilized foam $\mu_a$ in Fig. 5.6. Yet as foam films drained over time, the diffused nanoparticles might be stacked and cause cork formation, leading to improved foam stability.

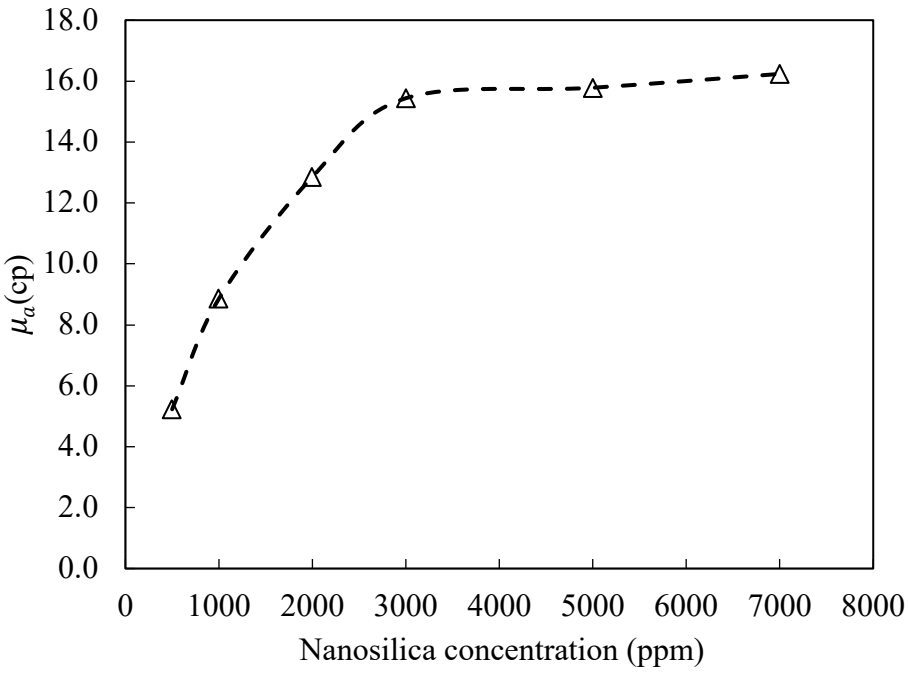


**Figure 5.6 $\mu_a$ versus nanosilica concentration.**

Foam generation results showed that a critical nanoparticle concentration was necessary to generate stable foams. As we can see from Fig. 5.7, separate foam bubbles with observable sizes were generated with a nanoparticle concentration of 500ppm, and the generated foam disappeared soon after the injection stopped. As nanoparticle concentration was increased to 1000ppm, a greyish-misty foam was generated, which looked finer than that of 500ppm and the foam lifetime was over 24 hours. When nanoparticle concentration was increased to 2000ppm and 3000ppm, the resulting foams displayed finer texture than that of 1000ppm, but the foam lifetime was almost the same as that of 1,000 ppm. The $CO_2$ foam generated with 5000ppm and 7000ppn nanosilica appeared brighter and finer-textured than the cases with 2000ppm and 3000ppm. The foam lifetimes were also greatly improved. Different mechanisms have been proposed regarding this improvement of foam stability above the threshold concentration.

To stabilize the interfaces between bubbles, a minimum concentration of 7000ppm nanoparticles was calculated to effectively cover the bubble films for 50μm diameter bubbles with 10nm of nanoparticle (Rio et al., 2014). The critical nanoparticle concentration 5000ppm obtained in this study from foam stability improvement is close to this estimated value. The improvement in the apparent viscosity and stability of foam indicates that increasing nanoparticle concentration in the aqueous phase can cover more interfacial space, prevents foam coalescence, and improves foam stability.

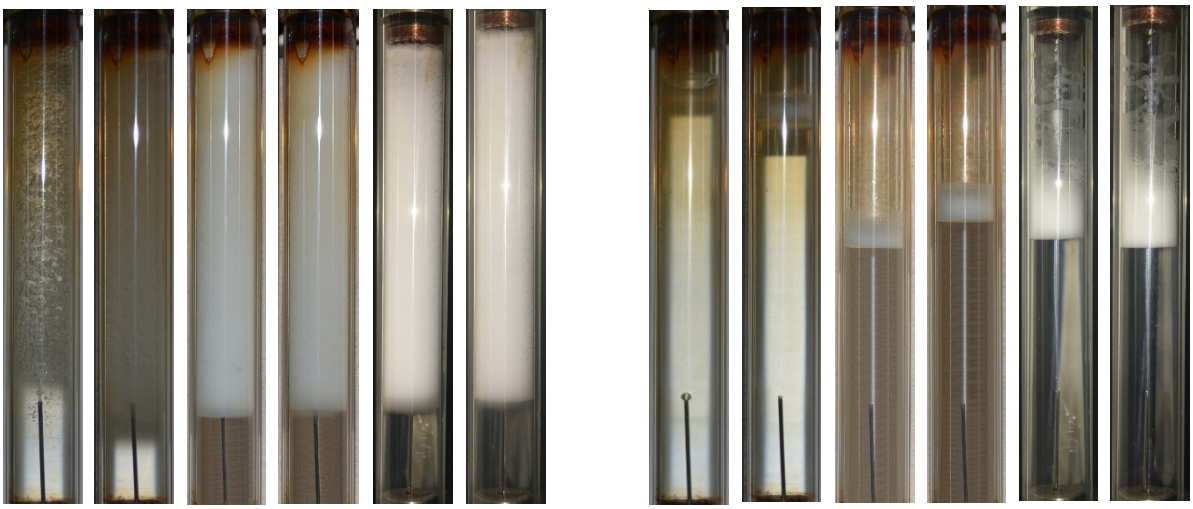


**Figure 5.7 Foam heights at different nanosilica concentrations:** Aa, Bb, Cc, Dd, Ee, and Ff (500, 1000, 2000, 3000, 5000, and 7000ppm). The left shows foam height at time 0 hour and the right shows foam height after 24 hours.

*5.1.2.4 Brine salinity effect on the foam rheology*

Reservoir fluid salinity is a critical factor that affects the foam stability and rheology. To investigate the effect of salinity, 70% $CO_2$ foams with different NaCl concentrations were generated at 5000ppm nanoparticles at 12mL/min total flow rate. The results in Fig. 6.8 show that $\mu_a$ increased from 3% to 9% salinity and kept increasing at a slower rate for higher salinities. As salinity increased from 3% to 11%, the $\mu_a$ increased from 11.3 cp to 34.5 cp. The increased NaCl concentration also improved foam stability. Figure 5.9 shows that the increasing salinity in the aqueous phase had resulted in brighter and finer foam textures, and the remaining heights of the foam after 24 hours increased with the increasing salinity.

Literature has documented the positive effects of salinity increase on improving nanosilica-stabilized foam stability (San et al., 2017). It was reported that an increasing electrolyte concentration in nanosilica dispersions could improve the hydrophobicity among the particles, which would contribute to better affinity among particles within the bubble films. The improved affinity between nanoparticles was further accounted by Kostakis et al. (2006), who found that the increasing concentration of electrolytes in the liquid phase could alter the energy state of the double-layer electrolyte around the nanoparticle. This effect would improve the liquid-particle contact angle and make it easier for nanoparticles to adsorb onto the bubble film, both of which could lead to better bubble stability. An electrolyte concentration higher than desired however, might result in the aggregation of nanoparticles. The aggregation could cause the disproportionation of nanoparticles around the bubble and the nanoparticles could not be distributed timely to cover the generated bubble, which undermined the foam texture and $\mu_a$ (Kostakis et al., 2006). *Figure* displays the incremental $\mu_a$ after 9% NaCl concentration gradually

decreases, as also found by Rahmani (2018) except for a lower 5% NaCl concentration in their study.

Foam stability and apparent viscosity responded to the increasing salinity in a similar pattern. The robust nanoparticle network required a higher force to deform, which contributed to a higher resistance for foam flow. The increasing NaCl concentration improved the affinity between nanoparticles, resulting in denser distribution of nanoparticles at the interfaces, which further improved the structural strength nano-network and thus better foam stability. Figure 5.10 displays that the half-life of foam reached 96hours for 70% quality $CO_2$ foam generated with 11% NaCl concentration, 5000ppm nanoparticle concentration at 12mL/min flow rate. The texture of the generated foam was also maintained for over 24 hours before bubbles with observable sizes occurred.

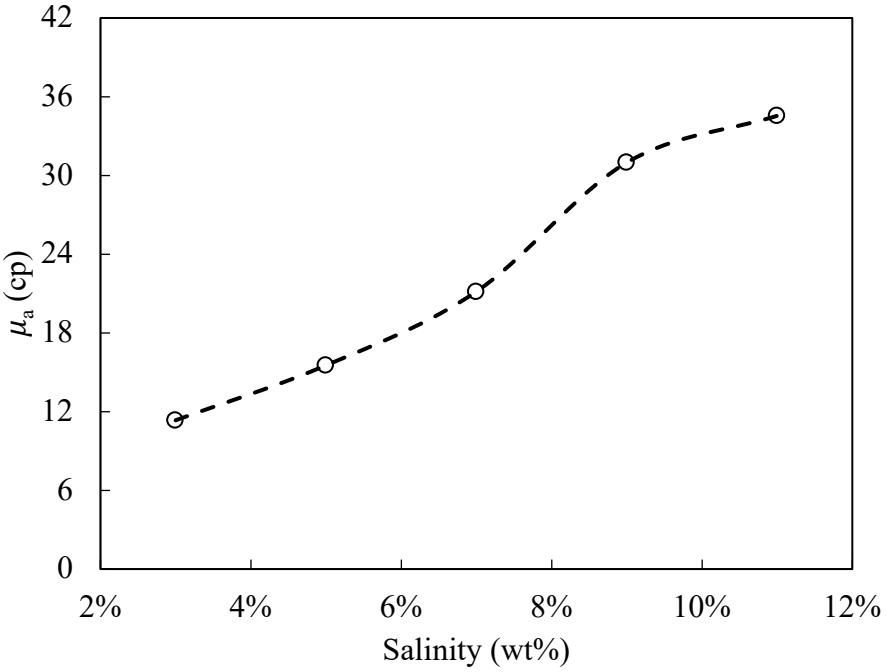


**Figure 5.8 Effect of NaCl concentration on $\mu_a$.**

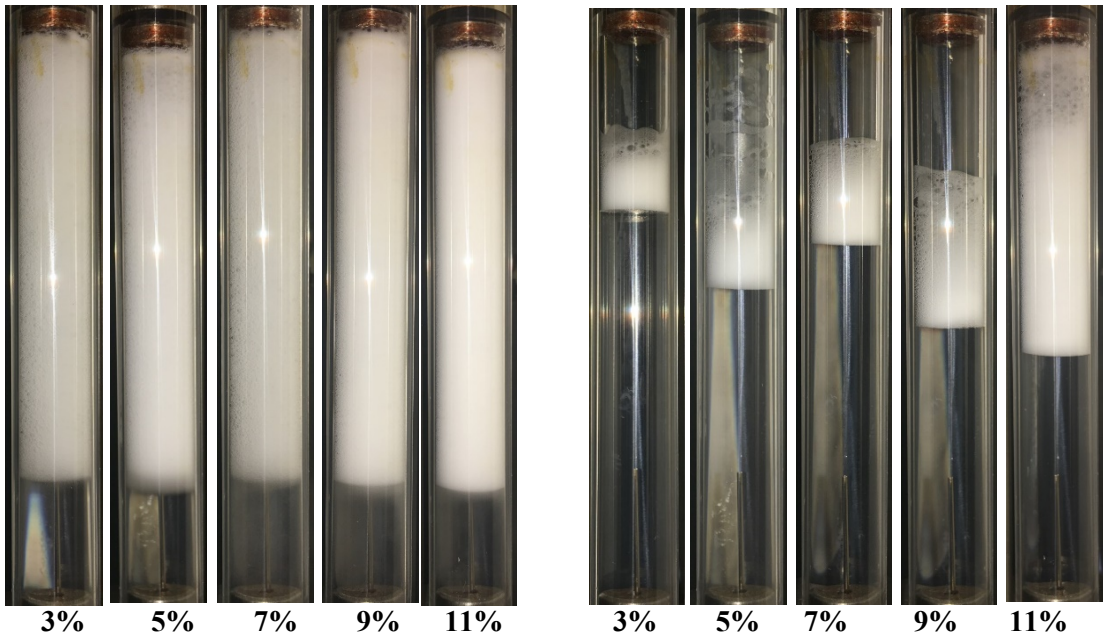


**Figure 5.9 $CO_2$ foam generated at different NaCl concentrations. The left shows foam height at 0 h and the right shows foam height after 24 hours.**

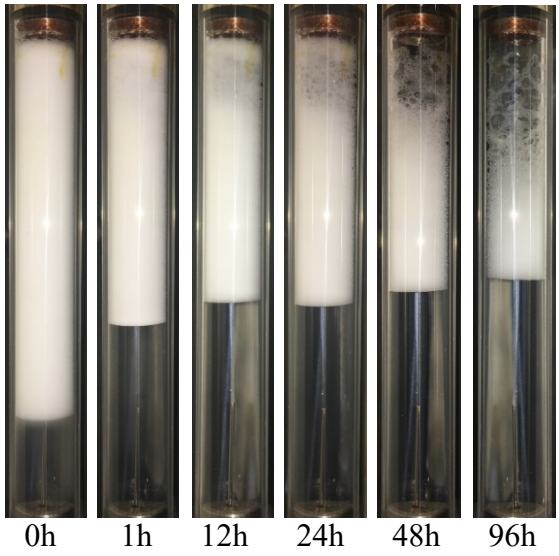


**Figure 5.10 Changes of foam height under 11% NaCl.**

*5.1.2.5 Shear rate effect on the foam rheology*

$CO_2$ foams were generated with different total injection rates to investigate how shear rate affected foam properties. The increase of the total injection rate increased both the shear forces in the beadpack to generate $CO_2$ foam and the shear rate in the capillary tube where the foam $\mu_a$ was evaluated. Figure 5.11 displays the results of the $\mu_a$ change under different shear rates. We can see that $\mu_a$ increased with the increase of shear rates from $1440s^{-1}$ to $4400s^{-1}$, showing a shear-thickening behavior, which had been commonly observed for foams generated in porous media

(Rahmani, 2018). The curves in Fig. 5.11 show that the foam $\mu_a$ increased with the increasing shear rate in the capillary tube, but the rate of increase decreased, showing a slight concavity. The reason for the concavity of the curve is that, during foam generation, higher total flow rates could provide stronger shear forces in the beadpack, which facilitated the passage of $CO_2$ into smaller pores resulting in the generation of finer-textured foams. Figure 5.12 shows that the foam got brighter with finer texture as the total flow rates increased. The improved foam texture led to a higher foam $\mu_a$. At the same time, the capillary shear rate was also increasing with the increasing total flow rate. The increase of capillary shear rates gradually took its thinning effects on the apparent viscosity of foam, which partially offset the thickening effect owing to the improved foam texture. The final apparent viscosity depends on which effect prevails. In this study, the investigated shear rate range is between 1440$s^{-1}$ and 4400$s^{-1}$, in which the effect of the improved foam texture dominates.

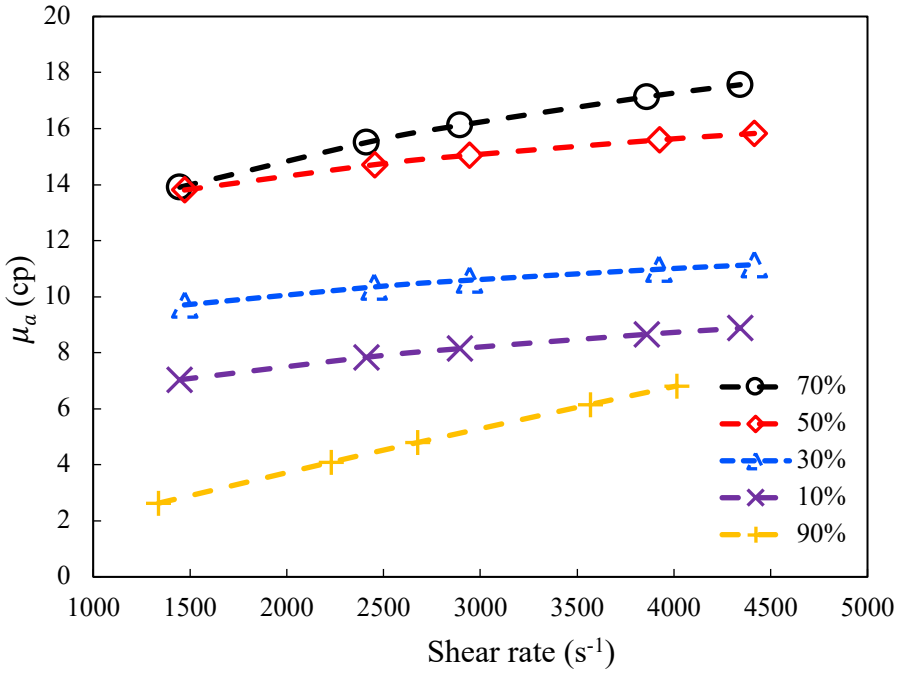


**Figure 5.11 $\mu_a$ versus shear rate at different Γ.**

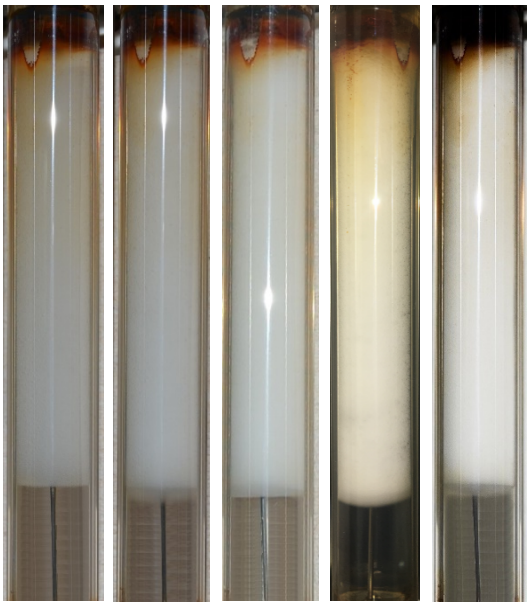


**Figure 5.12 $CO_2$ foam generated at different total flow rates; a to e represents 6, 10, 12, 16, 18mL/min, respectively.**

*5.1.2.6 Reservoir temperature effect on the foam rheology*

The thermal stability of foam is a critical factor affecting foam performance. The $\mu_a$ shown in Fig. 5.13 was obtained using a 70% Γ and 5000ppm nanosilica under a flow rate of 18mL/min. A higher flow rate is needed to generate foam at higher temperatures, which accounts for the flow rate increase from 12mL/min to 18mL/min. Figures 5.13 and 5.14 displayed the foam $\mu_a$ and stability at different temperatures, respectively. The $CO_2$ foam $\mu_a$ decreased with the increase of temperature. As the temperature began to increase from room temperature to 43 °C, foam $\mu_a$ decreases dramatically from 24.8cp to 5.5cp, and when the temperature continued increasing to 72 °C, foam $\mu_a$ gradually decreased from 5.5cp to 3cp. The decreasing viscosity of the continuous phase in the $CO_2$ foam in addition to the increased kinetic energy of the molecules has contributed to a less stable $CO_2$ foam system.

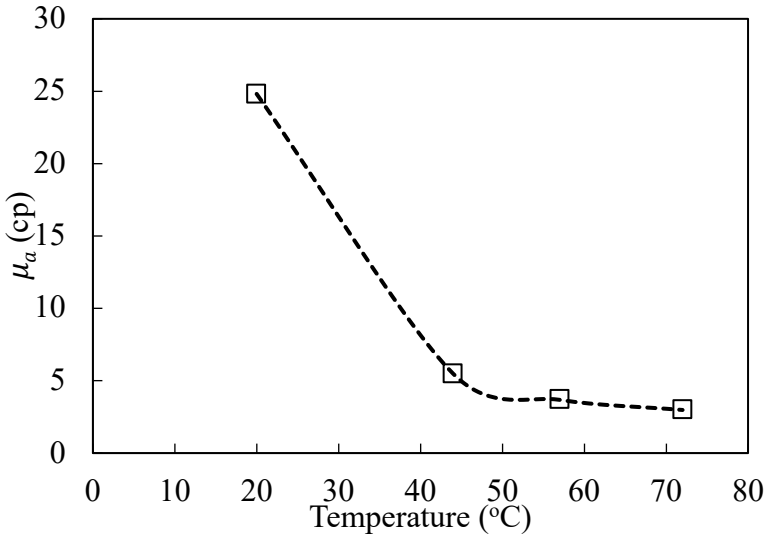


**Figure 5.13 Foam apparent viscosity versus temperature.**

The recorded foam heights (refer to Fig. 5.14) indicated that the generated foam became less bright and that the texture of the generated foam deteriorated with the increasing temperature. Besides, the amount of the generated foams was noticeably reduced, and the remaining foam heights also decreased faster under higher temperatures. As is shown in Fig. 5.14, the half-lives of the foams were around 12hours, 2 hours, 0.25hours under the temperatures of 20 °C, 43 °C, and 57 °C, respectively. The $CO_2$ foam generated at 72 °C barely lasted for 1 hour. The degradation of foams was accounted for by the accelerated foam bubble coalescence and film drainage under high temperatures over time. Bubbles with different sizes would coalesce with each other due to the difference in bubble pressure, and as the interface continued to drain, the bubble film gradually became thinner and eventually ruptured (Lv et al. 2015). By comparing the results of Fig. 5.13 and Fig. 5.14, the $CO_2$ foam displayed lower apparent viscosity values as the temperature increased, which was consistent with the poor foam stability under high temperature.

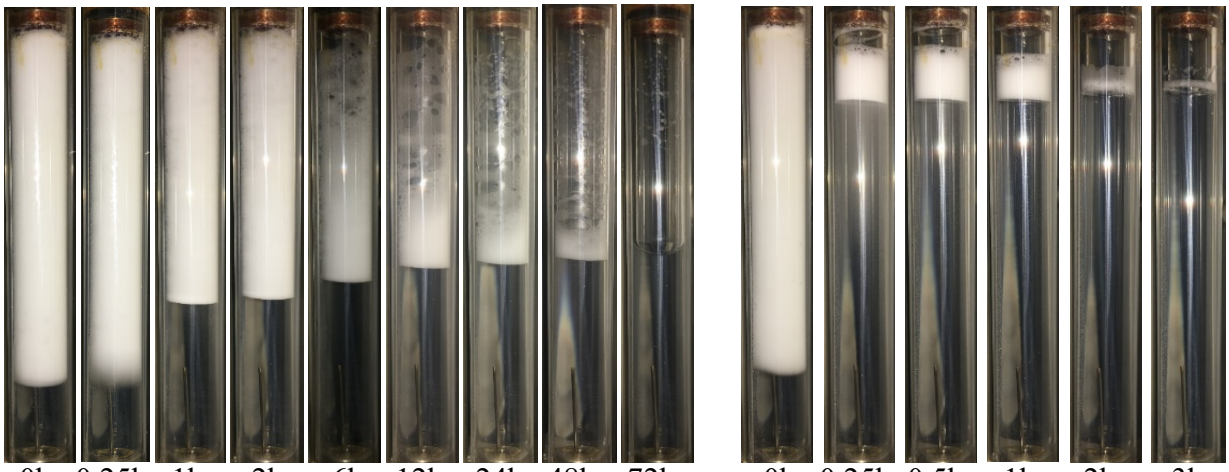


(a) 20°C (b) 43°C

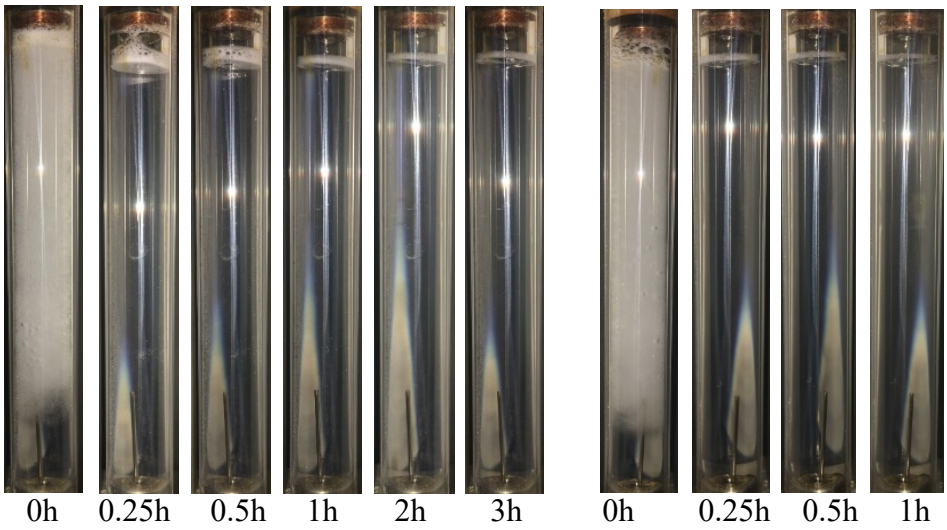


**Figure 5.14 Foam heights under different temperatures.**

*5.1.2.7 The addition of surfactant and polymer effect on the foam rheology*

Polymer is commonly used to thicken a fluid. The effect of polymer, 2-Hydroxyethyl Cellulose (HEC), on the stability and apparent viscosity of the $CO_2$ foam was investigated. The results are shown in Fig. 5.15. When a small amount of polymer (0.005%) was introduced to the $CO_2$ foam system with nanosilica, the $CO_2$ apparent viscosity dropped from 18.3 to 15.5cp, and the $CO_2$ foam apparent viscosity continued to increase to 20cp as the polymer concentration increased from 0.005% to 0.02%. It is known that the increase of concentration for both nanosilica and polymer will help improve the apparent viscosity of $CO_2$ foams. When a small concentration of polymer molecules was introduced to $CO_2$ foams with nanosilica, a portion of nanosilica became aggregated onto the long-chain polymer and decreased the active nanosilica concentration, which reduced the foam apparent viscosity. Although the presence of polymer may improve the foam apparent viscosity, the effect of reduced active nanosilica concentration was believed to prevail over the effect of the addition of polymer. As the polymer concentration continued increasing, the apparent viscosity was improved slightly but remained lower than the case without HEC. However, the effect of the increasing polymer concentration began to dominate after a concentration of 0.01%, which accounted for the increase of apparent viscosity after this polymer concentration. It is reasonable to expect that the foam apparent viscosity will continue increasing with the increasing HEC polymer concertation in Fig. 5.15 with a weak sign of leveling stable up to an HEC concentration of 0.02%.

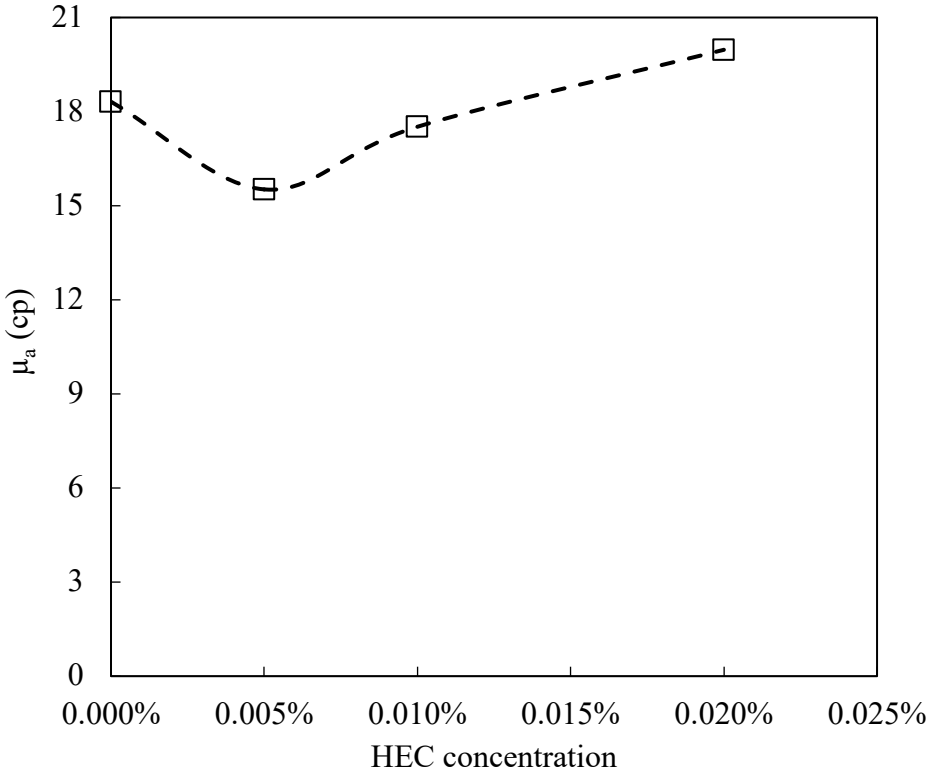


**Figure 5.15 Effect of HEC polymer concentration on foam apparent viscosity.**

To investigate foam performance at high temperatures, $CO_2$ foams were generated with a combination of nanosilica, Sodium Dodecyl Sulfate (SDS), and HEC polymer. The results were plotted in Fig. 5.16. The comparison of the curve of 0.02%SDS with (0.02%SDS+0.02%HEC) shows that the apparent viscosity of $CO_2$ foams was improved under higher temperatures with the presence of polymer. At a temperature of 57 $^oC$ and 72 $^oC$, the $CO_2$ foam apparent viscosity was improved by 36.6% and 24.1% with the addition of HEC polymer. The result implied that the nanosilica-SDS-polymer stabilized $CO_2$ foam system displayed less sensitivity towards elevated temperatures compared to the case without polymer. Overall, the presence of polymer in the nanosilica SDS stabilized $CO_2$ foam improved both the foam apparent viscosity and the foam thermal resistance.

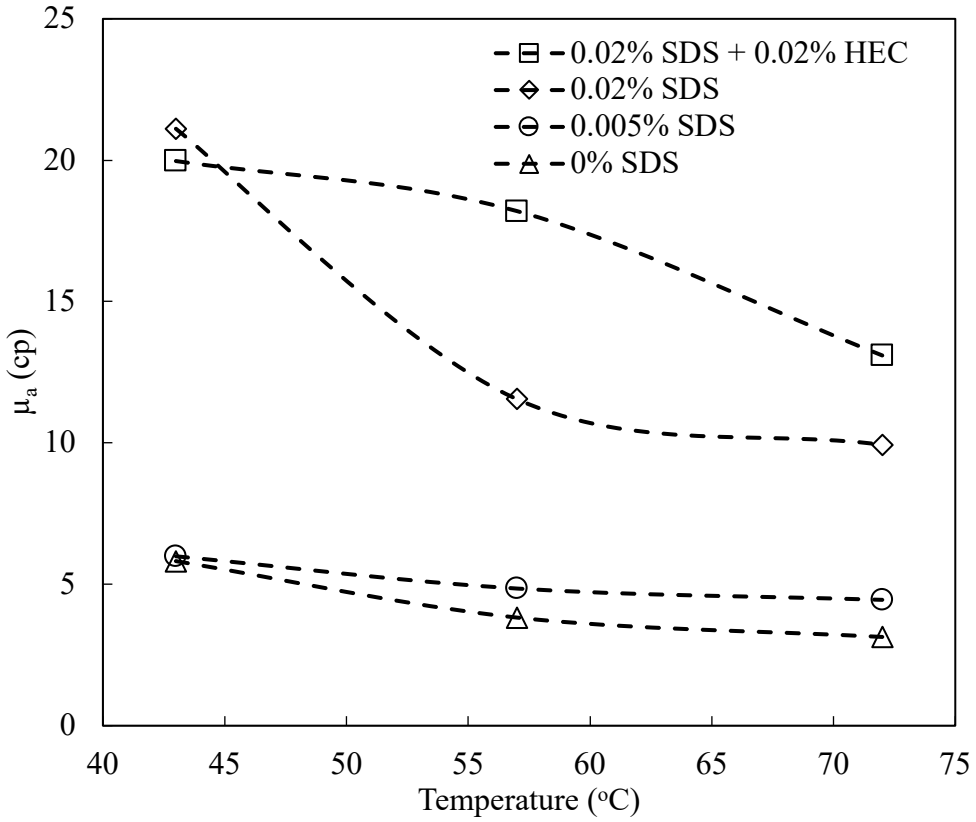


**Figure 5.16 Effect of polymer concentration on foam apparent viscosity under different temperatures.**

The stability of the $CO_2$ foam system was also improved with the addition of polymer. The change of $CO_2$ foam heights over time stabilized by 0.02%SDS and (0.02%SDS + 0.02% HEC) was shown in Fig. 5.17. As shown in Fig. 5.17, the $CO_2$ foam with 0.02%HEC polymer was more stable than the case without the polymer, and more foam was also generated with the addition of HEC polymer. The improvements in foam apparent viscosity and stability can also be explained from the perspective of the interweaved interactions among nanosilica, surfactants, and polymer. The polymer added to the nanosilica-SDS stabilized $CO_2$ foam system helped solidify the morphologic distribution of nanoparticles at the bubble interface, which strengthened the structural integrity of the spatial nanosilica network and improved foam stability. As illustrated in Fig. 5.18, the long-chain polymer interweaves through the aqueous interface among bubbles and connects the stabilizing nanosilica and foaming surfactant, which forms a three-dimensional structure that can not only maintain the interfacial morphology but also mitigates the drainage of the aqueous phase and ultimately improves foam stability.

It is worth mentioning that, though not shown, colloidal surfactant formed with polymer and SDS surfactants, or NP-SDS-HEC aggregates may also present in the aqueous phase, which helps slow down the drainage of the bubble film and increase foam interfacial strength and stability. It is believed that the degree of aggregation served more to stabilize the interfaces rather than forming large aggregates because the active concentration of the foaming and stabilizing SDS and

nanosilica were of the same charge and the HEC was of no charge. This still enables us to explain the effects of different combinations of additives on foam performance based on the interactive mechanism as illustrated in Fig. 5.16 and Fig. 5.18. Dehdari et al. (2020) assessed the rheology and stability of $N_2$ foams stabilized with different combinations of surfactants, nanoparticles, and polymers. They proposed that the synergy within the NP-SDS-HEC system followed a regularly layered pattern where the surfactant was distributed the closest to the interface, followed by nanoparticles and then polymer molecules. However, since the aqueous solution was usually prepared by mixing these additives before foam generation, an interactive mechanism was proposed here that the NP-SDS-HEC in the interfaces are irregularly interweaved together under the effect of various forces among these additives i.e. electrostatic forces, van der Waals force, adsorption, etc. As shown in Fig. 5.18, the interwoven structure at the bubble interfaces with nanoparticle, surfactant, polymer is illustrated. Surfactant molecules are mainly located around the bubbles and decrease the interfacial tension. Nanoparticles are located within the aqueous phase that function as rigid bricks for the structure, and the long-chain polymer interweaves through the aqueous interface that serves to stick everything together. This hypothesized interweaved structure enabled us to explain the results of foam property changes from the perspective of the interactions between nanosilica and different surfactants consistently, as has been extensively discussed earlier.

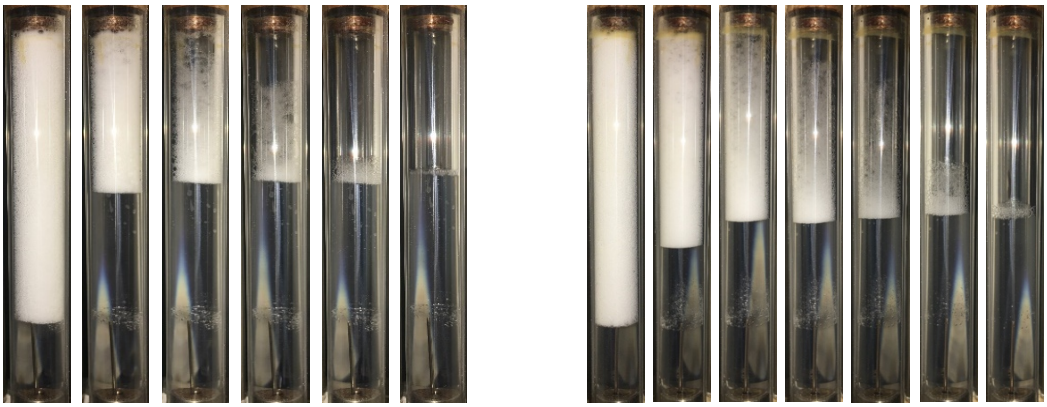


(a) 0.02%SDS (b) 0.02%SDS + 0.02%HEC

**Figure 5.17 Foam heights change over time with and without HEC at 72 °C.**

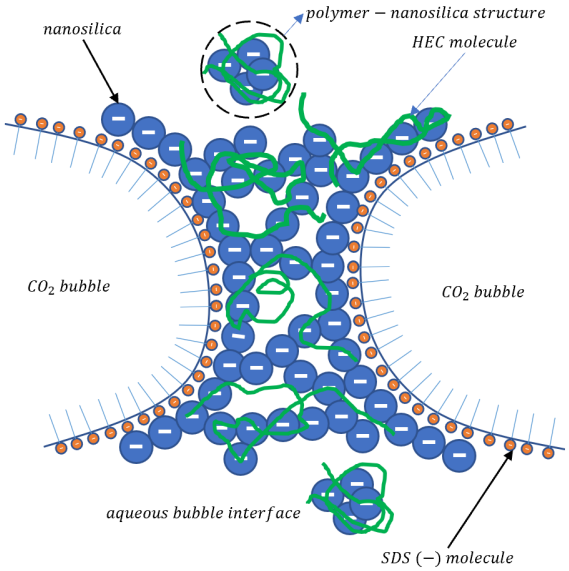


**Figure 5.18 Synergistic interactions among nanosilica, surfactant, and polymer at bubble interface.**

### *5.1.3 Leakoff assessment of nanoparticle-stabilized $CO_2$ foams*

#### *5.1.3.1 Experimental setup*

The schematic experiment setup for the $CO_2$ foam leakoff measurement is shown in Fig. 5.19. Two ISCO 500D pumps are used to pressurize two accumulators (2000mL from CoreLab) and provide constant flow rates during the experiment. One accumulator is used to store the gas phase $CO_2$ and the other to store the prepared nanosilica dispersion. Two Back Pressure Regulators (Equilibar H3P Series Precision BPR) are used to provide a threshold pressure of 1,500psi. The gas and liquid phase converge and is mixed in the beadpack, where shear forces are provided to generate a $CO_2$ foam. The generated $CO_2$ foam then flows across the surface of the core sample and then flows out to a buffer accumulator which is used to stabilize the pressure in the flow line. A BPR is installed at the end of the outlet to control the pressure (1,300psi) within the flowline of the system. During the leakoff test, $CO_2$ foam generated by the beadpack flows across the left cross-section of the core and flows out to the buffer accumulator. The core is placed inside a Hassler core holder from CoreLab is subject to a confining pressure of 2,000psi throughout the leakoff test. The BPR at the end of the core is bypassed and the end of the core is exposed to atmospheric pressure. The leakoff volume of gas is converted to calculate the leakoff coefficient under the system pressure of 1,300psi. The leaked liquid stays in the flask and the $CO_2$ exits the flask and flows across a flowmeter (Elehealthy MF5706/MF5712 Digital Gas Air Nitrogen Oxygen Mass Flowmeter 0-10L/min) that measures the accumulative volume of gas flow in real-time. The weight of the leakoff liquid is recorded every minute. The weight scale has an accuracy of 0.1 grams to distinguish the smallest weight change.

After each of the experiments, two sets of data, $V_{leakoff\ liquid}(mL)$ *vs.* time and $V_{leakoff\ gas}\ (mL)$ vs. time are obtained. The leakoff coefficients can then be calculated by the equations 1 and 2 shown in the section *Calculation of leakoff coefficients.*

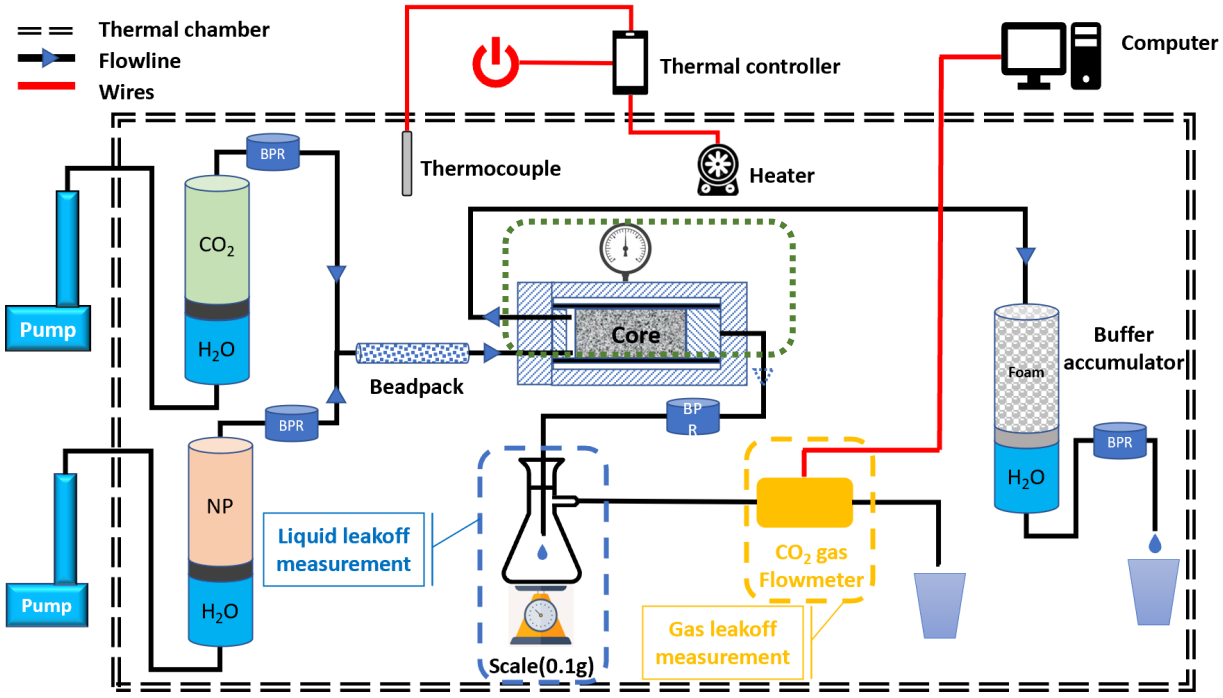


**Figure 5.19 Schematic experimental setup for foam leak-off test.**

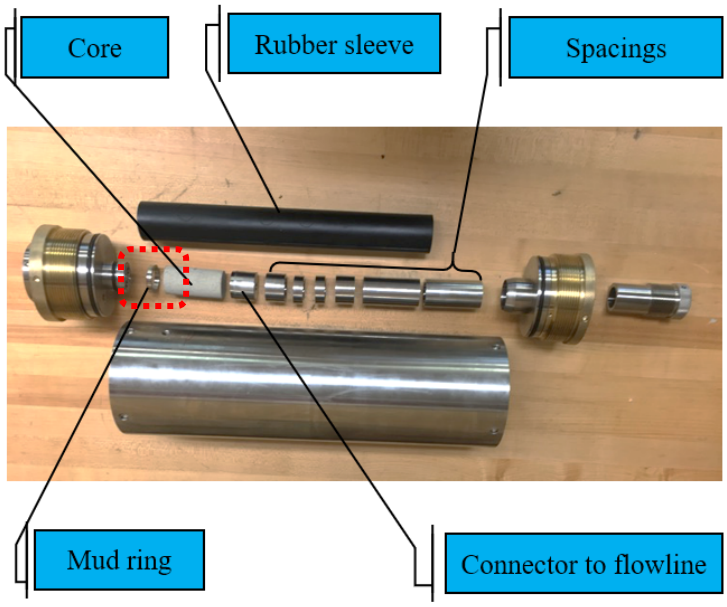


**Figure 5.20 Core holder assembly.**

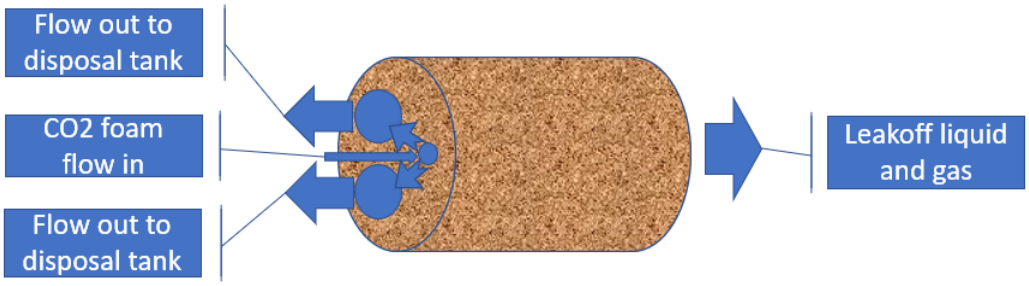


**Figure 5.21 Cross-section of Foam-Core contact.**

A detailed core holder assembly outlined by the green dotted line in Fig. 5.19 is shown in Fig. 5.20. The foam generated upstream flows onto the left cross-section of the core surface, which is preceded by a mud ring and flows out to the buffer accumulator. The gas and liquid phases of the $CO_2$ foam leak off through the core, which are then measured by the flowmeter and scale, respectively. The parts beginning from the mud ring to the rightmost spacing are all assembled into the rubber sleeve. A closer look at the Foam-Core contact area is shown in Fig. 5.21(outlined by the red dotted line in Fig. 5.19). There is a mud ring installed before the core. The entire cross-sectional area is in contact with the $CO_2$ foam. The blue arrows in *Figure* show the flow direction of foam. The $CO_2$ foam flows perpendicular to the core, flows along the core's sectional area, and then flows out through the flowline to the buffer accumulator. The leaked liquid and gas flow through the core and are measured by a scale and flowmeter.

Three types of cores are used in the leakoff test. Their properties are shown in Table 5.6. The cores are purchased from Kocurek Industries, Inc. at 8535 Hwy 36 South Caldwell, TX 77836. The permeability of the cores are selected with approximately one magnitude of difference apart to facilitate possible differences in experiment results. A core is used in different experiments where the permeability value is the same, which ensures that the core permeability is the same and eliminates potential heterogeneity issues when different cores with similar permeabilities are used. A core is also backflushed to the original permeability before it is used for the next experiment to ensure permeability consistency.

**Table 5.6** Properties of core samples.

| Sample # | Product ID | Diameter (inch) | Length (inch) | Porosity | Permeability ($mD$) |
|---|---|---|---|---|---|
| 1 | Berea Upper SS-105 | 1.5 | 3 | 17.3% | 46.41 |
| 2 | Carbon Tan SS-109 | 1.5 | 3 | 10.2% | 3.90 |
| 3 | Kentucky SS-114 | 1.5 | 3 | 13.3% | 0.43 |

The leakoff experiments are conducted to simulate the flow of the foam fracturing fluid during a fracturing operation. When the foam is injected into the formation, the flow is flowing across the

surface of the matrix, which we termed as dynamic leakoff; during the shutoff period, after foam injection is stopped, the foam is not flowing across the matrix surface, which is termed as static leakoff rate. Both leakoff rates are important as they are indicators of how foam leaks off into the matrix during different stages of fracturing.

According to Ribeiro and Sharma (2012), the leak-off coefficient can be calculated as,

$$V = V_{sl} + m * \sqrt{t} \quad (9)$$

$$C_w = 0.0328 * \frac{m}{A_c} \quad (10)$$

where V is the total leakoff volume, $cm^3$, $V_{sl}$ is the spurt leakoff volume before the steady leak off, $cm^3$, m is the slope of the $V_{leakoff}(mL)\ vs\ \sqrt{t}\ (\sqrt{min})$ curve, $t$ is the time elapsed, min, $A_c$ is the cross-sectional area of the core, $cm^2$, $C_w$ is the leak-off coefficient, $\frac{ft}{\sqrt{min}}$.

The volumes of the leaked liquid and gas are recorded and plotted over the square root of time. The slope of the plot m is used to calculate the leak-off coefficient $C_w$ as shown in the $C_w$ calculation equation. Both the dynamic and static leakoff coefficients of the liquid and gas are measured. The dynamic leakoff coefficient is measured during the foam flow. After the foam flow is stopped, the leakoff volumes of gas and the weight of liquid are continuously recorded to calculate the static leakoff coefficient. A higher leakoff coefficient indicates that a higher leakoff rate, so the leakoff coefficient and leakoff rate of the liquid or gas will be used interchangeably in this study.

*5.1.3.2 The $CO_2$ foam leakoff measurement under different conditions*

After the weight of the leaked liquid and the volume of the leaked gas are obtained over time, a typical leakoff curve can be distinguished into two parts: dynamic leakoff and static leakoff. The leakoff curve in Fig. 5.22 features a 10% foam stabilized only by nanosilica at 25°C.

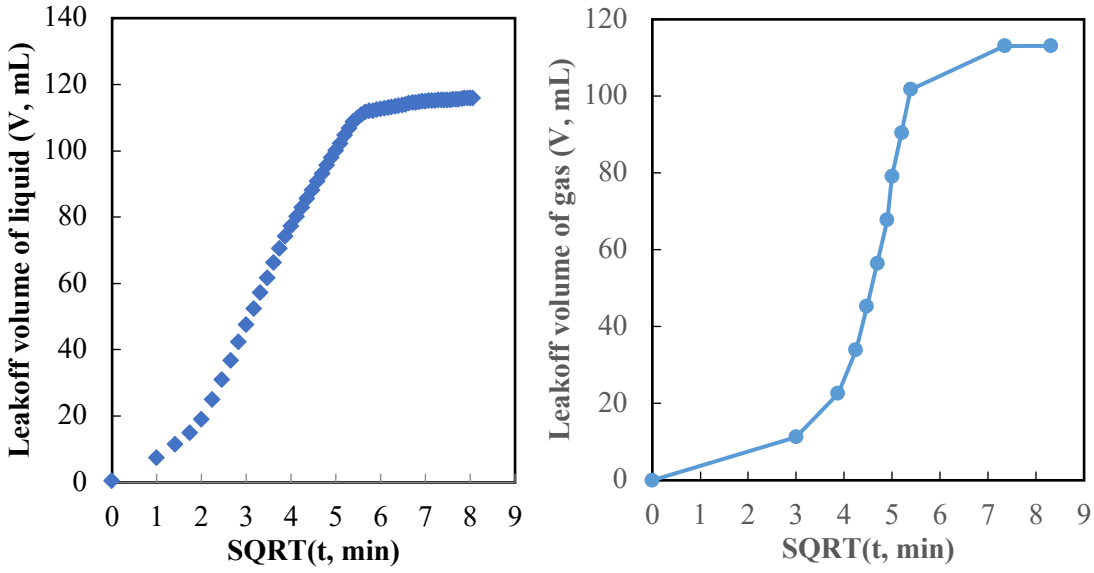


**Figure 5.22 Leakoff volume of liquid (left) and gas (right) with time for 10% foam stabilized solely by nanosilica at 25°C.**

The results of Fig. 5.22 indicate that the foam leakoff curve (liquid and gas) falls into two parts. A straight curve can be fitted for each of the two sections as shown in Fig. 5.23 (a b for liquid and c d for gas). After the slope of the $V_{leakoff}(mL)\ vs\ \sqrt{t}\ (\sqrt{min})$ is obtained, equation (10) can be used to calculate the leakoff coefficients. In this case, the calculated $C_{dynamic\_liquid}$ and $C_{static\_liquid}$ are $0.06738 ft/\sqrt{min}$, $0.004387\ ft/\sqrt{min}$, respectively. With the similar procedure, $C_{dynamic\_gas}$ and $C_{static\ \_gas}$ are obtained as $0.1716\ ft/\sqrt{min}$ and $0.01194\ ft/\sqrt{min}$. For comparison, the leakoff coefficient of brine was measured under the same conditions as the $CO_2$ foam. A clear linear trend was observed for both of the dynamic and static processes after fitted $V_{leakoff}(mL)\ vs\ \sqrt{t}\ (\sqrt{min})$. The leakoff coefficients for the $CO_2$ foam and brine are summarized in Table 5.7 for a comparison. The results in Table 5.7 indicate that the dynamic leakoff coefficient of brine is almost 4 times that of the liquid phase of the $CO_2$ foam. The static leakoff coefficient of brine is about 4.6 times that of the liquid phase of the $CO_2$ foam. These drastic reductions in liquid leakoff suggest that foam fracturing fluid can be a great candidate for stimulating water-sensitive formations while mitigating formation swelling.

**Table 5.7** Comparison of leakoff coefficients of the $CO_2$ foam and brine.

| Fluid configuration | Leakoff coefficients ($ft/\sqrt{min}$) | | | |
|---|---|---|---|---|
| | Dynamic $C_w$ | | Static $C_w$ | |
| Pure water, 1300psi, 18mL/min | 0.26430 | | 0.02000 | |
| 10% quality, 5% NaCl, 5000ppm NP, 1300psi, 18mL/min | $C_{wgas}$ | $C_{wliquid}$ | $C_{wgas}$ | $C_{wliquid}$ |
| | 0.1716 | 0.06738 | 0.01194 | 0.00439 |

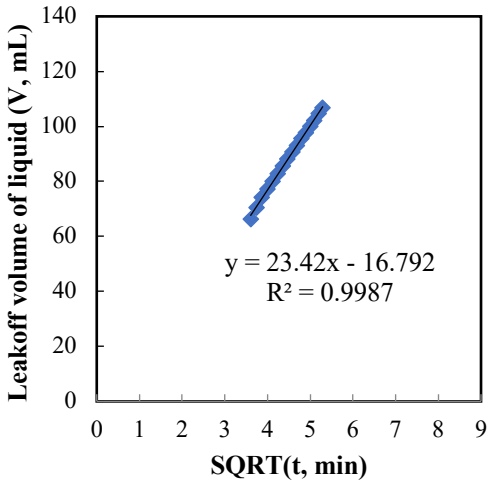


(a) Dynamic liquid leakoff

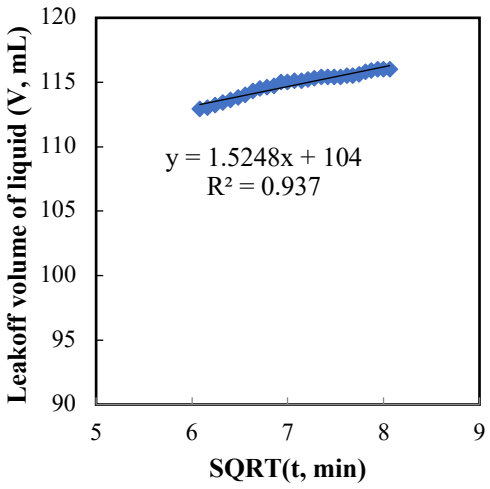


(b) Static liquid leakoff

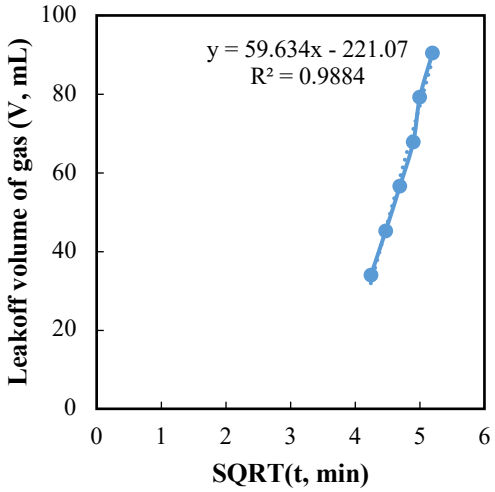


(c) Dynamic gas leakoff

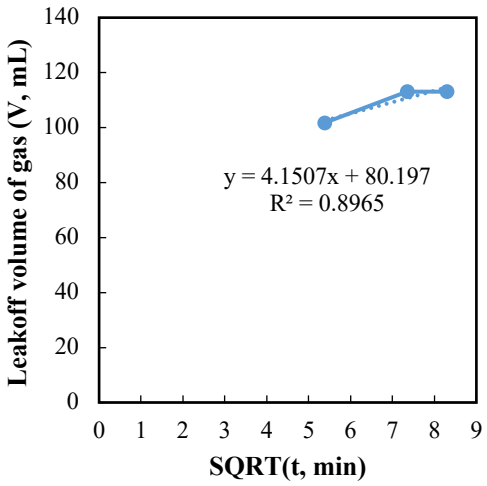


(b) Static gas leakoff

**Figure 5.23 Calculation of the slope m for the dynamic and static liquid leakoff.**

The results of leakoff coefficients in this study are summarized in Table 5.8. The sensitivity analysis of the effects of different parameters on leakoff coefficients is further discussed in the sections that follow.

**Table 5.8** Summary of leakoff coefficients.

| Number | Foam quality | HEC (wt%) | SDS (wt%) | k (mD) | Leakoff coefficient $ft/\sqrt{min}$ | | | |
|---|---|---|---|---|---|---|---|---|
| | | | | | Dynamic | | Static | |
| | | | | | Liquid | Gas | Liquid | Gas |
| 1 | 0% | 0% | 0.00% | 3.9 | 0.26430 | 0.00000 | 0.02000 | 0.00000 |
| 2 | 10% | 0% | 0.00% | 3.9 | 0.06738 | 0.1716 | 0.00439 | 0.01194 |
| 3 | 30% | 0% | 0.00% | 3.9 | 0.00371 | 0.36402 | 0.00536 | 0.01226 |
| 4 | 50% | 0% | 0.00% | 3.9 | 0.00492 | 0.36379 | 0.00129 | 0.45496 |
| 5 | 70% | 0% | 0.00% | 3.9 | 0.00073 | 0.39282 | 0.00061 | 0.41207 |
| 6 | 90% | 0% | 0.00% | 3.9 | 0.03978 | 0.04409 | 0.00000 | 0.15358 |
| 7 | 70% | 0% | 0.00% | 0.43 | 0.00036 | 0.19744 | 0.00049 | 0.07498 |
| 8 | 70% | 0% | 0.00% | 46.41 | 0.10562 | 1.37015 | 0.00060 | 0.43960 |
| 9 | 70% | 0.02% | 0.02% | 3.9 | 0.01206 | 0.03000 | 0.00134 | 0.20680 |
| 10 | 70% | 0% | 0.005% | 0.43 | 0.00074 | 0.00000 | 0.00122 | 0.00000 |
| 11 | 70% | 0% | 0.01% | 0.43 | 0.00139 | 0.00000 | 0.00053 | 0.00000 |

| | | | | | | | | |
|---|---|---|---|---|---|---|---|---|
| 12 | 70% | 0% | 0.02% | 0.43 | 0.00091 | 0.00000 | 0.00048 | 0.00000 |
| 13 | 70% | 0% | 0.03% | 0.43 | 0.00060 | 0.00000 | 0.00084 | 0.00000 |
| 14 | 70% | 0.02% | 0.02% | 0.43 | 0.00051 | 0.00000 | 0.00070 | 0.00000 |
| 15 | 70% | 0.06% | 0.02% | 0.43 | 0.00034 | 0.00000 | 0.00029 | 0.00000 |

*The $CO_2$ foam quality effect on the leakoff coefficients*

To study the effect of foam quality on the leakoff, the Carbon Tan core with a permeability of 3.9mD is used. $CO_2$ foam is generated at a foam quality of 10%, 30%, 50%, 70%, and 90%, and the corresponding leakoff coefficients of the gas and liquid phase are obtained. The results are plotted in Fig. 5.24.

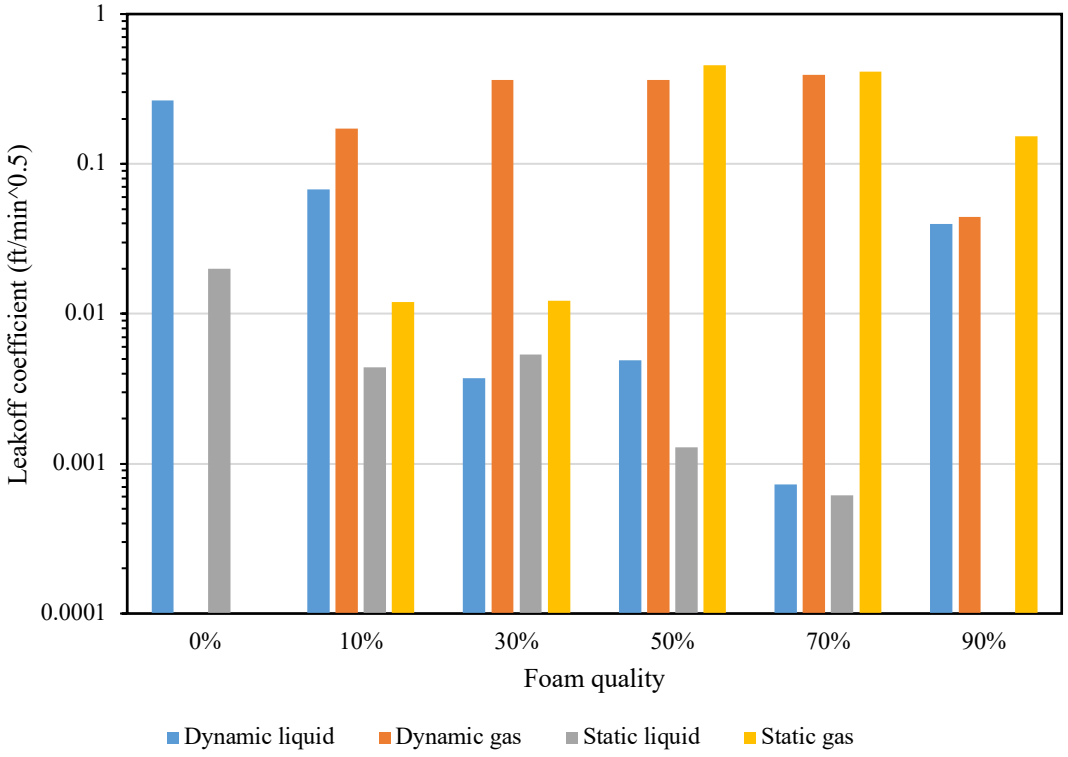


**Figure 5.24 Effect of foam quality on the dynamic and static leakoff coefficients for gas and liquid in the Carbon Tan core (3.9mD).**

Figure 5.24 shows that the gas phase generally shows higher leakoff coefficients than the liquid phase. As we can see that with the increase of the gas content in the $CO_2$ foam from 0% to 70%, the dynamic leakoff of the liquid phase is greatly reduced. The dynamic leakoff of the liquid in 90% foam shows a higher value than that of the 70% foam. This might be caused by the more stable foam generated in 70% foam which traps the liquid in the lamellae and reduces the liquid leakoff process. The dynamic gas leakoff coefficient during foam injection generally increases with the increase of foam quality from 10% to 70%. The 90% quality foam shows a much lower

dynamic gas leakoff coefficient. According to the results of the previous study, the $CO_2$ foam with 90% quality does not show a texture that is as fine as the 70% or the 50% foam. The bubble sizes are noticeably larger than foams with a lower gas percentage. Since the liquid content in the 90% foam is very small, the majority of the core contact area might be occupied by the gas phase. Before the foam breaks through the core, the gas phase is displacing the liquid phase during the injection process. This results in a higher liquid leakoff and a lower gas leakoff rate compared with that of the 70% foam.

*Core permeability effect on the leakoff coefficients*

The permeability of the core sample directly reflects the types of formation that the foam system is used upon. In this experiment, the permeabilities of the cores are selected so that they are approximately in a magnitude of difference, which are 0.43mD, 3.9mD, and 46.41mD. The leakoff coefficients for the liquid and gas phases using different permeabilities are shown in Fig. 5.25. The leakoff coefficients are shown on a logarithmic scale to demonstrate all values.

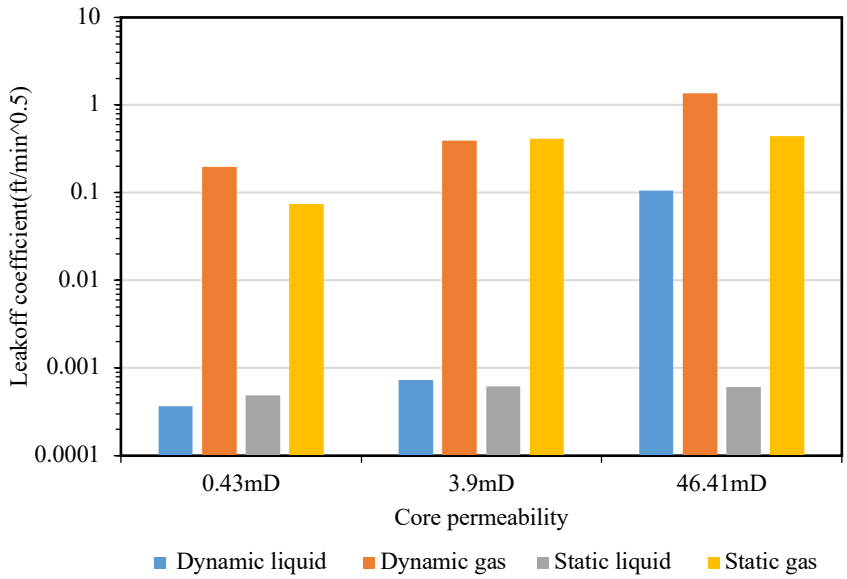


**Figure 5.25 Leakoff coefficients versus core permeability.**

Under the same experimental conditions, the liquid leakoff rate for cores with lower permeability (0.43mD, 3.9mD) foam flow is significantly lower than that with higher permeability (46.41mD). For dynamic leakoff of liquid, a 9 times increase of core permeability (from 0.43mD to 3.9mD) resulted in a 2 times increase in $C_{dynamic_{liquid}}$ from $0.000364 ft/\sqrt{min}$ to $0.000729\ ft/\sqrt{min}$; and when the permeability increased by 12 times from 3.9mD to 46.41mD, $C_{dynamic\_liquid}$ is increased by over 140 times from $0.000729 ft/\sqrt{min}$ to $0.1056 ft/\sqrt{min}$. The results indicate that the increase of core permeability from the lower permeability range to the higher permeability could significantly increase the liquid dynamic leakoff rate. For the gas leakoff, the dynamic leakoff coefficients are increased by 2 times and 3.5 times when the core permeability increased from 0.43mD to 3.9mD and from 3.9mD to 46.41mD, respectively.

The static leakoff rate of liquid or gas is also an important performance evaluation matrix for $CO_2$ foam. After the injection of $CO_2$ foam and proppants, the wellbore is shut down to allow for the settlement of the proppants. The liquid and gas phase in the newly generated fractures could leak off into the rock matrix as well, but the pressure drop from the fracture to the matrix will be lower compared to the injection period as there is no active pumping pressure during the shutoff period. In the measurement of the static leakoff coefficients, the left side of the core is still in contact with the foam phase. As the foam leakoff through the core, the pressure in the tank (which is connected to the high-pressure side of the core) will drop continuously. This process is intended to simulate the pressure drop in the fracture despite that it might not fully represent the pressure profile in the fracture because it is mainly the gas phase that is in contact with the core.

As shown in Fig. 5.25, the static leakoff of liquid is very low and is almost the same for each of the three permeabilities. For the static leakoff of gas, the 3.9mD and 46.41mD cores showed similar leakoff coefficients while the 0.43mD core corresponded to a much lower static gas leakoff. This much lower gas leakoff coefficient might be caused by the higher resistance for gas flow in the lower permeability cores. This high resistance could be attributed to the intrinsic small pore throat and higher capillary pressure.

*Surfactant concentration effect on the leakoff coefficient*

Nanoparticles and surfactants are reported to create a synergistic effect for a multiphase system. The leakoff coefficients of $CO_2$ foam are measured at different concentrations of surfactant. The dynamic and static leakoff coefficients for the liquid and gas phases are shown in Fig. 5.26.

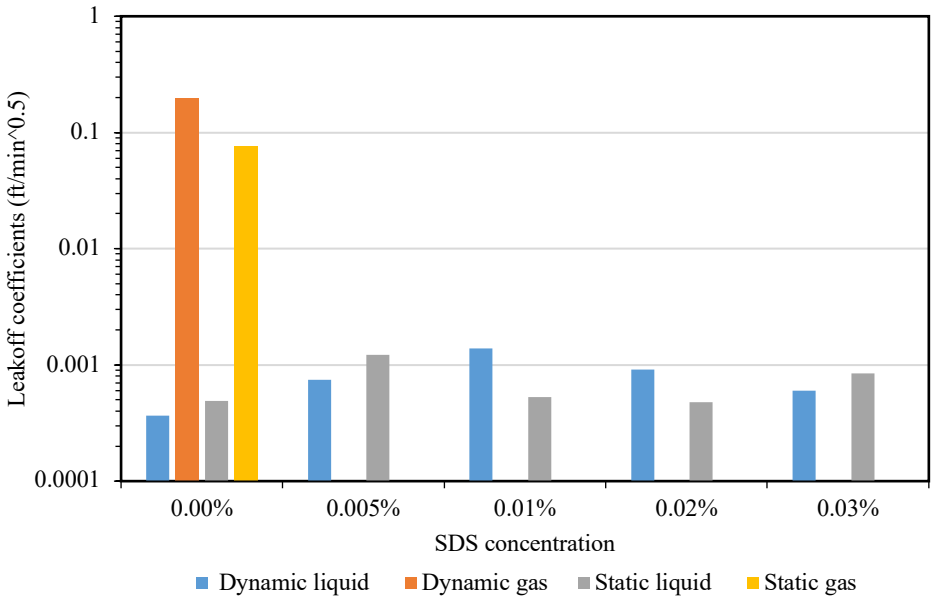


**Figure 5.26 Effect of SDS concentration on the dynamic and static leakoff of liquid and gas for the Kentucky core (0.43mD).**

Figure 5.26 shows the static leakoff coefficients under different surfactant concentrations using the Kentucky core with 0.43mD permeability. The results in Fig. 5.26 indicate that the introduction

of SDS into nanosilica dispersion can significantly reduce the gas leakoff coefficient. With the presence of SDS even at a small concentration, both the dynamic and static leakoff of the gas is reduced to the extent that no gas leakoff has been detected during the experiment. The dynamic leakoff of liquid is not affected much in low concentrations of SDS. As the concentration of SDS increased from 0% to 0.01%, the dynamic leakoff of liquid increases and then decreases as the concentration of SDS further increases from 0.01% to 0.03%. The addition of SDS may have produced finer-textured foams with higher apparent viscosity, which increased the resistance for the foam to flow in the porous media. The resultant finer texture of the foam and the higher apparent viscosity could reduce the possibility of $CO_2$ foam fingering in the porous media, which accounted for the absence of the leaked gas phase in the effluent when SDS is added.

*Polymer concentration effect on the leakoff coefficient*

Polymers are one of the common additives that are used to thicken a fluid system. The addition of long-chain polymers into the aqueous phase usually increases the apparent viscosity of the fluid and hence improves the fluid property to carry proppant. The higher the concentration of the polymer, the thicker the fluid will get. The addition of long-chain polymers can also help form a much less permeable filter cake at the fracture surface, thus reducing the leakoff of the fracturing fluid. In this study, the concentration of the polymer is controlled to be much lower than what is seen in the literature. This enables us to look into the interactive mechanism of how polymers can enhance the performance of the fluid system such as apparent viscosity or fluid/gas leakoff.

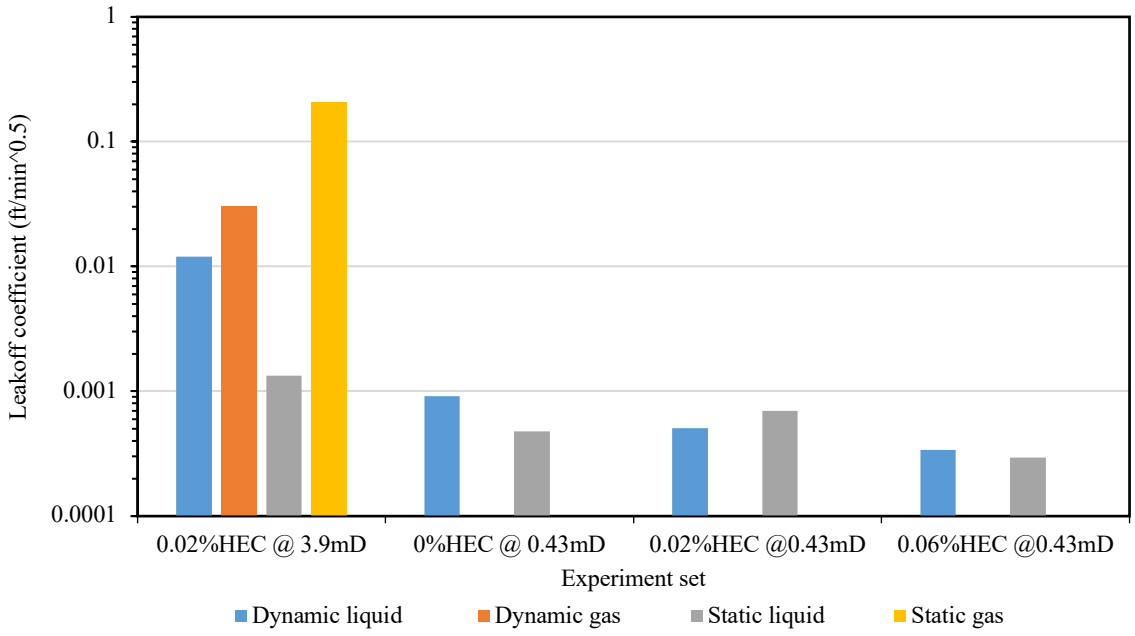


**Figure 5.27 Dynamic and static leakoff coefficients of liquid and gas.**

Figure 5.27 shows the dynamic and static leakoff of liquid and gas of four different systems: 1) 0.02%SDS + 0.02%HEC using 3.9mD core; 2) 0.02%SDS + 0%HEC using 0.43mD core; 3)

0.02%SDS + 0.02%HEC using 0.43mD core; 4) 0.02%SDS + 0.06%HEC using 0.43mD core. The addition of polymers in the aqueous phase has decreased the leakoff of the liquid phase, but the leakoff coefficient of the gas phase does not show a monotonous pattern nor induces significant changes in leakoff coefficients. This implies that the formed polymer filter cake on the rock surface mainly prevents the liquid leakoff and has little effect on gas leakoff. Comparing the effect of core permeability to that of polymer concentration, the results of Fig. 5.27 indicate that core permeability has a much stronger impact on leakoff than adding the polymer.

## 5.2 Fluid flow in superhydrophobic and hydrophilic proppant packed fractures

Two kinds of proppants, superhydrophobic and hydrophilic, are used for this study. The sessile water drop method was used to measure the contact angle of the proppants (Figs. 5.28 and 5.29). The core properties are shown in Table 5.9 and the core images in Fig. 5.30.

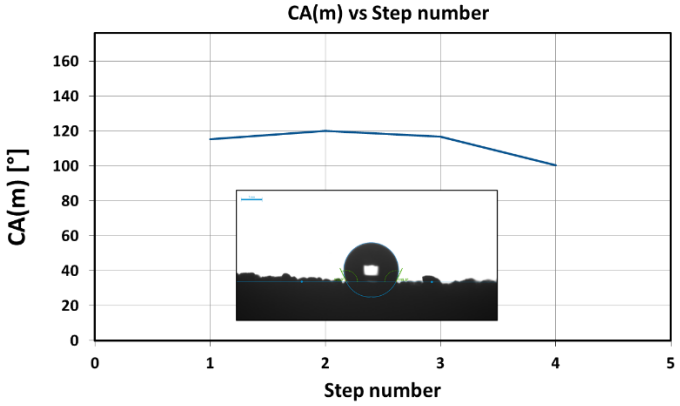


**Figure 5.28 Contact angle measurement for oil-wet proppants (Superhydrophobic).** Average contact angle= 113.19°

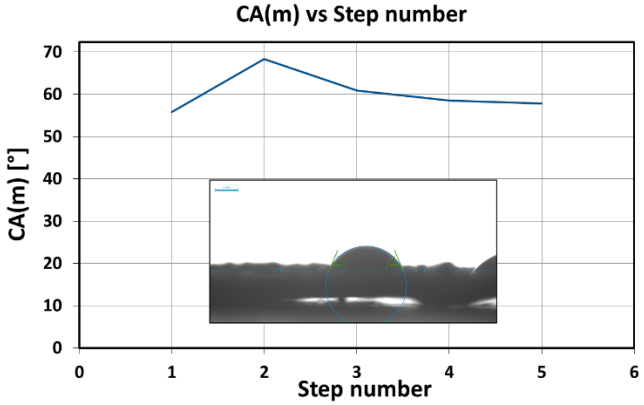


**Figure 5.29 Contact angle measurement for water-wet proppants (Hydrophilic).** Average contact angle= 60.25°

**Table 5.9** Core properties.

| **Core Properties** | C1 | C2 | C3 | C4 | C5 | C6 | C7 |
|---|---|---|---|---|---|---|---|
| Length (in.) | 2.5 | 2.43 | 2.42 | 2.6 | 2.4 | 2.42 | 2.45 |
| Diameter (in) | 2 | 2 | 1.5 | 1.5 | 1.5 | 1.5 | 1.5 |
| Weight (lbm) | 0.6812 | 0.533 | 0.4068 | 0.4256 | 0.3907 | 0.3814 | 0.3836 |
| Density ($lbm/in^2$) | 0.0867 | 0.0698 | 0.0951 | 0.0926 | 0.0921 | 0.0891 | 0.0886 |
| **Experimental conditions** | | | | | | | |
| Proppants type/ size/density | oil-wet ceramic 20/40 0.22 $lbm/ft^3$ | oil-wet ceramic 40/80 0.11 $lbm/ft^3$ | oil-wet ceramic 40/80 0.11 $lbm/ft^3$ | oil-wet ceramic 40/80 0.11 $lbm/ft^3$ | oil-wet ceramic 40/80 0.11 $lbm/ft^3$ | Water-wet ceramic 40/80 0.11 $lbm/ft^3$ | Water-wet ceramic 40/80 0.11 $lbm/ft^3$ |
| Fluid type | DI water | DI water | DI water | DI water | DI water | DI water | DI water |
| Confinement stress (psia) | 500, 700, 1000 | 500,1000, 1500, 2000 | 500,1000, 1500, 2000 | 500,1000, 1500 | 500,1000, 1500, 2000 | 500,1000, 1500, 2000 | 500,1000, 1500, 2000 |

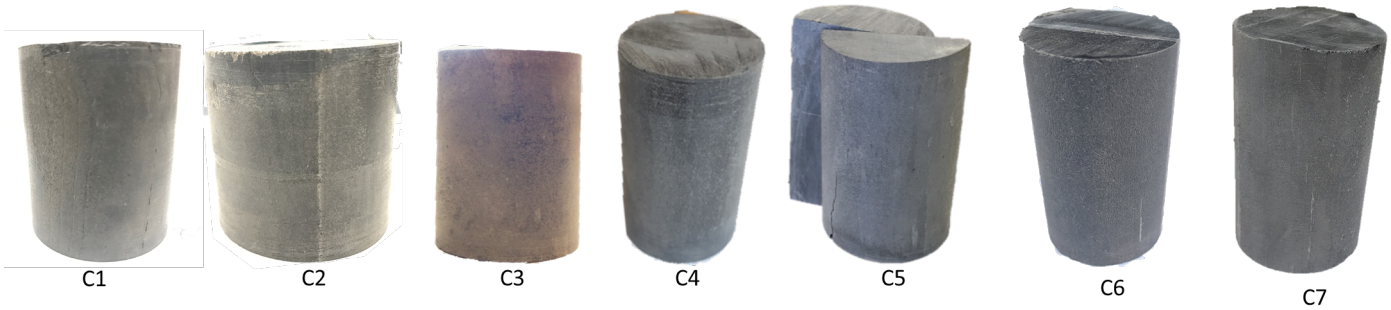


**Figure 5.30 Images of core samples used for the experiments. Sample C5 was already cut into two parts prior to taking the picture.**

Figs 5.31 and 5.32 show the time and stress dependent fracture conductivity of the tested cores for water-wet proppants while Figs. 5.33 and 5.34 presents the results with oil-wet proppants for two out of the five tested cores. The decline in fracture conductivity follows an exponential decline for both water-wet and oil-wet proppants. The conductivity values were generally low for water-wet proppants (below 2 md-ft) when compared with oil-wet proppants (ranged between 100 md-ft and 5md-ft) (Fig. 5.35). For the case of water wet proppants, the water adheres to the surface of the proppants, thereby restricting the flow of water and increasing pressure drop across the core. The presence of a second fluid such as oil, will see an increase in the relative permeability to oil. The wettability of the proppant pack could therefore be used to control recovery efficiency. Oil-wet proppants are hydrophobic and would essentially repel water. This means water easily flowed through the proppant pack.

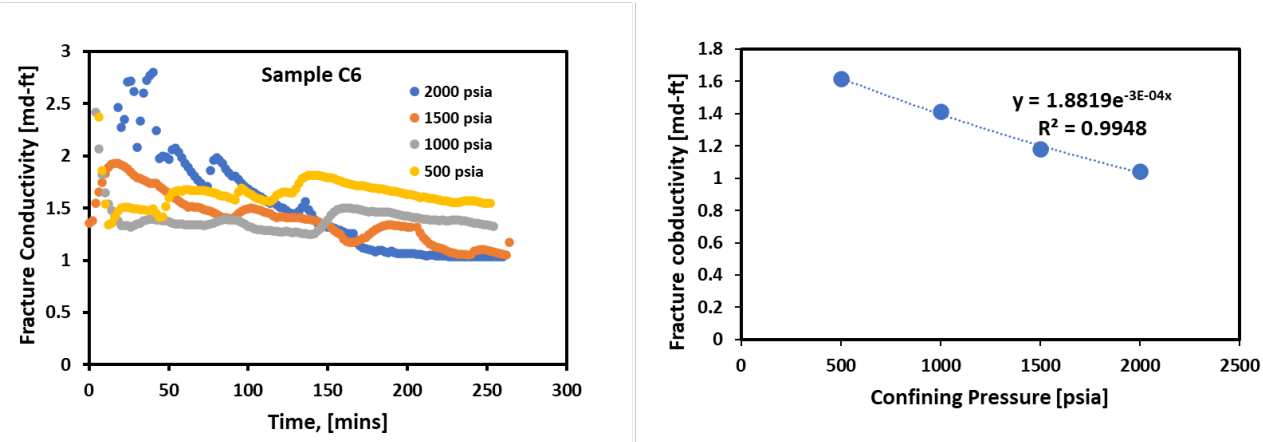


**Figure 5.31 Time and stress dependent fracture conductivity for sample C6 (water-wet proppants).**

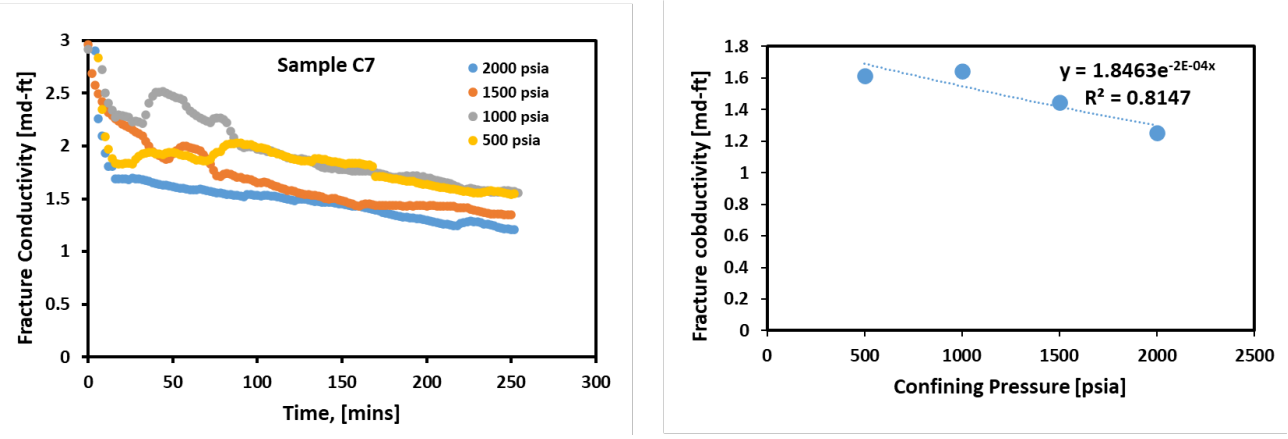


**Figure 5.32 Time and stress dependent fracture conductivity for sample C7 (water-wet proppants).**

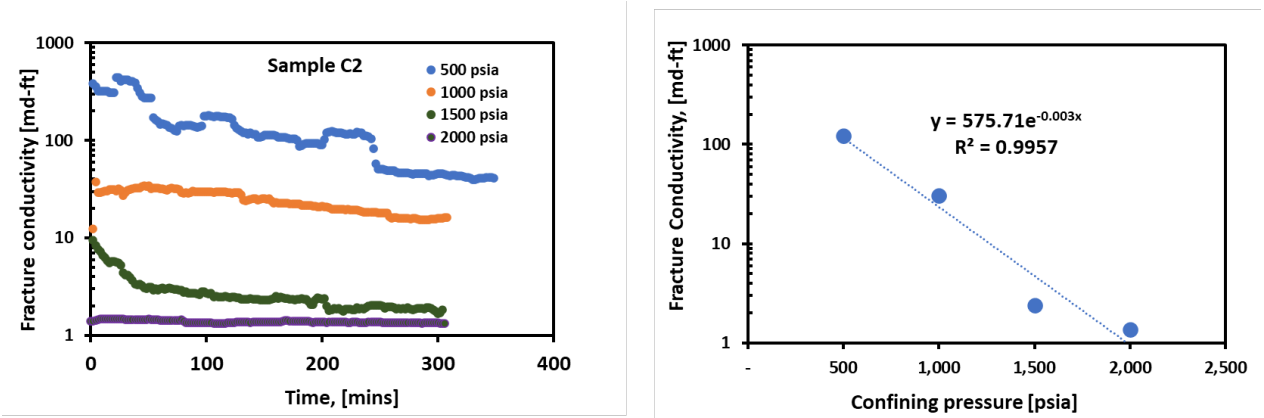


**Figure 5.33 Time and stress dependent fracture conductivity for sample C2 (oil-wet proppants).**

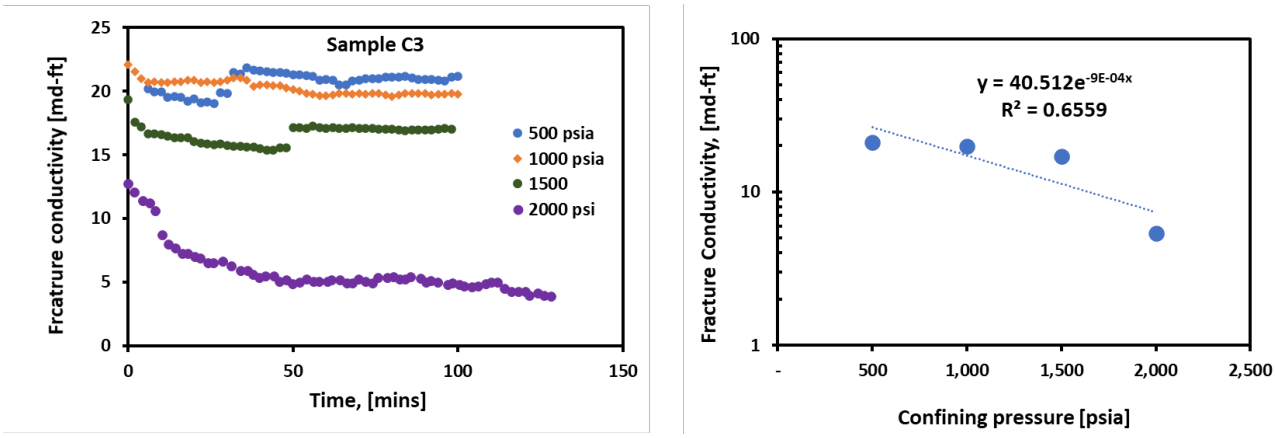


**Figure 5.34 Time and stress dependent fracture conductivity for sample C3 (oil-wet proppants).**

Table 5.10 compares the decline rates of the samples. The samples with water wet proppants showed a relatively small decline rate with an average decline rate constant of 0.0025 $psi^{-1}$. Because of the preferential sticking of the water to the proppants, there was likely less interaction between the water and the fracture face. This implies that, softening of the fracture face was limited and conductivity decline due to embedment was reduced (Fig. 5.35). In the case of oil-wet proppants, the water is repelled by the proppants and most likely, there was increase in interaction between the water and fracture face. For this reason, the decline rate was faster for oil-wet proppants with an average decline constant of 0.0022 $psi^{-1}$. Sample C1 was excluded from this average because a different proppant size was used. Figure 5.36 compares the fracture face of two samples after testing. The sample where oil-wet proppants were used showed significant damage on the fracture face due to softening of the face. The sample with water-wet proppants showed little interaction between the face and water.

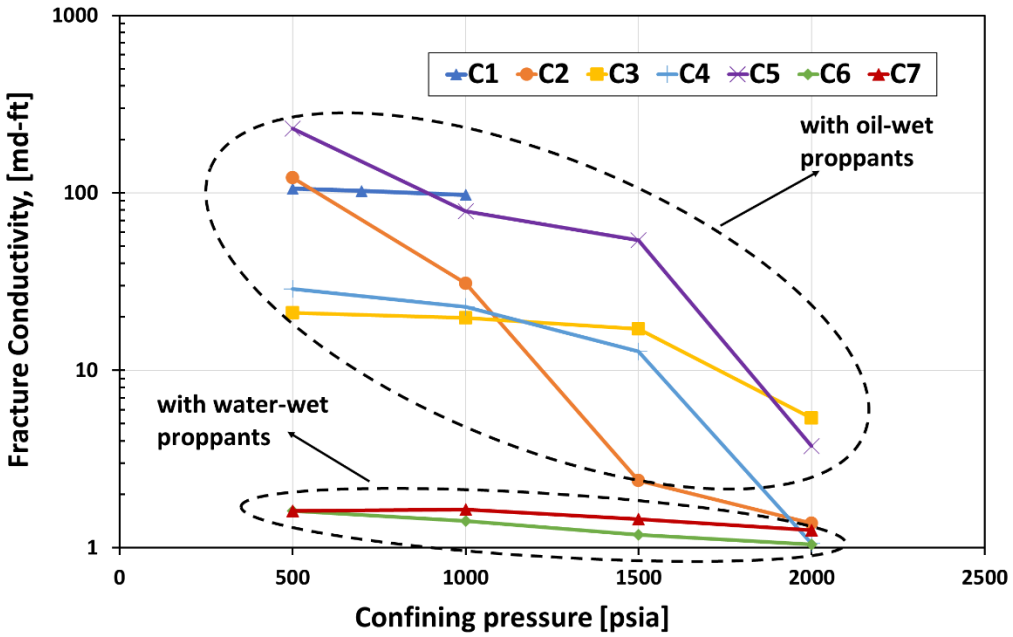


**Figure 5.35 Comparison of fracture conductivity decline with confining pressure for samples with oil-wet proppants (C1 to C5) and samples with water-wet proppants (C6 and C7).**

**Table 5.10** Parameters of exponential decline model.

| | Samples | Decline rate constant, $\lambda$ ($psi^{-1}$) | Person correlation coefficient (r) |
|---|---|---|---|
| Oil-wet proppants | C1 | 0.0002 | -0.9996 |
| | C2 | 0.003 | -0.9747 |
| | C3 | 0.0009 | -0.8526 |
| | C4 | 0.002 | -0.8929 |
| | C5 | 0.003 | -0.9388 |
| Water-wet proppants | C6 | 0.0003 | -0.9974 |
| | C7 | 0.0002 | 0.9026 |


**Figure 5.36 Fracture face of sample C3 after testing (Left) and fracture face of sample C7 after testing (right). The face of C3 showed significant damage compared to C7.**

*Fracture conductivity hysteresis*

The core samples (C6 and C7) were subjected to two cycles of confinement pressure loading and unloading (Fig. 5.37). Decline in fracture conductivity due to increase in effective stress may be due to proppant deformation, crushing or embedment. The most probable cause of decline for the tested cores is proppant embedment. The results in Fig. 5.37 indicate that the conductivity loss is irreversible or permanent—the fracture conductivity could not recover to the original state upon unloading.

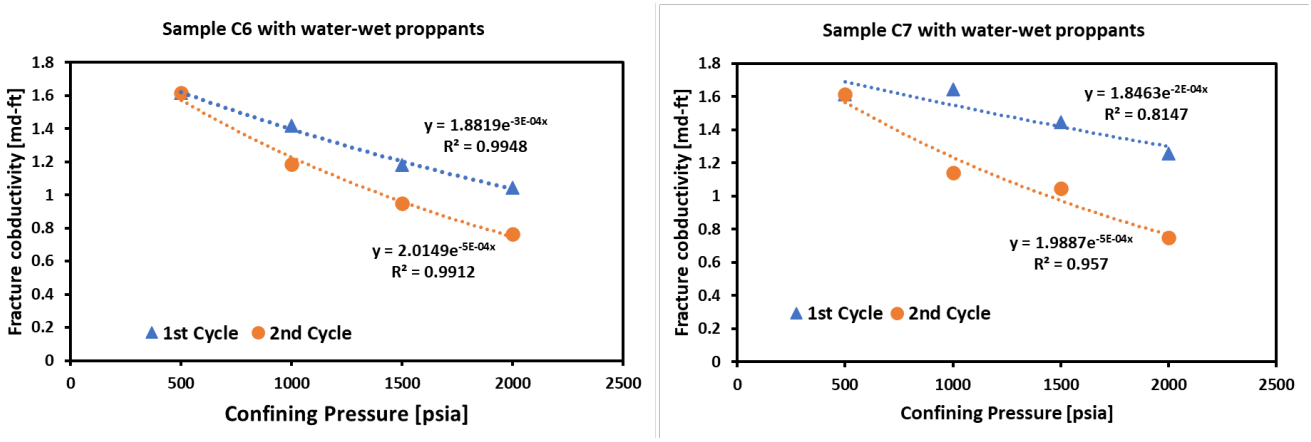


**Figure 5.37 Fracture conductivity hysteresis after 2 cycles of confinement pressure loading and unloading.**

## References

Aroonsri, A., Worthen, A.J., Hariz, T., Johnston, K.P., Huh, C., Bryant, S.L. 2013. Conditions for generating nanoparticle-stabilized $CO_2$ foams in fracture and matrix flow. SPE 166319. In: Proceedings of SPE Annual Technical Conference and Exhibition. 30 September – 2 October 2013 New Orleans, Louisiana, USA

Barbati A C, Desroches J, Robisson A, McKinley, G.H. 2016. Complex fluids and hydraulic fracturing. *Annual review of chemical and biomolecular engineering*, 7: 415-453.

Dehdari, B., Parsaei, R., Riazi, M., Rezaei, N., Zendehboudi, S. 2020. New insight into foam stability enhancement mechanism, using polyvinyl alcohol (PVA) and nanoparticles, *Journal of Molecular Liquids*, 307: 112755.

Dzinza L., 2018. An investigation into the effect of potential modifiers on the flotation of a copper sulphide ore. University of Cape Town.

Gu, M., Mohanty, K.K., 2015. Rheology of polymer-free foam fracturing fluids. *Journal of Petroleum Science and Engineering*, 134: 87-96.

Kostakis, T., Ettelaie, R., Murray, B.S., 2006. Effect of high salt concentrations on the stabilization of bubbles by silica particles. *Langmuir*, 22: 1273-1280.

Lv, Q., Li, Z., Li, B. Li, S., Sun, Q. 2015. Study of nanoparticle–surfactant-stabilized foam as a fracturing fluid. *Industrial & Engineering Chemistry Research*, 54: 9468-9477.

Rahmani, O., 2018. Mobility control in carbon dioxide-enhanced oil recovery process using nanoparticle-stabilized foam for carbonate reservoirs. *Journal of Colloids and Surfaces A: Physicochemical and Engineering Aspects*, 550: 245-255.

Ribeiro L H, Sharma M M. 2012. Multiphase fluid-loss properties and return permeability of energized fracturing fluids. *SPE Production & Operations*, 27(03): 265-277.

Rio, E., Drenckhan, W., Salonen, A., Langevin, D. 2014. Unusually stable liquid foams. *Advances in Colloid and Interface Science*, 205: 74-86.

San, J., Wang, S., Yu, J., Liu, N. 2017. Nanoparticle-stabilized carbon dioxide foam used in enhanced oil recovery: Effect of different ions and temperatures. *SPE Journal*, 22: 1416-1423.

Worthen, A.J., Bagaria, H.G., Chen, Y. Bryant, S.L., Huh, C., Johnston, K.P. 2013. Nanoparticle-stabilized carbon dioxide-in-water foams with fine texture. *Journal of Colloid and Interface Science*, 391: 142-151.

Xiao, C., Balasubramanian, S.N., Clapp, L.W., 2016. Rheology of Supercritical $CO_2$ Foam Stabilized by Nanoparticles. SPE 179621. In Proceedings of SPE Improved Oil Recovery Conference. 11-13 April 2016, Tulsa, Oklahoma, USA

# CHAPTER 6 Enhanced In-situ Supercritical $CO_2$ Hydrocarbon Extraction

## 6. 1 Introduction

The principal objective of this study is to evaluate the feasibility of enhancing hydrocarbon extraction in bituminous-rich shale lithologies at *in-situ*, downhole pressure and temperature conditions. Currently, unconventional shale reservoirs represent an important and necessary fossil fuel energy source for the United States. Increased efficiency in energy recovery via enhanced *in-situ* oil production from unconventional fuel sources will likely remain important over the next 3 decades as we transition to "greener" renewable energy solutions.

Fracking with supercritical fluids (e.g., $scCO_2$), coupled with horizontal drilling has resulted in tremendous production increases in unconventional shale reservoirs over the short term (months). Averaged over time however EOR is limited to the recovery of less than approximately 10% of the *in-situ* energy reserve. In the case of the Tuscaloosa Marine Shale, production is further impeded by (i) the reactivity of reservoir lithologies to aqueous fluids caused by the presence of montmorillonitic clay horizons, and (ii) the relatively low hydrocarbon reserves available (TOC $\leq$ 3 wt%). A potential solution is to enhance *in-situ* hydrocarbon production in the Tuscaloosa Marine Shale (TMS) and other Late Cretaceous oil shale plays in the U.S. (e.g., Eagle Ford shale) using non-aqueous, chemically-modified fracking fluids that enhance extraction via fluid-rock interactions at pressures and temperatures equivalent to reservoir depths of 10,000 -16,000 feet. In this study we propose to investigate the use supercritical carbon dioxide ($scCO_2$) with added co-solvent mixtures that act as modifiers that can breakdown heavier hydrocarbons at *in-situ* reservoir conditions (P >20MPa, and T = 40-80°C).

It has already been established that in addition to mitigating structural destabilization of the rock mass via swelling and pore collapse, anhydrous supercritical fluids such as $scCO_2$ exhibit favorable mass transfer characteristics where extraction times can be substantially shortened (Monin *et al.*, 1988). Carbon dioxide is known to be a powerful solvent when in a supercritical state, and over the past two decades has been extensively used as a fracking media in "water-sensitive" reservoirs. In this work we attempt to enhance the mass transfer characteristics of $scCO_2$ by the addition of small quantities of co-solvents to enhance the capacity of $scCO_2$ to breakdown heavier hydrocarbons (> C15) associated with bitumen and kerogen phases.

## 6.2 Experimental Method

To accomplish this research, we use an SFX-220 ISCO supercritical fluid extractor system (Fig. 6.1) that allows us to attain P-T conditions typical of deeper (11,000ft-15,000ft) reservoir conditions (P= 34MPa; T= 80°C). Eagle Ford (EF) oil shale sample (EF-McClanahan Well core; TOC = 7 wt%, provided by Statoil) was used as a test sample for this work to optimize

our analytical results and increase precision as the TMS shale sample available to us contained less hydrocarbon (TMS-Crosby Wells core; TOC = 1 wt%). Both the TMS and the EF shales are of Upper Cretaceous shallow marine origin, co-deposited during transgressions of the Cretaceous sea that extended far into the North American continent. They are the products of the same depositional environment formed at similar latitudes. To a first order, they are mineralogically similar and contain Type II/IIS kerogen and bituminous phases, so that the results from this study should be applicable to both reservoir formations. Samples from the Eagle Ford (EF) and Tuscaloosa Marine Shale (TMS) reservoirs were obtained from the Tuscaloosa Marine Shale Laboratory (TMSL) project (Fig. 6.2). Both samples were deposited in a Late Cretaceous shallow marine environment along the former southern margin of the N. American continental plate. The TMS rock specimen is a core sample from the Crosby Mineral Well # 12-1H1 collected from a depth of 12,118.5 to 12,119.0 feet. The Eagle Ford sample is a core from the McClanahan Well GU1-C4H#2 (13,810.5-13,811.0 ft).

**Figure 6.1 LANL Supercritical Fluid Extraction Facility.** The system is comprised of a ISCO Type 260D syringe pump and controller system (SFX220) an extraction chamber or P-T vessel and a capillary tube restrictor heating system.


**Figure 6.2 Eagle Ford and Tuscaloosa Marine Shale core samples used as experimental samples in this work.**

Upon receipt of the samples from Statoil and the TMSL, EF and TMS core sample splits were broken into small fragments using an Enerpac hydraulic press and were then crushed by hand using a mortar and pestle. An aliquot of each crushed sample was pulverized into powder form using a ball mill for the determination (i) bulk chemistry by X-ray Fluorescence (XRF), (ii) modal mineralogy by quantitative X-ray diffraction (qXRD), and (iii) bulk organic (TOC) and inorganic ($C_{TOT}$) carbon contents, and carbon isotopic ratios (d13C) by elemental mass spectrometry (EL-MS). The remaining bulk powders was sieved using a RoTap sieve shaker into size fractions of < 75 μm, and 75 μm to 350 μm for experimental testing.

- *Bulk X-ray Fluorescence (XRF) Spectroscopy*

Major elements were analyzed using the Rigaku Primus II wavelength-dispersive X-ray fluorescence (XRF) spectrometer. Samples were first crushed and homogenized in 5−10 g portions in a tungsten-carbide ball mill. Sample splits were heated at 110°C for 4 hours, and then allowed to equilibrate at ambient laboratory conditions for 12 hours to minimize weighing errors from atmospheric water gain. Fusion discs were prepared for analyses of the samples, by mixing 1.25 gram splits with 8.75 grams of lithium metaborate-tetraborate flux and heated in a muffle furnace for 45 minutes at 1050°C. Additional one-gram splits were heated at 1000°C to obtain the loss-on-ignition measurements used in the data reduction program.

- *Quantitative X-ray Diffraction (qXRD)*

Powder X-ray diffraction was used for phase identification and quantitative analysis using two Siemens D500 X-ray diffractometers and a Bruker D8 Discover using Cu-Kα radiation.

quantitative X-ray diffraction (qXRD) analyses of samples are made to determine relative mineral abundances. Samples were first crushed and homogenized in 5 g to10 g aliquots in a tungsten-carbide ball mill. Sample splits were heated at 110°C for 4 hours, and then allowed to equilibrate at ambient laboratory conditions for 24 hours to minimize weighing errors associated with atmospheric water gain. To obtain the aliquots for quantitative XRD analysis of the bulk rock specimen, 1.3 gram splits were mixed with 0.325 grams (~20 wt%) of corundum ($Al_2O_3$) used as an internal standard [5]. The aliquots are subsequently ground in acetone using a Brinkmann Grinder. Back-pack sample mounts were then obtained and scanned for 8 or 12 hours from 2 to 70 degrees (2θ) with a 0.02 degree (2θ) step-size and count times of 12 seconds per step. Quantitative XRD data was determined using whole pattern fitting in Jade© 9.5 X-ray data evaluation software with the ICDD PDF-4 database.

- *Elemental Mass Spectroscopy (EL-MS)*

Starting materials and over 30 experimental post extraction test solid sample residues were analyzed in triplicate for total organic carbon (TOC) and total inorganic carbon ($C_{TOT}$) contents, and isotopic carbon $\delta^{13}C$ ratios by elemental mass spectrometry (EL-MS) analysis, using a GV Instruments *Isoprime* isotope ratio mass spectrometer coupled to a GV Instruments *Eurovector Elemental Analyzer*.

All powder post-test samples were analyzed in triplicate and multiple times for TOC and $C_{TOT}$ after each experimental batch of tests in 2020 and 2021, with the amount of carbon in each sample based on a calibration using %C standards NIST 1547 and NBS 2704. Starting materials used in each experiment were also measured in triplicate for TOC and $C_{TOT}$ prior to, and after each experimental batch of tests. This was necessary as the mineralogy and organic content of the starting Eagle Ford McClanahan Shale core sample used for the tests varied from TOC values of 6.3 to 7.2 wt%. To differentiate organic and inorganic carbon contents, following the method of Larson *et al.* (2008) [6], samples were separated in splits and measured (i) unacidified to obtain their total carbon contents ($C_{TOT}$ = organic and inorganic), and (ii) acidified to remove carbonate phases (45 - 50wt% $CaCO_3$) to measure organic carbon only (TOC).

Based on the triplicate analytical EL-MS results the measurement errors for TOC and $C_{TOT}$ values for starting compositions and post extraction test solid residues were greatly diminished. The standard deviations for TOC and $C_{TOT}$ values are ± 0.36 wt% and ± 0.2 wt% respectively. These procedures were essential in determining as accurately as possible the hydrocarbon extraction values in pre- and post-test powder samples, in order to compare the results to the gas chromatography (GC) measurements on effluent extracts.

- *Gas Chromatography-Mass Spectroscopy (GCMS)*

The *Chemical Diagnostics and Engineering* (C-CDE) Group at LANL analyzed the total hydrocarbon content of effluent aliquots from post supercritical $CO_2$ extraction tests. Dynamic extraction flow tests at P-T conditions with supercritical carbon dioxide ($scCO_2$) and added cosolvents involve organic carbon recovery from both post-test solid residues and *in-situ* fluid

extracts. These effluent vials contain methylene chloride ($CH_2Cl_2$ or Dichloromethane, DCM) to dissolve the vented effluent and sequester the extracted organic carbon contained within and used for GC measurements. Procedures developed permit the GCMS method used to semi-quantitatively determine the total hydrocarbon content present in each effluent sample, and is used to evaluate the relative extraction efficiency of each supercritical $CO_2$ and co-solvent combination.

Prior to analysis of unknown samples, two certified standards are analyzed to define the retention times ($t_R$) of straight-chain alkanes applicable to the chosen instrument method. Alkane standards are used to determine where hydrocarbons (HC) of different masses elute. The first set of alkane standards are used to index masses $nC_7$ through $nC_{30}$, while the second set track masses $nC_8$ through $nC_{20}$. Both standards are injected in the GCMS at a known concentration of 10 µg/mL. Overlapping standards are used to ensure the correct identification of higher weight (heavier) hydrocarbons (HC) with a greater number of carbon atoms. It can be difficult to properly identify heavy HC using GCMS instrumentation due to the structural similarities of different mass fragments. Table 6.1 includes a list of all straight-chain alkanes that were defined by the instrument method using the aforementioned standard solutions. N-heptane ($C_7$) was not identified by the GCMS, as it had eluted before the end of the solvent delay of the instrument. Retention times of each straight-chain alkane are illustrated in Fig. 6.3, where chromatographic peaks are representative of alkanes $C_8$ through $C_{30}$. Each standard is shown, along with the locations of alkanes $C_8$, $C_{15}$, $C_{20}$, $C_{25}$ and $C_{30}$.

**Table 6.1** Straight-chain Alkanes Defined in the GCMS Instrument Method List.

| # of Carbon Atoms | Molecular Formula | Chemical Name |
|---|---|---|
| 8 | $C_8H_{18}$ | n-octane |
| 9 | $C_9H_{20}$ | n-nonane |
| 10 | $C_{10}H_{22}$ | n-decane |
| 11 | $C_{11}H_{24}$ | n-undecane |
| 12 | $C_{12}H_{26}$ | n-dodecane |
| 13 | $C_{13}H_{28}$ | n-tridecane |
| 14 | $C_{14}H_{30}$ | n-tetradecane |
| 15 | $C_{15}H_{32}$ | n-pentadecane |
| 16 | $C_{16}H_{34}$ | n-hexadecane |
| 17 | $C_{17}H_{36}$ | n-heptadecane |
| 18 | $C_{18}H_{38}$ | n-octadecane |
| 19 | $C_{19}H_{40}$ | n-nonadecane |
| 20 | $C_{20}H_{42}$ | n-icosane |
| 21 | $C_{21}H_{44}$ | n-henicosane |
| 22 | $C_{22}H_{46}$ | n-docosane |
| 23 | $C_{23}H_{48}$ | n-tricosane |
| 24 | $C_{24}H_{50}$ | n-tetracosane |
| 25 | $C_{25}H_{52}$ | n-pentacosane |
| 26 | $C_{26}H_{54}$ | n-hexacosane |
| 27 | $C_{27}H_{56}$ | n-heptacosane |

| | | |
|---|---|---|
| 28 | $C_{28}H_{58}$ | n-octacosane |
| 29 | $C_{29}H_{60}$ | n-nonacosane |
| 30 | $C_{30}H_{62}$ | n-triacontane |

In **Fig. 6.3**, each straight-chain alkane is illustrated, where the chromatographic peaks are representative of alkanes $C_8$ through $C_{30}$. Each standard is shown, along with the locations of alkanes $C_8$, $C_{20}$, and $C_{30}$. Total hydrocarbon content is determined by summing integrated peak areas within defined alkane regions for each chromatogram. Each region is defined by retention times (in minutes) of alkanes present in each of the two standard solutions. In this work, alkane regions are defined as carbon numbers of: less than 10 ($< nC_{10}$); 10 to 14 ($nC_{10}$ - $nC_{14}$) ; 15 to 20 ($nC_{15}$ - $nC_{20}$); 21 to 25 ($nC_{21}$ - $nC_{25}$); 26 to 30 ($nC_{26}$ - $nC_{30}$); and greater than 30 ($> nC_{30}$). It was assumed that all peaks integrated by *OpenLab* software were true hydrocarbons, although it is important to note that trace levels of non-hydrocarbon chemical species may be included in the final calculations. Carefully chosen integration parameters ensured that all integrated peaks are distinguishable from the baseline signal of the GCMS. Integration reports were generated for each sample, and a Python script was written to efficiently divide the total areas into their respective alkane regions by retention time interval.

The retention time intervals associated with each alkane region are shown in Table 6.2. The total integrated area sum of the GC response is reported for each alkane region. This step is repeated for all samples and the data provides important insights into which extraction solvent and/or co-solvent mixture is the most efficient at mobilizing different species of hydrocarbons with respect to the specificity of their individual masses.

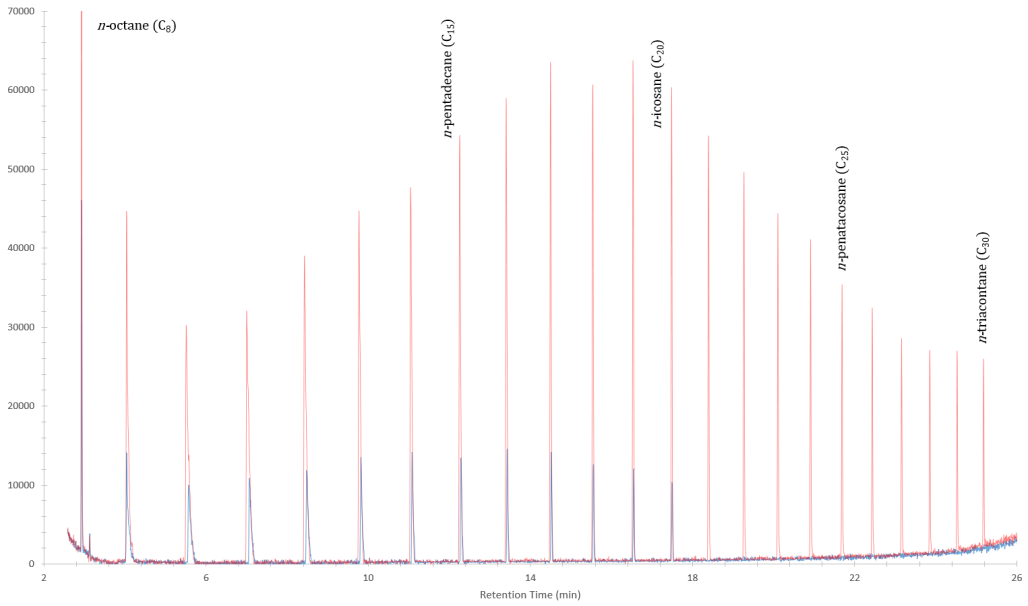


**Figure 6.3 Chromatogram of the two alkane standards used to define hydrocarbon regions in this work; the $C_7$-$C_{30}$ (red) and the $C_8$-$C_{20}$ (blue).**

**Table 6.2** Retention time intervals used to sum integrated peak areas for all hydrocarbons in each alkane region.

| Alkane Region by Carbon Number | Retention Time Interval (min) |
|---|---|
| $< C_{10}$ | $< 3.367$ |
| $C_{10}$ to $C_{14}$ | 3.367 to 12.229 |
| $C_{15}$ to $C_{20}$ | 12.229 to 18.908 |
| $C_{21}$ to $C_{25}$ | 18.908 to 23.237 |
| $C_{26}$ to $C_{30}$ | 23.237 to 26.825 |
| $> C_{30}$ | $> 30.000$ |

## 6.3 Eagle Ford and Tuscaloosa Marine Shale Characterization Results

Statoil provided a description of the Eagle Ford McClanahan well core sample (Fig. 6.4). This included the core depth, grain density (2.535 g.cm$^{-3}$), and bulk modal mineralogy and total organic carbon content (TOC = 6.96 wt%). In order to characterize the staring material for every test, the bulk chemical composition, organic carbon content (TOC) and modal mineralogy were characterized prior to testing for each split of core used as starting material. For this we used XRF, qXRD and EL-MS measurements, summarized in Table 6.3, and Figs. 6.5 and 6.6). Table 6.3 and Fig. 6.6 illustrate the variability in sample compositions within each shale and also the principal differences between the Eagle Ford shale (TOC = 7 wt%) that is lower in clay content (smectite clay = 17 - 23 wt%) but higher in calcite ($CaCO_3$ = 44 - 48 wt%) than the Tuscaloosa Marine Shale core sample (TOC = 1 wt%; , smectite clay = 21 -27 wt%; $CaCO_3$ = 18 - 24wt%).

| | |
|---|---|
| Top Depth | 13810.2 |
| Bottom Depth | |
| Weight % TOC | 6.9561 |
| A. Weight % Mineralogy (without TOC) | |
| **Whole Rock Data** | |
| Quartz | 16.3 |
| Plagioclase | 0.9 |
| Calcite | 50.4 |
| Dolomite & Fe-Dolomite | 0.0 |
| Fluorapatite | 0.0 |
| Pyrite | 4.7 |
| Marcasite | 0.9 |
| Total Clay | 26.7 |
| Sum Bulk | 99.9 |
| **Clay Mineralogy** | |
| Illite/Smectite* | 58.5 |
| Illite & Mica | 31 |
| Kaolinite | 7.5 |
| Chlorite | 3 |
| Sum Clay | 100 |
| B. Volume % Mineralogy (**TOC wt % = 6.9561) | |
| Quartz | 14.4 |
| Plagioclase | 0.8 |
| Calcite | 43.5 |
| Dolomite & Fe-Dolomite | 0.0 |
| Fluorapatite | 0.0 |
| Pyrite | 2.2 |
| Marcasite | 0.4 |
| Illite/Smectite* | 14.0 |
| Illite & Mica | 7.3 |
| Kaolinite | 1.8 |
| Chlorite | 0.7 |
| Kerogen** | 14.9 |
| Total | 100.0 |
| Vol clay | 23.8 |
| Calc. G.D. (g/cc) | 2.535 |

**Figure 6.4 Eagle Ford Shale Core Descriptions (Statoil, 2018).**

**Table 6.3** Modal mineralogy of EF-McCalahan and TMS Cosby Wells shale cores materials based on qXRD and XRF analyses (S. Chipera, Chesapeake Energy, Inc).

| Weight % | NORMALIZED Raw Data | | | | | | |
|---|---|---|---|---|---|---|---|
| EES-14-TMSL Shale Samples-04FEB19 | | | | | | | |
| WELL NAME | EF-McClanahan | | | Negev | TMS-Crosby Mineral | | |
| JOB NUMBER | | | | | | | |
| SAMPLE ID | GU1-C4H-A | GU1-C4H-B | GU1-C4H-C | OS-3 | CR 12-1-H1-A | CR 12-1-H1-B | CR 12-1-H1-C |
| SAMPLE DEPTH (ft) | 13,110.5 - 13,111.0 | | | | 12,118.5- 12,119.0 | | |
| | | | | | | | |
| NON-CLAY FRACTION | | | | | | | |
| Quartz | 15.6 | 15.7 | 16.4 | 2.6 | 18.0 | 18.7 | 19.1 |
| K-Feldspar | 0.0 | 0.0 | 0.0 | 0.9 | 0.0 | 0.5 | 0.2 |
| Plagioclase | 1.0 | 3.0 | 1.5 | 2.0 | 7.8 | 1.8 | 1.8 |
| Kerogen (TOC) | **6.8** | **7.1** | **6.6** | **11.9** | **0.9** | **1.0** | **1.0** |
| Apatite | 0.7 | 0.8 | 0.7 | 5.3 | 1.5 | 0.8 | 0.8 |
| Pyrite | 3.0 | 2.7 | 2.9 | 0.3 | 1.9 | 1.3 | 1.4 |
| Calcite | 44.1 | 47.5 | 45.2 | 60.4 | 23.5 | 17.9 | 18.4 |
| Dolomite | 0.3 | 0.5 | 0.0 | 8.6 | 0.5 | 0.1 | 0.0 |
| | | | | | | | |
| TOTAL | 71.4 | 77.3 | 73.2 | 92.0 | 54.1 | 42.1 | 42.7 |
| | | | | | | | |
| CLAY FRACTION | | | | | | | |
| Mica | 1.6 | 1.9 | 2.5 | 0.8 | 10.1 | 14.5 | 14.9 |
| I/S + Illite | 23.3 | 17.5 | 20.3 | 6.5 | 21.5 | 27.1 | 25.8 |
| Chlorite | 0.0 | 0.0 | 1.0 | 0.3 | 2.4 | 4.7 | 4.8 |
| Kaolinite | 3.7 | 3.3 | 2.9 | 0.4 | 11.9 | 11.6 | 11.9 |
| TOTAL | 28.6 | 22.7 | 26.8 | 8.0 | 45.9 | 57.9 | 57.3 |
| | | | | | | | |
| GRAND TOTAL | 100.0 | 100.0 | 100.0 | 100.0 | 100.0 | 100.0 | 100.0 |

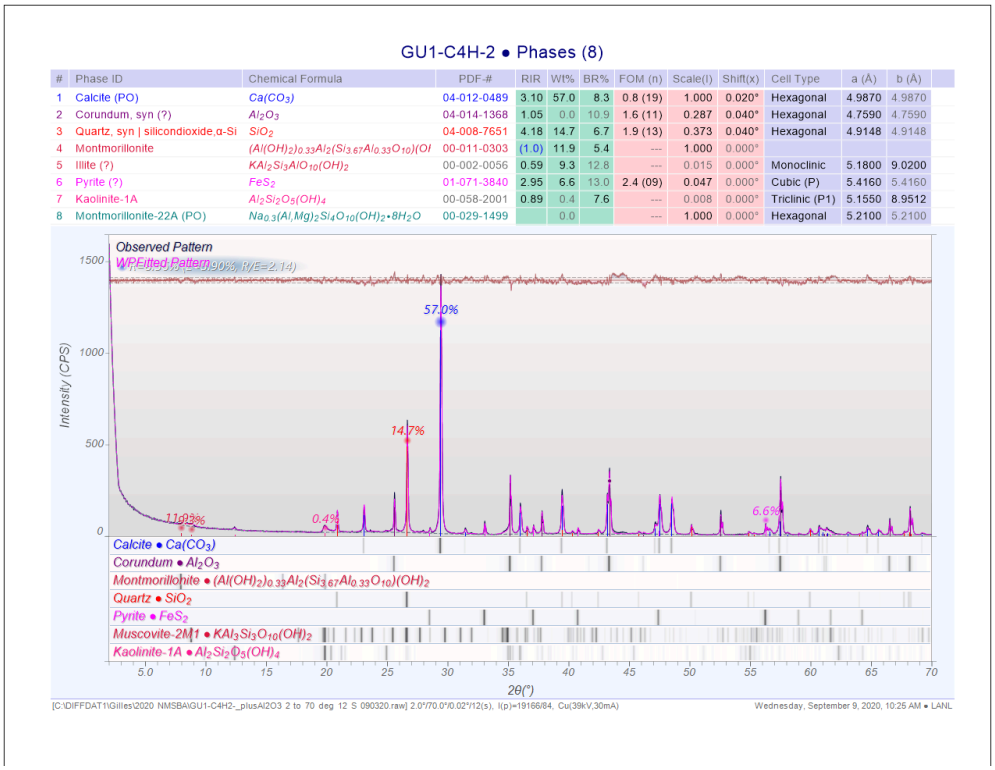


**Figure 6.5 Raw Quantitative X-ray Diffraction Spectrum for EF sample GU1-C4H.** Note that the principal phases present are calcite (57 wt%), smectite-illite clay (20-25 wt%), silicon dioxide (15 wt%), and pyrite (6 wt%). These values are consistent with the qXRD refinement values in Table 6.3.

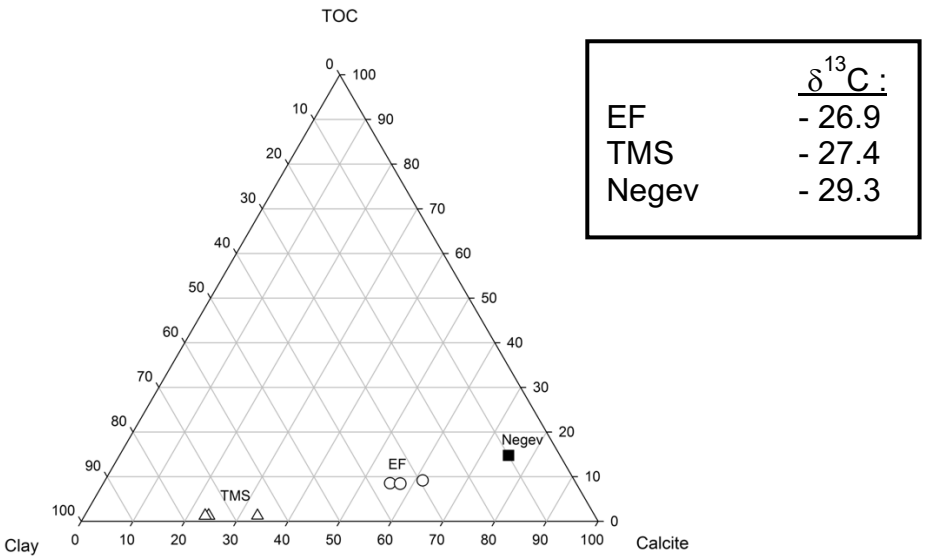


**Figure 6.6 Ternary diagram of EF and TMS shale bulk compositions for Calcite-Clay and TOC (based on Table 6.3).**

Both EF and TMS shales represent Late Cretaceous shallow marine sediments with Type II/IIS kerogen. The isotopic $\delta^{13}C$ values for saturates (Fig. 6.6) also indicate that the Eagle Ford shale ($\delta^{13}C$ = -26.9) is nearly of the same maturity as TMS sample ($\delta^{13}C$ = -27.7). Note that Type II/IIS Kerogen found in the EF and TMS samples is restricted to 'high maturity' oil shales with carbon saturates $\delta^{13}C$ values between -25 and -29 (Fig. 6.7). For comparison, a less mature ($\delta^{13}C$= -29.3) bituminous shallow marine limestone marl (TOC = 12 wt%) from the Negev desert (Israel) is also plotted. It is richer in calcite ($CaCO_3$ = 60wt%), and lower in clay content (smectite <7wt%) than either EF or TMS samples.

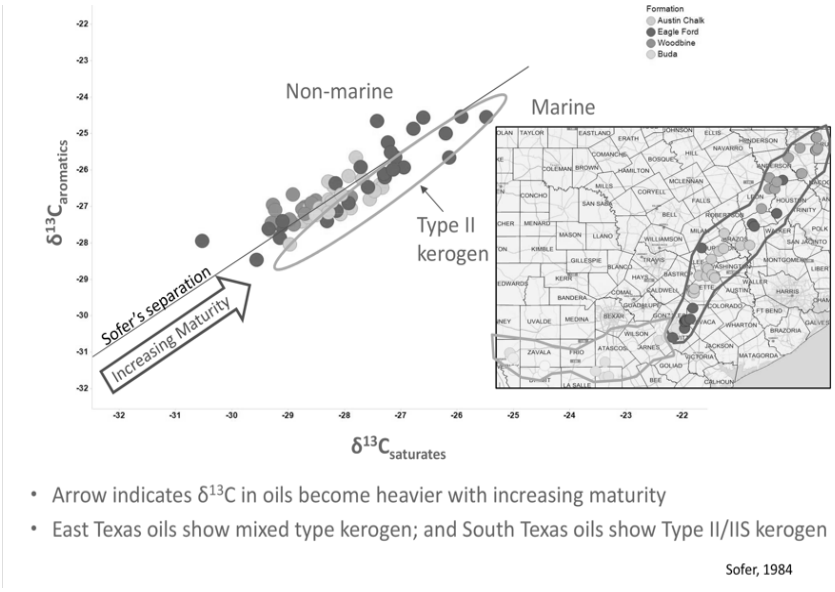


**Figure 6.7 Plot of Eagle Ford isotopic carbon $\delta^{13}C$ values for saturates and aromatic carbons (Sofer 1984).**

### 6.4 Experimental High P-T Extraction Methodology

For our HC extraction procedures, we used an ISCO SFX220™ *Supercritical Fluid Extractor* system (*Isco, Inc.*) with single and continuous flow set up with 2 ISCO pumps. The SFX220™ System schematic shown in Fig. 6.8 consists of :

- *ISCO pumps 260D and/or 100D*
- *SFX Controller* : to set P, T, extraction flow rate, and test duration for each experiment.
- *Reaction Chamber Vessel*: set at P = 34 MPa (5,000 psi), and T = 80°C
- *Capillary Restrictor*: with heater (not shown) can be set to 140°C to 200°C for clearing or cleaning restrictor line.
- *High purity compressed $CO_2$* : with Helium gas trap.
- Stainless steel tubing: 1/8" and 1/16" ss lines

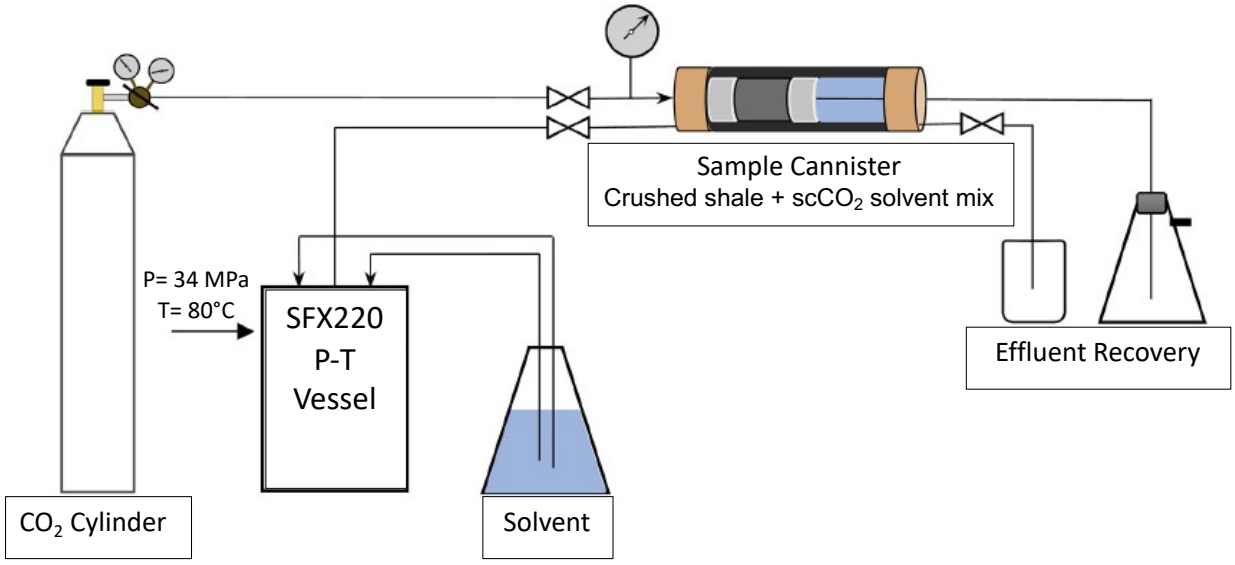


**Figure 6.8 Schematic representation of experimental SFX 220 ISCO high P-T extraction methodology.**

Prior to testing, a 10 ml peek cannister is loaded with 2 g of crushed shale powder (∅ <75 µm) in which a small volume of co-solvent mix is pipetted in prior to sealing and placing in the pressure vessel. The system in then brought to simulated reservoir conditions (T= 80°C) and $CO_2$ gas is pumped in until the desired pressure is reached (P= 34 MPa or 5000 psi). The sample is equilibrated in the presence of $scCO_2$ and co-solvents at 'static conditions" for 60 to 120 minutes, and then dynamically extracted at a rate of 1.3-1.4 ml/min until 29 ml (3 pore volumes) of effluent is extracted and collected in a vial containing approximately 10-15 ml of dichloro-methane (DCM).

Both the extracted solid powder residue and the effluent are preserved for EL-MS and GCMS analyses to determine the amount of extracted hydrocarbon from the sample.

### 6.5 Hydrocarbon Extraction Results

17 HC extraction tests were performed on Eagle Ford shale oil (Table 6.4). Of the 17 samples testes, 14 were successful. GB14-HOBX consisted of 4 individual tests (HOBX-1,2,3,4) run sequentially on the same sample and equivalent to a 4 x 3PV extractions process. Note that the TOC (wt%) and GC effluent total integrated area values represent early results prior to QA/QC analyses. Figure 6.9 compares the percent hydrocarbon extracted determined from measured EL-MS TOC values from 14 post-test solid residues, to the integrated GC peak spectra values from the effluent sample representing 3 pore volume extracts for each test. Though the TOC and GC measurement errors are not yet fully resolved for the new data, a positive correlation for tests using different co-solvents is confirmed (Fig. 6.9). Note that the reconnaissance tests conducted in 2019 include supercritical $CO_2$ ($scCO_2$), and in order of increasing extraction potential, $scCO_2$ with 5 vol% of different co-solvents added ($H_2O$, acetic acid, methanol, tetrahydrofuran (THF) and 2-propanol. The results indicate that when added to $scCO_2$, each cosolvent tested, $H_2O$, acetic acid, methanol, THF and 2-Propanol represents a factor increase in TOC sample extraction (relative to $scCO_2$ only) of x1.2, x2.2, x2.6, x3.0 and x3.3. Although the addition of water as a $scCO_2$ co-solvent shows significant variability, the other co-solvents show a positive correlation between solid residue TOC data and effluent GC chromatograms. Plotted in Fig. 6.9 are the revised test results for samples GB1 though GB 14. GC Integrated Peak Areas are derived from GC-MS measurements on effluent extracts and EL-MS values for the total organic carbon content (TOC) of extracted shale powder residues.

**TABLE 6.4** HC Test Results on Eagle Ford McClanahan Core.

| TEST ID | Co-Solvent(s) vol% | Post Test Residue HC Extraction (%) | Effluent GC Units Total |
|---|---|---|---|
| GB1-GQ22 | scCO2 only | 1.8 | 59945791 |
| GB2-HPUZ | 5% H2O | 4.3 | 61733034 |
| GB5-HWZU | 5% H2O | 6.4 | 76129759 |
| GB3-HOBY | 5% MeOH | 6.2 | 154547709 |
| GB4-HHB3 AA | 5% AA | 6 | 132226668 |
| GB7-HP37 | 5% THF | 7 | 176525513 |
| GB12-HK7 | 5% THF | 7.2 | 166923240 |
| GB8-GB13 | 5% PropOH | 12.2 | 193866735 |
| GB11-HPUU | 5% PropOH | 11.3 | 201638711 |
| GB13-HPU3 | 5% THF/2.5%PropOH | 12.3 | 198242926 |
| GB14-HOBX-1 | 5% THF/2.5%PropOH | | 208583985 |
| GB14-HOBX-ALL | 5% THF/2.5%PropOH | 17.4 | 236092671 |

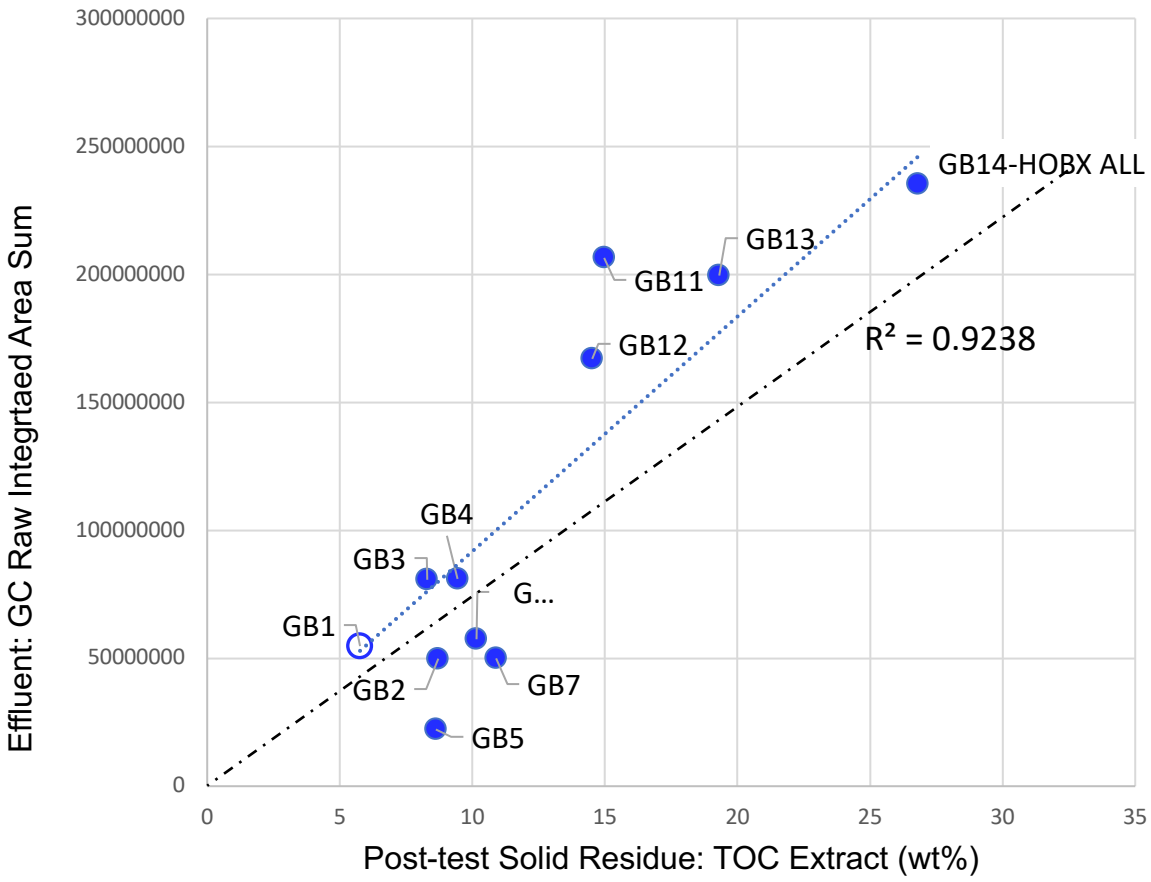


**Figure 6.9 Exploratory $scCO_2$ Hydrocarbon Extractions on Eagle Ford Shale.** Shown are the TOC extract values (wt%) vs effluent hydrocarbon extract (GC units) for extraction tests at P=34.4 MPa and T=80°C.

Figure 6.9 represents the overall preliminary results of HC extraction data for Eagle Ford (EF) shale samples GB1 though GB 14. Plotted are the extracts from post-test solid residue TOC values (wt%) measured by elemental mass spectrometry (EL-MS), against effluent hydrocarbon (HC) extracts measured by GCMS. Co-solvents include water (GB2, GB5), acetic acid (AA: GB4), methyl alcohol (MeOH: GB3), propanol (PropOH: GB8, GB11), and tetrahydrofuran (THF: GB7, GB12). Open blue circle represents "$scCO_2$ only" (GB1), GB13 and GB14 were extracted with $scCO_2$ and 2 co-solvent modifiers THF+PropOH respectively. All test samples were equilibrated at 34 MPa pressure and 80°C temperature for 60 minutes and then dynamically extracted at a rate of 1.4 (+/- 0.1) ml/min for 20 minutes or equivalent to 3 sample pore volumes (28-29 ml). After each test, the effluent collection vials and extracted solid powder residues were used to determine the quantity of organic carbon extracted using gas chromatography-mass spectrometry (GCMS) and elemental mass spectroscopy (EL-MS) techniques respectively.

Note that samples the TOC extracts on the post-test residues for samples GB1 through GB8 were not measured in triplicate so that the value errors are larger than for samples GB11 through GB14 when procedures were refined though not all analytical procedures were fully established for these exploratory tests. The chromatographs however clearly show the effect of single co-solvents on $CO_2$ (Fig. 6.10). Subsequent tests confirm the larger extraction values for samples GB11 through GB14 with THF and propOH as $scCO_2$ co-solvents. Sample GB1 (open circle) was tested at P-T in the presence of $scCO_2$ only (no co-solvents added) and falls in the range of the lowest HC extraction values ($TOC_{xtrct}$ = 6 wt%). Samples GB2 through GB 12 represent tests with 5 vol% of a single co-solvent added to $scCO_2$. All co-solvent tests effectively result in an increase in HC extraction from the EF shale at P-T compared to the GB1 ($scCO_2$ only). In order of enhanced extraction capacity, the single co-solvents used were distilled water ($H_2O$: GB2, GB5), methanol (MeOH: GB3), acetic acid (AA: GB4), tetrahydrofuran (THF: GB7, GB12), and isopropanol (propOH: GB8, GB11).

Based on the results of our first single co-solvent experiments (GB1-GB12) on Eagle Ford shale oil samples, we designed a $scCO_2$ mixture with two co-solvents. Samples GB13 and GB14 in Fig. 6.9 represent the first extraction of EF samples using $scCO_2$ with a 7.5 vol% mixture of 2 co-solvents, THF (5vol%) and propOH (2.5 vol%). Both resulted in higher HC extract values of 18wt% (GB13) and 26 wt% (GB14) TOC that also correspond to the highest effluent HC concentrations measured by GCMS (Fig. 6.9). This represents a four-fold increase ($\geq$ 4x) in percent hydrocarbon extraction compared to $CO_2$ alone. Sample GB14 represents the total of four sequential extraction stages of 3 pore volumes (PV) each. However over 95% of the extraction occurred within the first 3 to 4 pore volumes so that the last 2 extraction stages did not contribute to an increase in HC content in the effluent or an increase in TOC extraction in the sample powder (Fig. 6.11). This indicates that even though the extraction of HC from the EF shale is increased nearly 4-fold using small quantities of THF and isopropanol cosolvents with $scCO_2$, and it is associated with the mobilization of heavier alkanes nC15-nC28, the extraction of hydrocarbons using this method appears finite.

Though this data set was exploratory, we established a roughly linear correlation for HC extraction between the solid residue and the extracted liquid effluent for each test (Fig. 6.9). This relationship is interpreted as representing a mass balance between the extracted shale powders and the dissolved hydrocarbon in the extracted effluent phase.

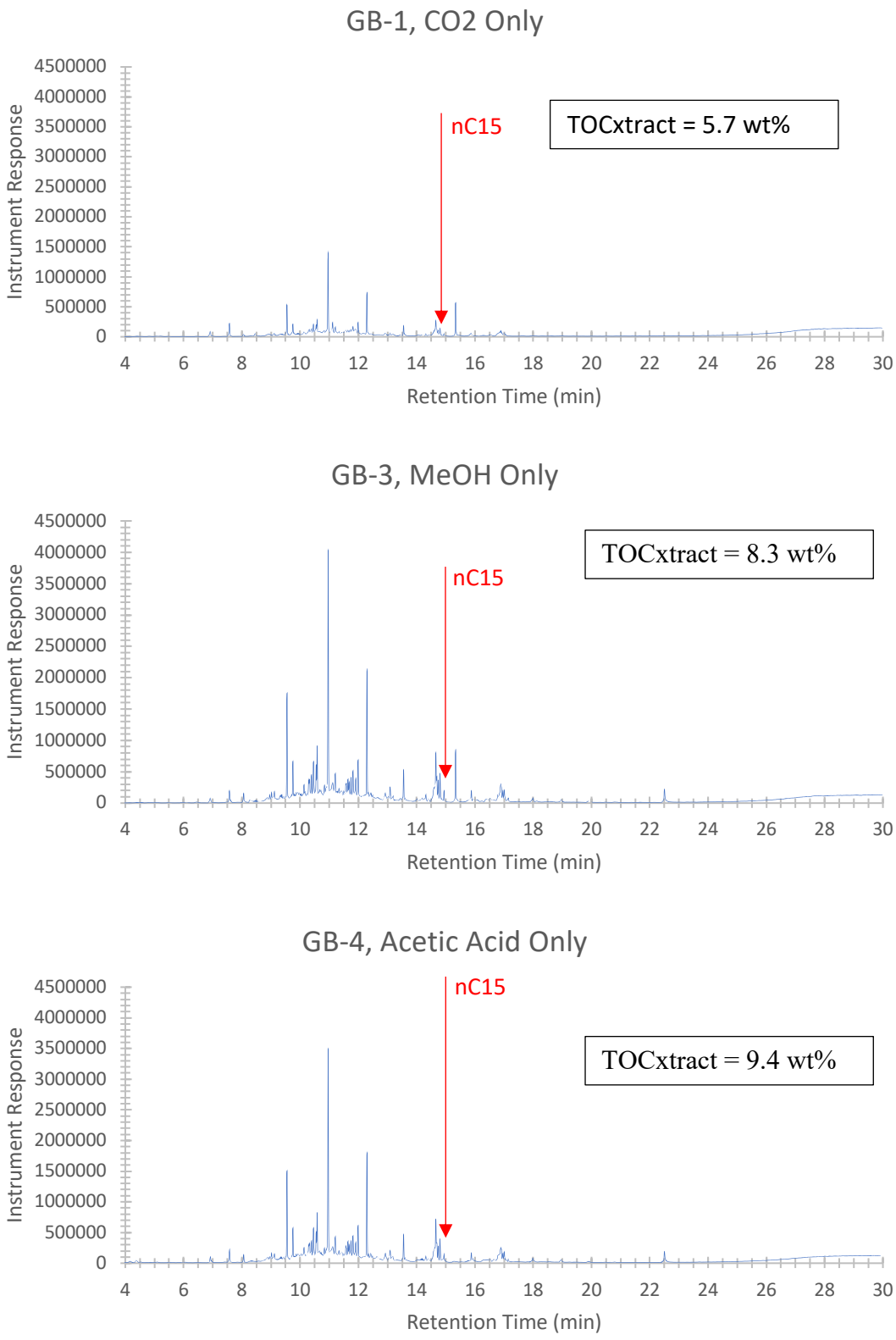


**Figure 6.10 Effect of single co-solvents on $CO_2$ extraction.**

After obtained the preliminary results, we focused our effort on performing repeat and new exploratory tests on $scCO_2$ extraction in the presence of two co-solvents THF and propOH. To this end we completed ten new tests using improved analytical methods and test procedures. These tests included 8 extraction experiments on both Eagle Ford and Tuscaloosa Marine Shale powders shown in Table 6.5. Post-test solid residue and effluent samples for each type of co-solvent allow us to determine both the total organic carbon (TOC %) extracted from the sample and the relative integrated GC spectra for each test. Within a series of repeat EF tests (GB21, GB24 and GB25) we also tested TMS core samples (GB23 and GB26). In order to investigate the effect of varying amounts of co-solvents we also added 2x and 10 x the co-solvent THF+propOH volumes to samples GB27 and GB20 respectively. In addition, we also tested 2 g of EF and TSM powdered samples (∅< 75 µm) at room conditions in 10 ml DCM for 28 days to verify that the extracts we obtained at P-T were not from lighter "free" oil phases in the samples. Results from these tests are represented in Figs. 6.10-6.16.

**Table 6.5** New Extraction Test Results on EF shale at reservoir P-T conditions.

| HC Extraction Information: | | | | Effluent Transfer Vial Information: 'Dry Weights' | | | Co-Solvent Information: | | | | | Sample Xtract Information | | | | |
|---|---|---|---|---|---|---|---|---|---|---|---|---|---|---|---|---|
| Test# | Sample ID | DATE | Time | Empty Vial w/cap | +Effluent | Effluent wt | THF | THF | propOH | propOH | THF+propOH | sample wt | Static EQ Time | Dynamic Xtrct Time | Vol. Xtract | Ave Xtract Rate |
| | | | | (g) | (g) | (g) | (≃ mL) | (g) | (≃ mL) | (g) | (g) | (g) | (min) | (min) | (mL) | (mL/min) |
| 1 | **GB20-EF**-HG4M | 6-Jan-22 | 17:40 | 15.6211 | 30.4424 | 14.8213 | 5 | | 2.5 | | 6.4981 | 2.006357 | 120 | 20 | 28.81 | 1.4405 |
| 2 | **GB21-EF**-HODC | 7-Jan-22 | 10:40 | 15.6509 | 28.6 | 12.9491 | 0.5 | 0.4764 | 0.23 | 0.2389 | 0.7153 | 2.002084 | 60 | 22 | 28.09 | 1.276818182 |
| 3 | GB22-TSM-HHSG | 7-Jan-22 | | | | | | | | | | | | | FAILED TEST/No Xtract | |
| 4 | **GB23-TSM**-HOBW | 7-Jan-22 | 15:00 | 15.6097 | 26.8782 | 11.2685 | 0.5 | 0.4254 | 0.25 | 0.2106 | 0.636 | 2.000958 | 120 | 22 | 29.12 | 1.323636364 |
| 5 | **GB24-EF**-HO5Q | 7-Jan-22 | 17:33 | 15.5459 | 30.543 | 14.9971 | 0.5 | 0.4483 | 0.25 | 0.2479 | 0.6962 | 2.005167 | 60 | 20 | 26.91 | 1.3455 |
| 6 | **GB25-EF**-HPWU | 8-Jan-22 | 14:01 | 15.5909 | 31.9561 | 16.3652 | 0.5 | 0.4447 | 0.25 | 0.2427 | 0.6874 | 1.998 | 120 | 22 | 29.05 | 1.320454545 |
| 7 | **GB26-TMS**-HT49 | 8-Jan-22 | 15:23 | 15.6418 | 29.2921 | 13.6503 | 0.5 | 0.4431 | 0.25 | 0.2309 | 0.674 | 1.99 | 60 | 22 | 26.78 | 1.217272727 |
| 8 | **GB27-EF**-HM87 | 8-Jan-22 | 18:00 | 15.758 | 26.4462 | 10.6882 | 1 | 0.9191 | 0.5 | 0.4356 | 1.3547 | 2.03846 | 120 | 23 | 27.92 | 1.213913043 |

N.B : **EF** = Eagle Ford Sample (TOC = 7.14 wt%) /B13/ **TMS** = Tuscalloosa Marine Shale Sample (TOC =1.13 wt%)

Figure 6.11displays the results of the EF and TMS extractions tests plotted as a function of post-test solid residue TOC extracts from EL-MS in wt% vs. effluent HC extracted values from GCMS in terms of the raw sum of integrated areas ($GC_{SIA}$). All samples were tested at P = 34.4 MPa and T = 80°C in the presence solvents $scCO_2$ with modifiers THF and propOH. Both EF (TOC= 7 wt%) and TMS (TOC = 1wt%) samples fall into two groups. The Eagle Ford shales tested GB21, GB24, GB25 and GB27 are tightly clustered around the HC extract values of $TOC_{xtrct}$ = 23.5 (+/- 0.7) wt% and $GC_{SIA} = 7 \times 10^6$. Samples GB21 and GB24 were equilibrated at P-T for 60 minutes prior to extraction, while sample GB25 was equilibrated for 120minutes, resulting in no change in degree of TOC extraction. GB27 was tested in similar conditions as GB25 but with $scCO_2$ with twice (2x) the total volume of co-solvents added. This also resulted in no change in extraction capacity. Conversely, sample GB20 was also tested in conditions similar to GB25 and GB27 (120 min equilibration time) but with 10x the total co-solvent volume added to $scCO_2$. In this case the total TOC wt% extract from the residue remained similar to the other EF samples (TOC = 22.7 wt%) but the GCMS response was a factor of 1.3x higher ($GC_{SIA} > 9 \times 10^6$). The Tuscaloosa Marine Shale samples tested (GB23 and GB26) have similar GCMS responses ($GC_{SIA} \sim 1 \times 10^6$) that are lower than the EF value ($\sim 7 \times 10^6$) proportional to their TOC contents of 1 wt% and 7 wt% respectively. Conversely, the solid residue extract TOC values for GB 23 and GB26 are appreciably different, 10.3 wt% and 15.7 wt% respectively. Again, this cannot be explained by the time difference at static equilibration

(GB23: $t_{eq}$ = 120 min; GB26: $t_{eq}$ = 60 min). The difference in the extraction capacity for the THF and propOH $scCO_2$ cosolvents however may be related to differences in the composition of the organic carbon phases, and/or lower analytical accuracy of the EL-MS technique for samples with lower hydrocarbon contents.

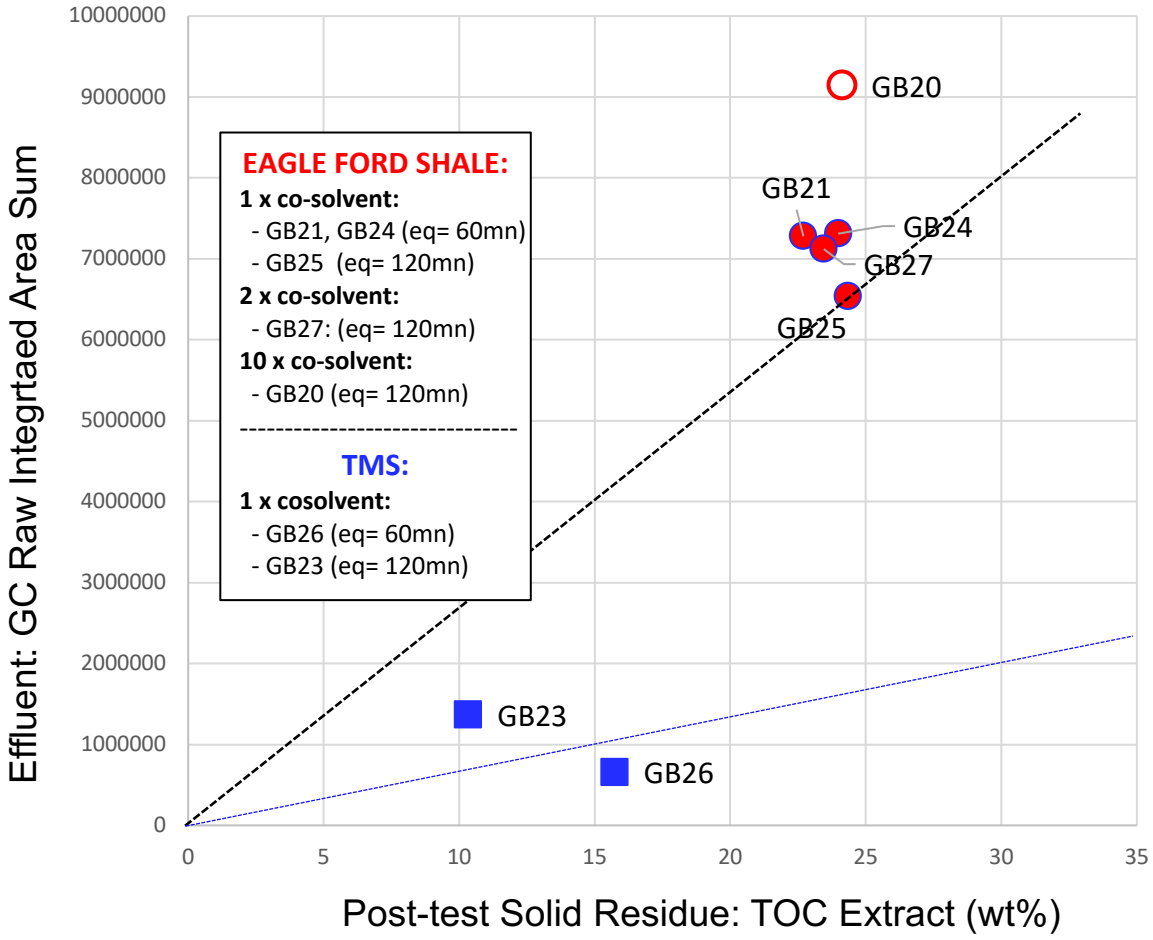


**Figure 6.11 $scCO_2$ hydrocarbon extractions on EF and TMS shales.** Plotted for samples GB2 though GB 27 are EL-MS measured values for the total organic carbon content (TOC) of extracted shale powder residues vs. GC sums of integrated peak areas derived from GCMS measurements on effluent extracts.

### *Effluent 'dry weight' method*

In order to further elucidate the GC response of EF sample GB20, subsequent to the first GC analyses, the remaining effluent sample still diluted in approximately 12 ml of DCM, was dried in air until only a solid residue remained (~ 48 hours). The empty effluent collection vial and the vial with the dry effluent mass were weighed to determine the total 'dry weight' of HC effluent dissolved in the vial during GCMS. The results are presented in Fig. 6.12 using the effluent 'dry weight' determination to calculate the amount of extracted HC from the sample and comparing it to the GCMS results previously obtained in Fig. 6.11.

As in Fig. 6.11, the data in Fig. 6.12 show that the EF and TMS extraction values are generally grouped. The EF samples extract values based on the effluent 'dry weight' measurements are clustered around a value of 19.9 +/- 0.9 wt%, and the TMS samples around a value of 11.8 +/- 0.6 wt%. Conversely, the effluent 'dry weight' value obtained for EF test sample GB20 results in an apparent total HC extraction value of only 7.4 wt% that is much lower than the TOC extract value of 22.7 wt% (Fig. 6.11).

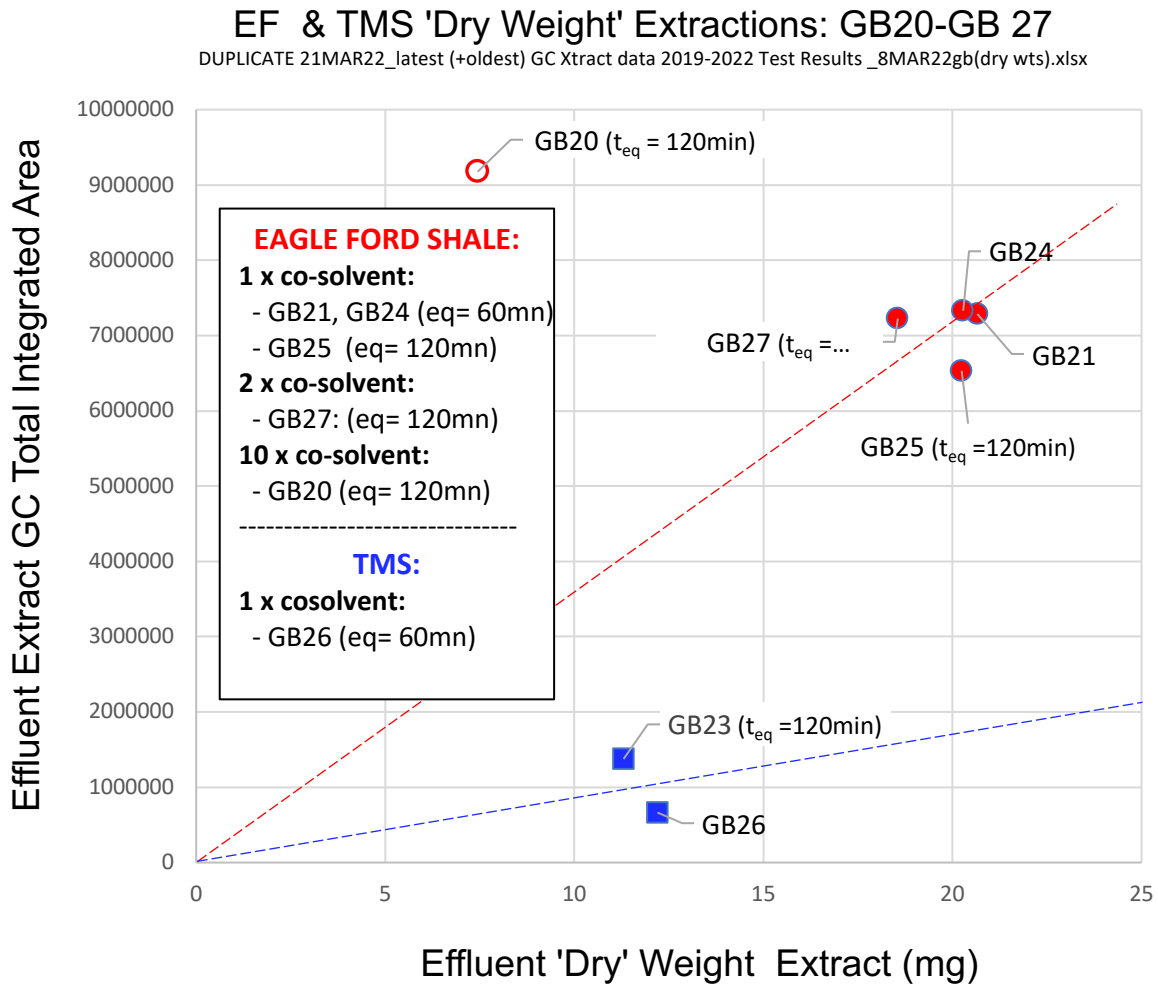


**Figure 6.12 Extracted HC in EF and TMS Effluent Samples. Evaluation of new "dry weight" effluent extraction method.**

In order to help clarify this result, the vials with the 'dry' effluent were redissolved in 5 ml of DCM and re- analyzed by GCMS. The dissolved 'dry' effluent chromatograph (blue spectra) is superimposed on the original chromatograph (orange spectra) are superimposed for EF sample GB20 (Fig. 6.13).

As suspected the "dry weight' procedure for this sample resulted in a strong preferential loss of lighter alkanes (< nC13) and the total loss of lighter aliphatic hydrocarbon peaks around (nC9/10). These nC9/10 carbon peaks, originally strong in the GB20 'undried' effluent are not substantial in other samples GB 21-25 EF effluent samples except for GB27 that has slightly more light carbon peaks. This implies that these lighter aliphatic hydrocarbons formed due to the presence of excess co-solvents, as suggested in Fig. 6.14 where GB20 the 10-fold increase in total co-solvent volume is proportional to the increase in effluent GCMS response, in the absence of any change in the residual solid extraction values ($TOC_{GB20}$ = 22.7 wt%; Fig. 6.11).

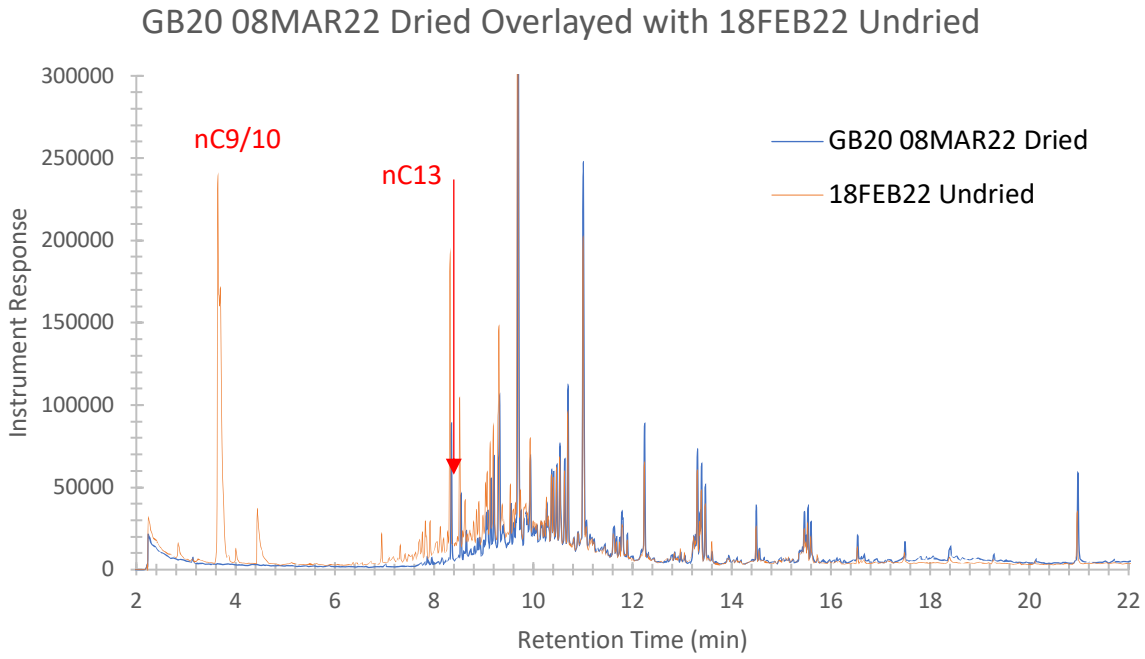


**Figure 6.13 GC-MS chromatograph of test GB20 before (undried, orange spectra) and after the effluent "dry weight" sample preparation ('dried', blue spectra).** Note the disappearance of the lighter aliphatic hydrocarbons (nC9/13) where the nC9/10 peaks have completely disappeared.

The presence of an abundance of very light aliphatic hydrocarbons (nC9/10) in the original EF GB20 effluent also explains why the sample has the highest GCMS response values in Figure 13 but the same solid residue extract weight (TOC = 24 wt%) as the other samples. Note that when the two extract determination methods, TOC extract in solid residue and effluent 'dry weight' extract are compared, the 'dry weight' method systematically underestimates the percentage of HC extraction (Fig. 6.15). This is attributed to the loss of lighter more volatile carbons during the evaporation procedure.

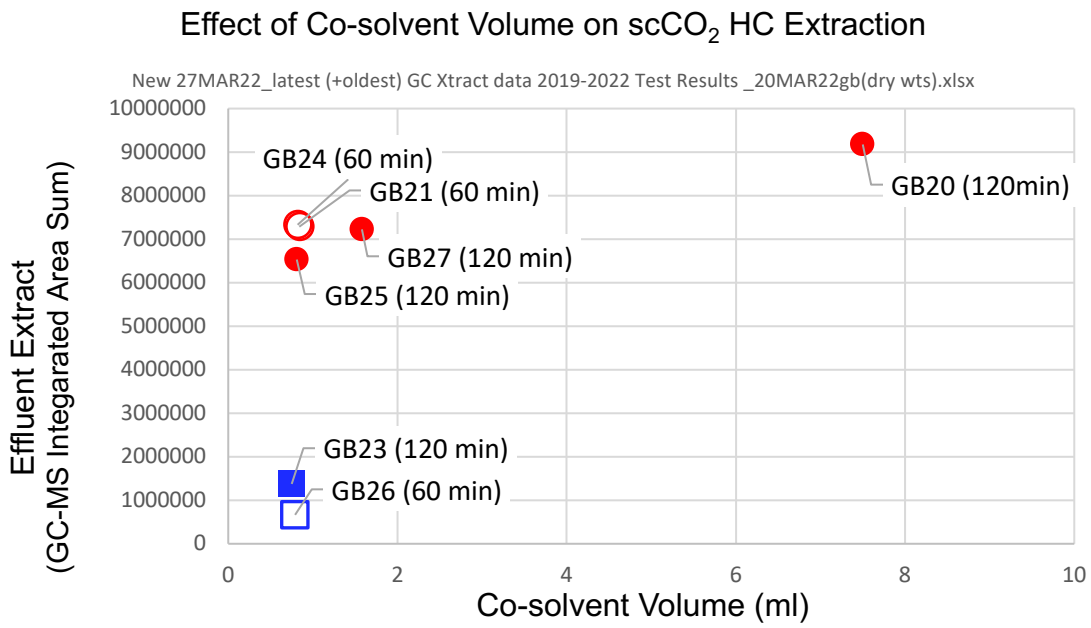


**Figure 6.14 Effect of increased [THF+PropOH] co-solvent volume on HC extract determinations.**

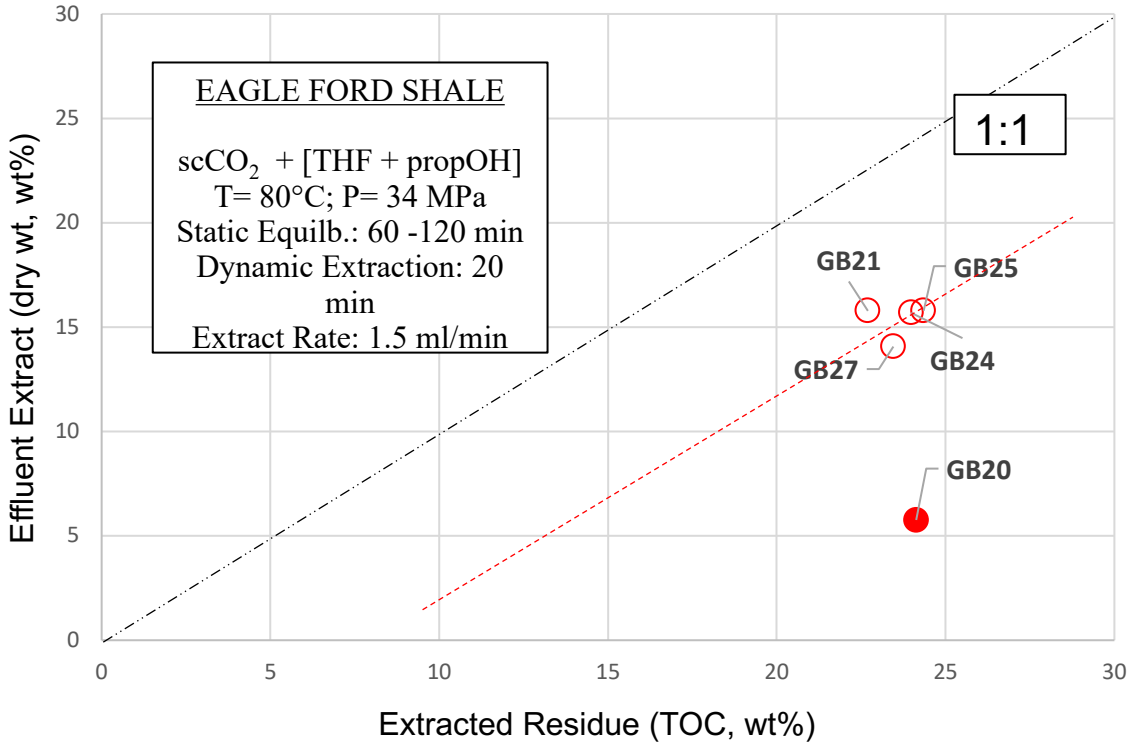


**Figure 6.15 Loss of Aliphatic Hydrocarbons During 'dry weight' Effluent Extract Determinations.** Note that all effluent HC extract values for the Eagle Ford shale samples measured

by the ‘dry weight’ method are systematically a factor of 1.3x lower than the extract values measured from the solid residues by EL-MS. Sample GB20 however is a factor of 4x lower.

Though the Eagle Ford sample all ‘dry weight’ HC extract measurements are systematically lower than the residue TOC extract values, for the TMS extracts, the values are systematically higher (Fig. 6.16). In the case of the EF samples this is attributed to the loss of aliphatic carbons during the drying procedure, but for the TMS values the difference is attributed to errors in the EL-MS measurements due to the low carbon content (<1wt%) and high carbonate content that may results in the loss of material during acidification of the samples (Figs. 6.17 and 6.18).

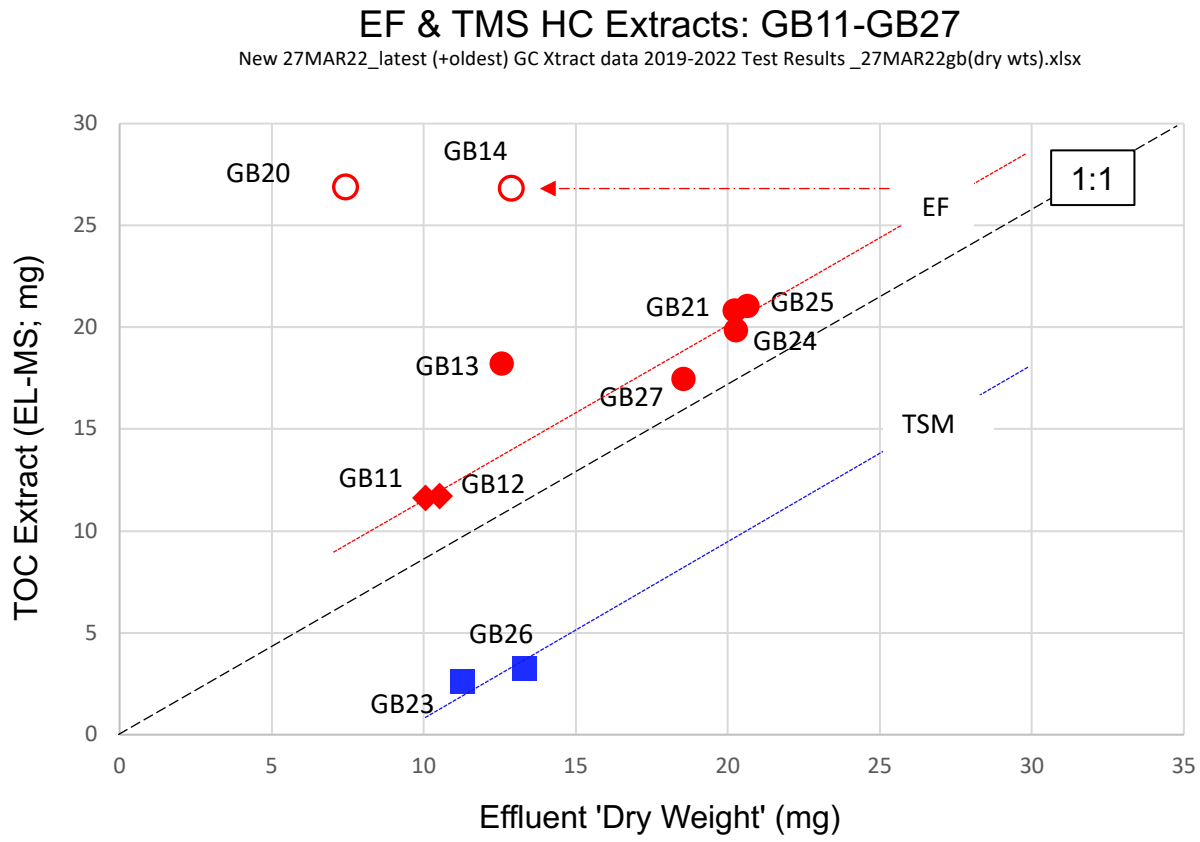


**Figure 6.16 Comparison of ‘dry weight’ HC extract determination in effluent vs. TOC extract in pot-test solid residue.**

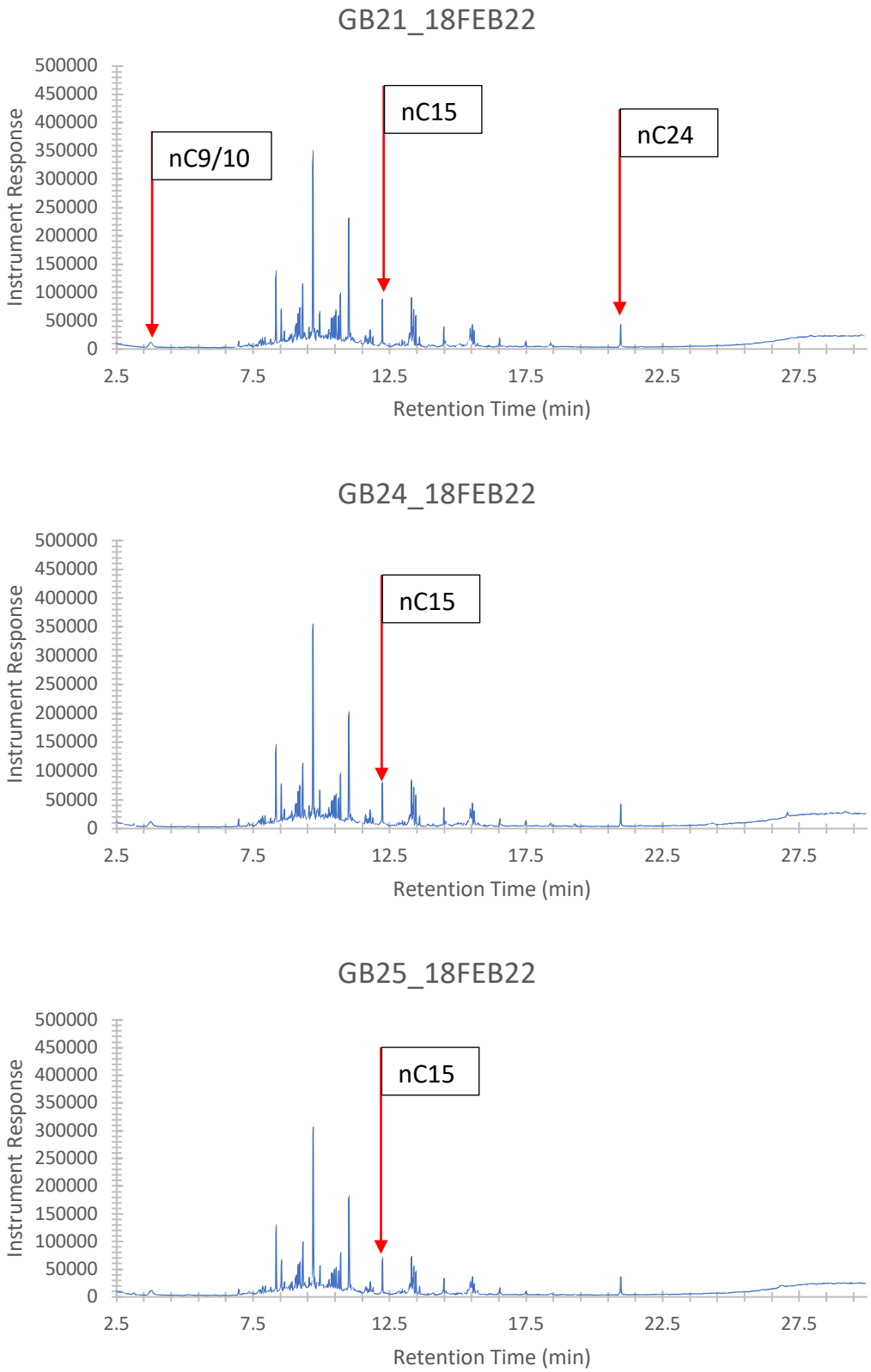


**Figure 6.17 GCMS Chromatograms for Eagle Ford shale samples GB21, GB24 and GB25.**

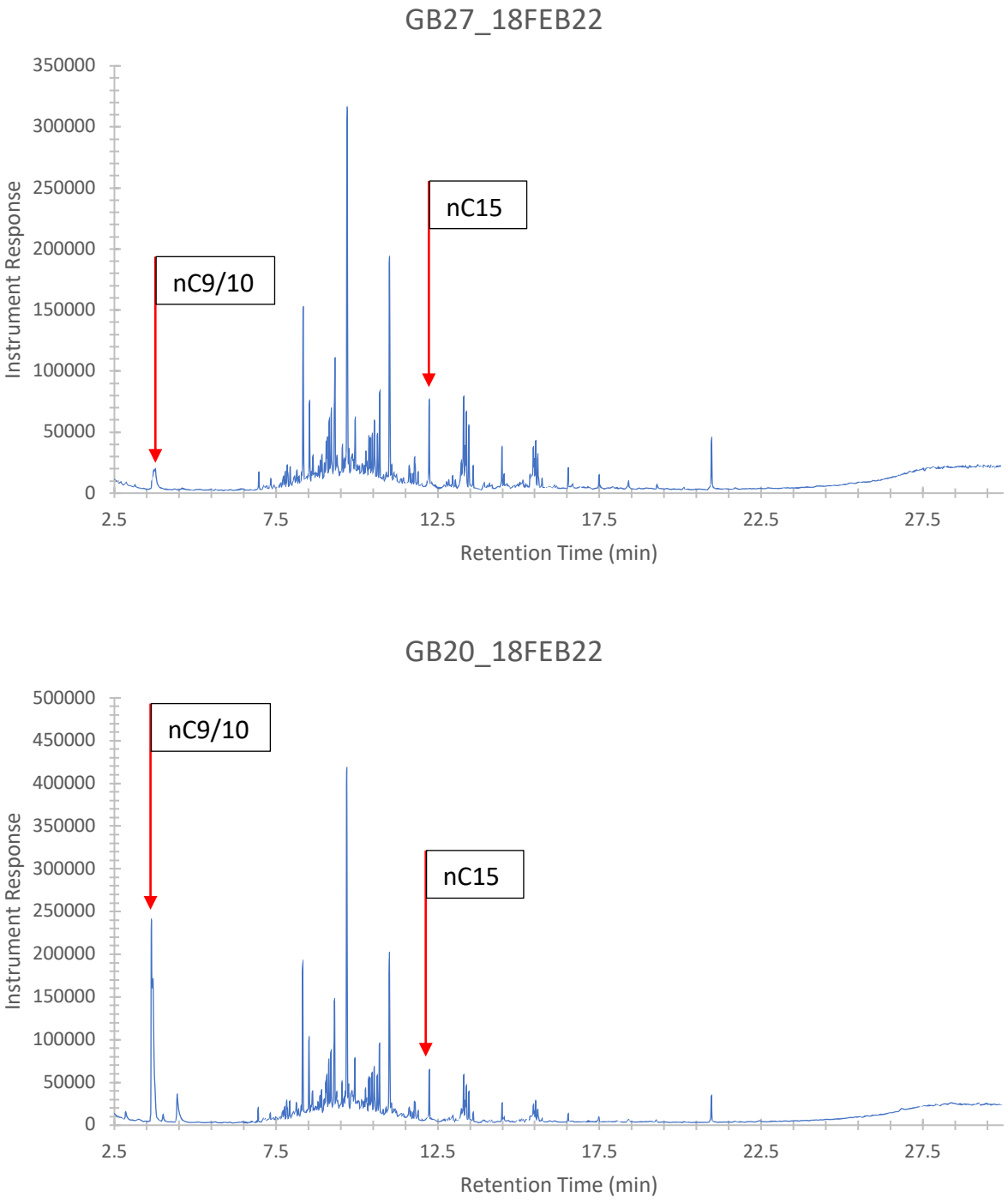


**Figure 6.18 GCMS Chromatograms for Eagle Ford shale samples with larger co-solvent volumes GB27 (2x) and GB20 (10x).**

The new experimental and analytical constraints obtained in this study on Eagle Ford and Tuscaloosa Marine Shale are internally consistent and allow us to quantitatively determine the extraction capacity of supercritical $CO_2$ modified by small volumes of co-solvent additives tetrahydrofuran (THF, 5 vol%) and isopropanol (propOH, 3 vol%). The percent total hydrocarbon (TOC) extracted determined by elemental mass spectrometry (EL-MS) is linearly correlated to the amount of HC dissolved by the effluent during extraction, which allows us to confirm that material balance of product and reactants resulted during the extraction of HC at *in-situ* reservoir P-T conditions (P= 34.4 MPa; T = 80°C). Furthermore, the extraction capacity of $CO_2$ is enhanced 4-fold by this method compared. The increase in extraction yields are attributed in part to selective extraction properties of Propanol and THF. Combined, propanol and THF break down polar NSO-compounds (>C15) and increase extraction yields of high molecular weight carbon compounds (Greibrokk et al. 1992).

Extraction kinetics are high as these results are identical for 60 min and 120 min equilibration time at P-T. Gas chromatography indicates that the mixed co-solvent method proposed results in an increase in both light aliphatic and heavier carbon (nC15-24) $scCO_2$ extraction over other single co-solvent mixtures tested (dichloromethane, water, methanol, acetic acid, tetrahydrofuran and isopropanol). Conversely, the extraction capacity (25 wt%) appears limited to approximately 3 pore volumes indicating that polar kerogen phases may not affected integrated GC peak spectra values from the effluent sample representing 3 pore volume extracts for each test.

It is difficult to ascertain the extraction processes though the influence of smectite-illite clay minerals on the aliphatic hydrocarbons is critically dependent on temperature, the water concentration and the presence of calcite. Illite and montmorillonite preferentially retain large amounts of the polar constituents of bitumen, but not n-alkanes or acyclic isoprenoids. Therefore, bitumen fractionation according to polarity differences occurs in the presence of these clay minerals. No carbon or nitrogen isotopic fraction was detected by EL-MS in our tests indicating that the fractionation of n-alkanes or acyclic isoprenoids relative to the polar constituents of bitumen is insignificant, presumably due to the presence of calcite in the Eagle Ford and TMS shales (Huizinga et al. 1987; Tannenbaum et al. 1986).

All of this work is in effect exploratory and requires further experimentation and analysis in order to investigate its relevance to field production conditions. However, the benefit of using powders of known grain size ( $\varnothing < 70$ μm) for these tests is that the results can be related to the exposed surface area. In a fracture network that would be related to the fracture density, which can be estimated by hydro-geophysical methods.

## References

Huizinga, B.J., E. Tannenbaum, I. R. Kaplan (**1987**). The role of minerals in the thermal alteration of organic matter--IV. Generation of n-alkanes, acyclic isoprenoids, and alkenes in laboratory experiments, *Geochim Cosmochim Acta*; 51:1083-97.

J.C.Monin**,** D.Barth**,** M.Perrut, M.Espitalié, B.Durand (**1988**). Extraction of hydrocarbons from sedimentary rocks by supercritical carbon dioxide, *Organic Geochemistry*, 13, 1079-1086.

Sofer, Z. (**1984**). Stable carbon isotope compositions of crude oils: application to source depositional environ- ments and petroleum alteration. *AAPG Bulletin*, 68, 31–49.

T.Greibrokk**,** M.Radke**,** M.Skurdal, H.Willsch (**1992**). Multistage supercritical fluid extraction of petroleum source rocks: application to samples from Kimmeridge clay and Posidonia Shale formations, *Organic Geochemistry*, 18, 447-455.

Tannenbaum, E., Huizinga, B.J., Kaplan, I.R. (**1986**). Role of minerals in thermal alteration of organic matter--II: a material balance, *Am Assoc Pet Geol Bull*. 70 (9):1156-65.

# CHAPTER 7 Socio-Economic Studies of TMS and Community Engagement

## 7.1 Introduction

The TMS region of southwest Mississippi and Louisiana is economically distressed with a declining population, low earnings, and high unemployment. The population in the counties and parishes where hydraulic fracturing is occurring has declined by 1.9% since 2014 and is expected to decrease by 1.4% between 2019 and 2024 (EMSI 2020). Average earnings are $19,700 below national averages. Before the pandemic unemployment was up to 9.1%. The distressed region needs to find ways to increase jobs and wealth.

When considering the specific TMS region and surrounding localities, the oil and gas industry and its supply chain currently support over 5,000 well-paying jobs so it is important for the region's economy. This includes 1,916 direct industry jobs from 131 businesses. These jobs have average earnings of $96,706 which is double average earnings. The oil and gas industry is important to the region and community leaders interviewed viewed the industry favorably.

Oil and gas have been extracted from Louisiana and Mississippi since the 1900s so there is an established supply chain in the region, but the shale play is still experimental. By all standards, the TMS play is still in its infancy (Fig. 7.1). Leasing activities began in 2008. The first well began being dug in the play at the end of 2012. The shale play has opportunities and challenges (Hoffman and Borrok 2020). A few pioneering firms have moved into the area and began exploration, but most activities stopped when oil prices fell.

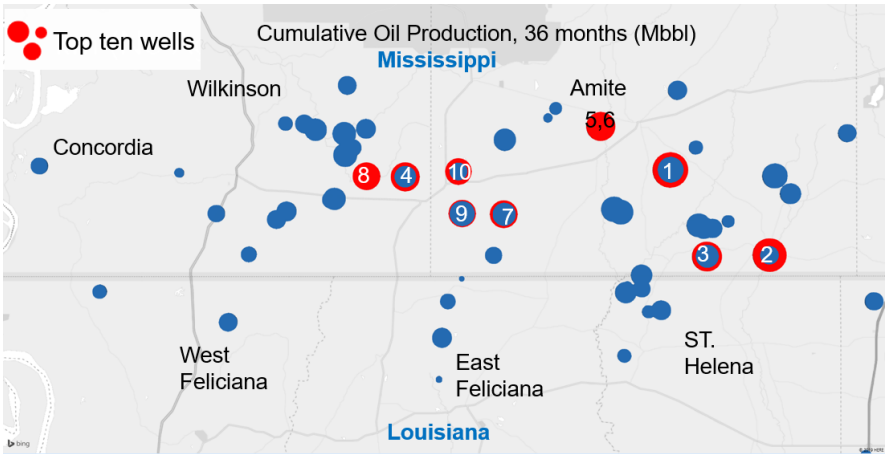


**Figure 7.1 Map of Hydraulic Fracturing Wells in the TMS.**

The hydraulic fracturing activity is focused along the border in the Mississippi counties of Wilkinson and Amite and the Louisiana parishes of West Feliciana, East Feliciana, and St. Helena. The labor shed area, where workers commute in from, includes the following parishes in

Louisiana: Allen Parish, Avoyelles Parish, Beauregard Parish, Concordia Parish, East Feliciana Parish, Evangeline Parish, Pointe Coupee Parish, Rapides Parish, St. Helena Parish, St. Landry Parish, Tangipahoa Parish, Vernon Parish, Washington Parish, and West Feliciana Parish. It also includes the following counties in Mississippi: Amite, Pike, and Wilkinson (Fig. 7.2). This labor shed area is used for target industry analysis.

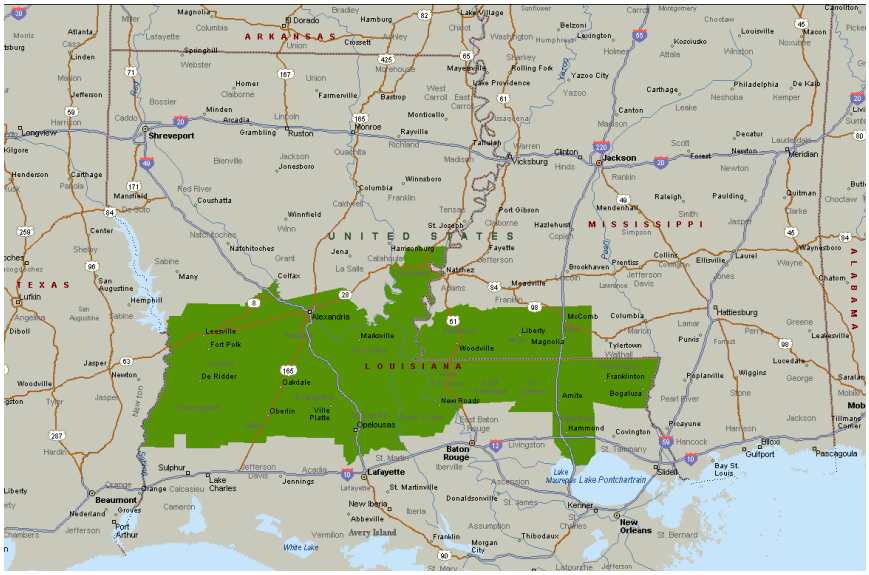


**Figure 7.2 Map of Parishes and Counties in the Study Region.**

## 7.2 Theory and/or Methods

This research uses secondary data and interviews to explore the supply chain and workforce programs coordinated by government agencies and local citizen groups to help economic developers and community leaders to operate in a cyclical shale economy environment. It utilizes benchmark and cluster gap analysis methodology compared to commercially developed regions including the Bakken, Eagle Ford, Barnett, and Haynesville shale regions for supply chain opportunities. This is combined with a methodology for regional economic development industry targeting to identify upstream and downstream industries for which the region is competitive.
The specific data tools used for this study are the EMSI Labor Analytics, Gazelle.AI. and Nexus-Uni. The supply chain targeting analysis is done with cluster gap analysis (Fig. 7.3). The target industry analysis in the report uses a modified Clemson's Regional Economic Development Research Laboratory (REDRL) industry targeting approach to screen for industries and companies with the most potential for recruitment.

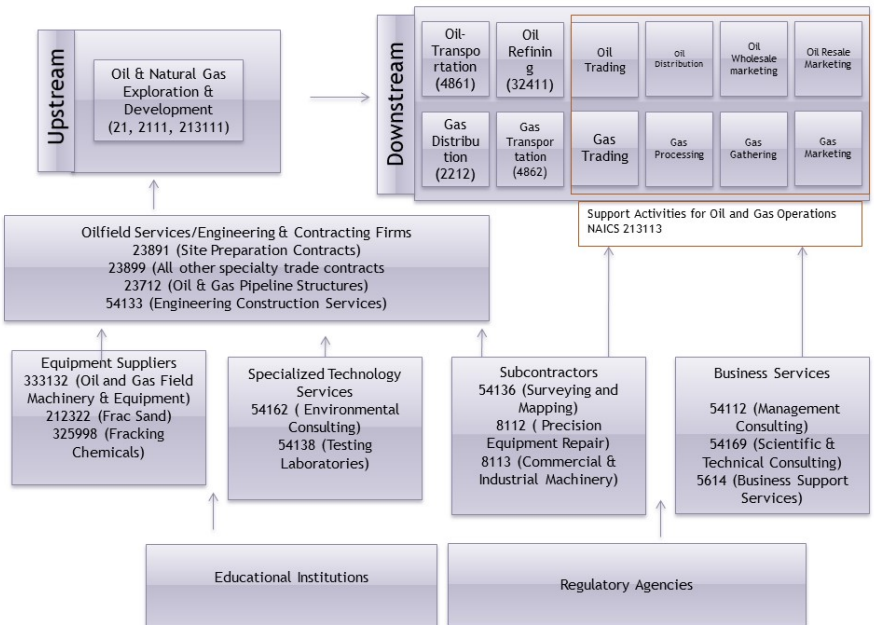


**Figure 7.3 Hydraulic Fracturing Industrial Cluster Diagram (***Source: Modified from Porter 2007***).**

## 7.3 Analysis of the Hydraulic Fracturing Supply Chain in TMS Operations Technical Report

Based on an industry concentration comparison to other regions and the cluster diagram, Oil and Gas Field Machinery and Equipment Manufacturing (333132) has significant potential to be attracted to the region (Table 7.1). Chemicals specific to hydraulic fracturing (325998) is another industry that should be explored. Specific service-related companies including Scientific and Technical Consulting Services (54169), Geophysical Surveying and Mapping Services (541360), although some interviews report that 3D seismic survey services are well covered in the area, and Environmental Consulting Services (541620) are underrepresented in the region. Upstream, Pipeline Transportation of Crude Oil (4861) is not as concentrated as expected so this could be another area for development.

**Table 7.1** Comparison of TMS Oil and Gas Supply Chain Concentrations to Established Shale Regions.

| Industries | | TMS | Established Regions | |
|---|---|---|---|---|
| | | LQ | Avg LQ | Standard Deviation |
| **Business Services (5- Digit)** | | | | |
| 54161 | Management Consulting Services | 0.24 | 0.48 | 0.31 |
| 54169 | Other Scientific and Technical Consulting Services | 0.55 | 1.35 | 0.54 |
| 56149 | Other Business Support Services | 0.40 | 0.59 | 0.65 |
| **Oilfield Services/ Engineering Contracting Firms (6- Digit)** | | | | |
| 237120 | Oil and Gas Pipeline and Related Structures Construction | 0.54 | 7.99 | 7.28 |

| | | | | |
|---|---|---|---|---|
| 238910 | Site Preparation Contractors | 1.13 | 2.06 | 0.67 |
| 238990 | All Other Specialty Trade Contractors | 1.25 | 2.44 | 2.04 |
| 541330 | Engineering Services | 0.41 | 0.60 | 0.27 |
| **Subcontractors (6- Digit)** | | | | |
| 541360 | Geophysical Surveying and Mapping Services | 0.19 | 1.24 | 0.58 |
| 811219 | Electronic and Precision Equipment Repair and Maintenance | 0.93 | 0.78 | 0.5 |
| 811310 | Commercial and Industrial Machinery and Equipment | 1.58 | 1.85 | 0.85 |
| **Support Activity for Oil and Gas Operators (4- Digit)** | | | | |
| 2212 | Natural Gas Distribution | 0.70 | 0.86 | 0.37 |
| 4861 | Pipeline Transportation of Crude Oil | 0.28 | 14.29 | 25.46 |
| 4862 | Pipeline Transportation of Natural Gas | 5.83 | 8.10 | 5.67 |
| **Support Activity for Oil and Gas Operators (5- Digit)** | | | | |
| 32411 | Petroleum Refineries | 2.09 | 0.88 | 0.68 |
| **Specialized Technology Services (6- Digit)** | | | | |
| 541380 | Testing Laboratories | 0.39 | 1.18 | 0.43 |
| 541620 | Environmental Consulting Services | 0.30 | 0.67 | 0.63 |
| **Equipment Suppliers (6- Digit)** | | | | |
| 333132 | Oil and Gas Field Machinery and Equipment Manufacturing | 0.75 | 3.00 | 2 |
| **Oil & Natural Gas Exploration and Development (6- Digit)** | | | | |
| 213111 | Drilling Oil and Gas Wells | 2.74 | 19.11 | 22.85 |
| **Oil & Natural Gas Exploration and Development (4- Digit)** | | | | |
| 2111 | Oil and Gas Extraction | 0.30 | 8.26 | 7.48 |
| **Hydraulic Fracking Supplies (6- Digit)** | | | | |
| 212322 | Frac Sand | 1.53 | 4.41 | 7.89 |
| 325998 | Hydraulic Fracturing Chemicals | 0.26 | 3.20 | 5.81 |

The hydraulic fracturing industrial cluster diagram (Fig. 7.3) frames the industries classified by the *North American Industry Classification System* (*NAICS*) which are expected to be present in developed shale regions. Employment by industry was identified in each of the four benchmark shale regions using EMSI. Location quotients (LQ), which identify the concentration of the industry, and averages for the four benchmark regions were calculated (Table 8.1). An LQ above 1.25 shows a significant concentration. By comparing LQs in an emerging shale region to developed shale regions, industries which might be attracted or developed with increased production can be identified.

Not captured in the gap analysis based on secondary data, but mentioned in industry interviews, utilities, housing, water, transportation, and frac sand are parts of the supply chain that should be further developed locally. Comparative to other shale regions, there is abundant water, but the operators in the region have high water usage. Meeting the future demand for water from increased hydraulic fracturing is a supply chain issue that needs to be planned and will require public/private efforts. Currently, frac sand is brought in from great distances so local sources of this input could potentially lower costs.

The second part of this report uses target industry analysis to identify industries with the potential to be developed or recruited to the Tuscaloosa Marine Shale region of Louisiana and Mississippi. It uses a series of screens including existing competitive industries, supply chain, regional benefit, and industry outlook. The findings from this approach can help economic developers target these types of firms for recruitment and in particular those that serve the oil and gas industry.

Target industry analysis using the screening methodology to determine the most competitive industries for attraction or development for the TMS region are in the Wood Products Manufacturing (321) and Cement and Concrete Manufacturing (3273) sectors. Within these industry sectors, the best potential for attraction and development include:

- Truss Manufacturing (321214)
- Engineered Wood Member Manufacturing (321213)
- Ready-Mix Concrete Manufacturing (327320),
- Concrete Block and Brick Manufacturing (327331)
- Concrete Pipe Manufacturing (327332)
- Other Concrete Product Manufacturing (327390).

Of these industries, companies in the Cement and Concrete Manufacturing (3273) have the most potential to be diversified suppliers (e.g., well cementing) to the oil and gas sector as it develops in the TMS.

Other industries that are growing and concentrated in the region include Pipeline Transportation of Natural Gas (4862), Support Activities for Water Transportation (4883), and Heavy and Civil Engineering Construction (2379). Local trucking is an opportunity identified in several interviews. As hydraulic fracturing increases in the TMS region, there is an opportunity to expand and develop these sectors. The existing companies in these sectors should be included in economic development organizations' business retention and expansion programs. Also, public planning for the transportation infrastructure needs of the region should begin well in advance of expanded production.

Finally, energy-intensive manufacturing industries that rely on petroleum products as a feedstock should be targeted as the region's oil and gas production expands. Cement and Concrete Manufacturing (3273) is one of these energy-intensive industries. The region already has a growing concentration of Basic Chemical Manufacturing (3251) and reducing the costs for natural gas for this industry as an input could make the region even more competitive.

### 7.4 Evaluation of Workforce Training in the Tuscaloosa Marine Shale Region

The inventory and interviews of existing workforce training programs in the TMS region found that by reaching out to adjacent communities, the region has a significant workforce training capacity. Within the region, Southwest Mississippi Community College has the Oil and Gas Production Technology program and a Well Construction program. Nearby there are five (5) more industry-specific oil and gas associate programs. There are three (3) petroleum engineering

programs in Louisiana and Mississippi. Both states have strong community college systems that offer the general and specific skills needed by the industry.

Benchmarking against more developed shale regions found the broader TMS region had competitive training programs following similar curriculums. These programs include important skills such as safety, which applies to many industries. Best practices included close ties with industry and cross-cutting knowledge areas and skills (e.g., mechanical, operation monitoring, management, etc.). Where the TMS region, with a 50% black and 47% white population, could standout is to promote diversity in the industry, which is 78% white and 73% male (Table 7.2).

**Table 7.2** Racial Make-Up of Industry Compared to TMS Region **(***Source: EMSI 2019***).**

| Race/Ethnicity | Jobs | Percent of Industry Workforce | TMS Population |
|---|---|---|---|
| White | 111,506 | 77.50% | 46.91% |
| Hispanic or Latino | 18,269 | 12.70% | 1.19% |
| Black or African American | 6,075 | 4.20% | 49.59% |
| Asian | 4,865 | 3.40% | 0.40% |

The skills competency model and skills transferability matrix identified construction as a closely aligned industry based on knowledge, skills, and abilities (KSAs). Important knowledge needed includes mathematics and engineering technology; skills needs include operation control, critical thinking, quality control, and monitoring (Table 7.3). Ability needs include perceptual speed, oral comprehension, and problem sensitivity. All these skills, with further workforce training, can be applied to the targeted industries.

**Table 7.3** Skill Competency Model for Main Industry Occupation **(***Source: EMSI 2020***).**

| Competency | Level | Competency | Level | Competency | Level |
|---|---|---|---|---|---|
| *Knowledge* | | *Skill* | | *Ability* | |
| Mechanical | 61 | Operation Monitoring | 68 | Perceptual Speed | 57 |
| Education and Training | 50 | Operation and Control | 55 | Oral Comprehension | 55 |
| Mathematics | 46 | Critical Thinking | 54 | Problem Sensitivity | 55 |
| Engineering and Technology | 42 | Quality Control Analysis | 54 | Inductive Reasoning | 54 |
| Public Safety and Security | 42 | Monitoring | 54 | Oral Expression | 54 |

Improving local hiring opportunities will be challenging, and workforce training is important. However, improving K-12 education and soft skills will be even more important as those are the foundations of workforce development. This can be challenging because the earning opportunities of shale booms influence traditional education decisions. Carpenter et al. (2019) concluded drilling increases immigrant high school dropout rates but has insignificant overall effects, while other studies found reductions in high school attainment and enrollment (Cascio and Narayan 2015; Rickman et al. 2017). The region's workforce in general lags competitive regions so improving the educational pipeline is essential.

Combining the findings of the two reports on target industries for attraction and development along with an analysis of workforce programs shows that the skills needed for the oil and gas are complementary to the needs of industries that the TMS region could target. When designing workforce programs this transferability needs to be considered. Also, the supply chain, which creates significantly more local jobs than the extraction itself, should be the focus.

Many shale plays within the United States, such as the Bakken and Eagle Ford Shale Plays, have experienced population growth and job creation. However, studies indicate most of the job gains are attributable to non-resident workers who temporarily migrate to the region (Wrenn, et al. 2015). Some job creation is attributable to locals hires mostly through supply chain employment. Non-resident workers in shale regions, specifically the Bakken, account for most of the jobs in oil field development activities such as drilling, hydraulic fracturing, construction, and other specialized construction (Hodur and Bangsund 2016). The itinerate nature of the industry creates challenges for creating lasting employment for residents unless they are in diversified industries.

The TMS has few assets. The oil and gas industry is one of those assets. Should the shale play in the region become economical, that would be a significant asset upon which to build economic growth. However, the nature of the shale economy requires that community leaders take a business cycle management perspective (Miller and Bolton 2015). They need to be planning now for the future of a post-pandemic recovery.

The approach of identifying target industries for development and attraction can be utilized by other regions. This methodology can help rural regions more efficiently and effectively use their economic development resources. The approach can further be refined to help identify industries for growth based on the phases of shale development. This research was based on fully developed regions, but in practice industries will want to locate in a region only when certain levels of activity are reached.

Once the community knows what industries are going to be needed by expanded oil and gas extraction, economic development programs can be put in place. As part of business retention and expansion (BRE) programs, existing industries can be made aware of opportunities to expand production and service lines to meet the growing local needs of the oil and gas industry. Entrepreneurs can be encouraged to fill gap needs. Working with the state economic development organization, businesses can be attracted to set up facilities in the region to supply the increase in oil and gas extraction. Finally, once the region has steady production levels, energy-intensive manufacturing concerns can be attracted.

In addition to establishing programs to spinoff economic development supply chain opportunities, communities should work closely with the shale operators. They need to become part of a well-developed BRE program, so the community is aware of the industry needs and concerns. Identifying workforce needs and conveying those KSAs to the workforce development programs (e.g., community colleges) should be a priority.

Workforce has become the most important component of economic development. Economic developers need to focus on talent development with a long-term perspective. A region cannot be successful unless it develops a workforce pipeline that fits with its current and future industry

needs. This requires having the training and education systems in place to respond to current and future industry needs.

### *References:*


Carpenter, C. W., Anderson, D., & Dudensing, R. 2019. The Texas Drilling Boom and Local Human Capital Investment. *Journal of Agricultural and Applied Economics,* **51**(2), 199-218.

Cascio, E. U., & Narayan, A. (2015). *Who Needs a Fracking Education? The Educational Response to Low Skill Biased Technological Change*, Washington, DC: National Bureau of Economic Research.

EMSI: Labor Market Analytics, 2020. Moscow, Idaho.

Hodur, N. M., and Bangsund, D. A. 2016. Assessment of the Oil and Gas Industry Workforce *Agribusiness & Applied Economics Report 748*. Fargo, ND: North Dakota State University

Hoffmann, A. A., and Borrok, D. M. 2020. The geochemistry of produced waters from the Tuscaloosa Marine Shale, USA. *Applied Geochemistry*, 104568-104578.

Miller, C., and Bolton, J. F. 2015. Economic Development Strategies for Fracking. *The Journal of Energy and Development,* **41**(1/2), 201-222

Miller, C., and Johnson, R. 2019. *Subtask 8.1 Analysis of the Hydraulic Fracturing Supply Chain in TMS Operations,* Tuscaloosa Marine Shale Laboratory Hattiesburg, MS: University of Southern Mississippi College of Business & Economic Development.

Miller, C., and Willis, J. 2020. *Subtask 8.3 Evaluation of Workforce Training in the Tuscaloosa Marine Shale Region,* Tuscaloosa Marine Shale Laboratory Hattiesburg, MS: University of Southern Mississippi College of Business & Economic Development.

Porter, M. 2007. *The Houston Oil and Gas Cluster*, Cambridge, MA: Harvard Business School.

Rickman, D. S., Wang, H., & Winters, J. V. 2017. Is Shale Development Drilling Holes in the Human Capital Pipeline? *Energy Economics,* **62**, 283-290.

Wrenn, D. H., Kelsey, T. W., and Jaenicke, E. C. 2015. Resident vs. Nonresident Employment Associated with Marcellus Shale Development. *Agricultural and Resource Economics Review,* **44** (2), 1-19.

# Chapter 8 Technology Transfer

A considerable number of papers and presentations were generated in the pursuit of this research project. These include:

### Peer-Reviewed Journal Publications

1. F. Nath, R.J. Kimanzi, M. Mokhtari, S. Salehi. **2018**. A novel method to investigate cement-casing bonding using digital image correlation, *Journal of Petroleum Science and Engineering*, 166, 482-489.

2. Boyun Guo, Xu Yang, **2019**. Use of a New Analytical Model to Match Production Data and Identify Opportunities to Maximize Well Productivity in the Tuscaloosa Marine Shale Reservoir. *SPE Production & Operations* 34, 770-780.

3. Borrok, D.M., Yang, W., Wei, M., and Mokhtari, M., **2019**. Heterogeneity of the Mineralogy and Organic Content of the Tuscaloosa Marine Shale, *Marine and Petroleum Geology*, 109, 717-731.

4. Yang, X., Guo, B., Mokhtari, M. **2019**. Productivity analysis of multi-fractured shale oil wells accounting for the low-velocity non-Darcy effect, *Journal of Petroleum Science and Engineering*, 183, 106427.

5. Fu, C., and Liu, N., **2019**. Waterless fluids in hydraulic fracturing – A Review. *Journal of Natural Gas Science and Engineering*, 67, 214-224.

6. Yang, X., Guo, B., Zhang, X., **2019**. An Analytical Model for Capturing the Decline of Fracture Conductivity in the Tuscaloosa Marine Shale Trend from Production Data, *Energies*, 12, 1938.

7. Yang, X., and Guo, B., **2019.** A Data-Driven Workflow Approach to Optimization of Fracture Spacing in Multi-Fractured Shale Oil Wells, *Energies*, 12, 1973.

8. Kramarov V. Parrikar P.N. and Mokhtari M., **2020**. Evaluation of Fracture Toughness of anisotropic Rocks using Digital Image Correlation and Semi-Circular Bend Test, *Rock Mechanics and Rock Engineering* 53, 4231-4250.

9. Ahmadov, Jamal, Mehdi Mokhtari, **2020**. Experimental evaluation of ultrasonic velocities and anisotropy in the Tuscaloosa Marine Shale Formation. *Interpretation* 8, SL113-SL125.

10. Ruse C., and Mokhtari M., **2020**, Characterization of Elastic Mechanical Properties of Tuscaloosa Marine Shale from well Logs using VTI Model, *Interpretation* 8, T1023–T1036.

11. Mark Mlella, Ming Ma, Rui Zhang, Mehdi Mokhtari, **2020**. Machine learning for geophysical characterization of brittleness: Tuscaloosa marine shale case study. *Interpretation*, 8, T589-T597.

12, Guo, B., Shaibu, R., & Hou, X., **2020**. Crack Propagation Hypothesis and a Model To Calculate the Optimum Water-Soaking Period in Shale Gas/Oil Wells for Maximizing Well Productivity, *SPE Drilling & Completion*, 35, 655-667.

13. Huang, Z.; Guo, B.; Shaibu, R., **2020**. Lab-Supported Hypothesis and Mathematical Modeling of Crack Development in the Fluid-Soaking Process of Multi-Fractured Horizontal Wells in Shale Gas Reservoirs, *Energies,* 13, 1035.

14. Hoffmann A.A., Borrok D., **2020**, The geochemistry of produced waters from the Tuscaloosa Marine Shale, USA, *Applied Geochemistry*, 104568.

15. Kimanzi, R., Wu, Y., Salehi, S., Mokhtari, M., Khalifeh, M., **2020**. Experimental Evaluation of Geopolymer, Nano-Modified, and Neat Class H Cement by Using Diametrically Compressive Tests. *J. Energy Resour. Technol*. 142(9), 092101.

16. Zhang, H., Nath, F., Parrikar, P., Mokhtari, M., **2020**. Analyzing the Validity of Brazilian Testing Using Digital Image Correlation and Numerical Simulation Techniques, *Energies*, 13(6), 1441.

17. Wu Y., Patel H., Salehi S., Mokhtari M., **2020**. Experimental and Finite Element Modelling Evaluation of Cement Integrity under Diametric Compression, *Journal of Petroleum Science and Engineering*, 188, 106844.

18. Xu Yang, Boyun Guo, **2020**. Statistical analyses of reservoir and fracturing parameters for a multifractured shale oil reservoir in Mississippi. *Energy Sci Eng*. 8, 616-626.

19. C. Fu, N. Liu, **2020**. Study the synergistic effect of nanoparticle-surfactant-polymer on $CO_2$ foam rheology and stability under high pressure and temperature, *Energy & Fuels*, 34,13707-13716.

20. Konate, N.; Salehi, S., **2020**. Experimental Investigation of Inhibitive Drilling Fluids Performance: Case Studies from United States Shale Basins. *Energies*, *13*, 5142.

22. Rashid Shaibu, Boyun Guo. **2021**. The Dilemma of Soaking a Hydraulically Fractured Horizontal Shale Well Prior to Flowback – A Decade Literature Review. *Journal of Natural Gas Science and Engineering,* 94, 104084.

23. Boyun Guo, Chunkai Fu, Ning Liu, **2021**. A Transient Flow Solution to Describe Fluid Flow to Horizontal Fractures Applied to Frac-Packed Wells. *Energy Science & Engineering,* 9, 1935–1945.

24. Rashid Shaibu, Boyun Guo, Philip Wortman, Jim Lee, **2022**. Stress-Sensitivity of Fracture Conductivity of Tuscaloosa Marine Shale cores. *Journal of Petroleum Science and Engineering*, 210, 110042.

## Conference Publications

1. Naik Parrikar P., Zhang H., and Mokhtari M., Evaluation of tensile properties of transversely isotropic rocks using Brazilian disc test and digital image correlation, International Digital Image Correlation Society Conference, October **2019**.

2. Kramarov V., Naik Parrikar P., and Mokhtari M., Evaluation of fracture toughness of laminated rocks using digital image correlation, International Digital Image Correlation Society Conference, October **2019**.

3. Borrok, D.M. Improved utilization of discrete and heterogeneous petrophysical data: An example from the Tuscaloosa Marine Shale. Presented at the U.S. DOE's Addressing the nation's energy needs through technology innovation – **2019** review meeting in Pittsburgh, PA.

4. Kimanzi, R.J., Harshkumar, P., Salehi, S., Teodoriu, C. and Khalifeh, M. 2019. Potentials of Nano-designed plugs: Implications for short and long term well integrity. 38th International Conference on Ocean, Offshore and Arctic Engineering, 9-14 June, **2019**.

5. Hoffmann, A.A., Thompson A., Borrok, D.M. The origin and evolution of produced waters from the Tuscaloosa Marine Shale in Mississippi and Louisiana. Geological Society of America Joint Regional Meeting, Manhattan, Kansas, March 25-27, **2019**.

6. Borrok, D.M., Hoffmann, A.A., Wei, M., Yang, W. Heterogeneity of the mineralogy and organic content in the Tuscaloosa Marine Shale. Geological Society of America Joint Regional Meeting, Manhattan, Kansas, March 25-27, **2019**.

7. Konate, N., Ezeakacha, C. P., Salehi, S., and Mokhtari, M., Application of an Innovative Drilling Simulator Set Up to Test Inhibitive Mud Systems for Drilling Shales. SPE Oklahoma City Oil and Gas Symposium at Oklahoma City, Oklahoma, USA, on 9-10 April, **2019**.

8. Kiran, R., Salehi, S., Mokhtari, M., and Kumar, A., Effect of Irregular shape and Wellbore Breakout on Fluid Dynamics and Wellbore Stability. 53rd US Rock Mechanics/Geomechanics Symposium. American Rock Mechanics Association **2019**.
9, Chavez N.A., Chuprin M., Mokhtari M., Nath F., Evaluation of Tuscaloosa Marine Shale stability using Capillary suction time and Roller Oven Tests, Unconventional Recourses Technology Conference (URTeC), Houston, Texas, July 20-22, **2020**.

10. Mokhtari M., Parrikar P., Saidzade A. Microscopic Measurement of Shale Swelling: Impact Of Salinity, Unconventional Recourses Technology Conference (URTeC), Houston, Texas, July 20-22, **2020**.

11. Mokhtari M., Ezeakacha C., Storage and Flow Properties of an Oil-Prone/Clay-Rich Shale Play: Tuscaloosa Marine Shale, Unconventional Recourses Technology Conference (URTeC), Houston, Texas, July 20-22, **2020**.

12. Saidzade A., Parrikar P., Mokhtari M., Experimental Investigation of Main Factors Affecting Spontaneous Imbibition in Shales, Unconventional Recourses Technology Conference (URTeC), Houston, Texas, July 20-22, **2020**.

13. Miller C., Economic and Workforce Development in Rural Shale-Based Economies, Unconventional Recourses Technology Conference (URTeC), Houston, Texas, July 20-22, **2020**.

14. Parrikar P.N., Mokhtari M., Analysis of Brazilian Disc test Experiments using Digital Image Correlation, 54th US Rock Mechanics/Geomechanics Symposium. American Rock Mechanics Association, Golden, Colorado, 28 June- 1 July, **2020**.

15. Konate, N., Magzoub, M., Salehi, S., Ghalambor A., Mokhtari M., Laboratory Evaluation of Mud Systems for Drilling High Clay Shales in Dynamic Conditions: Comparison of Inhibitive Systems. Paper presented in SPE International Conference and Exhibition on Formation Damage Control at Lafayette, Louisiana, on February 19-21, **2020**.

16. Yang, W., Borrok, D.M., Mokhtari, M., Depositional environments and stratigraphic hierarchy of upper cretaceous Tuscaloosa Marine Shale in central U.S. Gulf Coast - A core observation: Geological Society of America Abstracts with Programs. Vol 52, No. 6, **2020**.

17. Wu, Y. and Salehi, S. A Numerical and Experimental Study On Cement Integrity Based On a Novel Method. ARMA 54th us rock mechanics/geomechanics symposium, June 28-July 1, **2020**.

18. Wu, Y. and Salehi, S. Numerical Study of Well Integrity in High-Temperature Wells. ARMA 54th us rock mechanics/geomechanics symposium, June 28-July 1, **2020**.

19. Wu, Y. and Salehi, S. The Effect of Pressure Cycling on the Development of Micro-Annulus in Cement Sheath. Unconventional Resources Technology Conference, July 20-22, **2020**.

20. D. M. Borrok, W. Yang, M. Mokhtari, H. Beitel, 2020, New Insights into the Mineralogy and Organic Content of the Tuscaloosa Marine Shale. AAPG Annual Meeting, Houston, TX, (**2020**).

21. Borrok, D.M., Yang, W., Mokhtari, M., Beitel, H. New insights into the mineralogy and organic content of the Tuscaloosa Marine Shale. American Association of Petroleum Geologists Annual Convention and Exhibition (September 30, **2020** Houston, TX).

22. Hoffman, A., and Borrok, D.M. Experimental physiochemical investigation of high-temperature brine-shale interactions. Geological Society of America Joint 55th annual North-Central/South Central Meeting (**2021)**.

23. Ruse, C.M., Ahmadov, J., Liu, N., Mokhtari M. An integrated analytics and machine learning solution for predicting the anisotropic static geomechanical properties of the Tuscaloosa Marine Shale. Unconventional Resources Technology Conference (URTec: 5625) (**2021**).

24. S M Shamsul Hoque, Rui Zhang, TOC estimation of Tuscaloosa Marine Shale (TMS) using multiattribute analysis, IMAGE **2021** Conference in Denver.

## Thesis and Dissertation

1. Kimanzi, R., **2019**. Experimental Investigation of the cement bond integrity by application of digital image correlation (DIC) technique, M.Sc. Thesis, University of Oklahoma.

2. Nippes, V., **2019**, Production Behavior and Decline Curve Analysis of Tuscaloosa Marine Shale Wells in Wilkinson and Amite Counties Mississippi, M.Sc. Thesis, University of Louisiana at Lafayette.

3. Ruse C., **2020**, Characterization of Elastic Mechanical Properties of Tuscaloosa Marine Shale from Well Logs using the VTI Method, M.Sc. Thesis, University of Louisiana at Lafayette.

4. Kramarov V., **2020**, Fracture Toughness Determination and Strain analysis of anisotropic rocks using Semicircular Bend Test and Digital Image Correlation, M.Sc. Thesis, University of Louisiana at Lafayette.

5. Mlella M., **2020**, Geophysical Characterization of Unconventional reservoir Properties using Machine Learning Techniques, a Case study from Tuscaloosa Marine Shale, M.Sc. Thesis, University of Louisiana at Lafayette.

6. Konate N., **2020**, Experimental Investigation of Shale-Drilling Fluid Interaction and Implications on Drilling Efficiency, M.Sc. Thesis, University of Oklahoma.

7. Xu Yang, **2020**, Production Data Analysis and Potential Evaluation of Tuscaloosa Marine Shale Oil Wells. PhD thesis, University of Louisiana at Lafayette, Lafayette, LA.

8. Md Nahin Mahmood, **2020**, Optimization of Perforation Cluster Spacing in Multi-Fractured Horizontal Wells in Shale Oil Reservoirs. MS thesis, University of Louisiana at Lafayette, Lafayette, LA.

9. Beitel, Hayley, **2021**, Relationships among mineralogy, geochemistry, and oil and gas production in the Tuscaloosa Marine Shale. MS thesis in University of Missouri Science and Technology.

10. Wu, Y., **2021**. Investigation of Short-Term and Long-Term Cement Integrity: An Advanced Computational Modelling Study. PhD Thesis. The University of Oklahoma, Norman, OK.

11. Konate, N., **2021**. Experimental Investigation of Shale-drilling Fluid Interaction and Its Implications on Drilling Efficiency. Master Thesis. The University of Oklahoma, Norman, OK.

12. Chunkai Fu, **2021**, A Laboratory Assessment and Optimization of Nanoparticle-Stabilized $CO_2$ Foams for Hydraulic Fracturing Applications. PhD Thesis, University of Louisiana at Lafayette, LA

13. Konate, N., **2020**, Experimental Investigation of Shale-Drilling Fluid Interaction and Its Implication on Drilling Efficiency. MS Thesis ,University of Oklahoma

14. Rashid Shaibu, **2021**, Fracture Conductivity, Cracking, and Proppant Embedment of Tuscaloosa Marine Shale Formation Cores. PhD thesis. University of Louisiana at Lafayette, Lafayette, LA.